Technische Universität München
TUM School of Natural Sciences

Applied Photoemission Chronoscopy

Christian Andreas Schröder, M. Sc.

Vollständiger Abdruck der von der TUM School of Natural Sciences der Technischen Universität München zur Erlangung eines

Doktors der Naturwissenschaften (Dr. rer. nat.)

genehmigten Dissertation.

Vorsitz: Prof. Dr. Michael Knap

Prüfer*innen der Dissertation:

1. Prof. Dr. Reinhard Kienberger
2. Prof. Dr. Franz Pfeiffer

Die Dissertation wurde am 30.05.2023 bei der Technischen Universität München eingereicht und durch die TUM School of Natural Sciences am 30.06.2023 angenommen.

"Find full reward Of doing right in right!
Let right deeds be Thy motive, not the fruit which comes from them."
– Bhagavad Gita [1], Chapter II

Contents

Zufammenfassung

In dieser Promotionsschrift werden Experimente zur Photoemissionschronoskopie an ausgewählten Systemen vorgestellt. Photoemissionschronoskopie ist die Messung der Zeitverzögerung zwischen der Absorption eines Photons aus dem Spektralbereich des extremen Ultravioletts (XUV) durch ein Atom, ein Molekül oder einen Festkörper und das Erscheinen eines Photoelektrons im Vakuum. Bei Anregung mit XUV-Licht ist diese zeitliche Verzögerung in der Größenordnung von einigen bis einigen zehn Attosekunden ($1\,\mathrm{as} = 10^{-18}\,\mathrm{s}$). Die Messung derart schneller Prozesse erfordert selbstverständlich spezialisierte experimentelle Werkzeuge.

Voraussetzung für ein Photoelektronenspektroskopie-Experiment mit Zeitauflösung im Bereich der Attosekunden ist eine Strahlungsquelle, die XUV-Licht mit sub-Femtosekunden ($1\,\mathrm{fs} = 10^{-15}\,\mathrm{s}$) Zeitstruktur erzeugt. Höchstnichtlineare Frequenzaufkonversion von Laserpulsen mit einer Dauer von nur wenigen Femtosekunden und darauffolgendes spektrales und räumliches Filtern ermöglicht es XUV Lichtpulse mit einer Dauer von wenigen hundert Attosekunden zu erzeugen. Diese lösen Elektronen aus dem zu untersuchenden System heraus, welche dann durch den nach der Aufkonversion verbleibenden Teil des Laserpulses in ihrer kinetischen Energie moduliert werden. Diese Modulation bildet die zeitlichen Eigenschaften des herausgehenden Wellenpaketes auf Photoelektronen-Energiespektren ab, welche als Funktion der interferometrisch variierbaren Verzögerungszeit zwischen XUV und Laserpuls aufgnenommen werden.

Die erste Gruppe an Systemen die Untersucht werden sind die Iodalkane, beginnend mit Iodmethan bis hin zu 2-Iodbutan. Unter Benutzung einer kürzlich entwickelten Referenzierungstechnik kann die absolute Photoemissionszeit, d.h. die Zeit zwischen Photonenabsorption und Elektronenemission, des I4d-Kernniveaus im energetischen Bereich der *giant resonance* im I4$d \rightarrow \varepsilon f$ Photoemissionskanals gemessen werden, um zu untersuchen wie sich die Verzögerungszeit der I4d-Emission bei Austausch des Elternmoleküls verhält. Dies ist, soweit unser Wissen geht, die erste systematische Studie dieser Art und dieses Umfangs. Es ergeben sich aus dem Experiment große Unterschiede von bis zu (23 ± 4) as in der I4d-Emissionszeit zwischen den kleineren Iodalkanen, welche in ihrer Ursache starker intra-molekularer Streuung des ausgehenden Photoelektronen-Wellenpakets zugeschrieben werden. Solche Unterschiede fehlen in den größeren Iodalkanen fast vollständig. Die dort gemessene Photoemissionszeit ist von nahezu ausschließlich atomarem Charakter, was durch Verlgleich mit einer atomaren Rechnung der I4d auf hohem theoretischem Niveaus, als auch durch die Auswertung der *giant resonance* im Rahmen eines Einelektronenmodells welches dann einen mit spektroskopischen Daten in guter qualitativer Übereinstimmung liegenden Wirkungsquerschnitt ergibt, bestätigt wird.

Desweiteren wird über die Photoemissionsdynamik der Wolfram (110)-Oberfläche berichtet. Diese ist – schließlich wurde an ihr die erste Photoemissionszeitmessung überhaupt vorgenommen[1] – ein Vorzeigesystem der Attosekundenphysik. Dennoch hat sich die Anregungsenergieabhängigkeit ihrer Photoemissionsdynamiks seither einer konsistenten Interpretation verwehrt. Eine kürzlich entwickelte *ab-initio* Theorie der Photoemissionszeiten an Oberfächen entwickelt von R. Kuzian und E. E.

---

[1] Cavalieri, A., Müller, N., Uphues, T. *et al.* Attosecond spectroscopy in condensed matter. *Nature* **449**, 1029–1032 (2007). `https://doi.org/10.1038/nature06229`

Krasovskii ist aber im Stande die experimentellen Ergebnisse zu erklären. Diese Theorie erlaubt die Auffassung der Photoemissionszeit an einer Oberfläche im Rahmen des Formalismus von Eisenbud, Wigner und Smith. Dadurch wird die konzeptionelle Lücke die seither zwischen der Interpretation von Photoemissionschronoskopie-Experimenten die in Atomen und Molekülen durchgeführt werden und denen die an Festkörpern unternommen werden geschlossen.

Abstract

This thesis reports systematic photoemission chronoscopy measurements on select physical systems. Photoemission chronoscopy is the measurement of the temporal delay between the absorption of an extreme-ultraviolet (XUV) photon by an atom, molecule or solid and the appearance of an ejected photoelectron in vacuum. For excitation within the XUV region of the electromagnetic spectrum this time delay is on the scale of single to tens of attoseconds ($1\,\mathrm{as} = 10^{-18}\,\mathrm{s}$), and its measurement consequently requires specialized experimental tools.

Attosecond temporal resolution in a photoelectron experiment requires a radiation source emitting XUV light with sub-femtosecond ($1\,\mathrm{fs} = 10^{-15}\,\mathrm{s}$) temporal structure. Highly nonlinear frequency upconversion of few-femtosecond laser pulses and subsequent spectral and spatial filtering is used to generate isolated XUV pulses of a few hundred attoseconds in duration. These initiate photoemission on the system under study, and the emanating photoelectron wave-packet is subjected to a modulation of its kinetic energy by the remainder of the co-propagating and accurately synchronized laser pulse, which encodes the temporal characteristics of the outgoing wave packet into a sequence of photoelectron spectra recorded as a function of an interferometrically variable time delay between the two pulses.

The first systems under study are the iodoalkanes from iodomethane to 2-iodobutane. Using a recently developed referecing scheme the absolute photoemission time delay (i.e. the time elapsing between photon absorption and electron emission) of the I$4d$ is measured across the giant resonance in the I$4d \to \varepsilon f$ photoemission channel in order to explore the changes in the photoemission time of a core-level brought about by a change of the host molecule. This is, to our knowledge, the first extensive and systematic study of its kind. Large differences in the I$4d$ emission delay of up to (23 ± 4) as are found in the smaller iodoalkanes which are attributed to intra-molecular scattering of the outgoing photoelectron wave packet. Such differences are, however, completely absent in the larger molecules. The photoemission delays observed there show almost purely atomic character, as confirmed via comparison with an accurate calculation as well as via the evaluation of a single-particle model of the giant resonance solely from the time domain, which yields a resonance cross section in good qualitative accord with spectroscopic data.

The second system reported on is the tungsten (110) surface. It is – due to being the first system on which a photoemission time delay has ever been recorded experimentally[1] – a poster child of attosecond physics, but the energy dependence of its photoemission dynamcis has so far eluded an explanation from first principles. A recently developed *ab-initio* theory of photoemission times at metal surfaces due to R. Kuzian and E. E. Krasovskii is, however, capable of explaining the experimental observations. This theory enables the interpretation of photoemission times measured in condensed matter systems within the framework of the Eisenbud-Wigner-Smith delay time. This closes the conceptual gap that has since existed in the interpretation of photoemission timing measuremens on atoms and molecules and those perfomed on condensed matter.

---

[1] Cavalieri, A., Müller, N., Uphues, T. *et al.* Attosecond spectroscopy in condensed matter. *Nature* **449**, 1029–1032 (2007). `https://doi.org/10.1038/nature06229`

List of publications

Attosecond dynamics of photoemission over a wide photon energy range

Christian A. Schröder, Johann Riemensberger, Roman Kuzian, Marcus Ossiander, Dyonisios Potamianos, Francesco Allegretti, Luca Bignardi, Silvano Lizzit, Ayman Akil, Adrian Cavalieri, Dietrich Menzel, Stefan Neppl, Raph Ernstorfer, Jürgen Braun, Hubert Ebert, Jan Minar, Wolfram Helml, Michael Jobst, Michael Gerl, Elisabeth Bothschafter, Andreas Kim, Konrad Hütten, Ulf Kleineberg, Maximilian Schnitzenbaumer, Johannes Barth, Peter Feulner, Eugene Krasovskii, Reinhard Kienberger

submitted to *Nature*

Attosecond Dynamics of *sp*-Band Photoexcitation

Johann Riemensberger, Stefan Neppl, Dionysios Potamianos, Martin Schäffer, Maximilian Schnitzenbaumer, Marcus Ossiander, Christian Schröder, Alexander Guggenmos, Ulf Kleineberg, Dietrich Menzel, Francesco Allegretti, Johannes V. Barth, Reinhard Kienberger, Peter Feulner, Andrei G. Borisov, Pedro M. Echenique, and Andrey K. Kazansky

Phys. Rev. Lett. 123, 176801 (2019)

Deep learning in attosecond metrology

Christian Brunner, Andreas Duensing, Christian Schröder, Michael Mittermair, Vladimir Golkov, Maximilian Pollanka, Daniel Cremers, and Reinhard Kienberger

Opt. Express 30, 15669-15684 (2022)

Photoemission chronoscopy of the Iodoalkanes

Christian Schröder, Maximilian Pollanka, Andreas Duensing, Michael Mittermair, Pascal Scigalla, Matthias Ostner, and Reinhard Kienberger

in preparation[†]

Probing photoemission times in well-aligned molecules on a surface

Pascal Scigalla, Sven Paul, Christian Schröder, Peter Feulner, Reinhard Kienberger

in preparation[†]

[†] title and author list may be subject to changes

Photoemission delays in molecular systems of similar size

Christian Schröder, Maximilian Forster, Maximilian Pollanka, Andreas Duensing, Michael Mittermair, Pascal Scigalla, Matthias Ostner, and Reinhard Kienberger

in preparation[†]

Molecular Photoionization Delay Across the Phase Transition into the Solid

Michael Mittermair, Andreas Duensing, Maximilian Pollanka, Christian Schröder, and Reinhard Kienberger

in preparation[†]

Photoionization dynamics of the $2a1$ **state in** H_2O

Andreas Duensing, Michael Mittermair, Maximilian Pollanka, Christian Schröder, and Reinhard Kienberger

in preparation[†]

[†] title and author list may be subject to changes

List of presented conference contributions and invited seminar talks

Photoemission Chronoscopy of the Iodoalkanes

Christian Schröder, Maximilian Pollanka, Pascal Scigalla, Andreas Duensing, Michael Mittermair, Maximilian Forster, Matthias Ostner and Reinhard Kienberger

Oral presentation, DPG SAMOP Hannover, 2023

Molecular environments in the time-domain

Christian Schröder, Maximilian Pollanka, Pascal Scigalla, Michael Mittermair, Andreas Duensing, Martin Wanckel and Reinhard Kienberger

Oral presentation, DPG SAMOP Erlangen, 2022

Photoemission Chronoscopy of the Iodoalkanes

Christian Schröder, Maximilian Pollanka, Michael Mittermair, Andreas Duensing, Alexandra Landsman, Liang-Wen Pi and Reinhard Kienberger

Poster, ECAMP14 Vilnius, 2022

Photoemission Chronoscopy of the Iodoalkanes

Christian Schröder, Maximilian Pollanka, Michael Mittermair, Andreas Duensing, Alexandra Landsman, Liang-Wen Pi and Reinhard Kienberger

Poster, ATTO VIII Orlando, 2022

Experimental Aspects of Attosecond Streaking Spectroscopy

Christian Schröder, Maximilian Pollanka, Pascal Scigalla, Michael Mittermair, Andreas Duensing, Matthias Ostner, Maximilian Forster and Reinhard Kienberger

invited seminar talk
Group of Zdeněk Mašín
Institute of Theoretical Physics, Charles University Prague
Oct. 03, 2022

Molecular Photoemission Chronoscopy

Christian Schröder, Maximilian Pollanka, Pascal Scigalla, Michael Mittermair, Andreas Duensing, Matthias Ostner, Maximilian Forster and Reinhard Kienberger

invited seminar talk
Group of Stephen Leone
College of Chemistry, UC Berkeley
Jan. 24, 2023

Units, conventions and acronyms

Units

Unless specified otherwise, Hartree atomic units [2] are used in all calculations. Numerical values, however are converted to the more familiar units of electronvolts, atto- and femtoseconds and Ångstrom (occasionally nanometers or micrometers). The table below gives some useful conversion coefficients (taken from [3]) used in this work.

Dimension	conversion from atomic units
atomic unit of energy	27.211385 eV
atomic unit of time	24.188843 as
atomic unit of length	0.529177 Å

False-color plots

Two-dimensional data sets are, unless explicitly stated otherwise, plotted with a linear color scale and either normalized to their maximum value, or, if a differential quantity is shown, normalized to the absolute maximum difference and use one of the following two color maps.

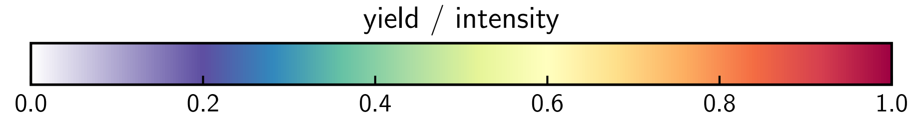

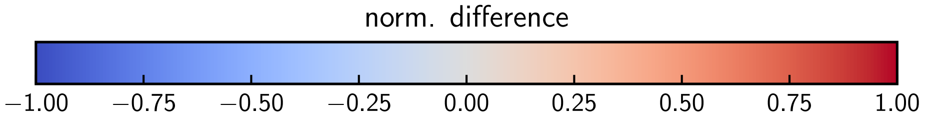

Acronyms

NIR near infrared

VIS visible

XUV extreme ultraviolet

SXR soft x-ray

FWHM full-width at half-maximum

CEP carrier-to-envelope phase

GVD group velocity dispersion

GDD group delay dispersion

GD group delay

SHG second harmonic generation

DFG difference frequency generation

HHG high-order harmonic generation

EWS Eisenbud-Wigner-Smith

CLC Coulomb-laser-coupling

WPA wave packet approximation

FT Fourier transform

FFT fast Fourier transform

rTDSE restricted time-dependent Schrödinger equation

COE center-of-energy

RHF restricted Hartree-Fock

SCF self-consistent field

CCD charge-coupled device

TOF time-of-flight (spectrometer)

UHV ultra-high vacuum

LEED low-energy electron diffraction

ePIE extended ptychographic iterative engine

CMA central-momentum-approximation

RABBITT reconstruction of attosecond beating by interference of two-color transitions

TIPTOE tunneling ionization with a perturbation for the time-domain observation of an electric field

Chapter 1

Introduction

Photoemission, i.e. the release of an electron from an atom, molecule or solid upon irradiation with sufficiently energetic light, is one of the processes the observation of which sparked the developement of quantum theory. First observed in experiments by Hertz [4] and Hallwachs [5], the phenomenon's interpretation is due to Albert Einstein [6], who in the context of photoemission from metal surfaces brought the relationship

$$E_{\mathrm{kin}} = hf - W \tag{1.1}$$

between the kinetic energy E_{kin} of the escaping electron, the frequency f of the impinging light and the minimal work W necessary to eject an electron from the surface forward. The slope h of the kinetic energy as a fucntion of frequency f is Planck's constant. This relationship was later thoroughly tested and verified experimentally in a beautiful and elaborate experiment by Millikan [7].

The analysis of electrons emitted upon irradiation from an atom, molecule or solid with respect to their kinetic energy, angular distribution and possibly their spin is referred to as photoelectron spectroscopy, and significant experimental and theoretical advances since the first observation of the photoelectric effect have made it an immensely powerful tool for the assessment of the electronic properties of matter, its chemical composition and even many-body quantum effects (cf. e.g. [8, 9, 10]). The amount of information available from a spectroscopic method is further increased by introducing a *time axis* to it whereby the dynamics of an excitation process and the subsequent evolution of the system under study becomes accessible. The requirement of time resolution on the order of the time scale on which the system under study evolves requires excitation and probing of the system to be facilitated with ultrashort (less than 10^{-12} s in duration) flashes of light as they are produced by pulsed lasers (cf. e.g. [11, 12] and references therein).

In photoelectron spectroscopy the time axis can now be introduced in essentially one of two distinct ways. Firstly, one can excite the system and probe its evolution following an initial excitation by observing its photoelectron spectrum at a later time, initiating photoionization via a probe pulse, which is temporally delayed w.r.t. to the excitation pulse (cf. e.g. [13, 14]), or one can set out to study the dynamics of the photoemission process itself. It is the latter, more fundamental approach with which is of concern here.

Photoemission and its inherent dynamics which take place on the scale of attoseconds (1 as = 10^{-18} s) are among the fastest physical processes ever observed (cf. e.g. [15, 16, 17]). Is is, however, nowadays possible to measure the absolute time delay elapsing between the absorption of a photon by a physical system and the appearance of the photoelectron in vacuum [18] with attosecond precision. The measurement of photoemission times and time differences shall be referred to as *photoemission chronoscopy*. The experimental methods underlying photoemission chronoscopy were developed in the early 2000s and are based on the cross-correlation of a visible/NIR laser pulse with ionizing XUV/soft x-ray radiation with temporal structure on the attosecond time scale. Depending on the desired photon energy range of the experiment one may either choose to use a trains of low-energy

XUV pulses for photoionization, giving rise to the *RABBITT* (reconstruction of attosecond beating by interference of two-photon transitions, [19]) technique, or isolated attosecond pulses in the *attosecond streak camera* technique (cf. [20, 21]). Both approaches can access the same information if the phase of the XUV radiation is properly taken into account [22] and should be seen as complementary. Aiming for photon energies exceeding 85 eV, the attosecond streak camera is the method of choice for the experiments presented in this work.

At first only relative timing measurements, i.e. the measurement of the time delay between the emission of photoelectrons from two bound states of a single system (cf. [15, 16]) or in a mixture of systems were possible. An accurate and absolute *time zero* has, however, been introduced to the attosecond streaking method very recently [23, 18, 24] and can now be applied to the study of photoemission times in more and more complex and diverse systems.

Here photoemission chronoscopy is applied to a group of molecular systems and to photoemission from solids, with the focus on the photon energy dependence of the photoemission time delay. The molecular systems under study are the iodoalkanes (iodomethane, -ethane, 1- and 2-iodopropane, 1- and 2-iodobutane), which are of particular interest as the I4*d* photoemission from iodomethane and -ethane has been used as a reference in the determination of the absolute duration of the photoelectric effect on a W(110) surface [18] at a single excitation energy. Furthermore, recent surprising results [25] on the photoemission time from the I4*d* in iodoethane call for closer scrutiny. The primary research question in this endeavour is how and whether a change of the host molecule of the iodine atom can change the photoemission time of its I4*d* core-level, and furthermore under which circumstances the core-level photoemission time observed in the iodine-containing molecule can be seen as representative of that of an isolated iodine atom.

The second system under study is the W(110) surface. The energy dependence of the time difference between the valence band photoemission and photoemission for the W4*f* states has been experimentally researched thoroughly (see [26, chap. 4] and references therein), but has until now eluded an interpretation from first principles. The available experimental data are re-evaluated and re-interpreted, and it is shown that state-of-the-art *ab-initio* theory of the photoemission process is capable of matching the experimental observations. Within this theory it is established that the photoemission times observed in atoms and molecules are in principle no different than those observed at surfaces and can be grasped within the same general formalism. These findings therefore close the conceptual gap in the interpretation of photoemission times from solids and isolated atoms that has existed since their first experimental assessment [15, 16].

Chapter 2

Ultrashort pulses of light

Now he looked ill, seriously ill, the knowledge of what he'd done to himself rising up to infest the swollen black pupils of his eyes. He looked to the ceiling, looked to the walls. "The light," he said. "The light."

– T. C. Boyle, *Outside Looking In* [27, p. 11]

The generation and characterization of ultrashort pulses of light is central to experimental attosecond physics, necessitating a concise and accurate way of describing these. For this we shall follow references [28, chap. 1] and [29, chap. 2]. The first section of this chapter will introduce the relevant quantities and relates them to what can be accessed in an experiment. The second section reviews the generation of ultrashort light pulses, following [28, chap. 5], and further references which are given in the text.

2.1 The electric field in the time and frequency domain

In many cases the interaction of an electromagnetic wave with a medium (or single atom) can be understood sufficiently well when only considering its electric field. Furthermore, when the spatial dependency of the electromagnetic wave is not important, one can restrict the description simply to a function $E(t)$ representing the evolution of the electric field at a fixed point in space. While $E(t)$ is nowadays accessible directly in the experiment, this requires the imlementation of specialized techniques (e.g. the attosecond streak camera [21] or the TIPTOE method[30]). The quantity more routinely accessed to characterize a light source on the other hand is the spectral intensity $S(\omega)$ (recorded e.g. with a grating spectrometer), which relates to $E(t)$ via its fourier transform

$$\tilde{E}(\omega) = \frac{1}{\sqrt{2\pi}} \int_{-\infty}^{\infty} E(t) \mathrm{e}^{-i\omega t} dt = \left|\tilde{E}(\omega)\right| \mathrm{e}^{-i\varphi(\omega)}, \tag{2.1}$$

and is ideally directly proportional to it's squared modulus $S(\omega) \propto \left|\tilde{E}(\omega)\right|^2$. The function $E(t)$ being real implies that the complex spectrum $\tilde{E}(\omega)$ obeys the symmetry relationship

$$\tilde{E}(\omega) = \tilde{E}^*(-\omega), \tag{2.2}$$

whereby we can conveniently ignore the negative frequencies in $\tilde{E}(\omega)$ as they carry redundant information, and define a complex-valued electric field in the time domain as

$$\tilde{E}^+(t) = \frac{1}{\sqrt{2\pi}} \int_{0}^{\infty} \tilde{E}(\omega) \mathrm{e}^{i\omega t} d\omega, \tag{2.3}$$

and correspondingly the complex spectrum

$$\tilde{E}^{+}(\omega) = \left|\tilde{E}^{+}(\omega)\right| \mathrm{e}^{i\varphi(\omega)} = \begin{cases} \tilde{E}(\omega), & \omega \geq 0 \\ 0, & \omega < 0. \end{cases} \tag{2.4}$$

The physical electric field $E(t)$ can be recovered as

$$E(t) = 2\mathrm{Re}\left\{E^{+}(t)\right\} = E^{+}(t) + E^{-}(t). \tag{2.5}$$

It seems tempting (and in fact can be appropriate) to describe the electric field of a light pulse as

$$E^{+}(t) = \frac{1}{2}a(t)\mathrm{e}^{i\omega_0 t} \tag{2.6}$$

i.e. a product of a carrier oscillating with ω_0 and a complex-valued envelope $a(t)$. When the duration of the pulse approaches the optical cycle though, such a description gradually loses its usefulness, but is still sometimes chosen e.g. for reasons of convenience or performance in a numerical problem. The more generally applicable description

$$\tilde{E}^{+}(\omega) = \sqrt{S(\omega)}\mathrm{e}^{-i\varphi(\omega)} \tag{2.7}$$

is one in the spectral domain in terms of the spectral intensity $S(\omega)$ and the spectral phase $\varphi(\omega)$, which has been introduced in eq. 2.1. From eq. 2.7 the time-domain representation can be obtained via an inverse Fourier transform.

2.2 Spectrum and spectral phase

At this point it is instructive to choose a parametrization for $S(\omega)$ and $\varphi(\omega)$ and investigate the influence of their respective shapes on the properties of $E(t)$. A common simple choice is to represent the spectral intensity as a gaussian function, and to expand the spectral phase into powers of $(\omega - \omega_0)$

$$\varphi(\omega) = \varphi_0 + \delta \cdot (\omega - \omega_0) + \frac{\beta_\omega}{2} \cdot (\omega - \omega_0)^2 + \frac{\varphi_3}{6} \cdot (\omega - \omega_0)^3 + \ldots, \tag{2.8}$$

where ω_0 is the frequency around which the spectrum is centered, and the expansion coefficients φ_0, δ and β_ω will be discussed in more detail further below. While spectra of ultrashort pulses as they are encountered in the laboratory are rarely of such a simple shape that a gaussian function can approximate them well, they do share some characteristics with it that we can use to intuitively understand the connections that exist between the spectral domain properties of a laser pulse and its shape in the time domain: real spectra are centered around some mean frequency ω_0, which could e.g. be taken as the fist moment of the spectrum, and they attain appreciable values only within a finite region around ω_0. A reasonable choice for characterizing the width $\Delta\omega$ of this region could e.g. be the full width of the spectrum at half its maximum intensity.

The spectral intensity

$$S(\omega) = S_0 \exp\left(-4\ln 2\frac{(\omega - \omega_0)^2}{\Delta\omega^2}\right) \tag{2.9}$$

is parametrized in terms of exactly these quantities and yields the complex spectrum

$$E^{+}(\omega) = \sqrt{S_0} \exp\left(-2\ln 2\frac{(\omega - \omega_0)^2}{\Delta\omega^2}\right) \mathrm{e}^{i\varphi(\omega)}. \tag{2.10}$$

With $\varphi(\omega)$ vanishing for all frequencies ω, the corresponding complex electric field

$$E^{+}(t) = \frac{\sqrt{S_0}\,\Delta\omega \mathrm{e}^{i\omega_0 t}}{\sqrt{4\ln 2}} \exp\left(-\frac{\Delta\omega^2}{8\ln 2}t^2\right) \tag{2.11}$$

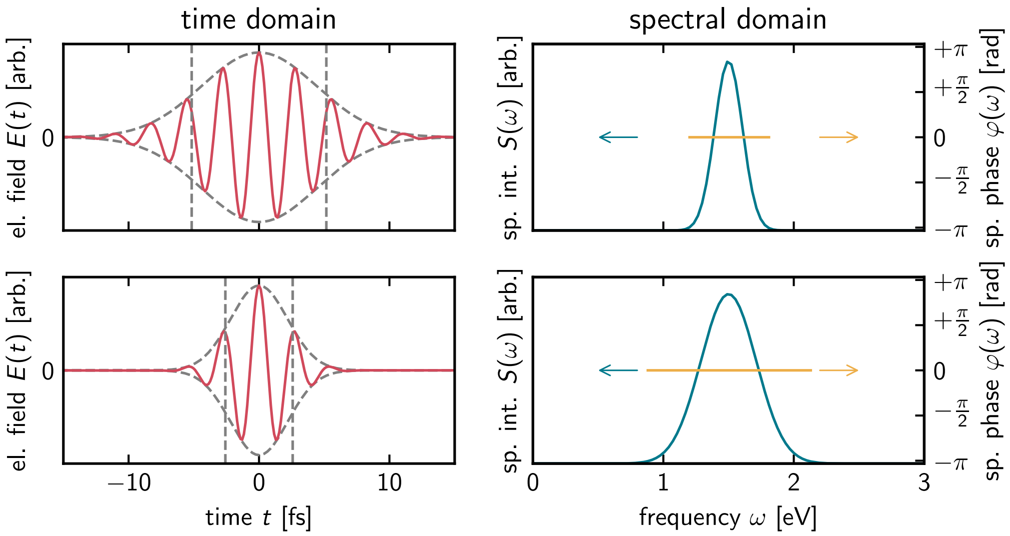

Figure 2.1: Gaussian spectra $S(\omega)$ (right column) of different widths and the corresponding time-domain electric fields $E(t)$ (left column). An increase in the width $\Delta\omega$ will result in a decrease of the FWHM duration $\mathscr{T}'$ (marked with grey dashed vertical lines) of the laser pulse.

is an oscillation with frequency ω_0 enveloped by a gaussian function with a temporal FWHM of

$$\mathscr{T} = \frac{4\sqrt{2}\ln(2)}{\Delta\omega}. \tag{2.12}$$

This result demonstrates that a broader spectrum can result in a shorter ligh pulse, as it is illustrated in fig. 2.1. In fact, the duration of a laser pulse is bounded from below where the bound is determined by some measure of the width of the spectrum, but its exact form is not necessarily as it is given by eq. 2.12, it rather depends on the shape of $S(\omega)$ and the definition of spectral width chosen to characterize $S(\omega)$. This lower limit is referred to as *Fourier limit*. Distortions of the spectral phase of second or higher order in $(\omega - \omega_0)$ will result in the laser pulse exceeding its minimal duration and also deviating from the gaussian shape, as it will be demonstrated below.

Carrier-to-envelope phase, temporal shifts and group delay

The effects of a non-vanishing spectral phase up to first order in $(\omega - \omega_0)$ can be derived directly by considering general properties of the Fourier transform. As a consequence of its linearity, a constant phase $\varphi(\omega) = \varphi_0 =$ const. will directly transfer to the time domain as a phase offset between the oscillating carrier and the envelope of the laser pulse. This is demonstrated in the first two rows of figure 2.2. This phase offset is referred to as carrier-to-envelope phase (CEP), and for pulses comprised of only a few oscillations of the electric field it significantly influences the pulse shape. Therefore precise control over it is central to experiments sensitive to the shape of $E(t)$ (and not only its envelope).

It is furthermore well known that a multiplication of a fuction with a linear phase factor $e^{i\omega\delta}$ in the spectral domain will result in its time-domain representation being shifted by δ. Therefore we can identify

$$\delta = \frac{d}{d\omega}\varphi(\omega)\bigg|_{\omega=\omega_0} \tag{2.13}$$

with a temporal shift of the laser pulse by δ (as well as a phase CEP phase shift of $\omega_0\delta$). This is demonstrated in the third row of fig. 2.2, where the CEP phase shift has been compensated for.

Generally, the first derivative of the spectral phase w.r.t. ω is referred to as group delay

$$\mathrm{GD}(\omega) = \frac{d}{d\omega}\varphi(\omega). \tag{2.14}$$

It encodes time-vs.-frequency information and can be seen as relating to which frequencies occur at which point in time in the light pulse.

Chirp and higher-order phase distortions

A second order term in the spectral phase will yield a linear group delay, which indicates that the different frequency components of the light pulse appear to an observer in sequence i.e. as a sweep of the oscillation frequency of the electric field under the pulse envelope. Whether the frequency sweeps upwards or downwards with time depends on the sign of the group velocity dispersion

$$\mathrm{GVD}(\omega) = \frac{d^2}{d\omega^2}\varphi(\omega) \tag{2.15}$$

at ω_0, which can be identified as the parameter β_ω in eq. 2.8. A positive sign of β_ω will result in an increase in frequency, and a negative sign in a decrease in frequency, respectively. Drawing a parallel to birdsong which changes its pitch over the duration of a vocalization of a songbird, a pulse across the duration of which the frequency sweeps up or down is referred to as *chirped*.

Higher-order distortions of the spectral phase can yield light pulses of considerable complexity in the time-domain, even if their spectral intensity $S(\omega)$ is comparatively simple. The fifth row of fig. 2.2 shows the pulse shape that emerges for a third-order spectral phase (and therefore second order group delay) and a gaussian spectrum. The small satellite pulses to the right of the main pulse are a result of the low- and high-frequency components of the spectrum being pushed out of temporal synchronization with the central portion of the spectrum. Their resulting interference causes the visible oscillations in the envelope.

An example from the real world, the problems of defining pulse duration and central frequency

The light pulses used to feed an attosecond beamline often have complex electric fields in the time domain, as they are carefully shaped using linear and nonlinear optical effects to suit the needs of the experiment. Figure 2.3 shows the electric field $E(t)$ of a light pulse recorded in an attosecond streaking measurement.

The complexity of this pulse illustrates the difficulties one encounters when trying to define a central frequency ω_0, a spectral width $\Delta\omega$ and a pulse duration $\mathcal{T}$ for any but the simplest light pulses. Acknowledging the problems associated with it we shall base our definitions of spectral width and pulse duration on the FWHM of the spectra and temporal envelopes we encounter in the hope that these will be behaved well enough to warrant this choice. For the central frequency ω_0 we shall choose the first moment of the power spectrum. For the pulse shown in figure 2.3 we find $\omega_0 = 1.77\,\mathrm{eV}$, $\Delta\omega = 0.6\,\mathrm{eV}$ and an FWHM pulse duration of $\mathcal{T} = 6.8\,\mathrm{fs}$.

2.3 Generation of ultrashort laser pulses

Mode-locked lasers are the standard sources of ultrashort pulses of light. They produce a regular train of short light pulses spaced by the resonator round trip time T_R, which corresponds to a pulse repetition rate $f_\mathrm{rep} = T_\mathrm{R}^{-1}$. The emergence of such a regular temporal structure can be considered somewhat surprising as it cannot be the result of a superposition of the (due to dispersion) generally unevenly spaced longitudinal modes of a laser resonator. The mode-locking action, however, introduces a non-linear phase shift which will compensate the dispersion whereby a comb of modes with

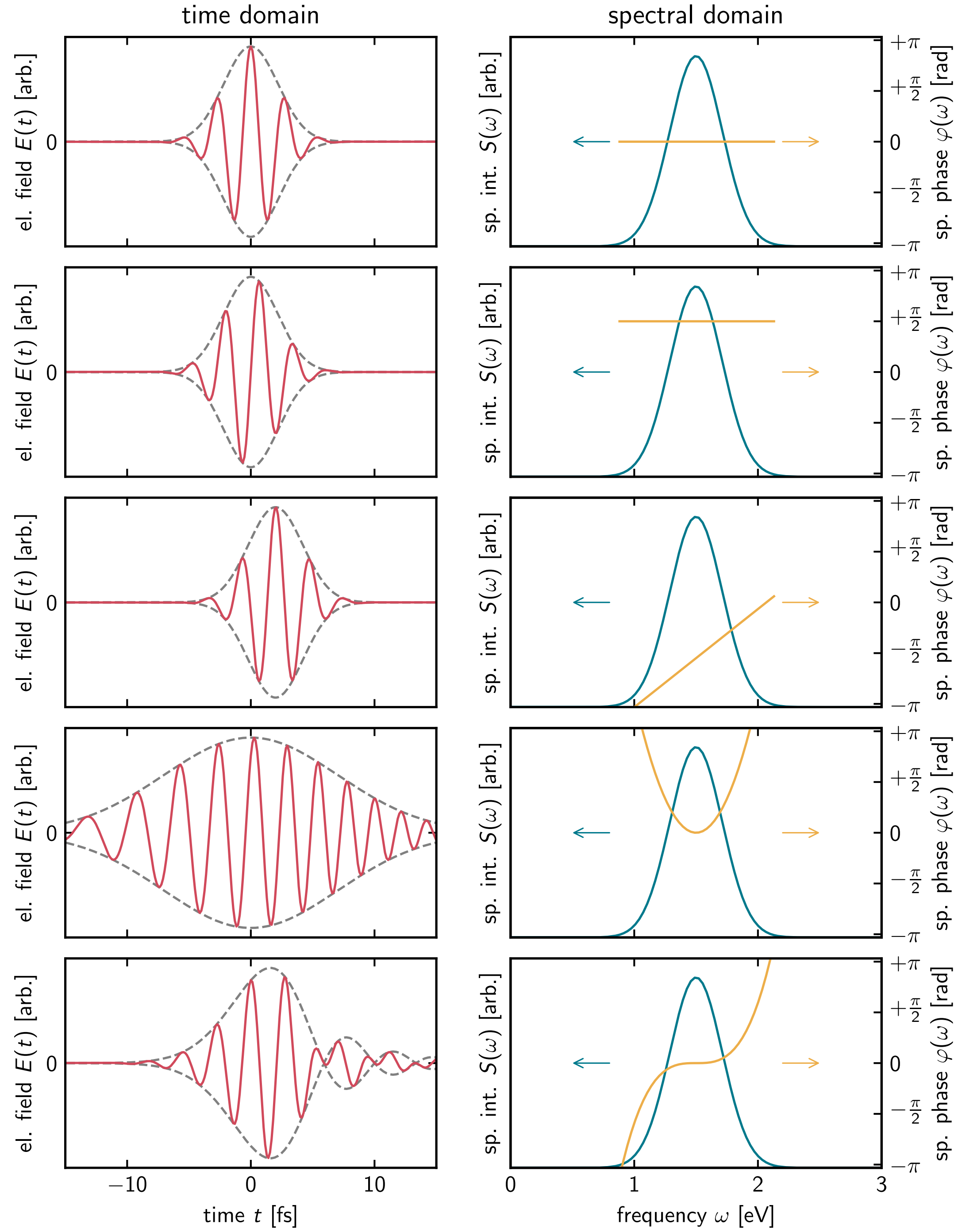

Figure 2.2: Gaussian spectra (blue, right panels) and spectral phases up to third order (yellow, right panels) and the corresponding time-domain electric fields (red, left panels) and their envelopes (dashed gray, left panels). A constant spectral phase maps directly to the phase of the laser pulse in time domain (first two rows). A linear spectral phase will shift the pulse in time (third row), and a quadratic spectral phase (fourth row) will temporally broaden the pulse by pushing the different frequency components out of temporal synchronization, thereby creating a pulse in which the electric field's period of oscillation will change over the duration of the pulse. Third- and higher-order distortions to the spectral phase will result in complex pulse shapes in the time domain (fifth row).

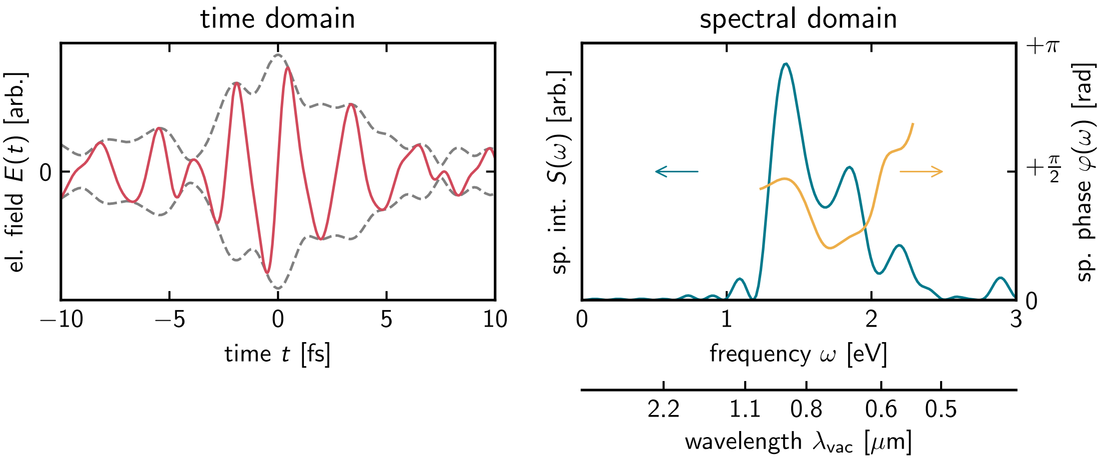

Figure 2.3: Electric field $E(t)$ of an ultrashort laser pulse extracted from an attosecond streaking measurement (left panel), together with the corresponding spectral intensity $S(\omega)$ and spectral phase $\varphi(\omega)$ (right panel) calculated via eq. 2.1. The temporal and spectral shapes of ultrashort laser pulses as they are encountered in the laboratory can be quite complex and elude a description via simple mathematical functions as it has been given in this section. Even so, definitions of central frequency, spectral width and pulse duration based on the first- and second moments of $S(\omega)$ and the envelope of $E(t)$ can be used to describe these pulses in comparatively simple terms. A wavelength scale is added as a guide to the reader. The attosecond streaking measurement has been performed by Maximilian Pollanka on the 1s-level of helium.

equal spacing is created. The properties of this comb and the corresponding train of short pulses are described in section 2.3.1.

Generally, mode-locking is induced via a roundtrip-synchronous modulation of the amplitude inside the laser resonator. This can be done actively, e.g. via electro- or acoustooptical components, or passively in a nonlinear optical component resulting in intensity dependent net gain (cf. e.g. [31]). For the latter case, which is the one of interest here, a differential equation to which the resulting laser pulse $a(t)$ is a solution can be constructed in the time domain under the assumption that the pulse envelope does not drastically change in shape during one trip through the oscillator. This assumption is no longer valid for the ultrabroadband sources generating few-femtosecond pulses which became available in the 1990s (cf. e.g. [32]) and have since become standard tools in ultrafast physics. A different model needs to be constructed. It is elaborated upon in section 2.3.2.

2.3.1 Properties of a train of short pulses

With typical repetition rates of some 80 MHz and broadband laser gain media spanning a bandwidth of around 150 THz, millions of comb-lines can participate in mode-locking. These comb-lines are found at frequencies

$$f_q = f_{\text{ce}} + q f_{\text{rep}} \text{ with } q \in \mathbb{N}_0, \tag{2.16}$$

but will only have appreciable intensity within the finite frequency interval where they experience sufficient gain. The frequency-comb and time-domain pulse-train generated by a hypothetical laser oscillator is shown in figure 2.4.

As the comb lines are generally offset by f_0 from integer multiples of f_{rep}, the maxima of the pulse envelopes (dashed red lines in fig. 2.4b) in the time domain will not coincide with with the maxima of the oscillations of the electric field. Instead, when the time-domain signal is viewed as an oscillating carrier modulated by an envelope function, the phase of the oscillation slips under the

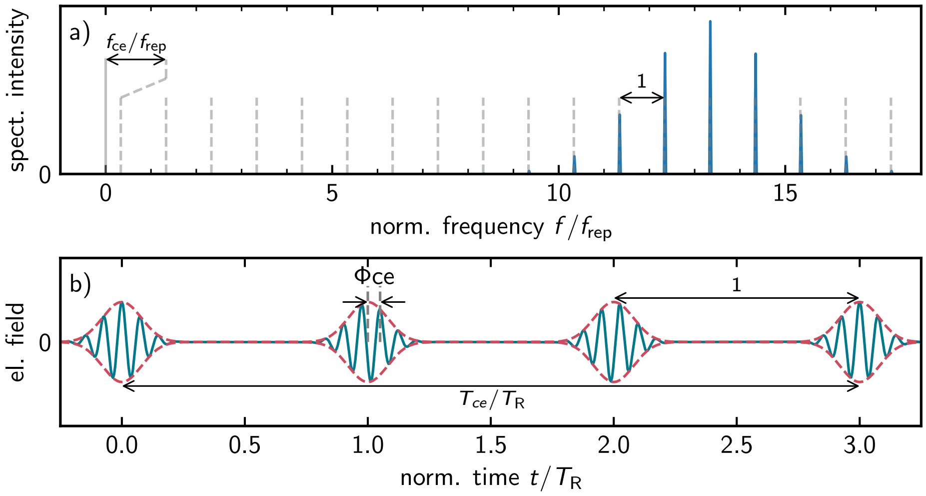

Figure 2.4: A hypothetical ideal mode-locked laser in the time- and frequency domain. Plotted against the normalized frequency f/f_{rep} the teeth of the frequency comb (blue in a)) have unitary spacing, but are offset by $f_{\mathrm{ce}}/f_{\mathrm{rep}}$ from integer values on the abscissa. In the (normalized) time domain (panel b)) this corresponds to a train of short pulses. When viewed as an oscillating carrier modulated with an envelope function, it can be seen that the carrier phase slips by Φ_{ce} under the envelope from pulse to pulse.

envelope by

$$\Phi_{\mathrm{ce}} = 2\pi f_{\mathrm{ce}} T_{\mathrm{R}} \tag{2.17}$$

per pulse. This carrier-envelope (ce) phase slippage can also be seen as being the result of the generally unequal phase- and group velocities in the laser oscillator. Due to the periodicity of the carrier- and envelope functions, after some N pulses the total accumulated phase slip will be an integer multiple of 2π, whereby all N-th pulses are indistinguishable. N is determined by $N^{-1} = T_{\mathrm{R}} f_{\mathrm{ce}}$ for $f_{\mathrm{ce}} \neq 0$. For $f_0 = 0$, every pulse is the same and therefore $N = 1$.

Is is easily understood that precise control over f_{rep} and more importantly f_{ce} is crucial for the reproducible generation of light wave forms, which are central to attosecond physics experiments. Schemes for their determination and control have been devised around the turn of the millenium and have revolutionized optical metrology (cf. e.g. [33] and references therein). The implications of ce-phase control for stong-field processes have been explored by Baltuška et al. [34], enabling the reproducible generation and control of broad continua spanning into the extreme ultraviolet (XUV) which are the foundation for generation of light pulses with sub-femtosecond temporal structure.

2.3.2 Parameters of mode-locking

Due to the incredible wealth of possible applications of mode-locked lasers the mode-locking process has received extensive theoretical treatment. References [31] and [35], which we want to follow in this section, give a comprehensive overview. As stated before, in a laser generating few-femtosecond pulses the pulse circulating in the resonator does not have a constant temporal width. The pulse drastically changes its duration and shape during its round trip, being periodically stretched and compressed in time considerably. For the treatment of mode-locking in these *stretched-pulse* lasers, H. Haus [31] brought the master equation 2.18 forward, which describes the pulse at the point of its minimal

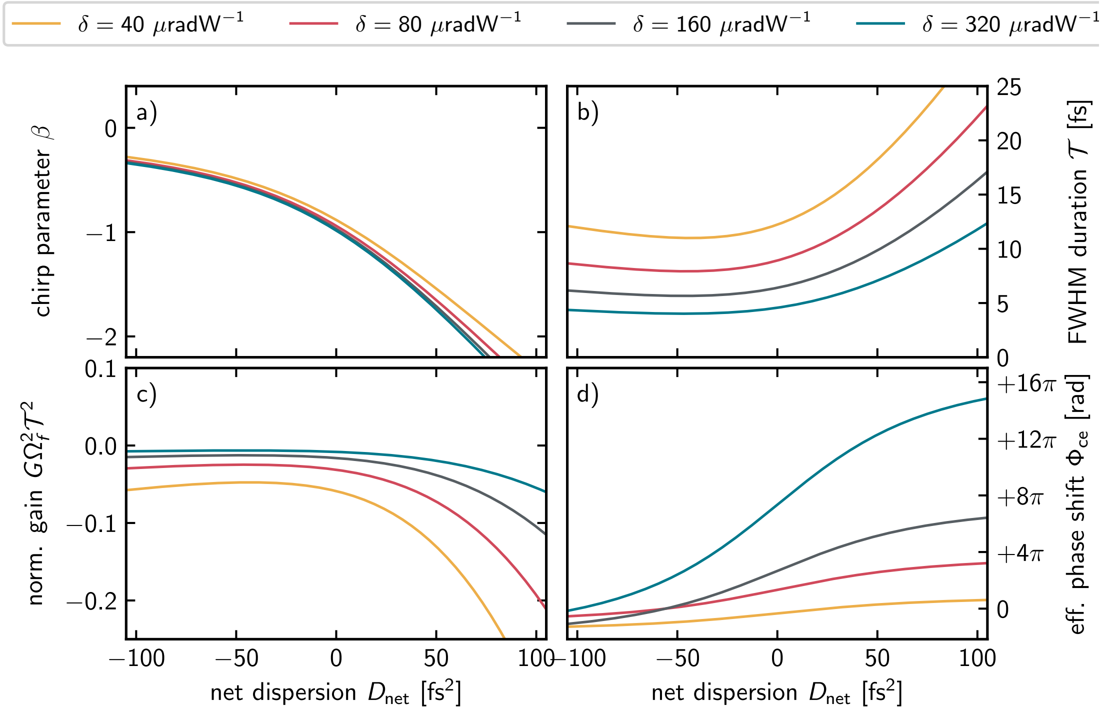

Figure 2.5: Chirp parameter (panel a)), pulse duration (panel b)), normalized gain (panel c)) and ce-phase-shift per pass (panel d)) predicted by the master equation 2.18 as function of net intracavity dispersion D_{net}. The shortest pulses are obtained for slightly negative values of net intracavity dispersion, but they will have non-zero chirp β. Overall gain is always negative which is necessary for stable operation. Positive gain facilitates the build-up of noise between pulses. The per-pass phase shift Φ_{ce} can be controlled by varying the net dispersion D_{net}, enabling control and regulation of f_{ce}.

duration in the oscillator.

$$\frac{1}{T_{\mathrm{R}}}\frac{\partial}{\partial T}a(t,T) = Ga(t,T) + \left(\frac{1}{\Omega_f^2} + iD_{\mathrm{net}}\right)\frac{\partial^2}{\partial t^2}a(t,T) + (\gamma_0 - i\delta_0)\,|A_0|^2\left(1 - \mu\frac{t^2}{\mathcal{T}_e^2}\right) \tag{2.18}$$

In eq. 2.18 G is the net gain per pass, Ω_f^2 determines the spectral filtering by the gain medium, D_{net} is the net dispersion in the resonator which can usually be varied using a prism pair. The parameters γ_0, δ_0 and μ in the last nonlinear term capture the amplitude and phase modulation the pulse inflicts on itself. As the pulse's duration varies greatly depending on its position in the resonator this nonlinear term needs to take the pulse's action into account in an *on-average* fashion, whereby the amlitude A_0 and the pulse width $\mathcal{T}_e$ enter the master equation, which are actually parameters of the proposed solution (eq. 2.19). Therefore the master equation is no longer an ordinary partial differential equation, and its parameters can only iteratively be estimated to match the behaviour of the laser oscillator in the laboratory as well as possible. At this point we need to simply accept the presence of this nonlinear term in the master equation. Optical nonlinearities and their origins will be elaborated upon in chapter 3.

This model is defined in terms of two times t and T, the former of which describes the pulse on a timescale of its temporal width $\mathcal{T}_e$, while per-roundtrip changes to $a(t,T)$ occur on the timescale T. As described in the previous section, the the pulse will change its carrier-to-envelope phase by Φ_{ce} from roundtrip to roundtrip, whereby we can set $1/T_{\mathrm{R}}\partial/\partial T a(t,T) = -i\Phi_{\mathrm{ce}}$ on the left hand side of the master equation. By inserting the ansatz

$$a(t) = A_0 \exp\left(-\frac{t^2}{\mathcal{T}_e}(1 + i\beta)\right) \tag{2.19}$$

with the chirp-parameter β into eq. 2.18 one can find expressions defining β, the pulse width $\mathcal{T}_e$, the net gain per pass G and the phase shift Φ_{ce} per pass as a function of the net dispersion D_{net} (see appendix A). The resulting curves are shown in fig. 2.5 for different values of δ. Parameters have been estimated very roughly to yield pulse durations compatible to what is expected from the laser oscillator in our laboratory, but some liberty has been taken to exaggerate them for the purpose of visualization. Details are given in appendix A.

Chapter 3

Interaction of intense light pulses with matter

"Life at low intensity is dull."

– Rick Trebino and John Buck - *Frequency Resolved Optical Gating* [29, p. 38]

With a source of ultrashort pulses of light at hand, light intensities far above of what is captured by linear optics come into reach as all the energy that would usually be spread out over many oscillation cycles of the electromagnetic wave is now crammed into very few of these. The arising nonlinear response can be used ingeniously to precisely control and shape light waveforms and ultimately enable access to the extreme ultraviolet (XUV) / soft x-ray (SXR) wavelength regime where light pulses of less than one femtosecond in duration can be generated. Next to their few-femtosecond optical counterparts, these attosecond XUV pulses are the central experimental tool for the work presented in this thesis.

The first section of this chapter will review perturbative nonlinear light-matter interaction in a classical manner following [29, chap. 3] and [36, chap. 8] with further references in the text, and then proceed towards the non-perturbative higher order response presented (relevant references given in the main text). Based on this groundwork, the synthesis and characterization of sub-femtosecond extreme ultraviolet pulses will be treated in the last section.

3.1 High intensities, low order nonlinear response

Classical nonlinear optics does not require the invocation of a new theory of optics radically different from what Maxwellian electrodynamics predict. Classical nonlinear optics arises naturally when one accepts that the polarization response $P(E(t))$ of a medium to the electric field $E(t)$ is not necessarily linear. Oftentimes, the relationship between the polarization response and the electric field is denoted as a linear one with the proportionality constant being the susceptibility χ, giving rise to the well known phenomena of refraction an extinction via the real- and imaginary part of χ (and consequently of the refractive index $n' = n + i\kappa$) respectively. This is certainly justified at low to moderate intensities, but once the intensity rises such that the electric field $E(t)$ is comparable in magnitude to inter-atomic electric fields nonlinear effects are expected to become observable, and the intensity cannot be considered low or moderate anymore.

The relationship between electric field $E(t)$ and polarization response $P(t)$ is then expressed via the nonlinear susceptibility

$$\chi(\mathbf{E}) = \chi^{(1)} + \chi^{(2)}\mathbf{E} + \chi^{(3)}\mathbf{E}\mathbf{E} + ..., \tag{3.1}$$

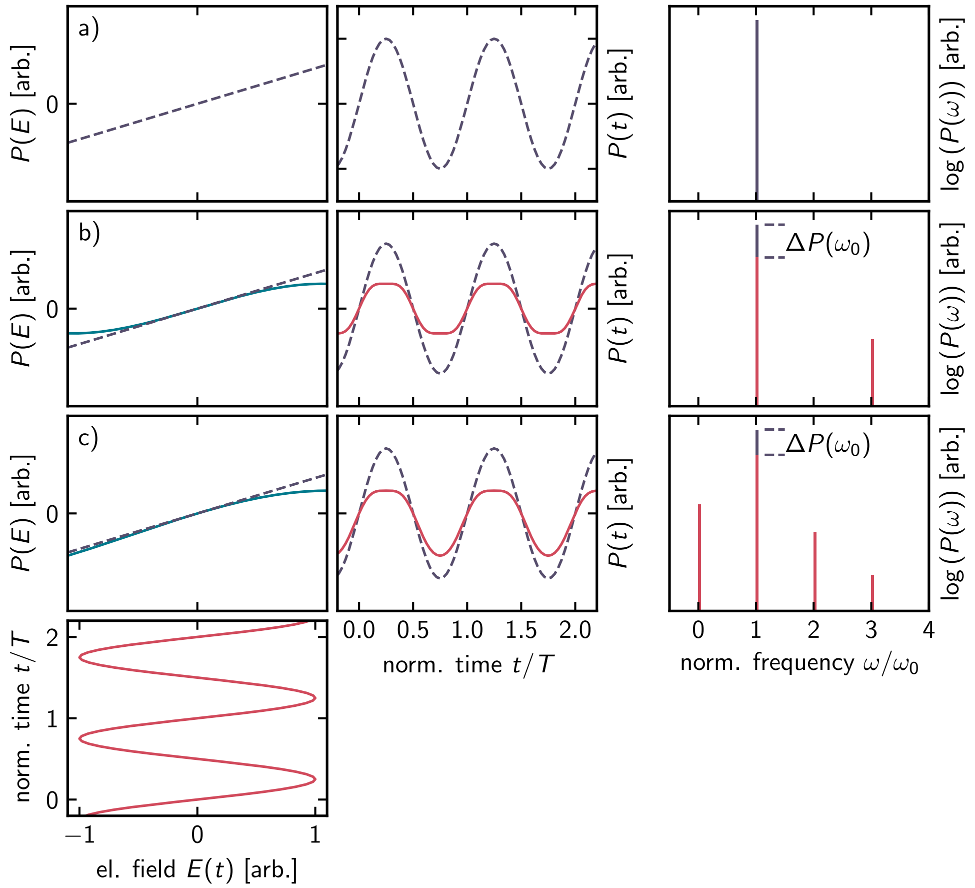

Figure 3.1: Schematic representation of linear (a)) and nonlinear (b-c)) polarization response to an oscillating field (leftmost bottom panel). Due to the distortion of $P(t)$ frequency components not oscillating with the original carrier frequency ω_0 emerge. Panels b) depict a third-order nonlinearity where it is especially noteworthy that in this case even the polarization at ω_0 can be affected, which results in an intensity-dependent refractive index. This is the origin of the optical Kerr-effect, which is responsible for the nonlinearity in eq. 2.18. In the general case (panels c)) where second- and third-order nonlinearities are present even a zero-frequency (dc) component of the electric field can be observed.

which depends on the electric field $E(t)$, whereby the polarization response takes the form of eq. 3.2.

$$\mathbf{P}(\mathbf{E}) = \varepsilon_0 \chi(\mathbf{E})\mathbf{E} = \varepsilon_0 \left(\chi^{(1)}\mathbf{E} + \chi^{(2)}\mathbf{E}\mathbf{E} + \chi^{(3)}\mathbf{E}\mathbf{E}\mathbf{E} + \ldots\right) \tag{3.2}$$

Just as in the linear case, $\chi(\mathbf{E})$ is a tensorial quantity. A consequence of this is that whether or not a certain nonlinear effect can be observed depends on the symmetry of the medium: in a centrosymmetric medium for example, second-order nonlinear effects cannot be observed as the second order susceptibility tensor must vanish [36, p. 335 and p. 66]. Figure 3.1 illustrates the nonlinear polarization response to an oscillating sinusoidal field. It is evident that the nonlinear distortion of $P(t)$ generates frequency components at $\omega \neq \omega_0$ in $P(t)$, which in turn drive the wave equation, acting as sources for electric fields oscillating with frequencies differing from ω_0. Therefore, nonlinear optics enables the conversion of optical signals from one frequency to another as well as the mixing of frequencies, which is what makes it indispensable for many applications in ultrafast physics.

Second-order nonlinearities e.g. can be used for optical frequency mixing, with which the carrier-envelope offset frequency f_{ce} in a femtosecond laser system (see section 2.3.1) can be detected, paving the way for its precise control. This is described in section 3.1.1. Third-order nonlinearities on the other hand are a central part of the mode-locking mechanism of ultrashort laser oscillators as they are described in section 2.3.2 and furthermore enable the spectral broadening of intense, amplified laser pulses. Spectra that support light pulses of a duration of only a few optical cycles are attainable with a dedicated pulse compression stage following the spectral broadening. Such light pulses drive the attosecond beamlines at the Technical University of Munich. Section 3.1.2 is dedicated to giving some detail about the use of third order nonlinearities for the mode-locking of ultrafast laser oscillators and the compression of amplified laser pulses.

3.1.1 Frequency mixing, f-2f and f-0 interferometry

A nonlinearity driven by an oscillating field lends itself to frequency mixing. Considering a second-order nonlinearity

$$\mathbf{P}^{(2)}(t) = \varepsilon_0 \chi^{(2)} \mathbf{E}(t)\mathbf{E}(t) \tag{3.3}$$

and an electric field

$$\begin{aligned} \mathbf{E}(t) = \frac{1}{2}\Big(&\tilde{\mathbf{E}}_1^+(\omega_1) \exp\left(i\omega_1 t\right) + \text{c.c.} \\ &+\tilde{\mathbf{E}}_2^+(\omega_2) \exp\left(i\omega_2 t\right) + \text{c.c.}\Big) \end{aligned} \tag{3.4}$$

oscillating at frequencies ω_1 and ω_2, one finds, inserting eq. 3.4 into eq. 3.3

$$\begin{aligned} \mathbf{P}^{(2)}(t) = \varepsilon_0 \chi^{(2)} \frac{1}{4}\Big(&(\tilde{\mathbf{E}}_1^+(\omega_1))^2 \exp\left(2i\omega_1 t\right) &&+ \\ &(\tilde{\mathbf{E}}_2^+(\omega_2))^2 \exp\left(2i\omega_2 t\right) &&+ \\ &2\tilde{\mathbf{E}}_1^+(\omega_1)\tilde{\mathbf{E}}_2^+(\omega_2) \exp\left(i(\omega_1 + \omega_2)t\right) &&+ \\ &2\tilde{\mathbf{E}}_1^+(\omega_1)\tilde{\mathbf{E}}_2^-(\omega_2) \exp\left(i(\omega_1 - \omega_2)t\right) &&+ \\ &\tilde{\mathbf{E}}_1^+(\omega_1)\tilde{\mathbf{E}}_1^-(\omega_1) &&+ \\ &\tilde{\mathbf{E}}_2^+(\omega_2)\tilde{\mathbf{E}}_2^-(\omega_2) &&+ \text{c.c.}\Big). \end{aligned} \tag{3.5}$$

Of special interest here are the first two terms, which oscillate with the second harmonic of ω_1 and ω_2 respectively, as well as the fourth term oscillating with the difference of ω_1 and ω_2.

When a frequency comb as it is described in section 2.3.1 is subjected to second harmonic generation (SHG) via the first or second term in 3.5 the comb lines initially found at $f_q = f_{\text{ce}} + qf_{\text{rep}}$ will appear at $2f_q = 2f_{\text{ce}} + 2qf_{\text{rep}}$. If the frequency comb spans across more than one octave the high-frequency end of the fundamental comb will overlap with the low-fequency end of the doubled comb such that the comb line f_{2q} of the fundamental comb will beat with the comb line at $2f_q$ of the doubled comb (fig. 3.2, top panel) at the difference of their frequencies

$$f_{\text{beat}} = 2f_q - f_{2q} = 2f_{ce} + 2qf_{\text{rep}} - f_{ce} - 2qf_{\text{rep}} = f_{\text{ce}}. \tag{3.6}$$

This enables a direct route to measuring the carrier-envelope offset frequency. Together with the dependency of f_{ce} on the intracavity dispersion worked out in sec. 2.3.2 measurement and regulation of f_{ce} via a feedback loop is possible. Such an approach has first been brought forward by Telle et al. in [37]. They furthermore suggested an alternative route based on difference frequency generation (DFG i.e. the fourth term in eq. 3.5) where instead of beating the comb with its frequency doubled replica the frequency difference between comb lines at opposing sides of the spectrum is taken and the result beats with the low-frequency end of the comb. The comb lines emerging from the DFG process will not be offset from integer multiples of f_{rep} as

$$f_{q_2} - f_{q_1} = f_{\text{ce}} + q_2 f_{\text{rep}} - f_{\text{ce}} - q_1, f_{\text{rep}} = (q_2 - q_1) f_{\text{rep}}, \tag{3.7}$$

whereby any such line will generate a beating signal at f_{ce} with the nearest line of the fundamental comb (fig. 3.2, bottom panel). An implementation of this scheme is described in [38].

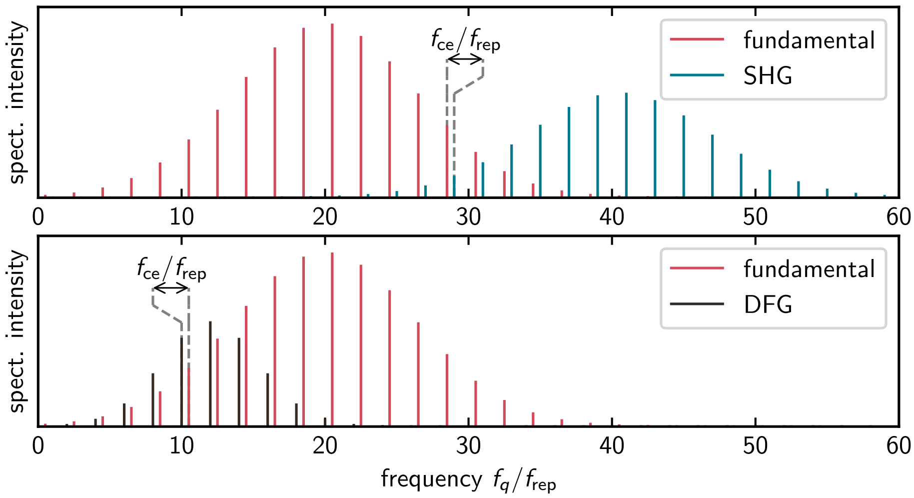

Figure 3.2: Principle of $f - 2f$ (upper panel) and $0 - f$ (lower panel) interferometry. In the former case the frequency comb exiting a mode-locked laser is subjected to second harmonic generation and the emerging frequency doubled replica overlaid with the fundamental comb. Given that both combs are of sufficient width the high-frequency end of the fundamental will overlap with the low-frequency end of the SHG comb, resulting in a beating signal at f_{ce} according to eq. 3.6 which can be detected with a fast photodiode. Alternatively to second harmonic generation one can subject the fundamental comb to difference frequency generation whereby the difference frequencies of lines from opposing ends of the fundamental comb will beat with the low-frequency end of the fundamental. As the DFG comb is not offset from zero, the beating will be at f_{ce} just as in the case of $f - 2f$ interferometry.

3.1.2 Optical Kerr effect and spectral broadening

Turning to the special case of linearly polarized light and a third-order nonlinearity in a material where $\chi^{(2)}$ vanishes, the nonlinear polarization can be written as a scalar

$$P^{(3)}(t) = \varepsilon_0 \chi^{(3)} \left(E(t)\right)^3 . \tag{3.8}$$

With $E(t) = \frac{1}{2}\left(\tilde{E}^+(\omega)\exp(i\omega t) + \text{c.c.}\right)$ this yields

$$P^{(3)}(t) = \frac{3}{8}\varepsilon_0 \chi^{(3)} \left(\tilde{E}^+(\omega)\tilde{E}^+(\omega)\tilde{E}^-(\omega)\mathrm{e}^{i\omega t} + \text{c.c.}\right) + \frac{1}{8}\varepsilon_0 \chi^{(3)} \left(\tilde{E}^+(\omega)\tilde{E}^+(\omega)\tilde{E}^+(\omega)\mathrm{e}^{i3\omega t} + \text{c.c.}\right) . \tag{3.9}$$

The first term oscillates with ω, which is quite remarkable, as it follows that a nonlinearity can influence the polarization response at the fundamental frequency. This is also apparent from fig. 3.1 panels b) and c). Moreso, this polarization response at ω is proportional to $\tilde{E}^+(t)\tilde{E}^-(t)$ which in turn is proportional to the intensity I. As a consequence, there's an effective intensity dependence of the refractive index n of the medium which can be approximated as

$$n \approx n_0 + n_2 I(t). \tag{3.10}$$

This intensity dependence is referred to as *optical Kerr effect*. For a beam of light with a transverse intensity distribution this leads to a lensing effect (cf. e.g. [36, p. 105] and [28, p. 194]). This phenomenon is central to the modelocking mechanism in ultrashort laser oscillators as they are described in section 2.3.2 (cf. e.g. [39, 31, 32]).

In the time-domain the analog of the intensity-dependent lensing effect is referred to as *self-phase modulation* [40, chap. 4] on the basis of which novel techniques for spectral broadening and subsequent pulse compression based on third-order nonlinearities in noble gases were devised in the mid- to late 1990s when femtosecond laser sources with high output pulse energies became available and the use of single-mode optical fibers was no longer feasible for this purpose due to the pulse energies exceeding their damage threshold (cf. e.g. [41, 42]). Together with guided propagation in a thin glass-capillary the noble gases as nonlinear media offer the key advantages of tunability of the nonlinearity via variation of the gas pressure and species, as well as there being virtually no damage threshold to the nonlinear element (multiphoton ionization can of course occur, but it is reversible). Pulse propagation in these gas-filled hollow-core fibers has of course received much attention from the theoretical side due to their usefulness. A complete model must include not only the nonlinear polarization, but also the ionization and plasma response as well as linear contributions stemming from waveguide dispersion and attenuation. Furthermore, it should allow for energy transfer between the modes of the waveguide mediated by the nonlinearities. Travers et al. have quite recently shown beautifully that such a model can in fact describe the pulse propagation in a hollow core fiber in excellent agreement with the experiment [43]. For the purpose of demonstrating that a third-order nonlinearity leads to spectral broadening which in turn – given suitable compression techniques are available – can be used to shorten the duration of a laser pulse a simplified model shall be brought forward here. Taking dispersion into account effectively via a constant D_{eff} and otherwise neglecting everything but the nonlinearity, the envelope $a(z,t)$ (cf. eq. 2.6) of a pulse propagating inside a hollow core fiber, which is aligned along z a pulse described by eq. 2.6 can be propagated by the differential equation 3.11, inspired by the model suggested by Nisoli et al. in [42].

$$\frac{\partial}{\partial z}a(z,t) = iD_{\mathrm{eff}}\frac{\partial^2}{\partial t^2}a(z,t) - i\gamma_{\mathrm{eff}}\left|a(z,t)\right|^2 a(z,t) - \delta_{\mathrm{eff}}\frac{\partial}{\partial t}\left(\left|a(z,t)\right|^2 a(z,t)\right) \tag{3.11}$$

The third-order nonlinearity enters eq. 3.11 in the last two terms on the right hand side which both contain a measure of the intensity i.e. proportional to $|a(t)|^2$. As this model is greatly simplified and not expected to be representative of the actual situation in the laboratory we are at liberty to choose the parameters such that they yield a result that is qualitatively consistent with what is observed in reality without needing to worry about picking physically reasonable values for D_{eff}, γ_{eff} and δ_{eff}. Figure 3.3 shows eq. 3.11 integrated along a 3m long hollow core fiber in comparison with what is observed in the laboratory. Even though our model is greatly simplified it can generate qualitative agreement with the experimentally observed spectrum after propagation through the fiber. Panel c) in fig. 3.3 shows how the envelope of a gaussian pulse with flat spectral phase (panel a)) is modified by the propagation through the fiber (blue dashed line). After ideal compression (i.e. setting the spectral phase to some constant) a significantly shorter pulse can be generated (yellow line), in the case presented here the pulse from panel a) has a temporal FWHM of $\mathcal{T} \approx 30\,\mathrm{fs}$ and can be compressed down to (yellow line, panel c)) $\mathcal{T} \approx 5\,\mathrm{fs}$ after spectral broadening, in consistency with the pulse shown in fig. 2.3 which has been generated via spectral broadening of an amplified laser pulse in a noble-gas filled hollow-core fiber.

3.2 Higher intensities, high-order harmonic generation

Experiments with intense laser fields ($10^{14} - 10^{16}\,\mathrm{W/cm^2}$) of low frequencies on solids (Burnett et al. [44]) and high frequencies on noble gases (McPherson et al. [45]) revealed that a nonlinear frequency conversion of the incoming laser light to high integer harmonics takes place, and that their intensities follow an unexpected dependency on the harmonic order. A series of key experiments [46, 47] performed with low-frequency lasers on noble gases confirmed this unexpected dependency and yielded more insight: the harmonic intensity falls off sharply in the first few orders, then very

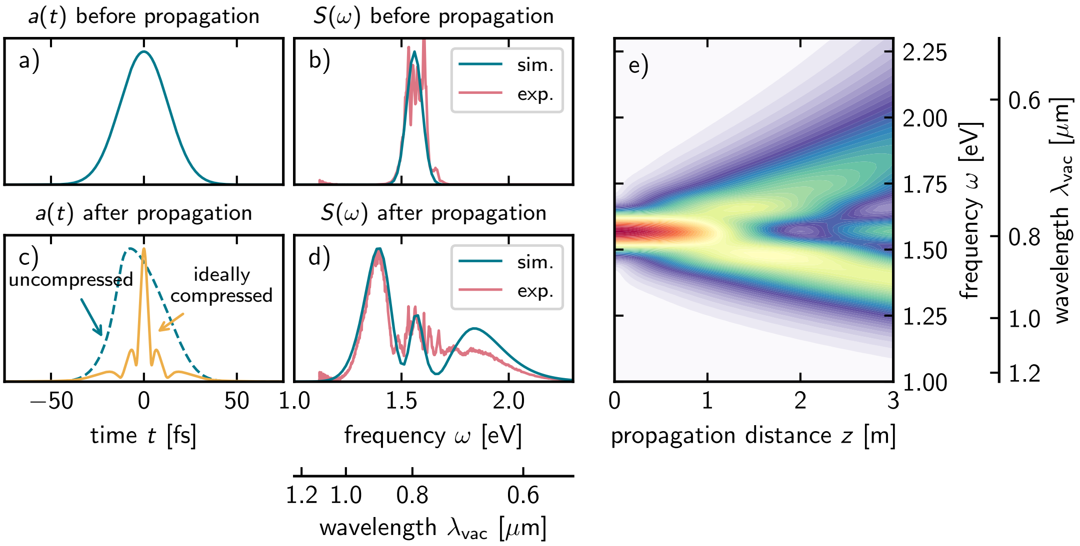

Figure 3.3: Spectral broadening and pulse compression based on the optical Kerr effect modelled via eq. 3.11 in comparison to the experiment over a propagation distance of 3 m. Before propagation the pulse spectrum is modelled as a gaussian (blue curve, panel b)) where the spectral width has been chosen to match that of the spectrum of the laser system in the laboratory (panel b), red curve). In the time-domain (panel a)) this corresponds to a pulse duration of about 37 fs. The optical Kerr effect is responsible for asymmetrically broadening the pulse's spectrum during the propagation through the noble-gas filled hollow-core fiber. Even though the model described by eq. 3.11 is very crude, qualitative agreement with the experiment can be achieved for the output spectra (blue and red curves in panel d)). In the time-domain (panel c)) the light pulse will be of essentially the same temporal width as before propagation through the fiber (blue dashed line), but due to the broader spectrum, a substantially shorter pulse duration is attainable after compression (yellow line). The model eq. 3.11 predicts pulse durations of ~ 5 fs being attainable i.e. consistent with the pulse shown in figure 2.3. Panel e) shows the evolution of the spectrum during its propagation along the fiber. Experimental spectra have been recorded by Andreas Duensing.

slowly over a broad region, again dropping abruptly for the highest observable orders. These three regions have been dubbed *perturbative region*, *plateau region* and *cut-off region* respectively. The authors of [46] and [47] realized that the perturbative picture of eq. 3.2 for the polarization response had broken down and the light intensity and thereby the electric field in these experiments alone was strong enough to facilitate ionization despite the ionization potential I_p of the noble gas exceeding the laser frequency by many times its value. Theoretical studies of the microscopic harmonic generation process by direct integration of the time-dependent Schrödinger equation [48] confirmed this interpretation and investigated the role of propagation effects which play a crucial role in the *phase matching* of the harmonic radiation (cf. sec. 3.2.3).

The developement of a semiclassical model of high harmonic generation (HHG) by P. B. Corkum [49] established an intuitive physical picture of the harmonic generation process and reproduced the observation that the cut-off region of the harmonic emission of a single atom is found at a photon energy of

$$E_{\mathrm{cut-off}} = I_p + 3.17U_{\mathrm{p}}, \tag{3.12}$$

where $U_{\mathrm{p}} = E_0^2/4\omega^2$ [50]. In this semiclassical model a valence electron is injected into the continuum via tunneling from its parent atom the potential of which is distorted by the electric field of the intense laser light such that a barrier sufficiently permeable to tunneling forms. During the sub-

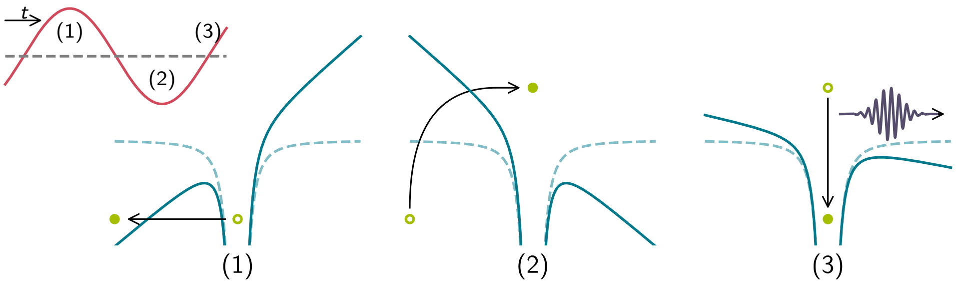

Figure 3.4: P. B. Corkum's semiclassical model of high harmonic generation (HHG). At one maximum value of the laser field (top left, red, (1)) the atomic potential (lower panels, blue) is distorted such that a barrier enabling tunneling of a valence electron forms. The electron is accelerated in the oscillating laser field which eventually reverses its direction (2) and may recombine with its parent ion, emitting radiation (3).

sequent propagation of the electron in the laser field it can gain kinetic energy which is released as harmonic radiation given it recollides with the atomic core upon reversal of the laser field's direction (cf. fig. 3.4).

A quantum theory of high harmonic generation has been brought forward in a seminal publication by Lewenstein et al. [51]. This was motivated by the previous observation that the 'cut-off law' (eq. 3.12) may be violated due to propagation effects in the nonlinear medium [52]. The central quantity of the Lewenstein model is the dipole moment $d(t) = -e\langle x(t)\rangle$ of the atoms subjected to the intense laser field. Its Fourier transform will yield the single-atom harmonic spectrum. Lewenstein's route towards calculating $\langle x(t)\rangle$ starts at the one-electron time-dependent Schrödinger equation for the atom in the laser field, for which under three key assumptions a solution can be brought forward. These assumptions are that all bound states of the system except for its ground state can be neglected, that the depletion of the ground state is small enough such that it does not need to be considered, and that the electron can be treated as a free particle in the continuum. If these conditions are met, applying the saddle-point method to only include electron trajectories that reencounter the parent atom, one can write for linearly polarized laser light and arbitrary pulse shapes $E(t)$ [53, p. 53-54]

$$\langle x(t)\rangle = i\int_0^\infty d\tau \left(\frac{\pi}{\varepsilon + i\tau/2}\right)^{\frac{3}{2}} d^*(p_{\mathrm{st}}(t,\tau) - A(t))d(p_{\mathrm{st}}(t,\tau) - A(t-\tau))E(t-\tau)\exp\left(-iS(t,\tau)\right). \tag{3.13}$$

In this expression, $E(t)$ is the laser pulse's electric field, $A(t)$ is the corresponding vector potential, $p_{\mathrm{st}}(t,\tau) = \int_{t-\tau}^{t} dt'' A(t'')/\tau$ is the *stationary momentum* i.e. the canonical momentum for which the electron released at the time $t-\tau$ returns to the parent atom at τ,

$$S(t,\tau) = \int_{t-\tau}^{t} dt'' \left(\frac{\left(p_{\mathrm{st}}(t,\tau) - A(t'')\right)}{2} + I_p\right), \tag{3.14}$$

is the *quasiclassical action* of the liberated electron in the laser field and $d(p)$ is the dipole transition matrix element, which for hydrogenic atoms may be approximated as

$$d(p) = i\frac{2^{\frac{7}{2}}\alpha^{\frac{5}{4}}}{\pi}\frac{p}{(p^2+\alpha)^3} \tag{3.15}$$

with $\alpha = 2I_p$.

Single-atom-response high-harmonic spectra can be calculated via evaluation of eq. 3.13 and subsequently applying the Fourier transform. A numerical implementation benefits greatly from the application of some mathematical transformations of the expressions underlying the Lewenstein model

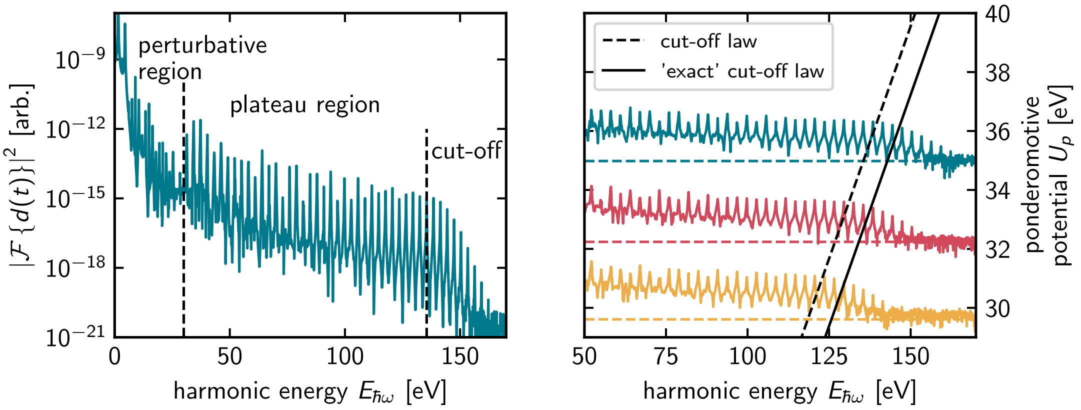

Figure 3.5: Application of the microscopic Lewenstein model to a continuous driver with $\omega_0 = 1.5\,\mathrm{eV}$. The separation of the harmonic spectrum into the *perturbative*, *plateau* and the *cut-off* region is easily seen (left panel). In a series of spectra calculated for different ponderomotive potentials (dashed colored lines in the right panel) one finds the cut-off energy to follow eqns. 3.12 or 3.16 respectively (dashed and solid black lines respectively). The full color curves in the right panel are the single-atom harmonic spectra for the three ponderomotive potentials $U_\mathrm{p} = 29.6\,\mathrm{eV}$ (yellow), $U_\mathrm{p} = 32.2\,\mathrm{eV}$ (red) and $U_\mathrm{p} = 35.0\,\mathrm{eV}$ (blue) respectively, shifted by their respective ponderomotive potential along the ordinate.

presented in chapter 3.2 of [54]. With such an implementation at hand one can study the effect of the driving pulse's parameters on the (single-atom) harmonic spectrum.

3.2.1 High Harmonic generation with long driving pulses

For long driving pulses the Lewenstein model reproduces the expected shape of the spectrum comprised of odd integer harmonics of the driving field and their dependency on the harmonic order (see fig. 3.5, left panel), and the position of the cut-off region follows the empirical eq. 3.12 very well (fig. 3.5, right panel). One achievement of the Lewenstein model is the refinement of the cut-off law as

$$E_\text{cut–off} = 3.17U_\mathrm{p} + I_pF(I_p/U_\mathrm{P}), \tag{3.16}$$

where $F(x) \approx 1.3$ for a broad range of arguments. As $F(x)$ varies very slowly, the effect of its curvature on the predicted cut-off position is not apparent in figures 3.5 and 3.6. The predicted cut-off position simply appears at higher harmonic energies.

3.2.2 High harmonic generation with few-cycle driving pulses

When driven with few-cycle pulses, the single-atom harmonic spectra change quite drastically with the structure of odd harmonics being smeared out considerably and the cut-off possibly exhibiting no modulations (cf. e.g. [55]). The differences to the case of a long driving pulse can be understood in terms of the electron reencountering its parent ion only a small number of times whereby only a few short bursts of XUV light are emitted [56, p. 1253]. In the same publication, Christov et al. furthermore pointed out that spectrally selecting a part of the cut-off e.g. with dedicated XUV optics would be a feasible way of extracting a single isolated XUV pulse from the harmonic emission which would have a duration of less than one femtosecond.

The Lewenstein model is applied to a few-cycle driving pulse in fig. 3.6. The top panels demonstrate that the cut-off laws retain their validity, while the bottom panels show that the cut-off region

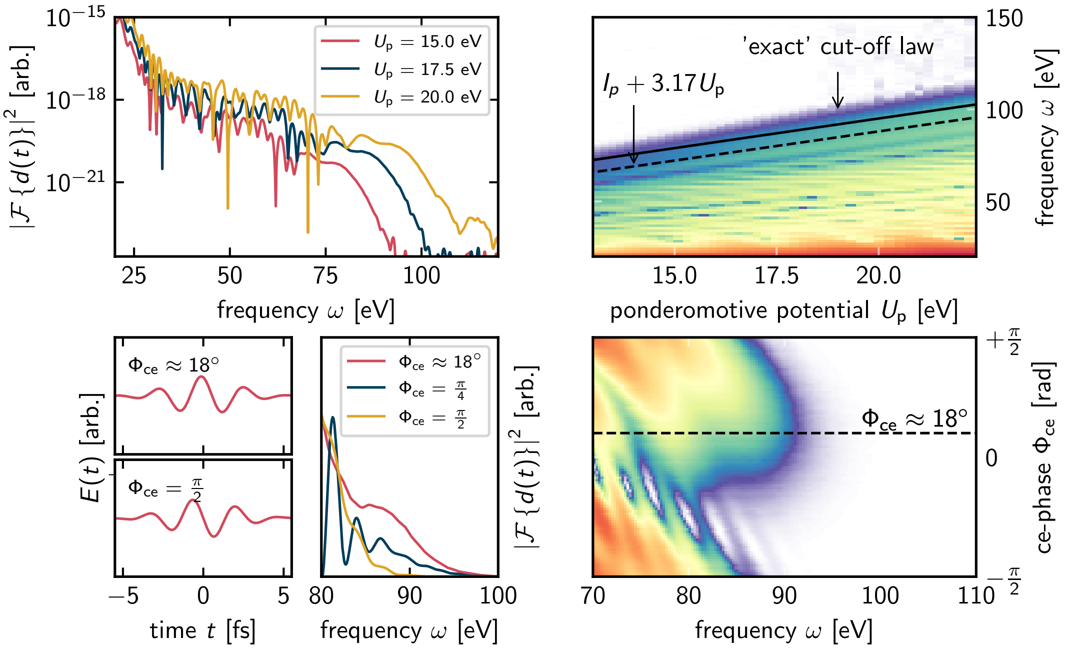

Figure 3.6: Application of the microscopic Lewenstein model to short gaussian pulses of 4.6 fs duration. The top panels show the dependency of the cut-off region on the ponderomotive potential U_p associated with the driving pulse: The cut-off can be shifted by varying the ponderotive potential (top left panel). The empirical cut-off law of eq. 3.12 is well reproduced even for feq-cycle pulses (top right panel, dashed line). The refined, 'exact' eq. 3.16 is shown in the top right panel as a solid line. The dependency of the shape of the cut-off region on the driving pulse's ce-phase is explored in the bottom panels. on the left, three lineouts from the ce-phase sweep displayed in the bottom right panel are shown, together with two respective driving pulses. Deep modulations in the cut-off spectrum appear for ce-phases between ~ 45° and 90°, while the smoothest cut-off with the highest photon energies is reached for $\Phi_\mathrm{ce} \approx 18°$. Color maps are non-linear.

of the spectrum is quite sensitive to the ce-phase of the driving pulse. This phase-sensitivity is especially relevant in the context of this work: explored by de Bohan and co-workers in 1998 [57] and experimentally confirmed by Baltuška et al. in 2003 [34] it was found that for nearly cosine-shaped few-cycle driver pulses the cut-off harmonic emission is smooth such that it lends itself to attosecond pulse generation via spectral filtering in the spirit of [56].

As it is presented here, the Lewenstein model describes only the response of a single atom. Real world sources of harmonic radiation however employ macroscopic gas media in which propagation effects can drastically reshape the harmonic emission. A numerical implementation of the Lewenstein model with progagation effects included is available as the `HHGmax` software package [58]. Phase matching is crucial to the efficident generation of high harmonic radiation in experimental sources and is (next to ce-phase control) at a fixed wavelength of the driving laser one of the main mechanisms by which the harmonic spectrum is shaped. Due to its importance it has been thoroughly researched (cf. e.g. [59, 60, 61, 62, 63]) and some key findings of this research shall be summarized in the following.

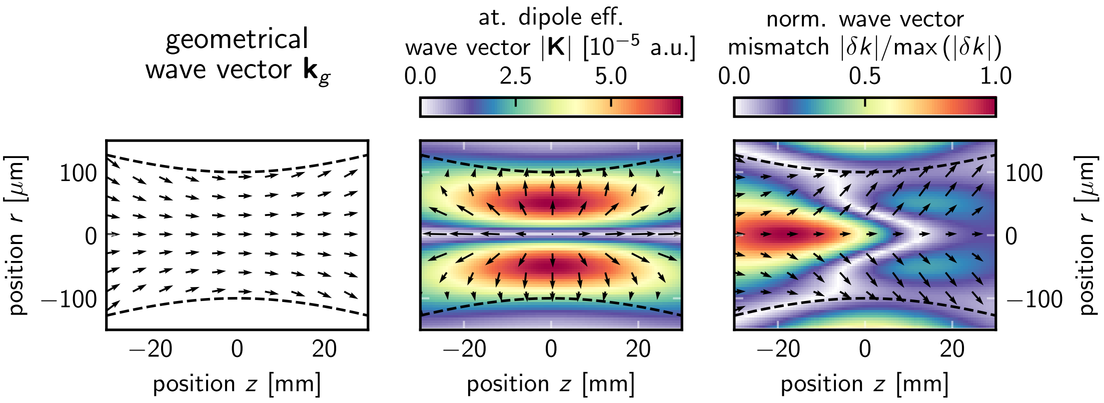

Figure 3.7: Phase matching of the high harmonic cut-off for negligible dispersive contributions. The geometrical wave vector $\mathbf{k}_g$ which points along the propagation direction of the driving beam and its spatial profile is shown in the leftmost panel with its envelope as dashed lines (in all panels). The center panel shows the effective wave vector of the atomic polarization $\mathbf{K}$ in its magnitude (false-color map) and direction (arrows). It consistently points outwards away from the focus. The resulting polarization wave vector (arrows) and its normalized absolute difference to the q-th harmonic wave vector $k_{\mathrm{harm}} = q\omega_0/c$ is shown in the rightmost panel. A region where phase-matched collinear harmonic generation is possible and the intensity is still appreciable arises about 15 mm after the focus. Two other regions of small wave vector mismatch exist before the focus at $z \approx -10$ mm and $r \approx \pm 90\,\mu$m, but the harmonic beam generated there will not be collinear and have unfavourable temporal properties. The radial components of all wave-vectors have been scaled for this visualization. A gaussian beam profile with a peak intensity of $I \approx 3.5 \cdot 10^{14}$ Wcm^{-2} was assumed which would yield a cut-off energy of ~ 90 eV.

3.2.3 Phase matching of high-harmonic generation

Central to the concept of phase matching is the observation that the efficiency of a frequency conversion process is maximized when the difference in phase between the polarization induced by the driving field and the generated harmonic field is minimized [60, p. 3777]. The mismatch between these phases can be measured via the difference of the magnitudes of the wavevectors of the polarization $\mathbf{k}$ and the field of the q-th harmonic $k_{\mathrm{harm}} = q\omega_0/c$ as

$$|\delta k| = \left|k_{\mathrm{harm}} - |\mathbf{k}|\right| . \tag{3.17}$$

The contributions to the total polarization wave vector

$$\mathbf{k} = \mathbf{k}_g + \mathbf{K} + \mathbf{k}_n + \mathbf{k}_p \tag{3.18}$$

are the geometrical $\mathbf{k}_g$ i.e. due to the focussing of the beam, the effective atomic dipole response wave vector $\mathbf{K}$, $\mathbf{k}_n$ which captures the dispersion of the neutral medium and $\mathbf{k}_p$ which is due to the dispersion due to the ionized fraction of the medium.

Neglecting the dispersive contributions to $\mathbf{k}$ for now and assuming (following [63, p. 2] and [61, p. 3205]) that $\mathbf{K} \propto -\nabla I(r,z)$ where $I(r,z)$ is the spatial intensity distribution of the driving beam close to the focus, one can make an interesting observation: the geometrical wave vector $\mathbf{k}$ points along the propagation direction and the profile of the waist of the beam, while the effective atomic dipole wave vector $\mathbf{K}$ points away from the focus everywhere near the origin of the (r,z) plane their sum may match the k_{harm} in a region where $z > 0$. Therefore, if the nonlinear medium is placed slightly after the focus one can attain phase matching. Taking a closer look at the direction of the polarization wave vector in this region furthermore reveals that the resulting harmonic beam will be collinear with the driving field. Another such region of favourable phase matching may depending on the parameters also be present before the focus, but the total polarization wave vectors point away from the fundamental beam whereby an annular beam profile is to be expected in the far field [61, p. 3207f.] with a distorted temporal shape [64, p. 4751]. The region after the focus is favourable for isolated attosecond pulse generation and therefore chosen for the experiments presented in this work. Figure 3.7 illustrates these arguments.

This discussion and figure 3.7 motivates using the position of the nonlinear medium (usually a gas jet) as a way of selectively phase matching harmonic emission at a particular photon energy $E_{\hbar\omega} = q\omega_0$ (even for non-integer q e.g. in the cut-off). Furthermore, an iris in the beam path before the focusing allows one to control the z-gradient of the intensity which will influence the atomic dipole response's phase. In summary, by operating the iris one chooses the q and thereby the cut-off photon energy for which one wants to phase-match. This also changes the position of the phase-matching region, whereby the gas jet must be moved. The cut-off photon energy becomes tunable over a wide range of energies.

Dispersive effects captured by the last two terms in eq. 3.18 are due to the (nonlinear) refractive index of the neutral atoms in the gas jet and the presence of plasma due to strong-field ionization. It is possible to balance these two effects as they contribute with opposing signs [62, p. 10517ff.]. For the simple case of a plane-wave beam an ideal ionization fraction η (eq. 3.19) where neutral and plasma dispersion cancel can be derived [65] which is a function of the atomic number density N_{atm} at 1 atm, the driving laser's wavelength λ, and the difference Δn between the refractive indices at the fundamental and the harmonic wavelengths.

$$\eta = \left(1 + \frac{N_{\mathrm{atm}} r_e \lambda^2}{2\pi \Delta n}\right)^{-1} \tag{3.19}$$

In this equation r_e is the classical electron radius. For the noble gases He, Ne and Ar which are often used for high harmonic generation, these are in the single-digit percents for near-infrared driving light (~ 800 nm). For longer driving wavelengths which according to the cut-off laws (eqs. 3.12 and 3.16) are favourable for the generation of high photon energies one finds smaller ionization fractions due to the λ^{-2}-dependency of eq. 3.19 [62, p. 10517].

In the experiment it is not clear whether phase matching is achieved by balancing the geometric terms and the dispersive terms separately or not, as e.g. both the ionization fraction and the refractive index of the gas species as well as the geometric contribution $\mathbf{k}_g$ as well as the atomic $\mathbf{K}$ depend on the laser intensity which can be adjusted via an iris and the position of the gas-jet along the focussed beam. Experience teaches though that most adjustment is done via the geometry of the high harmonic generation set-up and the gas pressure can be varied in order to slightly optimize the flux at the desired photon energy afterwards.

3.3 Synthesis and characterization of attosecond XUV pulses

The possibility of synthesizing XUV pulses of a duration of less than one femtosecond via high harmonic generation has first been realized by Farkas and Toth in 1992 [66], and the first experimental observation of this temporal structure is due to Paul and co-workers almost a decade later [67]. However, both the proposal and the first observation were not of isolated attosecond XUV pulses, but of a train of such pulses emerging mostly from the plateau region or a modulated cut-off region of the harmonic spectrum. The first isolated XUV pulses with a duration of less than a femtosecond were reporded by Hentschel et al. in 2001 in a groundbreaking experiment [68], heralding the age of attosecond metrology.

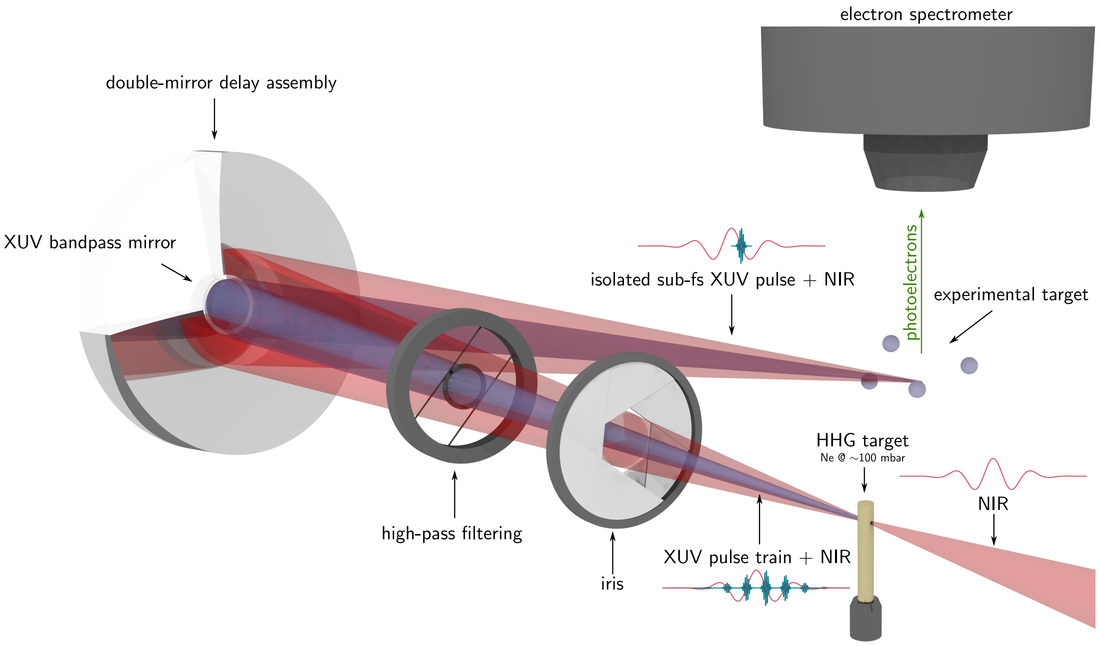

Figure 3.8: Principle of an attosecond streaking experiment. High harmonic radiation is generated in a noble-gas jet, yielding a train of XUV pulses co-propagating with the ce-phase controlled NIR driving field. An iris controls the strength of the residual diriving field at the location of the experiment. A thin metal foil suspended in the beam path spatially separates the harmonic radiation from the copropagating NIR. The cut-off region is spectrally filtered by a focusing XUV bandpass mirror which is inserted into a drilled focussing mirror for the XUV. By varying the insertion depth, the temporal delay between the XUV and the NIR pulse can be controlled. The XUV reflected off the mirror will be of only a single isolated attosecond XUV pulse which, together with the NIR is focussed onto the experimental target. For pulse characterization a noble gas not exhibiting any resonances near the excitation energy should be chosen. The photoelectrons liberated by the XUV pulse will be *streaked* by the NIR, resulting in a shift of their final kinetic energy as a function of the relative delay time between XUV and NIR. A set of photoelectron spectra recorded as a function of this relative delay will comprise a streaking spectrogram.

Today, isolated attosecond XUV pulses are routinely and reproducibly generated via high-harmonic generation with ce-phase controlled driver pulses, following the protocols developed in the groundbreaking experiments by Kienberger et al. [20] and Goulielmakis et al. [21]. The attosecond streak camera method experimentally developed in the same publications is also the most versatile tool to characterize subfemtosecond (or henceforth *attosecond*) XUV pulses: High harmonic radiation is generated in a gas target, resulting in a train of XUV pulses copropagating with the remainder of the driving pulse. The XUV is spatially separated from the NIR via a high pass filtering metal foil that is suspended in the beam path. Both beams, the XUV and the now annular NIR beam are reflected of a focussing mirror assembly, the central part of which acts as the focussing and band-pass filtering stage for the XUV, while the outer part simply reflects and focuses the NIR. The band-pass mirror, which selects a single attosecond pulse from the pulse train can be moved back and forth in the direction of the beam via a piezoelectric acutator, facilitating the introduction of a controllable delay $\Delta\tau$ between NIR and the attosecond pulse. Both pulses are brought onto a sample where the XUV pulse liberates photoelectrons which then propagate in the NIR field. The NIR pulse will modulate the photoelectrons' final kinetic energy as a function of the relative delay between the XUV and the NIR pulse. By scanning the relative delay and measuring photoelectron spectra a streaking

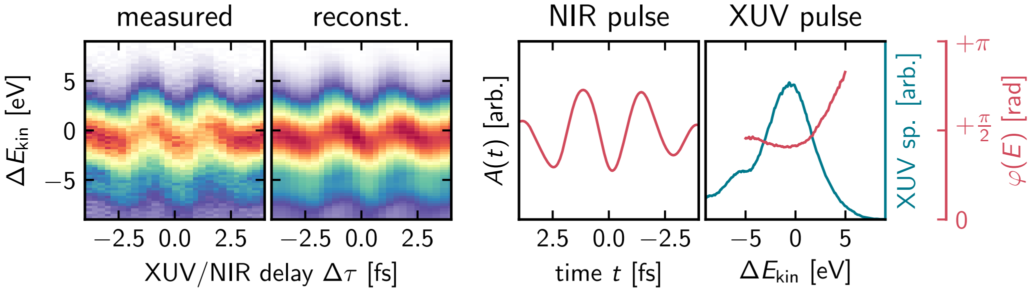

Figure 3.9: Characterization of isolated attosecond pulses with the attosecond streak camera. The ptychographic reconstruction algorithm (see appendix C.2 and [69]) has been applied for spectrogram inversion. The measured spectrogram is displayed in the leftmost panel, with a spectrogram calculated from the reconstructed NIR vector potential and the XUV pulse shown next to it. The NIR vector potential and the XUV pulse decomposed into an absolute spectrum and its spectral phase are shown in the rightmost panel. Its chirp as reflected in its spectral phase's curvature is responsible for the asymmetry beteween the rising and the fallig flanks of the NIR vector potential traced out by the streaking in the leftmost panel.

spectrogram is recorded in which the photoelectron distribution will trace out the variation of the NIR pulse's vector potential. Figure 3.8 shows the principle of an attosecond streaking setup as it has been used in the course of this work.

The attosecond streak camera maps the temporal properties of the ejected photoelectron wave packets onto spectral information [70], and as it shall be seen and further elaborated upon in the next chapter this is central to this work. When one chooses an experimental sample where the phase of the dipole transition matrix element for the ionizing transition does not significantly vary with energy any distortion of the photoelectron wave packet's phase will be due to the properties of the exciting pulse, enabling its characterization via various methods. Their common ground is that the two-dimensional streaking spectrogram can as a function of the kinetic energy E and XUV/NIR delay $\Delta\tau$ approximately be written as

$$S(E,\Delta\tau) \propto \left| \int_{-\infty}^{\infty} dt P(t-\Delta\tau) G(t) \mathrm{e}^{-iEt} \right|^2, \tag{3.20}$$

where $P(t)$ carries information on the XUV pulse and $G(t)$ the action of the streaking laser field. Powerful algorithms exist for the extraction of $P(t)$ and $G(t)$ exist (cf. e.g. [71], [72] and [69]). Figure 3.9 shows the results of the latter algorithm being applied to an attosecond streaking spectrogram recorded for the He1s photoemission recorded at a photon energy of $E_{\hbar\omega} = 90\,\mathrm{eV}$.

Chapter 4

Photoemission timing

Time delays occuring in atomic, molecular and solid-state photoemission are the primary observable of interest in the experiments presented in this work. Their assessment requires not only specialized experimental techniques, but also careful data analysis and the proper inclusion of measurement induced contributions in their interpretation. The notion of a time delay requires establishing a universal zero point to which all times are referenced. Intuitively, this time-zero is the arrival time of the photon in the interaction region in the experiment. Apart from not being well defined, it is unfortunately also not directly experimentally accessible. However, due to the groundbreaking work of Ossiander et al. [23, 18] an absolute reference can be introduced today. The concept of photoemission times itself may strike the reader as a strange one at first, but a firm connection to scattering theory can be established. This chapter will introduce the concept of scattering and photoemission time delays via classical and quantum mechanical arguments and then proceed towards how they can be assessed via the attosecond streak camera in an experiment. Finally, the referencing scheme developed by Ossiander [18] is discussed.

4.1 Time delays in scattering

The introduction into the topic given in Marcus Ossiander's dissertation [24] is excellent. Therefore we shall loosely follow his line of arguments, and borrow inspiration for some of the illustrations, starting with a classical example, then moving to the quantum mechanical case for short-ranged potentials and finally to the experimentally relevant case of coulombic systems.

4.1.1 Scattering delays for short-ranged potentials

In the absence of friction a person on a skateboard or on inline skates with a velocity v will keep their velocity for all times when travelling over flat ground, whereby after a time t their position will have changed by $\Delta x = vt$. A friend starting out at the same velocity and at the same place x_0 but encountering a shallow pit on their trajectory will momentarily be faster while traversing the pit due to having been accelerated on the way to the lowest point of the pit by gravity, decelerating again towards their initial velociy on the way out of the pit. At a point far away, when their velocities are equal again, the person encountering the pit will have gained an advance with respect to the person travelling over flat land, and they will be at a position x', which the person travelling over flat land will only reach at $t + \tau$. This time delay τ can be measured at a finish line placed at x_{end} at a large enough distance from the pit such that its action does not influence the motion anymore. As both skaters have the same velocity there it will be independent of the position of the finish line with respect to the pit, and as both skaters started out with the same velocity at x_0 and the action of the pit which creates the time delay is localized to a finite area it will also be independent of the position of the pit.

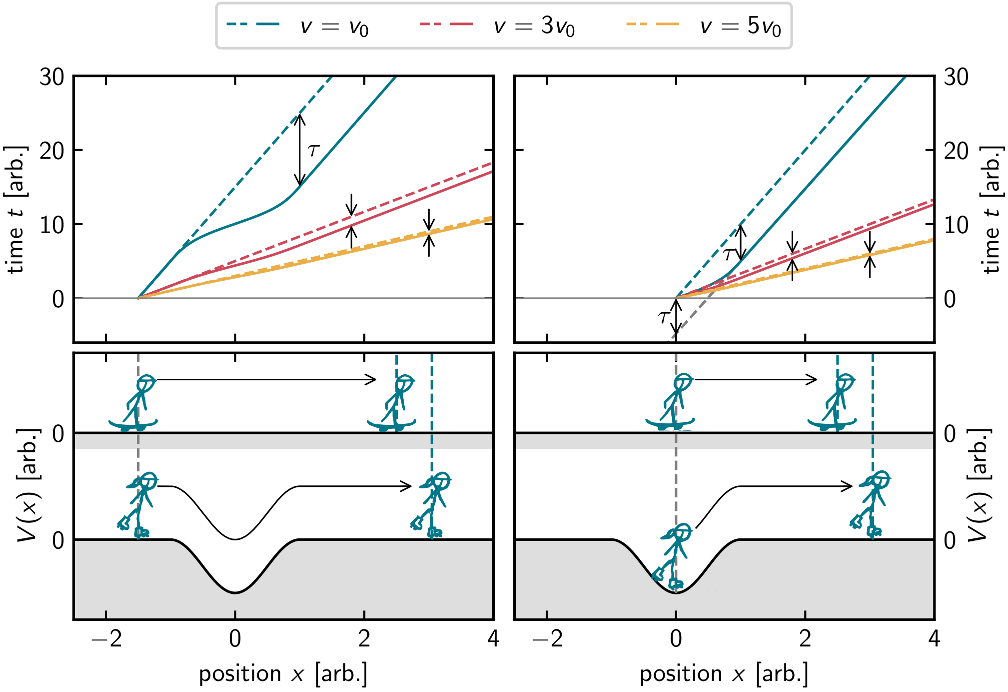

Figure 4.1: Time delay due to traversal of a potential. The left panels show two skaters in a time-vs.-position picture for one (inline skates) travelling over flat land and the other (skateboard) traversing a pit $V(x)$. While the inline skater moves uniformly corresponding to the straight dashed lines in the upper panel, the skateboarder's velocity is increased while traversing the pit whereby it gains a spatial advance with respect to the inline skater. At a finish line positioned far from the pit this spatial advance will become measurable as a temporal delay τ which, as the asymptotic velocities of the skaters are equal, does not depend on the position of the finish line. The right panels depict a situation where one of the skaters starts in the pit at the same time another starts out on flat land. In order for a time delay measured at a finish line to be well defined their final asymptotic velocities need to coincide, otherwise their spatial separation will grow with time. With the starting velocities chosen appropriately the skater originating from the pit is indistinguishable from one starting with a headstart of τ as the extrapolation towards negative times (dashed gray line) in the top right panel shows. In both cases a larger initial velocity results in a smaller asymptotic time delay.

The left panels in fig. 4.1 illustrate this situation. It also becomes intuitively clear that the absolute value of the time delay τ depends on the shape of the potential, and also the initial velocity v: for a small initial v the change in velocity due to the potential is significant, and it is less so for a large initial velocity, for which in consequence τ will be smaller.

If now instead of both skaters starting out on flat ground one of them starts *in* the pit (with enough excess velocity to leave it) it is clear that if their asymptotic velocities are not equal, the spatial separation between them will grow with time, and therefore a time delay measured between them at a finish line at x_{end} will depend on x_{end} and is not well defined. If the velocity of the skater starting in the pit is chosen such that its asymptotic velocity coincides with that of the skater on flat land though a time delay measured at the finish line will not be dependent on its position and thereby be well defined. In this case an interesting observation can be made: as the skater starting in the ditch will have to start with a higher velocity it'll traverse the distance to the edge of the pit faster than the skater on flat land traverses the same distance – it will be indistinguishable form a skater starting with a headstart, even if they started at the same time. For an observer at the finish line who does not know about the existence of the potential and the initial difference in velocities this may seem like a violation of causality, as if one of the skaters had started before the starting shot was fired. This situation is illustrated in the right panels in fig. 4.1.

The gist of this discussion is that time delays imparted on an object in motion by interaction with a potential can only be measured relative to a well defined reference sharing the same asymptotics as the scattered object. The reference in our example here is the skater moving freely over flat land with the same asymptotic velocity as the skater traversing the potential.

The insights from this discussion can be carried over to quantum physics. The scattering of a particle represented by a wave packet off a short-ranged potential shows a very similar behaviour. Enclosed in a finite-sized box, a propagating gaussian wave packet $\propto \exp(-ikx)$ can be assembled from the eigenstates of the potential $V(x)$ or plane waves respectively for the propagation in free space. After some time t one will find – just as in the classical case – that the wave packet scattering off the potential will have gained a spatial advance Δx with respect to the freely propagating wave packet, as measured at the position of their center of gravity. Figure 4.2 illustrates both cases, and in the top panel also shows the individual components of the respective wave packets in gray for propagation in free space and color coded for energy for the scattered wave packet. The increase in speed of the skaters in the classical picture is reflected in an increase in frequency of the individual components making up the wave packet as it is shown in the inset. This leads to an asymptotic energy dependent phase shift $\varphi(E)$ responsible for the time delay. A simple calculation [73] will link the scattering phase with the time delay: consider the superposition of two plane waves

$$\Psi(x,t) = \mathrm{e}^{i(k+\Delta k)x - i(E+\Delta E)} + \mathrm{e}^{i(k-\Delta k)x - i(E-\Delta E)} \tag{4.1}$$

with wavenumbers $k + \Delta k$ and $k - \Delta k$ and energies $E + \Delta E$ and $E - \Delta E$. The center of this wave packet will travel as

$$x = \frac{\Delta E}{\Delta k} t, \tag{4.2}$$

as this is where both waves are exactly in phase. If such a wave packet now encounters a scattering potential, the two components it is composed of will encounter a phase shift $\varphi + \Delta\varphi$ and $\varphi - \Delta\varphi$ respectively. Consequently one has

$$\Psi_{\mathrm{scat}}(x,t) = \mathrm{e}^{i(k+\Delta k)x - i(E+\Delta E) + i(\varphi+\Delta\varphi)} + \mathrm{e}^{i(k-\Delta k)x - i(E-\Delta E) + i(\varphi-\Delta\varphi)}. \tag{4.3}$$

These two waves are now in phase at

$$x = \frac{\Delta E}{\Delta k} t - \frac{\Delta\varphi}{\Delta k} = \frac{\Delta E}{\Delta k}\left(t - \frac{\Delta\varphi}{\Delta E}\right), \tag{4.4}$$

which for infinitesimal Δk and ΔE we can write as

$$x = \frac{\partial E}{\partial k}\left(t - \frac{\partial\varphi}{\partial E}\right). \tag{4.5}$$

Therefore, with respect to a reference wave packet with phase $\varphi_{\mathrm{ref}}(E)$, one will find the scattered wave packed to be delayed by

$$\tau^{\mathrm{EWS}}(E) = \frac{\partial}{\partial E}\left(\varphi_{\mathrm{scat}}(E) - \varphi_{\mathrm{ref}}(E)\right). \tag{4.6}$$

The interpretation of scattering phase shifts in terms of a time delay was first established by Eisenbud in their dissertation [74], where they identified it as the energy derivative of the scattering phase. Some further properties of this time delay were worked out by Wigner in 1955 [73], and the formalism was extended further by Smith in 1960 [75]. Honoring their achievements, this time delay is referred to as Eisenbud-Wigner-Smith (EWS) time delay τ^{EWS}.

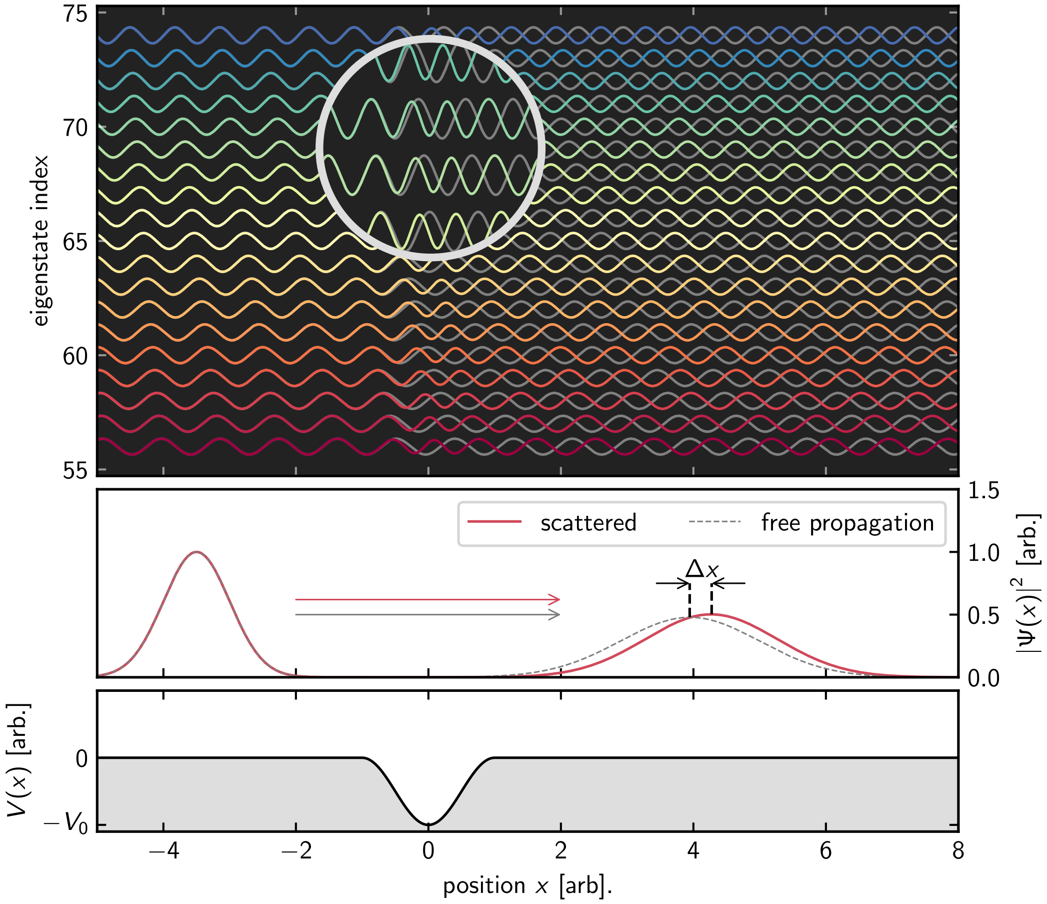

Figure 4.2: Propagation of a wave packet in free space and scattering of a potential in one dimension. A propagating wave packet can be assembled from eigenstates of a potential $V(x)$ (top panel). Its time evolution is determined by the Schrödinger equation. As expected, a wave packet propagating in free space (gray dashed line in middle panel) which is a superposition of plane waves will spread with time and its center of gravity will move with a group velocity $v_g(k) = k$. A wave packet started with the same velocity scattering off a potential $V(x)$ (bottom panel) that vanishes everywhere except for a finite region of space D will retain its initial velocity after the scattering has taken place, but will appear to have gained an advance with respect to the freely propagating wave packet (red line in middle panel). This is due to the phase shift imparted onto the individual plane-wave-like components of which the wave packet is comprised (top panel). The white circle shows a magnification of some of these components. Colored lines indicate the partial wave components from which the scattered wave packet is assembled with the colors indicating the energy corresponding to the respective wave (red stands for low energies while blue denotes high energies), gray lines show plane waves starting out with phase and frequency choosen equal to that of the respective colored wave before encountering the potential.

4.1.2 Scattering delays in Coulombic systems

The discussion in the previous section is for the case of a short-ranged scattering potential. Photoelectron wave packets created via ionization of a neutral system as they are of interest in this work are subject to the Coulomb potential of the residual ion though, which is not short-ranged. Asymptotically, the phase of a scattered wave with energy E and angular momentum ℓ in a Coulomb potential with charge Z is

$$\varphi(E,r) = -\frac{\pi\ell}{2} + \frac{Z}{\sqrt{2E}} \ln\left(2\sqrt{2E}r\right) + \arg\Gamma\left(1+\ell - i\frac{Z}{\sqrt{2E}}\right), \tag{4.7}$$

which explicitly depends on the energy E *and* the distance r of observation from the scattering center via its second term [76]. In consequence, the scattering time delay will be ill-defined and diverge for $r \longrightarrow \infty$ when referenced against a plane wave. This problem can be mitigated by choosing a reference with the same asymptotic behaviour, such that the divergence cancels: in the presence of a Coulomb field eq. 4.6 must be modified to read

$$\tau^{\text{EWS}}(E) = \frac{\partial}{\partial E}\left(\varphi_{\text{scat}}(E) - \varphi_{\text{ref}}(E) - \frac{Z}{\sqrt{2E}}\ln\left(2\sqrt{2E}r\right)\right), \tag{4.8}$$

as it follows from a 1979 publication by C. W. Clark [76]. This is the definition of the EWS delay that will be used in the following.

4.1.3 Relating scattering and photoemission

The discussion of scattering processes in the previous sections can now be linked to the phenomenon of photoemission. Figure 4.3 summarizes the similarities and differences. Considering an electron scattering experiment on a positively charged ion, a beam of electrons is directed at the ion. The interaction with the potential will modify its phase and give rise to an observable angular distribution. In principle complete phase (and therefore timing) information can be retrieved from this angular distribution, but this is experimentally infeasible due to the typically large number of partial waves contributing to the scattering signal [77, p. 770].

In a photoemission experiment the photoelectron can also be thought of as scattering off its positively charged parent ion. The key difference is that there is no incoming beam of electrons – the scatterer is created at the scattering center itself by the impinging photon. In the classical picture of scattering time delays developed in sec. 4.1.1 this corresponds to the situation where one skater starts out inside the pit, with the starting shot for both skaters being given by the arrival of the photon. Therefore, and also due to the interaction of the leaving photoelectron with its parent ion being coulombic, a reference with the same asymptotic behaviour as the photoelectron must be choosen in order to properly define a photoemission time delay (cf. sec. 4.1.1 and 4.1.2). This reference is however only conceptual, and can be thought of as a photoelectron created at the instant of photon arrival with the same logarithmic phase distortion as the photoelectron escaping the Coulomb potential, but otherwise behaving like a free electron. Just as in the classical case, the photoelectron will then appear to have a headstart with respect to the reference whereby it seems as if the electron had left the atom before the arrival of the photon if the observer is not aware of the potential the photoelectron traverses, whereby causality appears to be violated. This is not the case though, the negative photoemission time is simply due to the photoelectron evolving faster than the reference.

Another consequence of the photoelectron being created at the scattering center is that it will only have traversed 'half' the potential (as compared to an incident beam of electrons which completely cross the scattering center from left to right in fig. 4.3). In the spirit of [24] we can therefore refer to photoemission as a 'half-scattering' process.

4.2 Assessing photoemission timing with the attosecond streak camera

Originally intended as a technique for attosecond XUV pulse characterization, a quantum mechanical model of the streaking process has first been developed by Itatani et al. [78] and Kitzler et al.

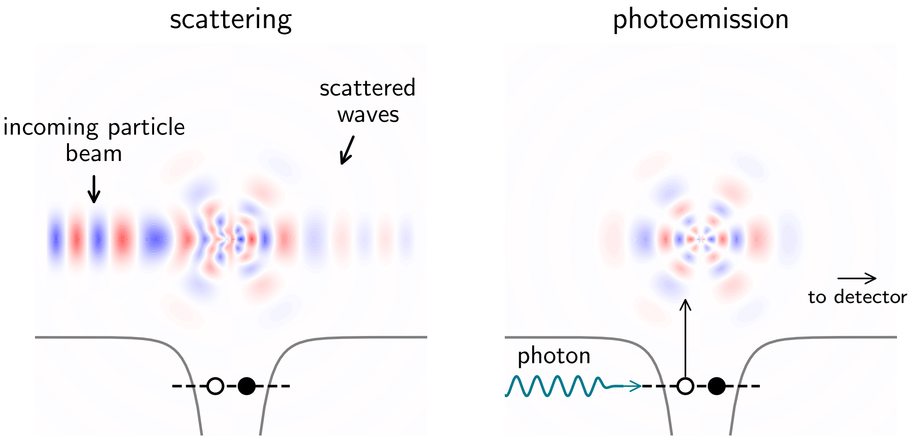

Figure 4.3: On the relationship between elastic scattering and photoemission, potentials (gray) and top-down view of the scattered/photoemitted waves (blue/red). In a scattering experiment a beam of electrons is directed onto a positively charged ion (left panel). The scattered waves which will have an angular distribution characteristic of the properties of the ion will be detected at a large distance where their associated kinetic energy is equal to that of the particles in the incoming beam. In the case of photoemission (right panel) the atom is initially neutrally charged. The positive ion as well as the electron to be scattered is created by an impinging photon *at* the scattering center. Therefore, when the electron is detected it will only have traversed 'half' the potential as compared to the true scattering case. In both cases the phase shifts imparted onto the individual partial waves describing the scattered or photoemitted electron contain the sought timing information.

[79] independently in 2002. The authors derived an expression for the photoelectron spectrum in the dipole approximation and in length gauge under the assumption that the effect of the Coulomb potential on the photoelectron is negligible once it is liberated. In the standard geometry of an attosecond streaking experiment both XUV and NIR pulse are polarized in parallel to the direction of photoelectron observation, and the expression for the photoelectron spectrum reads [70, p. 2]

$$S(p,\Delta\tau) \propto \left| \int_{-\infty}^{\infty} E^{+}_{\mathrm{xuv}}(t'+\Delta\tau) d\left(p + A_{\mathrm{nir}}(t')\right) \mathrm{e}^{-i\Phi_{\mathrm{V}}(p,t')} \mathrm{e}^{iI_p t'} \mathrm{e}^{i\frac{1}{2}p^2 t} dt' \right|^2 \tag{4.9}$$

where p is the photoelectron momentum component in the direction of observation, $\Delta\tau$ is a temporal delay between the XUV pulse $E^{+}_{\mathrm{xuv}}(t)$ and the NIR pulse $A_{\mathrm{nir}}(t)$ denoted by its vector potential, and $\Phi_{\mathrm{V}}(p,t)$ is the *Volkov phase*

$$\Phi_{\mathrm{V}}(p,t) = \int_{t}^{\infty} p A_{\mathrm{nir}}(t') + \frac{1}{2} A^{2}_{\mathrm{nir}}(t') dt', \tag{4.10}$$

I_p is the ionization potential and $d(p)$ is the dipole transition matrix element associated with the photoionization event. It is apparent from eq. 4.9 that attosecond streaking is sensitive to the dipole transition matrix element, the phase of which in turn relates to the dynamics of the photoionization process. In the following section, eq. 4.9 shall be re-cast into a form that makes it apparent that attosecond streaking is in fact able to characterize the photoelectron wave-packet ejected by the XUV pulse, and that this yields a route towards the assessment of photoionization dynamics.

4.2.1 Attosecond streaking encodes the photoelectron wave packet

It has been shown by Yakovlev et al. in 2010 ([70] and [80, p. 67ff]) that it is indeed possible to factor the integrand in eq. 4.9 into two functions $\chi(t)$ and $G(p,t)$ where the former relates to properties of the XUV pulse and the photoemission timing information, while the latter only contains the action of the streaking field. They define a *time-domain wave packet* which we shall simply call *wave packet* as

$$\chi(t) = \frac{i}{\pi}\int_{-\infty}^{\infty} \langle p|\varPsi^+\rangle \, p dp \tag{4.11}$$

with $|\varPsi^+\rangle$ being the part of the real wave packet launched by the XUV pulse which travels towards the detector and is only comprised of positive momenta p with its time-dependent spreading due to free propagation factored out (cf. [80, p. 68], and $|p\rangle$ being a continuum eigenstate of the Hamiltonian $\mathscr{H}_0$ of the system such that $|\langle p|\varPsi^+\rangle|^2$ is the probability density for detecting a photoelectron with momentum p at an infinite distance. They furthermore give an explicit expression

$$\langle p|\varPsi^+\rangle = -\frac{i}{2}\tilde{E}^+_{\mathrm{xuv}}\left(\frac{p^2}{2}+I_p\right) d(p)\mathrm{e}^{i\frac{1}{2}p^2 t} = \tilde{\chi}(p)\mathrm{e}^{i\frac{1}{2}p^2 t} \tag{4.12}$$

for $\langle p|\varPsi^+\rangle$ in terms of the dipole transition matrix element $d(p)$ and the complex spectrum $\tilde{E}^+_{\mathrm{xuv}}(\omega)$ of the XUV pulse, derived under reasonable approximations for the photoionization process. This expression directly relates to the momentum space representation $\tilde{\chi}(p)$ of $\chi(t)$. We can now use eq. 4.12 to express $E^+_{\mathrm{xuv}}(t)$ in eq. 4.9, yielding

$$S(p,\varDelta\tau) \propto \left|\int_{-\infty}^{\infty}\left(\int_{-\infty}^{\infty}\tilde{\chi}(p')\frac{d\left(p+A_{\mathrm{nir}}(t')\right)}{d(p')}\mathrm{e}^{i\frac{p^2}{2}(t'+\varDelta\tau)}p'dp'\right)\mathrm{e}^{-i\varPhi_{\mathrm{V}}(p,t')}\mathrm{e}^{i\frac{1}{2}p^2 t}dt'\right|^2 . \tag{4.13}$$

One proceeds by realizing that $d\left(p+A_{\mathrm{nir}}(t')\right)/d(p') \approx 1$ [80, p. 72], which reduces the inner integral to $\chi(t+\varDelta\tau)$ and one finds

$$S_{\mathrm{WPA}}(p,\varDelta\tau) \underset{\sim}{\propto} \left|\int_{-\infty}^{\infty}\chi(t'+\varDelta\tau)\mathrm{e}^{-i\varPhi_{\mathrm{V}}(p,t')}\mathrm{e}^{i\frac{1}{2}p^2 t}dt'\right|^2 \tag{4.14}$$

for the spectrogram, where the subscript WPA stands for *wave packet approximation*. We can immediately identify $G(p,t) = \exp\left(-i\varPhi_{\mathrm{V}}(p,t)\right)$ in above equation. Section 4.2.2 will elaborate upon how this factorization into $\chi(t)$ and $G(p,t)$ can be used to infer upon the photoionization dynamics of the system under study which are captured by $d(p)$ and $\chi(t)$'s dependency on it. The route towards the extraction of this information will always pass by implementing constraints on $\chi(t)$ and $G(p,t)$ in any algorithm that inverts eq. 4.14 – either by direct parametrization of the wave packet and the Volkov phase, or by exploiting that $|G(p,t)| = 1$ for all p and t. When the amplitude of the streaking field is not too large such that the photoelectron spectrum's excursion from its central momentum $p_0 = \sqrt{2E_0}$ in the *unstreaked* case (i.e. without any streaking field) is not substantial at any time delay $\varDelta\tau$ one can safely replace $p \rightarrow p_0$ in the gate function $G(p,t) \approx G(p_0,t)$, whereby the integral in eq. 4.14 reduces to a Fourier transform

$$S_{\mathrm{CMA}}(E,\varDelta\tau) \underset{\sim}{\propto} \left|\int_{-\infty}^{\infty}\chi(t'+\varDelta\tau)\exp\left(-i\varPhi_{\mathrm{V}}\left(\sqrt{2E_0},t'\right)\right)\mathrm{e}^{iEt}dt'\right|^2 . \tag{4.15}$$

The elimination of the explicit dependency of the integrand on p is a requirement for some spectrogram inversion algorithms, but it also enables the evaluation of eq. 4.15 via fast Fourier transform (`fft`) algorithms which is orders of magnitude faster than the direct integration of eq. 4.14. The subscript CMA in this case stands for *central momentum approximation*.

The photoelectron wave packet $\chi(t)$ itself can be understood in the same terms as the ultrashort light pulses described in chapter 2. Its spectral representation $\tilde{\chi}(E_{\text{kin}}) = \left|\tilde{\chi}(E_{\text{kin}})\right| \exp\left(i\varphi\left(E_{\text{kin}}\right)\right)$ can be decomposed into its observable photoelectron spectrum

$$|\chi(E_{\text{kin}})|^2 = \left|E^+_{\text{xuv}}\left(\tilde{E}_{\text{kin}} + I_p\right) d(E_{\text{kin}})\right|^2 \tag{4.16}$$

and the spectral phase

$$\varphi\left(E_{\text{kin}}\right) = \arg\left\{\tilde{E}^+_{\text{xuv}}\left(E_{\text{kin}} + I_p\right) d(E_{\text{kin}})\right\} = \left(\varphi_{\text{xuv}}\left(E_{\text{kin}} + I_p\right) + \varphi_{d(p)}\left(E_{\text{kin}}\right)\right). \tag{4.17}$$

For a $d\left(E_{\text{kin}}\right)$ which neither varies strongly in phase nor modulus this creates a link to section 3.3 where the attosecond streak camera is proposed as a means to characterize $E^+_{\text{xuv}}(t)$ as $\varphi\left(E_{\text{kin}}\right)$ will then be dominated by the spectral phase of the XUV pulse.

Figure 4.2.1 shows how the spectral phase $\varphi\left(E_{\text{kin}}\right)$ affects the observable streaking signature by numerically evaluating eq. 4.14 with different wave packets $\chi(t)$. For a completely flat spectral phase the streaking spectrogram looks very much as expected from the classical arguments made in sec. 3.3. A chirp on the wave packet will result in an asymmetry in the width of the individual photoelectron spectra between the rising and falling flanks of the streaking spectrogram. A first-order phase which corresponds to a temporal delay of the wave packet results in a lateral shift of the streaking spectrogram. In analogy to eq. 2.14 we define

$$\text{GD}_{\chi}(E_{\text{kin}}) = -\frac{d\varphi(E_{\text{kin}})}{dE_{\text{kin}}} = -\frac{d}{dE_{\text{kin}}}\left(\varphi_{\text{xuv}}\left(E_{\text{kin}} + I_p\right) + \varphi_{d(p)}\left(E_{\text{kin}}\right)\right) \tag{4.18}$$

as the energy-dependent group delay of the photoelectron wave packet. The next section will illustrate how the phase distortions $\varphi_{\text{xuv}}\left(E_{\text{kin}}\right)$ due to the XUV pulse can be cancelled and meaningful information can be extracted from $\text{GD}_{\chi}(E_{\text{kin}})$ in an attosecond streaking measurement.

4.2.2 Extraction of photoemission time delays from attosecond streaking measurements

The fundamental problem with extracting photoemission timing information in an experiment form single streaking traces as they are e.g. depicted in fig. 4.2.1 or fig. 3.9 is that the arrival time of the XUV pulse in the interaction region is generally not known and the '0' on the abscissa in these figures is therefore simply an arbitrarily chosen point in relative XUV/NIR delay time. While the unknown arrival time of the XUV pulse amounts to the photoelectron's wave packet's first-order spectral phase being unknown, the higher order terms in the spectral phase of the XUV pulse are also not inferrable whereby it becomes generally impossible to distinguish which part of a wave packet phase distortion recovered from a streaking spectrogram is due to the XUV pulse and which part is due to the phase of the dipole transition matrix element $d(p)$, which is the quantity of interest. These problems can however be mitigated by performing attosecond streaking experiments on a system (which can also be a mixture of e.g. two gaseous samples) where not just a single streaking trace is observed, but at least two. Considering then the two respective wave packets $\chi_1\left(t\right)$ and $\chi_2\left(t\right)$, one can in analogy to eq. 2.6 separate them into a complex envelope $\underline{\chi}\left(t\right)$ and a quickly oscillating carrier oscillating with the frequency corresponding to the wavepacket's central kinetic energy, whereby the energetic centers of the spectral representations

$$\underline{\tilde{\chi}_i}(\varDelta E) = |E^+_{\text{xuv}}\left(\varDelta E\right)|\,|d_i\left(\varDelta E\right)| \exp\left(i\varphi_{d_i(\varDelta E)}(\varDelta E)\right) \tag{4.19}$$

of the envelopes will be aligned at zero $\varDelta E$. Dividing now $\underline{\tilde{\chi}_2}(\varDelta E)$ by $\underline{\tilde{\chi}_1}(\varDelta E)$ will cancel the XUV field's influence in both magnitude and phase such that one has

$$\frac{\underline{\tilde{\chi}_2}(\varDelta E)}{\underline{\tilde{\chi}_1}(\varDelta E)} = \frac{|d_2\left(\varDelta E\right)|}{|d_1\left(\varDelta E\right)|} \exp\left(i\left(\varphi_{d_2(\varDelta E)}(\varDelta E) - \varphi_{d_1(\varDelta E)}(\varDelta E)\right)\right), \tag{4.20}$$

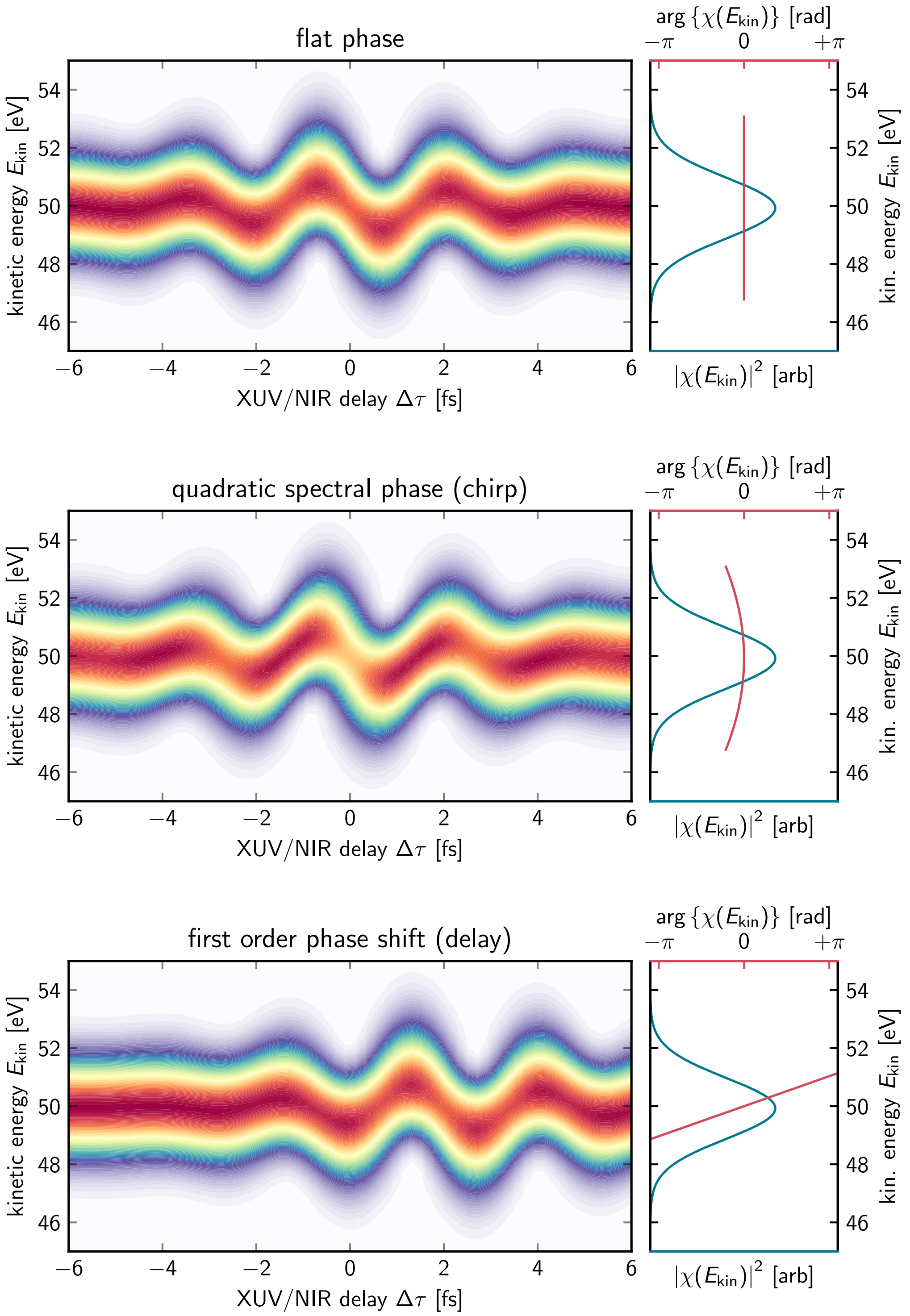

Figure 4.4: Numerical evaluation of eq. 4.14 (left panel) with different wave packets $\chi(\omega)$ in their spectral representation, decomposed into their modulus (blue lines) and spectral phases (red lines). For a completely flat spectral phase (top) the streaking spectrogram looks very much as expected from the classical arguments made in sec. 3.3. A second order phase distortion (chirp) causes an asymmetry in the width of the individual photoelectron spectra between the rising and falling flanks of the streaking spectrogram. A first-order phase which corresponds to a temporal delay of the wave packet simply results in a lateral shift of the streaking spectrogram.

and the group delay associated with this expression will be

$$\varDelta\mathrm{GD}(\varDelta E) = \frac{d}{d(\varDelta E)}\left(\varphi_{d_2(\varDelta E)}(\varDelta E) - \varphi_{d_1(\varDelta E)}(\varDelta E)\right) = \mathrm{GD}_2(\varDelta E) - \mathrm{GD}_1(\varDelta E). \tag{4.21}$$

In the following we shall use $\chi\,(t)$ and $\underline{\chi}\,(t)$ and their respective spectral representations $\tilde{\chi}\,(E_{\mathrm{kin}})$ and $\tilde{\underline{\chi}}(\varDelta E)$ interchangably and refer to both as 'wave packet'. Whether we are dealing with the complex envelope which is defined over $\varDelta E$ or the complete wave packet defined over the kinetic energies E_{kin} is indicated by the argument.

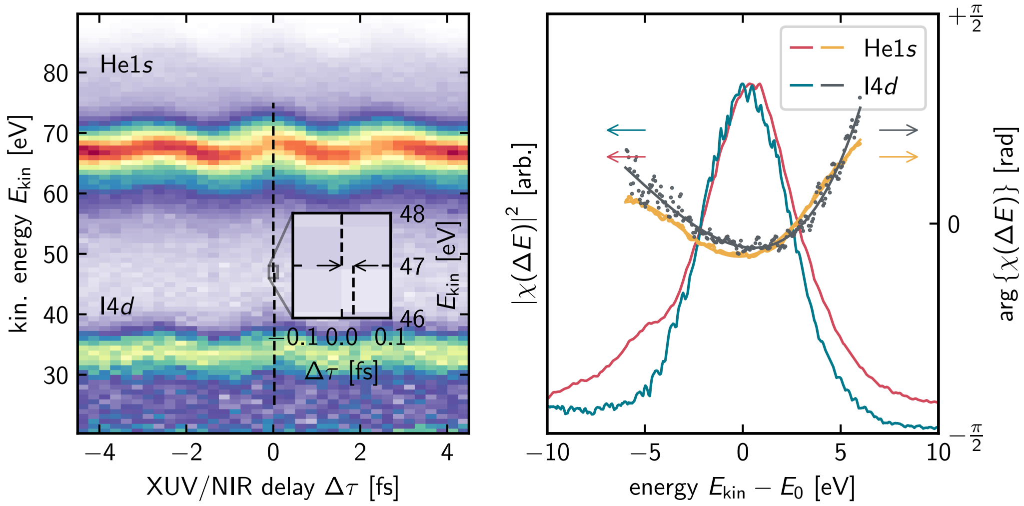

Figure 4.5: Determining relative photoemission times. An attosecond streaking spectrogram recorded on a mixture of helium and 2-iodopropane at a photon energy of 90 eV is shown on the left. While from this measurement alone neither the group delay for the He1*s* wave packet nor the I4*d* wave packet can be determined, the difference of their group delays is accessible. The central group delay difference manifests as a small lateral shift of the energetic centers of the two streaking features (inset in the left panel). It is not discernible by eye, and can only be reliably extracted by processing the spectrogram with specialized analysis algorithms which take all photoelectron spectra it is comprised of into account. The right panel shows the wave packet envelopes $\chi_{\mathrm{He1}s}\,(\varDelta E)$ and $\chi_{\mathrm{I4}d}\,(\varDelta E)$ retrieved with the extended ptychographic iterative engine (see appendix C.2). One possible way of exctracting the group delay difference is by fitting a polynomial to the spectral phases of the wave packets (solid yellow and gray lines) and inspecting the difference in their first order coefficients. For this particular scan one finds a central $\varDelta\mathrm{GD}_{\mathrm{I4}d-\mathrm{He1}s} = (23.8 \pm 2.1)$ as. Many scans will have to be recorded in order to obtain sufficient statistics from which the relative group delay can then be reported properly.

It is thus possible, by shifting two retrieved wavepackets such that their energetic centers coincide to extract relative timing information from an attosecond streaking measurement. Figure 4.5 shows a streaking spectrogram recorded on a gas mixture of helium and 2-iodopropane at an XUV photon energy of $E_{\hbar\omega} = 90$ eV. The full spectrogram is shown on the left, the spectral representations of the complex wave packet envelopes are shown on the right. In this example the group delay difference between these two wave packets is extracted via a polynomial fit to the respective spectral phases. Figure 4.5 furthermore illustrates another problem. The I4*d* photoemission is spin-orbit split into two components separated by 1.7 eV (see chap. 5) which are not individually resolved due to the necessarily large bandwitdh of the XUV pulse. In such cases (given the energetic spacing of the unresolved components is small enough) the photoemission time encoded in the spectrogram is to be seen as the *average* of that of the respective components incoherently adding to the observed photoelectron signal. Application of a reconstruction algorithm to the spectrogram will then yield an effective 'wave packet' from which time-energy information is still available.

The arguments brought forward so far illustrate that it is possible to extract wave packet group delays if the wave packets' spectral phases are accessible, but does not specify how these are obtained. Methods to invert spectrograms can loosely be grouped into *restricted methods* that directly parametrize the functions $G(p_0, t)$ and $\chi(t)$ and *unrestricted methods* which forgo a parametrization and reconstruct $G(p_0, t)$ and $\chi(t)$ pointwise. The former are usually configured to retrieve a single-valued group delay difference at the energetic center of the wave packets, while the latter access the group delay difference's energy dependency in a small interval around the energetic center.

The restricted Time-Dependent Schrödinger Equation (rTDSE) methods

The restricted Time-Dependent Schrödinger Equation (rTDSE) methods are based on a parametrization of the spectrogram and therefore belong to the class of restricted methods. A spectrogram comprised of multiple streaking features as e.g. shown in fig. 4.5 is modeled as an incoherent linear combination of terms of the form of eq. 4.15, asssuming a different $\chi_i(t)$ for each streaking feature but a single common streaking pulse from which the individual gate functions $G_i(p_0^i, t)$ are calculated. The streaking pulse is parametrized in the time domain as an oscillating (and possibly chirped) carrier with a gaussian envelope, where amplitude, ce-phase, frequency, temporal duration and chirp are free parameters. For the wave packets the ansatz is made in the spectral domain as a gaussian function with width and amplitude as free parameters, as well as their spectral phases expanded to second order with the zeroth order being fixed to zero as it is not resolvable in a streaking experiment. For each wave packet the first order spectral phase coefficient δ_i (cf. eq. 2.8) is its delay relative to the center of the streaking field. The parameters of the model spectrogram are then determined by least-squares fitting to the experimental data where good initial guesses can be obtained from static spectra of the system under study (for the central energies and energetic composition of the wave packets), and the energetic first-moments of the streaking features (for the streaking pulse). After successful fitting group delay differences can be obtained from the δ_i. The restriction is the parametrization of the streaking pulse and wave packets and therefore the restriction of their respective shapes.

The application of the rTDSE method in this formulation requires any time-independent but energy-dependent background to be subtracted from the spectrogram before fitting. The exact shape of the background is not known though, and assuming different shapes for it can influence the retrieved delay which is problematic. The safest way around this is to remove any time-independent contribution to the spectrogram by numerical differentiation along its delay axis and also fitting the delay-derivative of the model function. This approach is referred to as *differential rTDSE* or *diff. rTDSE*. These methods have been developed by Schultze et al. [16] and have successfully been applied in a number of studies (cf. e.g. [81, 18, 82, 83]). The implementation of the rTDSE methods used in this work is described in sec. C.1.

Ptychographic spectrogram inversion

Another route to the extraction of timing information is the realization that eq. 4.15 resembles the ptychographic problem encountered in diffractive imaging (cf. e.g. [84]) where a probe beam $P(\mathbf{r})$ is swept across an object $O(\mathbf{r})$ giving rise to the exit wave function $\Psi(\mathbf{r}, \mathbf{R}) = O(\mathbf{r})P(\mathbf{r}-\mathbf{R})$ of which the Fourier transform (cf. diffraction pattern) is observed. Switching variables $\mathbf{r} \rightarrow t$ and $\mathbf{R} \rightarrow \Delta\tau$ we can identify the function $G(p_0, t)$ as the object and $\chi(t)$ as the probe. The extended ptychographic iterative engine (ePIE) developed by Maiden and Rodenburg [85] which solves for object and probe from a series of diffraction patterns or spectra recorded for different shifts $\mathbf{R}$ or $\Delta\tau$ respectively was first applied to attosecond streaking by Lucchini and co-workers [69] for the purpose of XUV pulse characterization. The ePIE can also be configured to reconstruct multiple wave packets simultaneously under the constraint of being streaked by the same NIR pulse, whereby the relative phases between the wave packets and thereby timing information becomes accessible. As ePIE reconstructs the wave packets and also the NIR pulse pointwise it belongs to the class of unrestricted methods and can be a valuable tool to gain insight into the energy dependency of the group delay differences between two wave packets around their energetic centers. Just as the non-differential rTDSE algorithm its application requires background subtraction and therefore shares the same problem of the choice of background model possibly influencing the result. Therefore, when ePIE is applied one should cross-check the results with the diff. rTDSE method and compare the wave packet group delays extracted at the wave packets' energetic centers with either method. Section C.2 and the supplementary information to [86] elabotates upon the ePIE implementation used here.

Beyond the central momentum approximation (CMA)

The delay extraction methods discussed so far rely on the central momentum approximation eq. 4.15. For the rTDSE methods it drastically speeds the retrieval process up as the `fft` algorithm can be used for evaluating spectrograms which makes the iterative fitting procedure computationally feasible, and for ePIE it is a mathematical requirement. A discussion of spectrogram inversion methods would not be complete though without including approaches that forgo the central momentum approximation. These methods are generally used less frequently due to the significantly increased computational cost at which they come, which often outweights their increased precision. The most general of these methods is probably the *Volkov-transform generalized projections algorithm* (VTGPA) developed by Keathley and co-workers [87] which essentially starts out at eq. 4.9 or 4.14, discretizes it and iteratively solves for $E_{\text{xuv}}(t)$ or $\chi(t)$ and $A_{\text{nir}}(t)$ directly. A refinement that first applies ePIE and then a few iterations of VTGPA to a spectrogram has been developed by Lucchini et al. [88], but for either case the considerable computational overhead prohibits the method's use for the evaluation of large data sets. A close relative to the VTGPA is the ***a**bsolute **c**omplex **d**ipole transition matrix element re**c**ontstruction* (ACDC) algorithm [89] where the determination of $d(p)$ is included into the reconstruction. For photoelectrons with very low kinetic energy and extremely broadband XUV pulses, i.e. far outside of the region where the CMA can be considered a valid approximation, these methods may find their use, but this case is not of interest for the present work. The authors of [88] furthermore point out that the error introduced by the central momentum approximation only affects the NIR pulse and not the retrieved wave packets when using ePIE.

A completely different route is taken in [90] and [86]. In both cases neural networks are applied for spectrogram inversion which does not require the invocation of the CMA. In [90] this is done from the perspective of XUV pulse characterization and in [86] the focus is on delay extraction. While in both cases neuronal networks have demonstrated to be competitive with 'traditional' algorithms in terms of retrieval quality and the per-spectrogram retrieval time is cut-short by orders of magnitude, the generation of training data and also the training itself requires significant computational resources and possibly even dedicated and proprietary hardware. Furthermore, special care must be taken to avoid accidentally training the networks to retrieve biased results.

In summary, there's no point in abandoning the central momentum approximation or wave packet approximation for the promise of greater accuracy, at least in this work. In the parameter range of interest in this work (XUV bandwidth ~ 5 eV, $E_{\text{kin}} > 20$ eV) it serves us well and enables us the evaluation of large data sets in reasonable time. The size of the data sets is of concern here as photoemission chronoscopy experiments are expanding in their scope. Reporting single-valued photoionization time delays at one photon energy for a single system as it was state-of-the-art about a decade ago (cf. [15, 16]) is no longer sufficient to contribute significantly to the field. It is now necessary to plan experiments that assess the energy dependence of the photoemission time delay, or compare time delays between different but related systems, also across photon energies, whereby the number of recorded spectrograms can easily approach or exceed a thousand.

4.2.3 Coulomb laser coupling

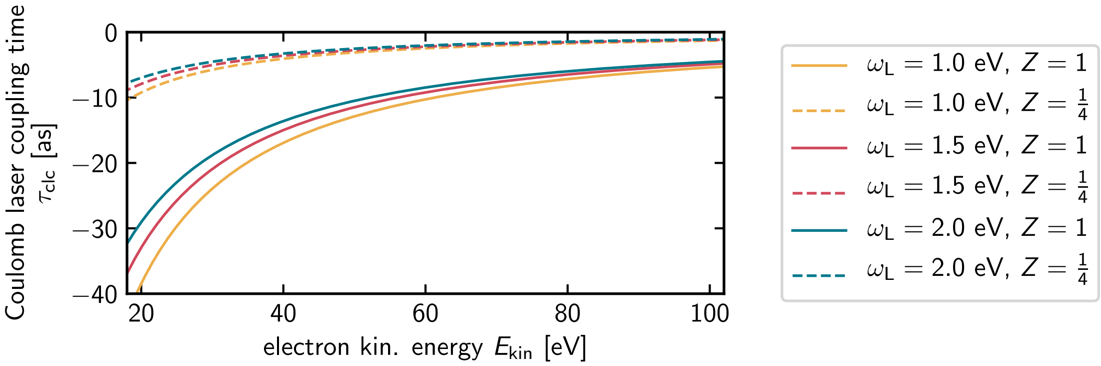

Figure 4.6: Evaluation of eq. 4.24 for different streaking laser frequencies ω_L and $Z = 1$ (for individual atoms and molecules) and $Z = \frac{1}{4}$ (for photoemission timing from metal surfaces).

While the previous sections elucidate how the photoelectron wave packet's temporal properties are mapped onto a streaking spectrogram and can be extracted from it, the question of whether and how the timing information is modified by the streaking measurement itself has remained open. Formally, any such modification can be absorbed into the phase of $\chi(p)$, but must be properly taken into account in the interpretation of experimental results.

The lateral shift τ_s of a streaking feature in a spectrogram with respect to the (generally unknown) time zero is

$$\tau_s\left(E_{\mathrm{kin}}\right) = \mathrm{GD}\left(E_{\mathrm{kin}}\right) + \text{distortions due to the XUV pulse} + \text{laser induced contributions.} \quad (4.22)$$

While as demonstrated in the previous section the delay distortions due to the XUV pulse can be canceled in a relative measurement, there's no guarantee that for two different photoelectron kinetic energies or two different systems in a mixture these laser induces contributions will be equal, whereby

$$\tau_{\mathrm{rel}}\left(E_{\mathrm{kin}}\right) = \varDelta\mathrm{GD}\left(E_{\mathrm{kin}}\right) + \text{laser induced contributions.} \quad (4.23)$$

Nagele et al. [91] have demonstrated via quantum mechanical and classical simulation that the attosecond streak camera does in fact access the EWS delay alone with attosecond precision for the case of the photoionization directly occuring from a short-ranged (e.g. Yukawa-type) potential, whereby in this case $\mathrm{GD}\left(E_{\mathrm{kin}}\right) = \tau_{\mathrm{EWS}}\left(E_{\mathrm{kin}}\right)$. Such systems are however not readily studied experimentally. In the case of photoionization occuring from an initially neutral atom or molecule the ejected photoelectron will propagate in the Coulomb potential of the residual ion, the scattering time of which can be described via eq. 4.7. In the same publication these authors found that the observarble photoionization time does *not* coincide with τ_{EWS} anymore, but has been modified by the presence of the streaking field. Further investigation into the matter (cf. e.g. [77, p. 359ff] and [77, p. 778ff]) revealed that the difference between the observed photoionization time and τ_{EWS} can be interpreted as being due to the streaking field mapping a finite portion of the infinitely-ranged Coulomb potential onto the photoionization time. Being due to the coupling of the interaction of the outgoing photoelectron with the Coulomb field of the ion as well as the streaking laser field this contribution

$$\tau_{\mathrm{clc}}\left(E_{\mathrm{kin}}\right) = \frac{Z}{\left(2E_{\mathrm{kin}}\right)^{3/2}}\left(2 - \ln\left(2\pi\frac{E_{\mathrm{kin}}}{\omega_{\mathrm{L}}}\right)\right) \quad (4.24)$$

where Z is the negative charge of the residual ion and ω_L is the streaking field's angular frequency has been dubbed *Coulomb laser coupling* (CLC). Most remarkably, this result is independent of the properties of the system under study and the streaking field's amplitude.

In the usual experimental setting of XUV induced single photon ionization one has $Z = 1$ for the case of a gas-phase experiment on individual atoms or molecules. The solid lines in figure 4.6 show eq. 4.24 evaluated for different laser frequencies and photoelectron kinetic energies between 20 eV and 100 eV. The Coulomb laser coupling time is negative and varies between ~ −40 as and about −5 as in all instances and increases monotonically with E_kin. A positive τ_clc can only be attained for $E_\mathrm{kin} < e^2\omega_\mathrm{L}/2\pi \approx 1.2\omega_\mathrm{L}$ which is experimentally not feasible.

In the case of photoemission from metal surfaces instead of isolated atoms or molecules the photoelectron leaving the system is subject to the action of its image potential which with the distance z from the surface varies as $V(z) \propto -1/4z$ (cf. e.g. [26, p. 56], [92, p. 4678], [93, p. 330]) whereby the resulting Coulomb laser coupling time is scaled by a factor $\frac{1}{4}$ compared to the atomic case, pushing it to the single-digits for all kinetic energies depicted in fig. 4.6. This is usually negligible in the context of photoemission timing on surfaces where photoemission delays in the multiple tens of attoseconds are expected (cf. e.g. [18]).

For each individual streaking feature in a spectrogram the time shift will then be

$$\tau_s = \tau_\mathrm{EWS} + \tau_\mathrm{clc}, \tag{4.25}$$

where we'll drop the kinetic energy dependency from now on for notational clarity.

4.3 Measuring total and absolute photoemission times

The measurement of absolute photoemission times requires the introduction of a *chronoscope species* into the experiment of which total (and possibly also the absolute) photoemission time is known. The term *absolute photoemission time* is taken here to refer to the EWS time delay associated with the photoemission event, while the *total photoemission time* is the the time directly accessible via attosecond streaking spectroscopy which will still contain the laser induced contributions. With a suitable chronoscope species at hand the experimental determination of total photoemission times boils down to a remarkably simple procedure. We shall now first concern ourselves with this procedure before returning to the experimental reality and the difficulties associated with finding a suitable chronoscope species.

Given we can somehow mix the chronoscopy species with our system of interest (this may e.g. be feasible in gas-phase measurements) whereby a streaking measurement on the chronoscope and the system can be performed simultaneously, and furthermore the photoemission features of chronoscope and system under study are energetically separated well enough to facilitate delay extraction as presented in the previous sections, the relative photoemission time delay $\mathit{\Delta}\tau_\mathrm{smpl.-chron.}$ between the photoline of interest in the sample and the chronoscope species is accessible. From this relative time delay we can solve for the total photoemission delay of the sample as

$$\tau^\mathrm{tot}_\mathrm{smpl.} = \mathit{\Delta}\tau_\mathrm{smpl.-chron.} + \tau^\mathrm{tot}_\mathrm{chron}. \tag{4.26}$$

If the laser induced contributions to the time delay of the sample are sufficiently described by the Coulomb-laser-coupling (cf. sec. 4.2.3) we can determine the absolute (EWS) photoionization time delay as

$$\tau^\mathrm{abs}_\mathrm{smpl.} = \mathit{\Delta}\tau_\mathrm{smpl.-chron.} + \tau^\mathrm{tot}_\mathrm{chron} - \tau^\mathrm{clc}_\mathrm{smpl.}. \tag{4.27}$$

Helium as an atomic chronoscope species

The absolute zero in photoemission chronoscopy cannot be set by experiment alone. Theoretical assessment and verification of the results via experiment are crucial and go hand in hand. Helium is

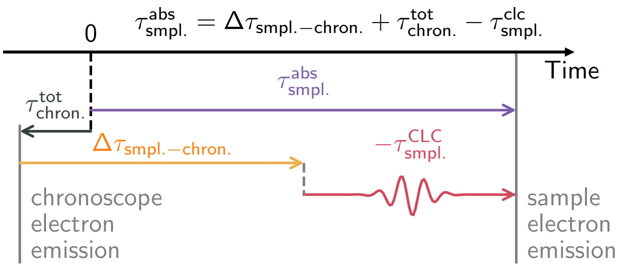

Figure 4.7: Absolute photoemission timing in attosecond streaking spectroscopy via a chronoscope species. With the total photoemission time of the chronoscope species known the determination of the absolute photoemission time of the sample boils down to simple addition and subtraction given all laser induced contributions are known and it takes the possibility of a negative total photoemission time for the chronoscope into account. This figure depicts the case for the CLC delay being the only relevant laser induced contribution for the sample.

especially suited as a chronoscope species due to being an inert noble gas with a single direct photoline due photoemission from its 1*s* orbital and also simple enough as a system to make an exact numerical treatment feasible.

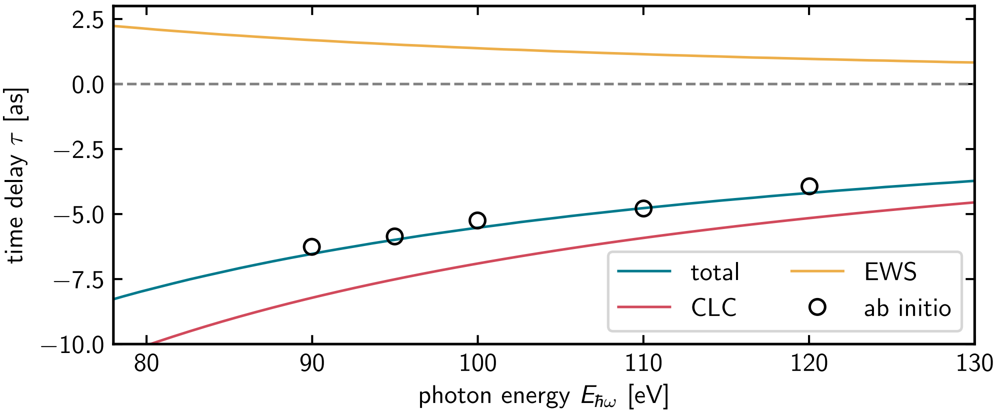

Figure 4.8: Total and absolute photoemission time delay of He1*s* photoelectrons. The absolute EWS photoemission time (yellow curve) can be determined via a quantum scattering calculation. The total observed photoemission time delay (blue curve) is the sum of the EWS time delay and the Coulomb-laser-coupling (red curve, $\omega_L = 1.55$ eV, sec. 4.2.3) contributions and matches the result of an ab-initio calculation (black circles, digitized from [24, p. 50]) to sub-attosecond precision.

The direct He1*s* ($E_{\text{bin}} = 24.6$ eV) photoemission is accompanied by shake-up satellites appearing at lower energies in the photoelectron spectrum. The relative time-delay between the direct 1*s* photoemission and the $n = 2$ shake-up emission appearing at $E_{\text{bin}} = 65.4$ eV has been studied theoretically by Pazourek and co-workers [94] in a fully *ab-initio* calculation and their results were experimentally confirmed by Ossiander et al. [23]. This excellent agreement motivated extracting the total and absolute photoemission times for the direct He1*s* emission from the calculations where the photon arrival time is known exactly. Figure 4.3 shows the result of the *ab-initio* calculation (digitized from [24, p. 50]) at photon energies between 90 eV and 120 eV. These results are supplemented by a scattering calculation performed with the `ePolyScat` software suite [95, 96] using a Hartree-Fock (Sapporo non-relativistic triple-ζ basis set) calculation performed with `GAMESS` as input. As the scattering calculation only treats direct photoionization in absence of the streaking field it is not surprising that the resulting EWS time delay does not match the *ab-initio* calculation. The effect of the streaking laser field is captured by the Coulomb-laser-coupling time delay τ_{clc} (sec. 4.2.3). Once taken into account the *ab-initio* calculation is matched to sub-attosecond precision.

Loosely speaking, the blue curve in fig. 4.3 is the reference for all measurements in the gas-phase presented in this work. It takes the place of $\tau^{\mathrm{tot}}_{\mathrm{chron.}}$ in fig. 4.3.

Iodine as an atomic chronoscope species

Once the absolute or total photoemission time delay of a species has been determined e.g. via the helium reference discussed above, it can be used as a chronoscope species itself. This approach was pioneered also by Ossiander and co-workers [18] where the helium reference was used in a gas-phase experiment to determine the absolute photoemission time delay of the I4d photoemission in iodomethane and -ethane at 105 eV which was then in turn used to absolutely time the photoemission from a tungsten (110) surface in a groundbreaking experiment.

Iodine is valuable as a chronoscope species for essentially three reasons: firstly, a giant resonance in the I4$d \rightarrow \varepsilon f$ photoemission channel (cf. e.g. [97, 98]) around ~ 90 eV ensures a large photoelectron yield over a broad range of energies of interest even at low concentrations, secondly it can covalently bind to organic molecules in place of a hydrogen atom facilitating their study via photoemission chronoscopy and thirdly it can be used as an adsorbate on metal surfaces (cf. e.g. [99, 100, 101, 18]) where the giant resonance again ensures sufficient photoelectron signal even at low coverages.

However, whether an iodine atom adsorbed on a metal surface and an iodine atom in an organic molecule are equivalent chronoscopy references is an open question. The influence of the molecular environment of the iodine atom in such molecules is far from fully understood. That the molecular environment of the iodine atom may have an influence on the observed I4d photoemission time delay has been demonstrated by Biswas et al. [25] experimentally, but their results raise more questions than they answer. Therefore, a general survey of photoemission times in small organic molecules is called for. The determination of the absolute I4d photoemission time is of general interest to the field of photoemission chronoscopy and the establishment of small iodine-containing molecules as useful chronoscope species will be a by-product of this. This survey is the topic of the following chapter.

Chapter 5

Photoemission chronoscopy of the iodoalkanes

"We never see a bare resonance. All we ever see are shadows on the wall."

– freely quoting Zdeněk Mašín

It is well known that the core-level photoemission of an atom is altered by its chemical environment. In the energy domain this is reflected in *chemical shifts* [8, p. 65ff.] of the binding energy, which allow for precise determination of the chemical environment of an atom (i.e. its neighboring atoms and bonds), making them an immensely powerful spectroscopic tool. That intra-molecular scattering of the leaving photoelectron sensitively affects the angular distribution of core-level photoelectrons emitted from an un-oriented molecule as well and is therefore also reflective of the chemical environment has been demonstrated by Patanen and co-workers [102] in 2013. In the context of photoemission chronoscopy it then may naturally follow to ask: will the chemical environment also affect the photoemission time of a core level in a detectable manner? As briefly introduced at the end of the previous chapter the I$4d$ core-level is of particular interest in this regard as it has been used as a photoemission chronoscopy reference in varying chemical environments before [18]. Furthermore, surprising results on the I$4d$ photoemission time in iodoethane [25] reported by Biswas et al. call for closer scrutiny of the role of the chemical environment in the formation of the observable photoemission time delay. We therefore perform a systematic photoemission chronoscopy study on the primary and secondary iodoalkanes up to 2-iodobutane between 90 eV and 118 eV photon energy in a mixture with helium and thereby determine absolute and total photoemission times. The variation of the length of the hydrocarbon chain attached to the iodine atom as well as its position on the chain amount to the variation of the chemical environment. As the experiment is conducted in the gas-phase on un-oriented molecules it has no angular resolution and records the average of all molecular orientations. The photon energies were chosen such that they sweep across the *giant resonance* in the I$4d \rightarrow \varepsilon f$ photoemission channel. Comparison with an atomic calculation for the I$4d$ photoemission time reveals a surprising dependency of the molecular photoemission time on excitation energy and species.

The experiments presented in this chapter have been performed with the help of Maximilian Pollanka, Pascal Scigalla, Maximilian Forster and Martin Wanckel. The influence of the NVV-Auger-Meitner emission on the timing results at 90 eV photon energy was assessed by Matthias Ostner. Martin Wanckel and Andreas Duensing furthermore assisted with the scattering calculations.

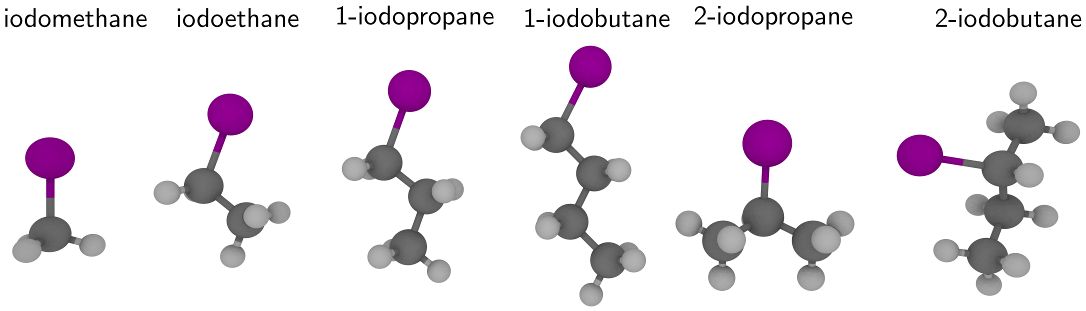

Figure 5.1: Stick-and-ball models of the iodoalkanes form iodomethane to 2-iodobutane. Dark gray: carbon atoms, light gray: hydrogen atoms, purple: iodine atoms.

5.1 The Iodoalkanes

The iodoalkanes consist of a hydrocarbon chain of varying length in which one hydrogen atom is substituted by an iodine atom. Depending on the chain length multiple unique substitution sites are possible. The iodoalkanes studied here derive from up to *n*-butane, ball-and-stick models are shown in figure 5.1. Being staple compounds in organic chemistry they are commercially available in high quality. The samples for this experimental campaign were purchased from VWR at > 98% purity. The absence of contaminants was confirmed via mass spectrometry which justifies using the substances without further purification.

5.1.1 Molecular structure and thermodynamical properties

Organic molecules are prone to conformational isomerization, i.e. the change of arrangement of their constituend atoms by torsion of a bond [103]. In the alkanes specifically it is known that torsions around the carbon–carbon bonds readily occur at room temperature [104]. Therefore, it is necessary to consider the effect such structural changes can have in the iodoalkanes in the context of determining photoemission times in these molecules. Starting out with iodomethane, it is immediately apparent that a rotation of the methyl group around the C–I bond is equivalent to a rotation of the entire molecule around this axis and therefore cannot have an effect on the observed photoemission time delay in an orientationally averaged experiment. Moving on to iodoethane, a rotation of the terminal methyl group of the hydrocarbon chain only affects the three hydrogen atoms attached to its central carbon atom. The resulting difference in structural configuration is minuscle and we do not expect the resulting difference in photoemission time delay to be observable in our experiment.

This changes when moving on to 1-iodopropane. A torsion of the first C–C bond as counted from the iodine atom (marked in yellow in fig. 5.2) results in a very different overall molecular structure. This is even exacerbated in 1-iodobutane where a rotation of the residual hydrocarbon chain around the first two bonds needs to be taken into account (blue and red in fig. 5.2). The potential energy associated with a bond torsion was estimated by performing self-consistent field (SCF) Hartree-Fock calculations on 1-iodopropane and 1-iodobutane with the `GAMESS` quantum chemistry suite [106], sampling the possible orientations of the residual part of the hydrocarbon chain on a 10° grid at a low level of theory (restricted Hartree-Fock, Pople STO-3G basis set, frozen bond lengths). The results are shown in fig. 5.2, together with a calculation on *n*-butane for comparison. The two energy minima ($\vartheta = 0^\circ$ and $\vartheta \approx 100^\circ$) correspond to different conformations of the hydrocarbon chain. Qualitative agreement with *n*-butane is easily seen, on which an experimental conformational analysis reveals an equilibrium constant $K_{\mathrm{eq}} \approx 0.5$ for its *trans* and *gauche* isomers at room temperature [105] which arise due to a rotation around the *n*-butane molecule's central C–C bond (cf. the bond marked in red in 1-iodobutane in fig. 5.2). The value of K is indicative of

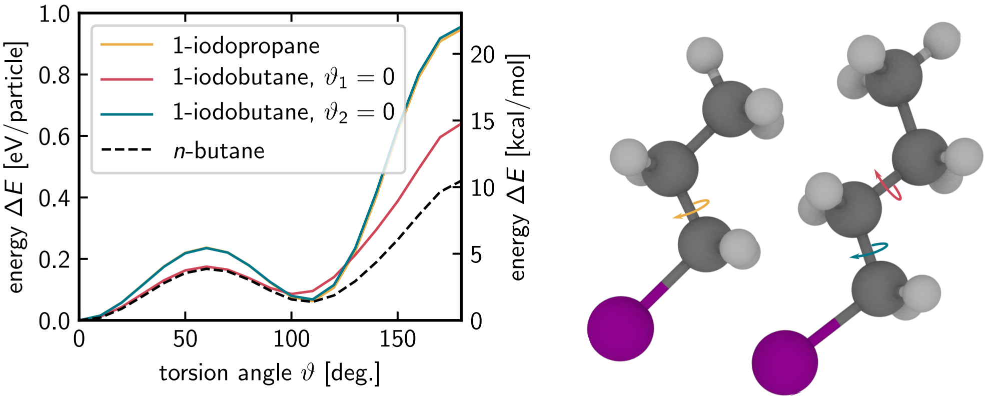

Figure 5.2: Estimation of the torsional barriers of the larger iodoalkanes 1-iodopropane and 1-iodobutane. Rotation around the bonds marked in color is possible and the energetic barriers for such a torsion is rather low. While the simple calculations presented here overestimates the torsional energy (cf. e.g. [104] and references therein) one finds that both 1-iodopropane and 1-iodobutane behave quantitatively very similar to *n*-butane at the same level of theory for which rotational isomerization has been observed at room temperature (cf. e.g. [105]).

both isomers coexisting in a 1:2 fraction. The qualitative similarity of the rotational barrier potential for bond torsions in 1-iodopropane and 1-iodobutane (see fig. 5.2) therefore permits the conclusion that one can expect conformational isomers of the larger iodoalkanes (1-iodopropane, 1-iodobutane, 2-iodobutane) to coexist in a similar ratio to what is found for *n*-butane under similar conditions. Therefore, for 1-iodopropane, 1-iodobutane and 1-iodobutane the molecular structure is not well defined at and above room temperature. This has implications for the scattering part of the observable photoemission time delay: one cannot expect to be able to infer detailed information about the molecular environment from the photoemission time delay as the molecular environment itself is not well defined. For 2-iodopropane one finds a different situation though. The two methyl groups attached to the central carbon atom may rotate around their respective axes, but to each of them the same line of arguments as for the terminal methyl group in iodoethane applies. The structural change brought about by the displacement of the hydrogen atoms is expected to not result in a detectable change in photoemission time delay in our experiment.

In summary we can expect to be able to resolve differences in photoemission time delays between iodomethane, iodoethane and 2-iodopropane, but the situation is everything but clear for 1-iodopropane, 1-iodobutane and 2-iodobutane. It is useful to classify the molecules into *rigid* (iodomethane, iodoethane and 2-iodopropane) and *floppy* (1-iodopropane, 1-iodobutane, 2-iodobutane) species and study them separately. For the rigid molecules the research question is how the observable I4*d* photoemission time delay changes with the progressive addition of carbon atoms to the alkane, while for the floppy molecules the question is whether differences in photoemission time delay between species can still be measured in the presence of multiple conformational isomers. From this vantage point a very interesting candidate to investigate would of course be tert-butyl-iodide. The large tert-butyl-group and its three-fold symmetry would be an interesting testing case for extrapolating the results presented here to larger functional groups. However, we found it to be too corrosive to handle in our set-up without implementing major modifications. In the future an attosecond streaking experiment on this molecule would be a worthwhile endeavor, given one modifies the sample delivery system to work with e.g. glass tubing.

Among the thermodynamical properties that make the iodoalkanes favorable for an experiment

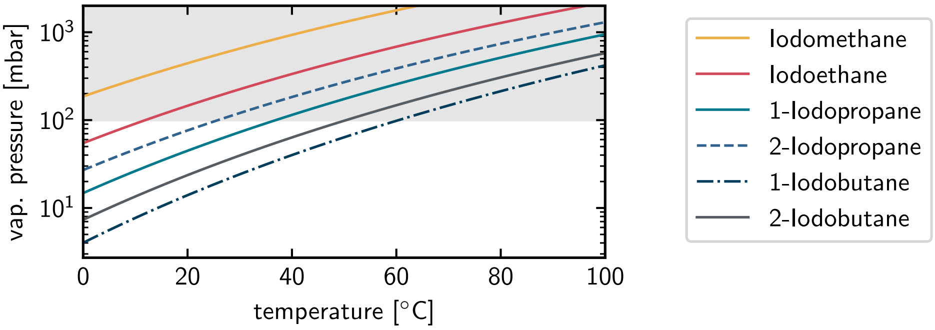

Figure 5.3: Vapor pressures of the iodoalkanes [107, 108, 109]. Their volatility enables using Iodomethane, -ethane directly at room temperature (~ 20°C) while larger iodoalkanes need to be brought to elevated temperatures in order to attain sufficient concentration in the mixture with helium to conduct the gas-phase experiment. For these the gas reservoir holding the mixture and the conduits to the effusive nozzle in the experimental chamber are usually held at ~ 70°C.

in the gas-phase is their low vapor pressure. The vapor pressure p_{vap} of a substance can be calculated with the Antoine equation for which the parameters for the iodoalkanes can be found in literature [107, 108, 109]. Figure 5.3 shows the dependence of their p_{vap} on the temperature. The pressure p_{vap} determines the amount of iodoalkane in the gas reservoir in the experiment, and we found $p_{\mathrm{vap}} \gtrsim 100\,\mathrm{mbar}$ to be required in order to attain sufficient photoelectron signal in mixture with helium in the experiment. This region is shaded in fig. 5.3 and indicates that the sample delivery system needs to be heated for 1-iodopropane and above, firstly in order to ensure that enough amount of substance is evaporated and secondly to ensure that no condensation forms on the inside of the tubing of the sample delivery system.

5.1.2 The I4d photoemission

The most striking feature in the I4d photoemission is the *giant resonance* in the I4d $\rightarrow$ εf photoemission channel. A giant resonance is marked by a dramatic increase in photoabsorption or equivalently photoelectron yield that spans over a large energy range. They occur in the spectra of atoms in the vicinity of xenon in the periodic table [110, p. 44f.] for which the first observation of one was made. A description of the line-shape of giant resonances based on effective single-particle potentials has been brought forward where the resonance arises due to the transient trapping of the outgoing electron in a photoionization event in a short-ranged potential well that forms within the atom [111]. While this description is very convenient and intuitive one must not be misguided into believing that this description captures the full picture. The emergence of giant resonances is a consequence of the many-electron nature of the atom which makes their accurate description and characterization a challenging matter but the phenomenon itself all the more interesting to study. The reader shall here be referred to ref. [112] and references therein for more details. We will, however, revisit the giant resonance in its single-particle scattering interpretation in sec. 5.4.1.

For now we want to proceed by examining published experimental data for traces of how the chemical environment of an iodine atom changes the character of the giant resonance (or generally the I4d photoemission) in the energy domain. This is of particular interest as it has been found that if a giant resonance is present in an isolated atom then one can expect to also observe it in an experiment on a solid or molecule containing this atom [111, p. 11]. It is therefore tempting to proclaim a giant resonance as unaffected by its chemical environment and use it as an intrinsic reference in a photoemission chronoscopy experiment, attributing the measured time delays to the propagation of the photoelectron through the molecule and neglecting any possible modifications of the electronic structure of the iodine atom possibly imparted by its chemical environment as it has been done in [25]. It is a similar line of thought that we follow here, but the discussion below shall illustrate that one must be cautious of oversimplifying the situation.

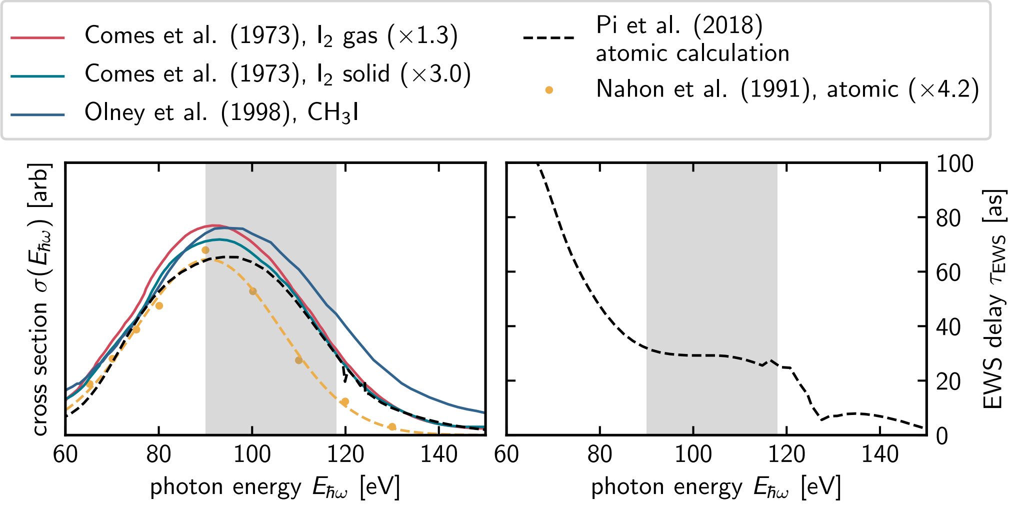

Figure 5.4: The giant resonance in the I4d → εf photoemission channel is marked by a dramatic increase of photoabsorption/total photoelectron yield between 60 eV and 150 eV photon energy as it is seen in the left panel (scaled for better comparison, see legend). The shaded gray area indicates the photon energy region accessed in our experiment, references for the data are given in the main text. The EWS photoemission time delay associated with the resonance is shown in the right panel.

Profiles of the I4d → εf resonance observed in different environments of the iodine atom as reported in literature are shown in fig. 5.4 in comparison with an atomic calculation. Molecular iodine (I_2) was studied by Comes and co-workers [113] in the gas- and solid phase. Olney et al. [98] used electron-impact techniques to investigate the photoionization of CH_3I. Atomic iodine was prepared by Nahon et al. by dissociation with a strong laser and subjected to spectroscopic investigation in [114] where they also note that their experiment underestimates the resonance's width. We find this to be consistent with an accurate atomic calculation by Pi et al. [115] which matches position and shape of the other curves very well. In addition to a cross-section Pi et al. further report a scattering time delay for the giant resonance which is shown in the right panel of fig. 5.4. In the investigated photon energy region it is mostly flat and amounts to ~ 30 as. Overall, the time delay decreases with increasing energy. Around 120 eV small kinks appear in the spectrum as well as in the time delay. These are attributed in [115] to the opening of the 4p photoionization channel around this energy and have also been observed in an experimental study of the giant resonance in iodomethane [97, p. 242].

At a fixed photon energy the I4d photoelectron spectrum is comprised of the two spin-orbit split I4$d_{\frac{3}{2}}$ and I4$d_{\frac{5}{2}}$ components which are separated by 1.7 eV in their binding energy (cf. left panel in 5.5). In a given chemical environment further splitting and an overall shift due to the ligand field can occur which has been researched in depth by Cutler and co-workers [116]. In figure 5.5 we compare Cutler's results for iodomethane and molecular iodine recorded at 90 eV photon energy with the result of Nahon [114] at 80 eV, finding a progressive shift towards lower binding energies. If the giant resonance were now truly unaffected by its chemical environment its maximum should copy this progression but in the opposite direction, but we do not find this to be the case: the resulting shift is significantly larger. Of course total quantitative agreement may not be expected when comparing results from different studies as it is done here, but the overall magnitude of the shifts seems to be too large to be purely coincidental.

In summary, differences in the iodine atom's chemical environment are definitely resolvable in the energy domain and the observed chemical shifts of the I4*d* states' binding energies do not transfer to the giant resonance in a 1-to-1 manner. Therefore, when aiming to use the giant resonance as an intramolecular reference it is beneficial to *preserve* its immediate chemical environment across investigated species, but alter its *more remote* parts. Of course the study of photoemission times through a giant resonance in explicitly different chemical bonding scenarios is also of great interest, but it motivates a complete study in its own right and is beyond the scope of what is presented here.

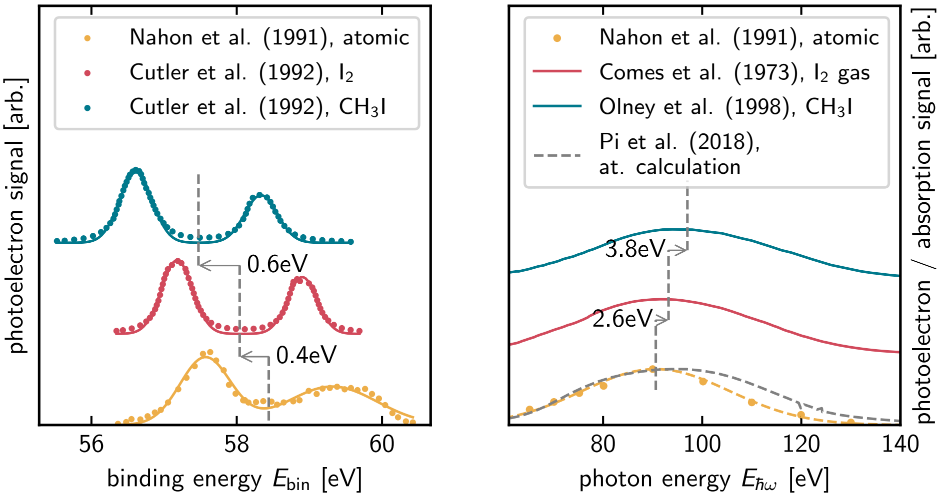

Figure 5.5: Chemical shifts of the I4*d* levels (left panel) and the accompanying shift of the giant resonance (right panel). Going from atomic iodine to iodomethane one finds a steady progression towards lower binding energies. The magnitude of this progression is not matched by the accompanying shift of the maximal position of the giant resonance. While total quantitative agreement of experimental values between different studies cannot necessarily be expected the overall magnitude of the shifts seems too large to be purely coincidental. Points in the left panel are extracted from the referenced publications, solid lines show a fit performed for the determination of the binding energy.

5.2 Experiment

The experiments are conducted at the AS101 beamline at the Technische Universität München (cf. [117]). It is driven by a commercial mode-locked Ti:Sa laser oscillator (cf. sec. 2.3) with subsequent two-stage amplification and custom-built spectral broadening and pulse compression (cf. sec. 3.1.2). The ce-phase of the pulses exiting the spectral broadening stage is stabilized and can be controlled. High-harmonic radiation (cf. sec. 3.2) is generated in a neon gas target with an interaction length of about 0.5 mm and around 100 mbar of gas pressure. Spectral filtering of the harmonic radiation for the generation of isolated attosecond pulses happens via a thin Zirconium foil and custom-made XUV multilayer mirrors with reflectivities centered at 90 eV, 105 eV and 118 eV (see fig. 5.6). Its gas-phase end-station has been specifically modified to enable attosecond streaking experiments on substances with low vapor pressure [117] via a heated gas reservoir and heated conduits (up to ~ 90°C). Apart from attosecond streaking spectroscopy the setup implements mass spectrometry as a

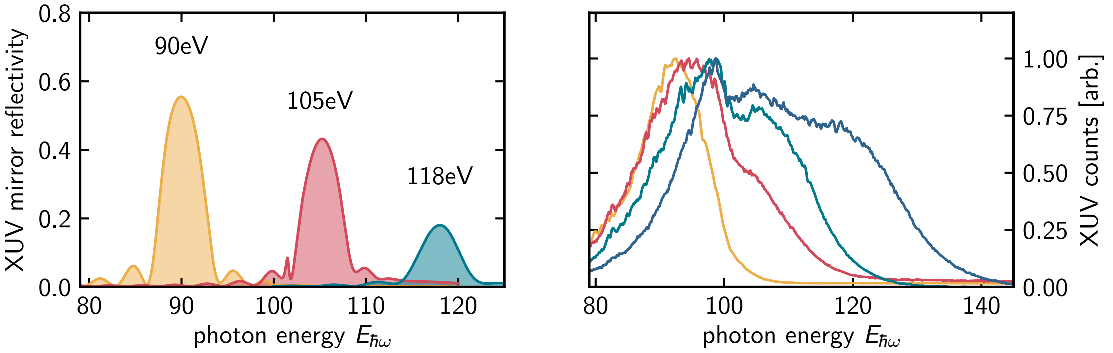

Figure 5.6: Reflectivity curves of the XUV mirrors (left panel) employed in the experiments. With the XUV mirrors isolated attosecond pulses centered at 90 eV, 105 eV and 118 eV photon energy can be extracted from the cut-off part of the high-harmonic spectrum. Raw high-harmonic spectra not corrected for the XUV spectrometer's transmission are shown on the right. The sharp dip at 99.2 eV photon energy is due to enhanced absorption of the XUV CCD detector's Silicon substrate at its L-edge and the slow rise on their low energy side is due to the transmission of the Zirconium foil mounted in front of the detector (cf. [118, 119]). These spectra showcase the wide photon energy tunability of the AS101 beamline's high harmonic source. The 90 eV and 105 eV mirrors have been manufactured by Yang Cui, the 118 eV mirror by Alexander Guggenmos.

diagnostic tool to assess sample purity.

The iodoalkanes are stored in dark glass bulbs in preparation for the experiment. Before being transferred to the experimental setup the more volatile species were cooled to ~ −20°C which reduces their vapor pressure to a safe level for handling the toxic substances. Further purification was not deemed necessary as confirmed via mass spectrometry. Due to their volatiliy Iodomethane and -ethane can readily be evaporated into the gas reservoir at room temperature (see fig. 5.3) where helium is added. A total pressure of up to ~ 2.5 atmospheres is attainable in the reservoir facilitating enough background pressure to perform the experiment for several hours. The mixture is typically replaced about once or twice on a typical measurement day. The larger iodoalkanes do not have sufficient vapor pressure at room temperature and need to be brought to elevated temperatures (cf. fig. 5.3). We found about ~ 70°C to be a comfortable temperature to work at where even for 1- and 2-iodobutane the photoelectron signal is strong enough for the experiment to succeed. Photoelectrons are detected with a time-of-flight (TOF) electron spectrometer which is equipped with an electrostatic Einzel lens, enabling us to cut down the spectrogram acquisition time to 15-30min by increasing the detectors acceptance angle to ~ 20°. About 15 to 25 spectrograms are recorded every measurement day and the experiment is repeated for each molecule and photon energy for at least three days so that systematic errors due to the day-to-day alignment of laser and beamline can be quenched.

5.3 Photoemission time delays in rigid iodoalkanes

As argued above, the effect of a change in chemical environment on the observable photoemission time delay is best explored in the rigid molecules. Exemplary attosecond streaking spectrograms for iodomethane, -ethane and 2-iodopropane are shown in fig. 5.11 for each photon energy. Relative photoemission times $\tau_{\mathrm{I}4d-\mathrm{He}1s}$ are extracted via the diff. rTDSE method (cf. sec. 4.2.2) and statistics shown in fig. 5.9.

The static photoelectron spectrum of a mixture of 2-iodopropane and helium recorded with isolated attosecond XUV pulses at 105 eV shown in fig. 5.7 is representative of the photoelectron spec-

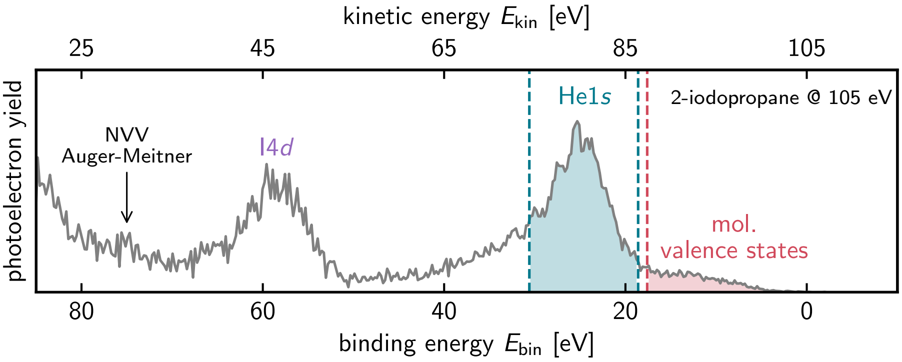

Figure 5.7: Static photoelectron spectrum of a mixture of 2-iodopropane and helium at 105 eV photon energy recorded with isolated attosecond pulses. The main spectral features are the He1*s* and I4*d* photoemission as well as a broad and weak signature of the molecular valence states at low binding energies. The NVV Auger-Meitner spectrum is visible but not clearly resolved. Shaded areas indicate where the photoelectorn yield for He1*s* and I4*d* was determined for the correlation with the delay shown in fig. 5.3.

tra observed in the iodoalkanes. The spectrum is dominated by the He1*s* and I4*d* photoemission features found at binding energies of 24.6 eV and 58.6 eV respectively. The large (5 eV) bandwidth of the XUV pulses smear out the I4$d_{\frac{3}{2}}$ and I4$d_{\frac{5}{2}}$ spin-orbit components which are therefore not resolved. In the delay extraction procedure the I4*d* peak is modeled as a sum of two components of roughly equal cross-section separated by 1.7 eV. At low binding energies one finds a broad but weak feature due to photoemission from the molecular valence states which overlaps in energy with the He1*s* photoemission. At low kinetic energies one finds the characteristic NVV Auger-Meitner emision of iodine compounds (cf. [120, p12] results in iodomethane) which are not clearly resolved here due to the bandwidth of the XUV pulse and the electrostatic lens not set to amplify them. Spectral overlap between photoemission from the He1*s* and the molecular valence states is unavoidable, but care was taken in the experiment to ensure that the valence state photoelectron signals peak height does not exceed ~ 10% of the maximum of the He1*s* photoemission peak. In order to assess whether the amount of spectral overlap influences the observed photoemission time the ratio of photoelectron yield from the He1*s* and the valence states is correlated with the deviation of the measured delays from the mean of their respective statistical population (i.e. for each molecule and photon energy the average is determined and subtracted from the value extracted from each spectrogram in these sets). The regions in which the photoelectron yield was determined are shaded in figure 5.7. Figure 5.3 shows the result of the correlation which indicates insignificant correlation between the spectral overlap and the observed delay across all evaluated spectrograms over a large range of ratios. This includes different mixing ratios of helium and the iodoalkane and different alignments of the laser and beamline.

5.3.1 Estimation of the NVV Auger-Meitner decay influence on the measured I4*d* photoemission delay

At a photon energy $E_{\hbar\omega} = 90$ eV the NVV Auger-Meitner emission observed in iodine compounds at kinetic energies around 27 − 33 eV (cf. [120, p. 12] and [121, p. 3005]) overlaps with the I4*d* photoemission at $E_{\mathrm{kin}} \approx 31$ eV. Auger-Meitner electrons are subject to the streaking effect and show a distinct signature with a strong dependence on the core-hole lifetime τ_1. Fig. 5.10 shows streaking spectrograms calculated for Auger-Meitner electron emission modeled after [122].

Most strikingly, depending on the lifetime one finds the Auger-Meitner electron wavepacket to

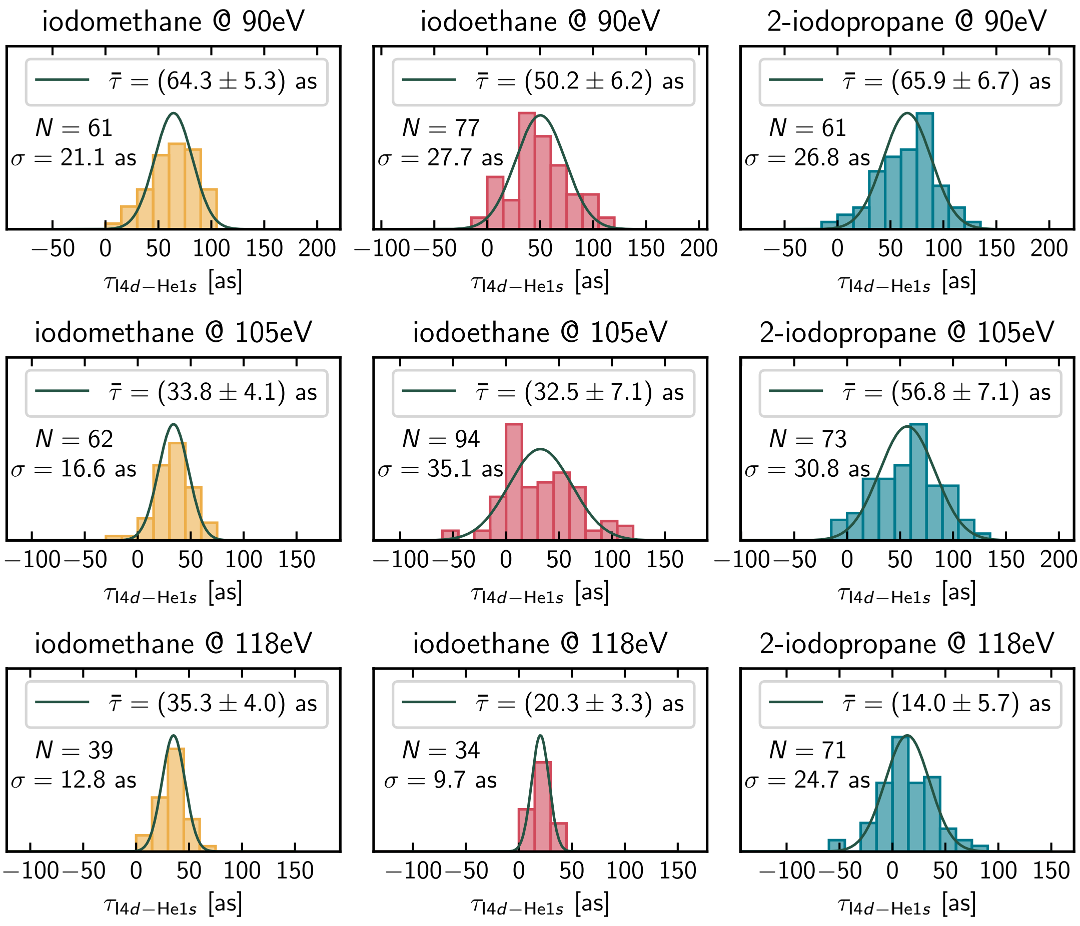

Figure 5.8: Statistics for the experiments on rigid molecules. In excess of 30 spectrograms were recorded per molecule and photon energy. The near-normal distribution of measured delays extracted with the diff. rTDSE method justify reporting average, standard deviation σ and 95% confidence intervals. A normal distribution with these parameters is shown in each plots as a dark gray line.

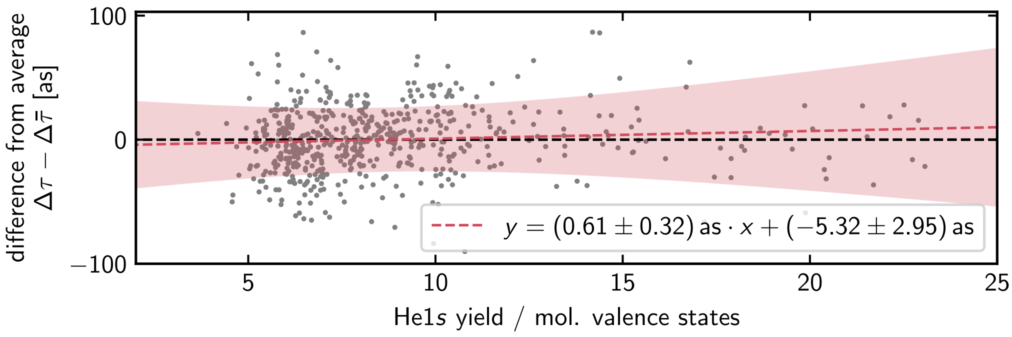

Figure 5.9: Correlating the ration of photoelectron yield in the He1s / mol. valence state region across all spectrograms recorded on the rigid molecules reveals only a minuscle dependency of the deviation of the relative photoemission times with respect to the average of the respective distribution for each molecule and photon energy. Shaded area corresponds to the standard error of the fit line.

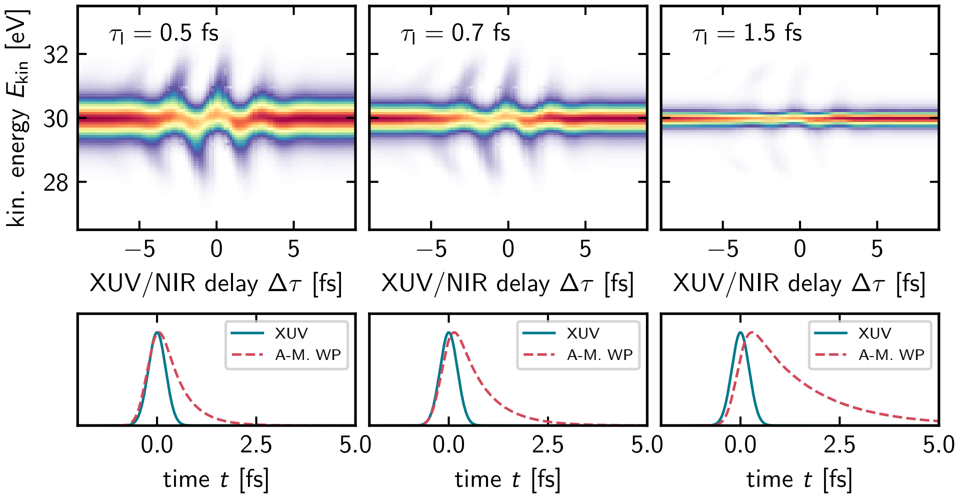

Figure 5.10: Streaking signature (top panels) of Auger-Meitner electrons calculated with the model from [122]. The asymmetric shape of the emitted photoelectron wave packet (dashed red, lower panels) results in a distorted spectrogram. As the lifetime increases the maximum of the Auger-Meitner wave packet furthermore shifts towards larger times compared to the XUV excitation, which is assumed to instantaneously create the photohole.

be delayed with respect to the XUV excitation with the delay depending on the lifetime. In order to assess how the delayed Auger-Meitner emission influences the photoemission times retrieved from experimental spectrograms lifetimes and the spectral distribution of the Auger-Meitner features were extracted from literature (cf. e.g. [121, 120]) combined in various ways to yield spectrograms that within reasonable bounds model the Auger-Meitner emission in the experiment. These were then added in multiple ratios to synthesized spectrograms resembling the experimental spectrograms but with zero relative delay. Any delay extracted from these must be interpreted as a systematic error imparted by the Auger-Meitner electrons. We found an influence of at most −6.33 as which will be taken into account by extending the uncertainty interval for the experiments at 90 eV by this value towards lower delays. The details of the procedure can be found in the Bachelor's thesis of Matthias Ostner [123].

5.3.2 Absolute photoemission delay times

Absolute photoemission times were determined according to the protocol described in sec. 4.3. Table 5.1 summarizes the results and figure 5.12 shows them in comparison with the atomic prediction published in [115].

Iodomethane and -ethane have previously been independently measured before at 105 eV and 92 eV [24, p. 57ff] with different XUV reflectors, noting that for either energy the results for both molecules are so similar they can be averaged and interpreted as the absolute photoemission time of the I4*d* at these energies. Our result at 105 eV are in excellent agreement with the previous results, but about 10 as higher than the atomic calculation. Furthermore we find a $\varDelta = (14.1 \pm 4.2)$ as difference between iodomethane and -ethane at 90 eV. This study extends the data on iodomethane and -ethane towards 118 eV where we find iodoethane to coincide with the atomic calculation and iodomethane assuming a $\varDelta = (15.0 \pm 2.6)$ as larger delay. It should be noted at this point that the result of Biswas et al. [25] at 93 eV also coincides with the atomic calculation within its uncertainties. This is in conflict with the 92 eV result of Ossiander, and in extension also with the results presented

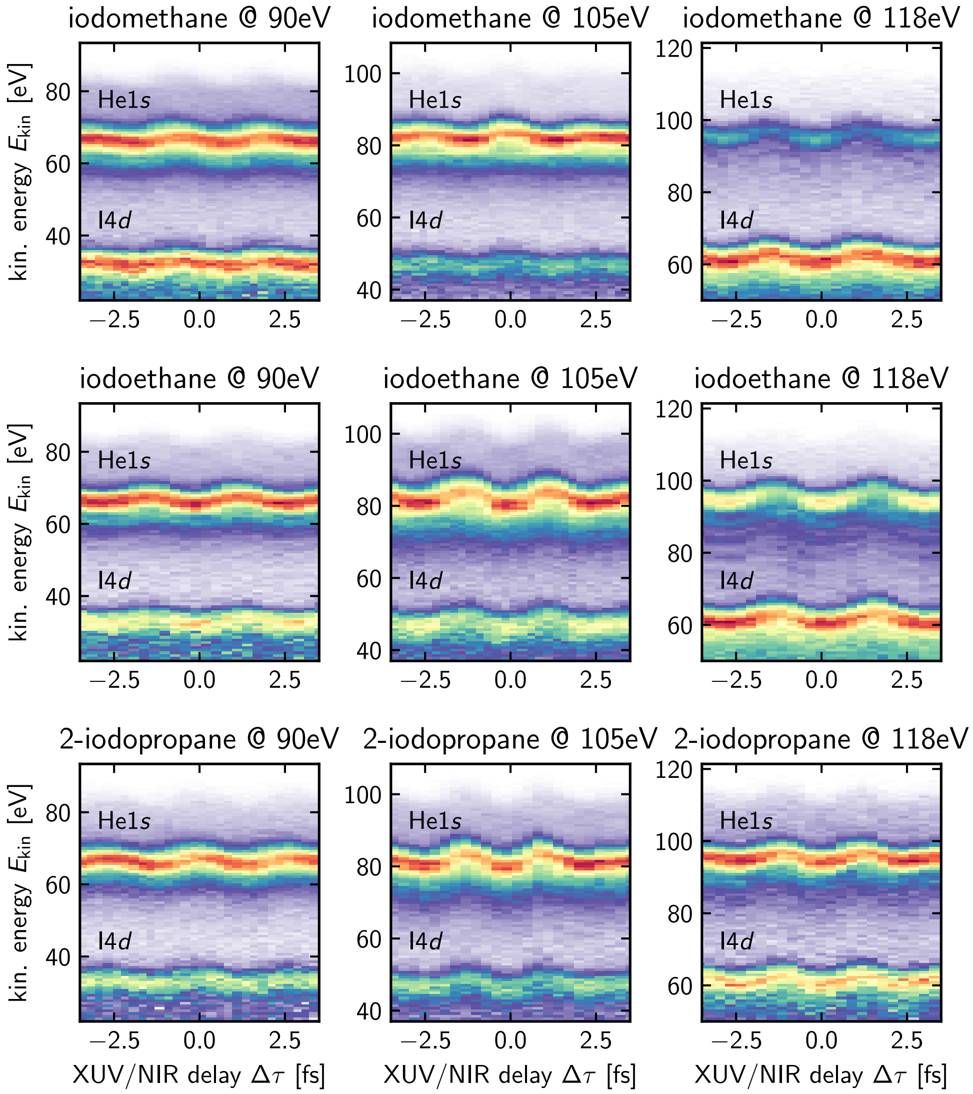

Figure 5.11: Exemplary streaking spectrograms for each photon energy and each rigid molecule in mixture with elium. The photoelectron signal is dominated by the He1*s* and I4*d* photoemission. The molecular valence states' photoemission can be seen to weakly contribute to the spectrograms. It is found at a binding energy of ~ 10 eV. Care was taken in the experiment to ensure that it amounts to no more than 10% of the height of the He1*s* peak which should suppress its influence on the delay retrieval procedure to negligible levels.

here. Biswas et al. used the Ne2*p* photoemission as a chronoscopy reference and a different data analysis method in their study. Furthermore, their statistics are quite weak being comprised of only 15 individual measurements at 93 eV. We attribute this mismatch between their experimental result and ours to their insufficient statistics and unfamiliar data analysis method, and find it likely that their agreement with the atomic calculation is coincidental.

For to 2-iodopropane we find an interesting behavior of the photoemission time delay. While monotonously decreasing, it stays elevated at 105 eV exceeding the atomic calculation by 35 as and iodomethane and -ethane by (23.7 ± 5.5) as on average before dropping below it at 118 eV. Overall we find the largest delays of all rigid molecules for 2-iodopropane at 90 eV and 105 eV.

We therefore show unambiguously here that it is possible to resolve differences in the photoe-

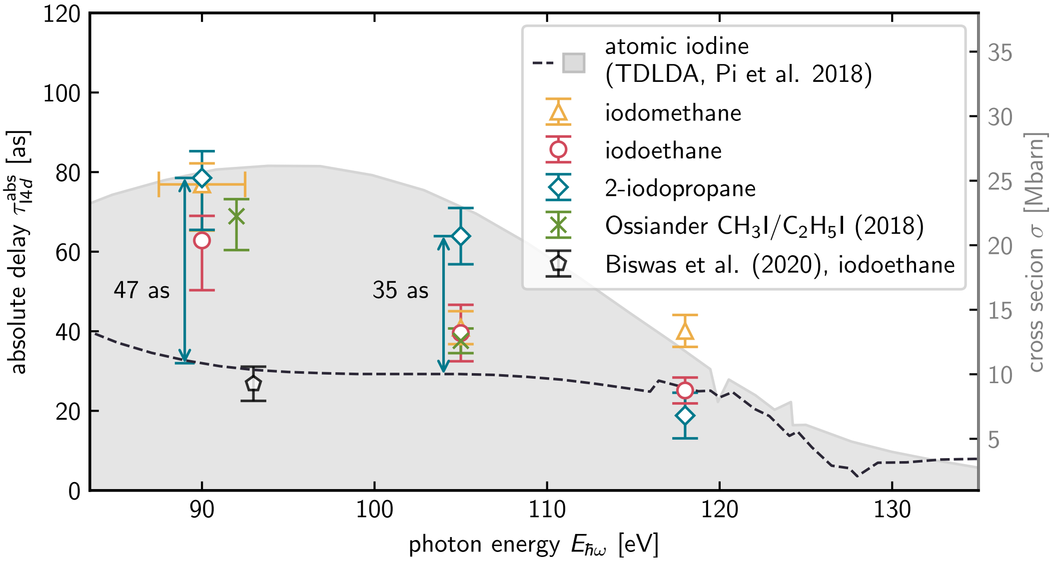

Figure 5.12: Absolute photoemission times measured for the rigid iodoalkanes (numerical values in table 5.1). The profile of the giant resonance (shaded gray, right ordinate) and the atomic I4*d*-EWS delay are shown for orientation. Overall we find the largest delays for 2-iodopropane at 90, eV and 105 eV. Previous results by Ossiander [24] are reproduced well at 105 eV but we find a slight difference between our results at 90, eV and their value reported at 92 eV. Results for iodoethane at 93 eV were reported by Biswas et al. [25] and are close to the atomic calculation. Vertical error bars denote the 95% confidence interval, horizonal error bars (see iodomethane at 90 eV correspond to the XUV mirrors' 5 eV bandwidth throughout but are only shown for one point for clarity.

mission time of a core-level between different species of molecules in which this core-level is present. Before proceeding, an important consequence of the approach followed here shall be brought to the attention of the reader: Even if the procedure for evaluating absolute photoemission times were not applicable to the systems studied here for some reason or were to suffer from inaccuracies the *delay differences* between the molecules reported here will remain unaffected. It has been pointed out [124] that the interpretation of time delays measured between initial states of different binding energy (e.g. I4*d* vs. He1*s*) can be problematic, but this study circumvents the issue by directly comparing systems where the binding energy of the investigated initial states (i.e. the I4*d* across all studied molecules) explicitly coincide.

Another interesting point to remind oneself of is that the experiment is not resolving the molecular orientation or the angular distribution of emitted photoelectrons. Yet we find large differences

Table 5.1: Overview of the absolute chronoscopy results on the rigid iodoalkanes.

photon energy	90 eV	105 eV	118 eV
total He1*s* $\tau^{\mathrm{tot}}_{\mathrm{He}1s}$	−6.5 as	−5.1 as	−4.3 as
I4*d* CLC $\tau^{\mathrm{clc}}_{\mathrm{I}4d}$	−19.2 as	−12.2 as	−9.1 as
at. calculation $\tau^{\mathrm{at.}}_{\mathrm{I}4d}$ [115]	32.0 as	29.2 as	25.8 as
iodomethane $\tau^{\mathrm{abs}}_{\mathrm{I}4d}$	$\left(76.9^{+5.3}_{-11.6}\right)$ as	(40.9 ± 4.1) as	(40.1 ± 4.0) as
iodoethane $\tau^{\mathrm{abs}}_{\mathrm{I}4d}$	$\left(62.8^{+6.2}_{-12.5}\right)$ as	(39.6 ± 7.1) as	(25.1 ± 3.3) as
2-iodopropane $\tau^{\mathrm{abs}}_{\mathrm{I}4d}$	$\left(78.5^{+6.7}_{-13.0}\right)$ as	(63.9 ± 7.1) as	(18.8 ± 5.7) as

between molecular species. Our results therefore indicate that intra-molecular scattering of the leaving photoelectron may not be suppressed by the orientational averaging. This has previously been observed by Patanen and co-workers in the spectral domain [102] and has implications for the use of atoms embedded in molecules as chronoscope species (see sec. 6.4.3). In an angularly resolved experiment one may then in consequence find an even more drastic variation of the photoemission time.

5.3.3 Correlation of the absolute photoemission time with a measure of molecular size

As it will be reiterated in section 5.3.4, the interpretation of molecular photoemission time delays is far from straightforward. In [25] Biswas et al. present semiclassical calculations which predict that the photoemission time delay should increase with the *size* of the molecular rest attached to the iodine atom. A definition of a precise measure of the size is not given, but with the data available here we can define a measure of our own and test whether such a correlation exists.

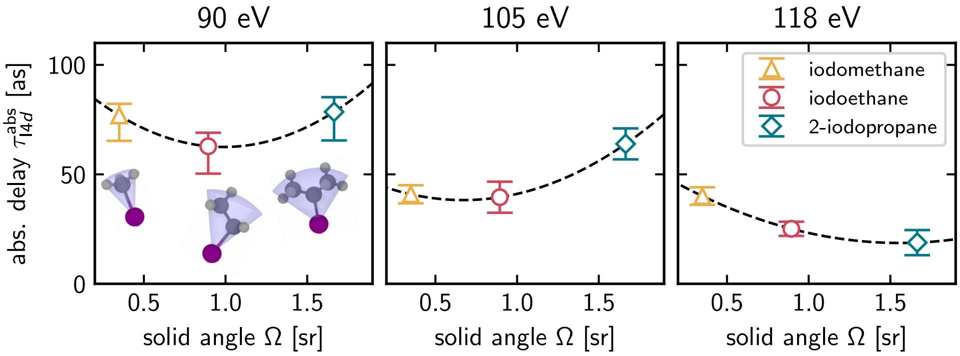

Figure 5.13: Correlation of the absolute photoemission time with the molecular size as defined via the solid angle occupied by the hydrocarbon rest attached to the iodine atom. A second order polynomial fit is shown in each panel as a guide to the eye. It is clearly visible that no simple correlation between size and observed photoemission time delay exists. Renderings of the rigid iodoalkanes and the solid angle cones which define the abscissa are shown in the first panel.

The molecular mass, or alternatively the number of carbon atoms is not suitable for this purpose as e.g. 1-iodopropane and 2-iodopropane are equivalent by this measure but have very different structures as discussed above. Here we propose using the solid angle Ω the molecular rest occupies as seen from the center of the iodine atom to the outermost hydrogen atoms as seen from this perspective as a measure (see tabl. 5.2, fig. 5.13). We find, however, no clear correlation between this measure of *size* and the observed absolute photoemission delay time as it is apparent from figure 5.13.

Table 5.2: Solid angles occupied by the hydrocarbon rest as seen from the iodine atom in the rigid iodoalkanes, determined from the molecular geometries listed in appendix B.

species	sol. angle Ω
iodomethane	0.34 sr
iodoethane	0.90 sr
2-iodopropane	1.67 sr

5.3.4 Quantum scattering calculations for the interpretation of photoemission time delays

Photoemission time delays can nowadays be calculated to (sub-)attosecond precision for isolated atoms (cf. [94, 23] and [125]). For photoemission from solids very recent progress (see chap. 6 and [126]) has brought satisfactory agreement between experiment and calculation into reach. For small molecular systems at low photon energies similar developements have brought about accuracy comparable to the atomic case and fundamental insight into the two-photon ionization process underlying the time delay measurement [127], which is a tremendous achievement. The regime of higher photon energies as they are of interest for this work and especially larger molecules is however not quite accesible yet, and interpretations of the observed delays is a rather qualitative one, just as it is in this work.

An approach that has gained some popularity in recent years in molecular photoemission chronoscopy studies is using the `ePolyScat` suite of scattering calculation programs [95, 96] to determine the one-photon photoionization matrix elements and infer from them the photoemission time delay observed in the experiment [128, 129, 25], though the accuracy of the time delays obtained this way is questionable. In the case of the iodoalkanes (or generally iodated hydrocarbons) its inapplicability becomes clear very quickly: `ePolyScat` fails to reproduce the giant resonance in the I$4d \rightarrow \varepsilon f$ channel.

In an `ePolyScat` calculation the molecule's initial state is determined via a Hartree-Fock calculation for which we used `GAMESS` ([106], RHF, Sapporo non-relativistic triple-ζ basis set). Photoemission cross sections were calculated for iodomethane and for hydrogen iodide, i.e. the smallest iodine compound which can be assessed with `ePolyScat`. It shall serve here as an approximation to an atomic calculation. Matrix elements and final states are described in `ePolyScat` in terms of a spherical harmonic expansion. We chose $\ell_{\max} = 16$ for both molecules which quenches the expansion error for the initial state to below 2% in all cases. A calculation on iodoethane or any larger molecule comes at an unfeasibly increased computational cost given the computing power available to our group at the time of writing. For a photon energy $E_{\hbar\omega}$ and a certain direction of observation and molecular orientation can be extracted from the output of `ePolyScat` with a custom-made post processing suite (see [117, p. 40f. and chap. 4.2]). The resulting cross sections and orientationally averaged delays are shown in fig. 5.14.

As the left panel in fig. 5.14 demonstrates, the calculation does unfortunately not reproduce the giant resonance very well. Its position and width are severely underestimated. This is due to neglecting the many-particle nature of the resonance, as it has been similarly observed by the authors of [130] for the case of the Xe $4d$ photoemission. The calculated time delays in the right panel show a fleeting resemblance to the general shape of the atomic calculation, but the mismatch between the cross sections predicted by `ePolyScat` and experimental data as well as the accurate atomic calculation by Pi et al. [115] discourages direct comparison with experimental data. Differences between the scattering calculation for iodomethane and hydrogen iodide (yellow line) as well as for the experimental data and the atomic calculation (black triangles) are shown in the inset in the right panel, where it becomes apparent that also the effect of the change of molecular environment (i.e. the addition of a methyl group) is not reflected well in the `ePolyScat` calculations. We therefore surmise that generally a high level of theory is necessary to capture the photoemission dynamics in the molecules studied here. A promising candidate there is the R-Matrix method [131, 132] which is actively developed by our collaborators in the group of Zdeněk Mašín at the Charles University of Pague, Czech Republic. A recently submitted joint grant application focuses on the extension of the R-Matrix codes towards the iodoalkanes on the computational side and on the implementation of access to photoemission timing in the molecular frame of reference on the experimental side (cf. sec. 5.5).

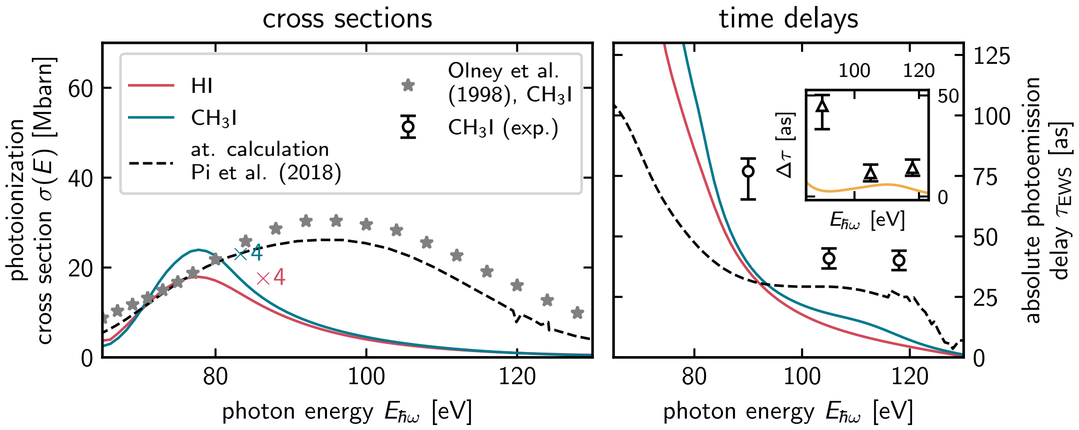

Figure 5.14: On the inadequacy of quantum scattering calculations performed with `ePolyScat` to predict photoemission time delays in iodine-containing molecules. Hydrogen Iodide (HI) as the smallest iodine compound which can be assessed with `ePolyScat` is here contrasted with a calculation for iodomethane (CH_3I) and experimental results [98], as well as the accurate atomic calculation by Pi et al. [115]. From the photoionization cross sections shown in the left panel it is apparent that `ePolyScat` does not reproduce the giant resonance correctly. The time delays shown in the right panel loosely resemble the general shape of the accurate atomic calculation. The difference between the calculation for iodomethane and hydrogen iodide is shown in the inset as a yellow curve, together with the difference of the experimental results (black triangles) from the atomic calculation. It is clear that unfortunately the level of theory `ePolyScat` offers is not sufficient to faithfully describe the photoionization process in iodine compounds.

5.3.5 A closer look: photoelectron 'wave packet' reconstruction

Before proceeding to the floppy iodoalkanes we shall make use of the ability to extract the photoemission time delay's energy dependency in a small region around the central photon energy via ptychographic spectrogram inversion (cf. sec. 4.2.2).

The individual spectrograms were subjected to 10^3 iterations of the extended ptychographic iterative engine with the NIR field being frozen after 600 iterations. One wave packet is retrieved for the He1*s* photoemission, and one for the I4*d* photoemission. Due to the lack of molecular orientation and furthermore the unresolved splitting of the I4*d* photopeak in the experiment the latter is to be understood as an effective 'wave packet'. Group delay differences of the 'wave packets' are determined (eq. 4.21) and averaged for each molecule and energy. Absolute photoemission times are determined again via the protocol defined in sec. 4.3, taking the energy dependence of the He1*s* photoemission time (cf. fig. 4.3) and CLC time delay (eq. 4.24) into account. Figure 5.15 shows the absolute I4*d* photoemission times.

Except for iodomethane and -ethane at 118 eV the diff. rTDSE delays are reproduced well within the respective uncertainty margins. The discrepancy at 118 eV may be attributed to the onset of I4*p* photoemission in this energy region. Its influence on the calculated atomic I4*d* delay has been noted in the original publication [115, p. 6], and a peculiar behaviour of the asymmetry parameter of the I4*d* photoionization in iodomethane has been observed around 120 eV experimentally [97, p. 242]. It is possible that the expected spectral variation in this energy region associated with the I4*p* threshold may influence the delay retrieval procedure albeit being unresolved in its details due to the large XUV bandwidth.

A pronounced structure in the I4*d* delay's energy dependence is seen at 90 eV in iodomethane. The I4*d* delay varies between the atomic calculation and the diff. rTDSE result within only a few electron volts. The transition from the methyl group attached to the iodine atom to an ethyl group (iodoethane) raises the entire energy dependence around 90 eV with only slight changes when progressing to 2-iodopropane. At 105 eV the results for iodomethane and -ethane are qualitatively very similar, in agreement with their respective diff. rTDSE results. In 2-iodopropane the delay curve tilts towards lower delays on its high energy side. Qualitative similarity of the results for iodomethane and -ethane at this energy to the iodomethane result at 90 eV must be noted.

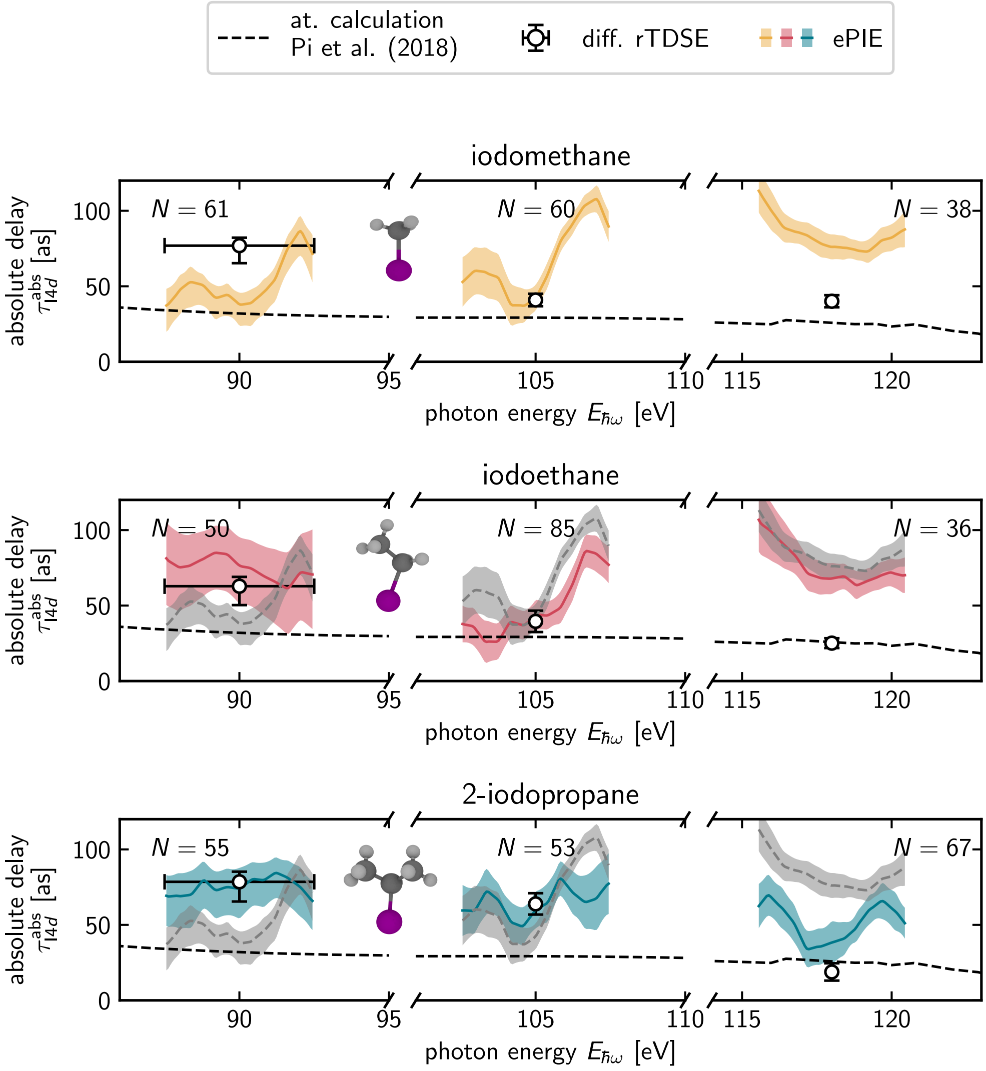

Figure 5.15: Energy dependence of the absolute I4*d* photoemission time delay in the rigid iodoalkanes determined with the ptychographic method are shown over the 5 eV FWHM bandwidth of the XUV reflectors. Within their respective uncertainties (95% confidence interval, including the systematic uncertainty due to the NVV Auger-Meitner decay at 90 eV) good agreement with the diff. rTDSE method is found, except for iodomethane and -ethane at 118 eV. The results for iodomethane are shown in the lower two panels in gray for comparison. While the change in chemical environment of the iodine atom already became apparent in the delay differences determined via the diff. rTDSE method, the ptychographic method gives a more detailed picture. Horizontal errorbars indicate the XUV reflectors' 5 eV bandwidth and are only shown at 90 eV for clarity. The number of spectrograms for which the ptychographic method converged to a meaningful result is given in the figure.

Overall, strong changes of the I4*d* photoemission time delay within small energy intervals as the ptychographic method reconstructs them are surprising. Whether the variations observed here are truly representative of the true photoemission delay in these molecules or simply artifacts of the analysis is not entirely clear yet and cannot be clarified without a calculation at an appropriate level of theory. Still, the general agreement between the ptychograpy results and the diff. rTDSE results is encouraging, as are the results on the floppy iodoalkanes presented further down. Furthermore, as it will be seen in chap. 6, time delays observed in the photoemission from solid surfaces *do* show strong variations in their magnitude with only small changes of the incident photon's energy. Assessment of photoemission dynamics with the ptychographic method can therefore be expected to yield interesting and detailed insights into the dynamics of molecular photoemission if used in combination with the diff. rTDSE method.

5.4 Photoemission time delays in floppy iodoalkanes

While we found large variations in the I4*d* photoemission time delay in the rigid iodoalkanes, the floppy 1-iodopropane, 1-iodobutane and 2-iodobutane display no such behaviour. Absolute I4*d* photoemission time delays were again determined following sec. 4.3 with the results compiled in fig. 5.16 and table 5.3. Exemplary streaking spectrograms are shown in fig. 5.4. Due to their lower vapor pressure the helium to molecule ratio is usually quite large and in consequence the molecular valence photoemission is significantly quenched, and again a correlation between the relative I4*d*–He1*s* photoemission time with the mixing ratio was not found (fig. 5.18). Figure 5.4 summarizes the experimental statistics.

Table 5.3: Overview of the absolute chronoscopy results on the floppy iodoalkanes. All measured delays are remarkably close to the atomic calculation, with the average across all molecules even coinciding with it within less than 2 as throughout.

photon energy	90 eV	105 eV	118 eV
total He1*s* $\tau^{\mathrm{tot}}_{\mathrm{He1}s}$	−6.5 as	−5.1 as	−4.3 as
I4*d* CLC $\tau^{\mathrm{clc}}_{\mathrm{I4}d}$	−19.2 as	−12.2 as	−9.1 as
at. calculation $\tau^{\mathrm{at.}}_{\mathrm{I4}d}$ [115]	32.0 as	29.2 as	25.8 as
1-iodopropane $\tau^{\mathrm{abs}}_{\mathrm{I4}d}$	$\left(38.9^{+4.4}_{-10.7}\right)$ as	(23.1 ± 7.2) as	(10.3 ± 5.6) as
1-iodobutane $\tau^{\mathrm{abs}}_{\mathrm{I4}d}$	$\left(33.0^{+6.8}_{-13.1}\right)$ as	(31.7 ± 6.4) as	(35.4 ± 7.0) as
2-iodobutane $\tau^{\mathrm{abs}}_{\mathrm{I4}d}$	$\left(28.8^{+4.4}_{-10.7}\right)$ as	(35.3 ± 6.2) as	(32.0 ± 6.0) as
average $\tau^{\mathrm{avg}}_{\mathrm{I4}d}$	$\left(33.6^{+9.2}_{-15.6}\right)$ as	(30.0 ± 11.5) as	(25.8 ± 10.8) as

In terms of absolute photoemission times we found the I4*d* delay in all floppy iodoalkanes to be remarkably close to the atomic prediction, with the largest deviation for 1-iodopropane at 118 eV. Interestingly, the averages for all molecules agree with the atomic calculation within less than 2 as. This is especially remarkable as we found large delay differences between the molecules in the case of the rigid iodolakanes and also large deviations of the absolute delays at 90 eV from the atomic calculation for all rigid molecules. These are completely absent in the floppy iodolakanes.

This finding now raises two questions: Firstly, which mechanism is responsible for quenching the molecular part of the photoionization delay in large molecules? A currently running experimental campaign investigates photoemission time delays in similarly sized molecules (sec. 5.5.1) with the aim of closing in on the answer to this question, specially focussing on the role of conformational isomerization in the formation of the observable photoemission time delay and rigid double bonds stabilizing the molecular backbone. Secondly, can the floppy iodoalkanes be used as substiutes for

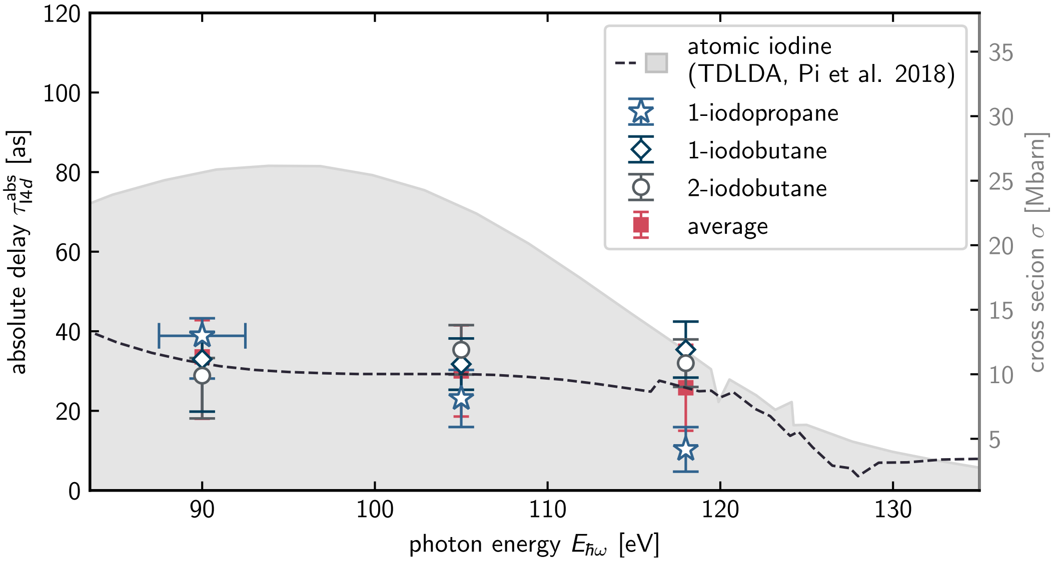

Figure 5.16: Absolute photoemission times measured for the floppy iodoalkanes in comparison with the atomic prediction by Pi et al. [115]. The calculated cross section is shown for orientation. With the exception of 1-iodopropane at 118 eV all measured delays fall within a few attoseconds of the atomic prediction, even moreso their averages (red boxes). This remarkable agreement and especially the only minuscle differences between different molecules motivates using the experimental results to evaluate the dynamics of the giant resonance directly in the time domain.

atomic iodine in a chronoscopy experiment? The results presented here are encouraging, but one must not hasten a conclusion without having more calculations for the specific investigated molecules available. A foray into the interpretation of the absolute delays reported here as purely atomic is waged in sec. 5.4.1. We have, however, also gathered experimental evidence that across the molecules studied the molecular I4*d* photoemission is not necessarily equivalent and therefore representative of its atomic counterpart, finding e.g. delays between (23.1 ± 3.7) as for 1-iodopropane and (63.9 ± 3.6) as for 2-iodopropane at 105 eV where previously the I4*d* photoemission times of iodomethane and -ethane ((40.9 ± 2.1) as and (39.6 ± 3.6) as measured here, respectively) have been used in place of that of atomic iodine adsorbed on a surface in the pursuit of absolutely timing the photoemission from a tungsten (110) surface [18]. As it will become more clear in sec. 6.4.3 our results here are not strictly in disagreement with what is presented in [18], but call for either revisiting and recalibrating the atomic chronoscope, which will become feasible once the molecular photoemission time delays can be calculated to sufficient precision, or raising the uncertainties on the absolute photoemission times reported on W(110).

5.4.1 The giant resonance in the time domain

The remarkable agreement of the average absolute photoemission times between molecules and furthermore with the accurate atomic calculation motivates revisiting the giant resonance and its dynamics, and it is tempting to see the average absolute photoemission times in the floppy iodoalkanes as representative of atomic iodine which we shall do for this purpose.

Within the influential work of J. P. Connerade an intuitive interpretation of the complex phenomenon in terms of single-particle scattering was developed (cf. [133, 111] and references therein). In essence, a short-ranged potential well forms inside the atom due to the interplay of centrifugal forces and incomplete nuclear screening [134, p. 1449]. This well is characterized by its depth *D* and width *a* (see inset in lower panel of fig. 5.20). Pointing out that the low energy scattering spectrum

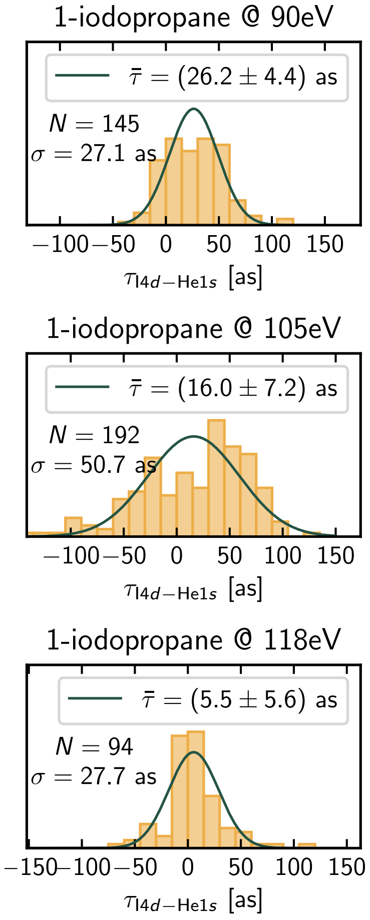

Figure 5.17: Statistics for the experiments on floppy molecules.

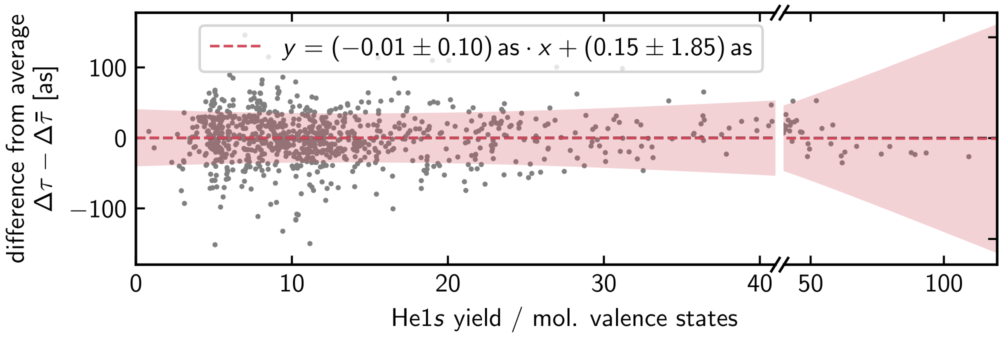

Figure 5.18: Correlating the ration of photoelectron yield in the He1s / mol. valence state region across all spectrograms recorded on the floppy iodoalkanes reveals only a negligible variation of the deviation of the relative photoemission times with respect to the average of the respective distribution for each molecule and photon energy. Shaded area corresponds to the standard error of the fit line.

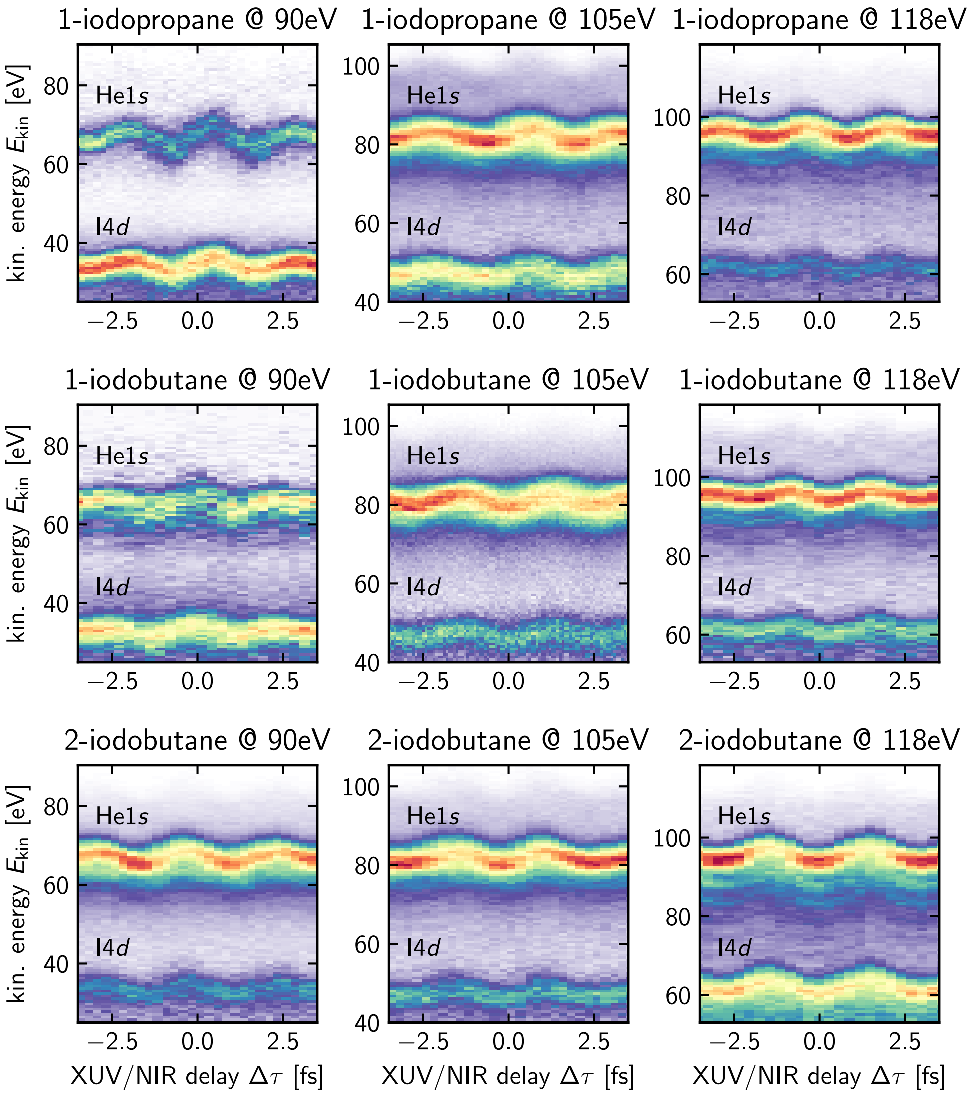

Figure 5.19: Exemplary streaking spectrograms for each photon energy and each floppy molecule in mixture with helium. In each case the photoelectron spectra are strongly dominated by the He1*s* photoemission which is usually amplified using the electrostatic Einzel lens of the TOF spectrometer and the I4*d* photoemission which does not require amplification as the photoelectron yield is large due to the photon energy being close to the giant resonance in all cases.

of a short ranged well does not depend on its precise structure, Connerade brings eqn. 5.1 for the scattering phase shift δ forward which is that of a spherical square well with angular momentum ℓ,

$$\tan(\delta) = \frac{z j_\ell(z') j_{\ell-1}(z) - z' j_\ell(z) j_{\ell-1}(z')}{z j_\ell(z') j_{-\ell}(z) + z' j_{-\ell-1}(z) j_{\ell-1}(z')}. \tag{5.1}$$

There, $z = ka$, $z' = k'a$ and $k = \sqrt{E}$ is the wave vector outside of the well while $k' = \sqrt{E+D}$ is the wave vector inside the well and the $j_\ell(z)$ being the spherical Bessel functions using Rydberg units [133, p. 165-167]. The ℓ quantum number specifies the angular momentum of the final state. In the case of the I4$d \rightarrow \varepsilon f$ transition this means $\ell = 3$. Any background phase shifts δ_0 can be neglected in the spectral region of the giant resonance [134, p. 1450], whereby the time delay associated with the resonance is the energy derivative of δ (cf. eq. 4.6). The parameters a and D are determined via a least squares fit to the averaged absolute delays of the floppy iodolakanes (tab. 5.3) yielding $a = (4.2 \pm 0.5)$ a.u. and $D = (36.8 \pm 26.9)$ Ry. The large uncertainty of D is indicative of the delay and in consequence the phase shift and also the cross section being quite insensitive to a change of the depth of the potential well within the scattering model. Figure 5.20 shows the delay and phase shift associated with the giant resonance in the two upper panels.

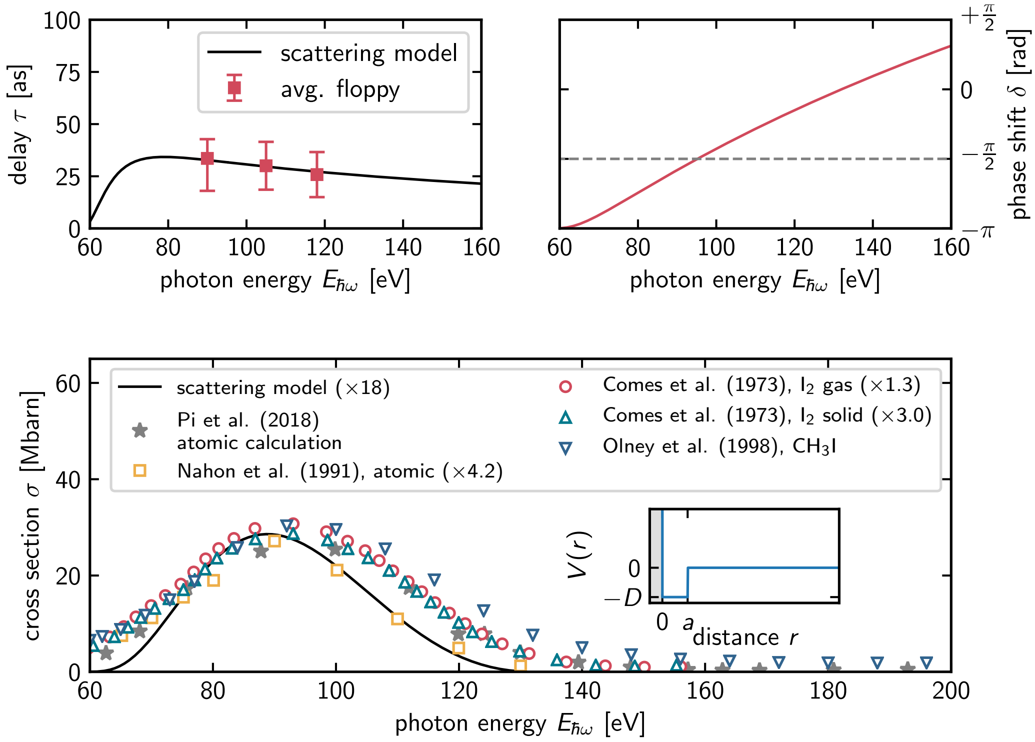

Figure 5.20: Evaluation of the giant resonance in the time domain. The top panels show the fit of the time delay associated with the resonance to the average absolute photoemission times determined experimentally for the floppy iodoalkanes (left) and the phase shift δ. The phase shift increases slowly and passes through $-\frac{\pi}{2}$ at $E_{\hbar\omega} = 95.5$ eV. This traversal of a multiple of $\pi/2$ is responsible for the excursion in the cross section which is shown in the lower panel. We find qualitative agreement in shape and position with published data (scaling factors given in the legend). The inset in the lower panel shows a sketch of the radial well potential.

The cross section is proportional to $\sigma(k) = 4\pi/k^2(2\ell+1)\sin^2\delta$ [134, p. 1450] and shown in the lower panel of fig. 5.20. We note good qualitative agreement with the atomic calculation [115] and previously cited literature [115, 114, 113, 98]. The phase shift δ increases slowly with energy and passes $\pi/2$ at $E_{\hbar\omega} = 95.5$ eV, defining the center of the resonance at this energy. In summary, evaluation of the giant resonance purely from the time domain in its scattering interpretation is possible and yields results consistent with spectral investigations.

5.4.2 Ptychographic reconstruction: remnants of the molecular environment?

The question of why the molecular influence is not detected in the central photoemission time delays for the floppy iodoalkanes remains open. Application of the ptychographic 'wave packet' reconstruction algorithm reveals though that while the energy dependence of the absolute photoemission times is strongly damped, it does not collapse to the atomic prediction completely (see fig. 5.21).

We find the familiar discrepancy at 118 eV wich we attributed to the opening of the 4*d* photoionization channel (cf. sec. 5.3.5). Otherwise, for 1-iodopropane at 90 eV 1- and 2-iodobutane at 105 eV a striking variation of the photoemission delay with the photon energy is seen. Without proper theoretical assessment these variations cannot readily be interpreted, but they illustrate that even in molecular targets that do not have a well-defined structure due to rapid conformational isomerization at room temperature photoelectron wavepacket reconstruction may yield valuable insight. Once the calculation of photoemission times for the iodolakanes is possible with sufficient accuracy the energy dependence of the I4*d* delay extracted via this method should be compared to the energy dependence predicted by the calculation as it is done in chapter 6 for the W(110) photoemission.

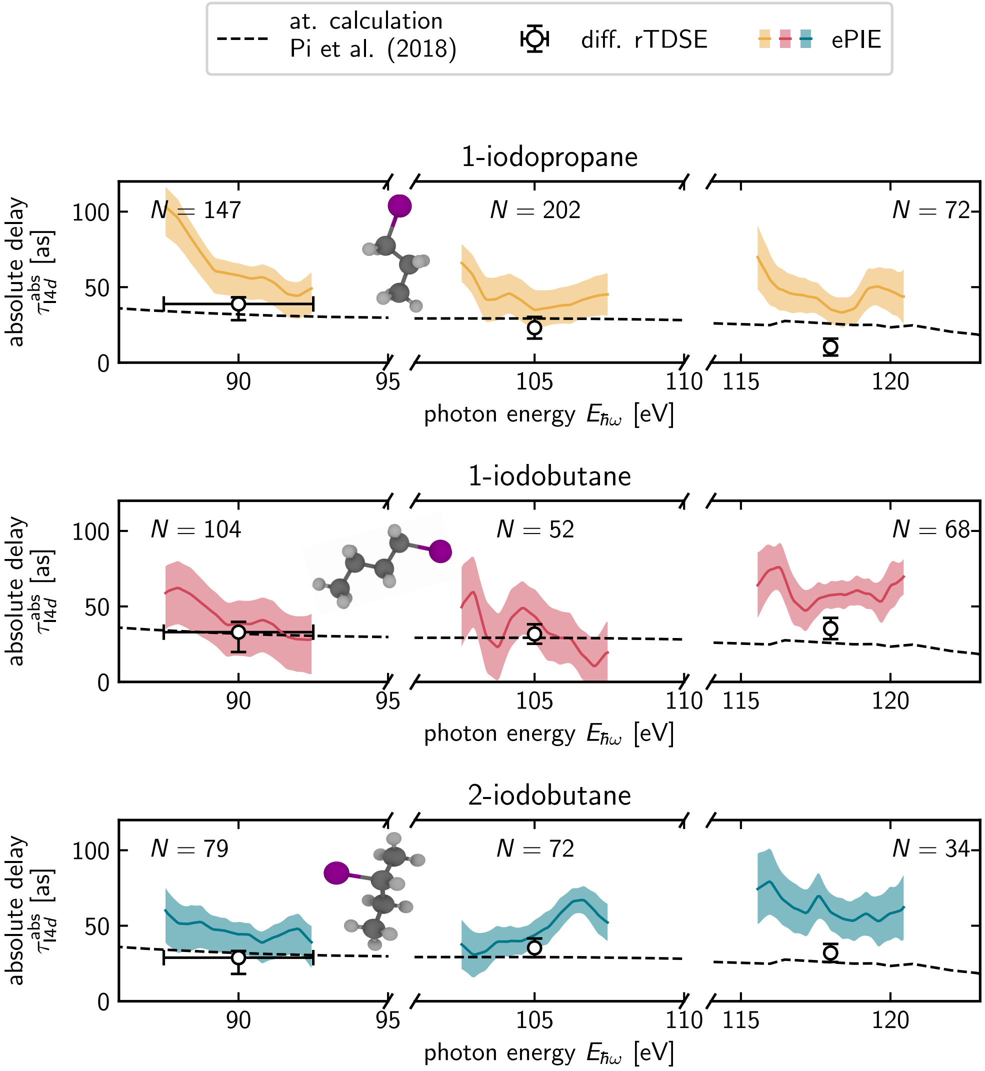

Figure 5.21: Energy dependence of the absolute I4*d* photoemission time delay in the floppy iodoalkanes determined with the ptychographic method. Shown here is the delay over the 5 eV FWHM bandwidth of the XUV reflectors (colored curves). As for the rigid iodoalkanes we find good agreement with the diff. rTDSE results within their respective uncertainties (95% confidence interval, including the systematic uncertainty due to the NVV Auger-Meitner decay at 90 eV), with larger deviations at 118 eV. While (as discussed in the text) the diff. rTDSE delays mostly mimic the atomic calculation the ptychographic results show some more structure. It should especially be pointed out that their qualitative shapes do not match those observed in the rigid iodoalkanes. This makes it unlikely that the structures observed there are artifacts e.g. due to the XUV optics or the photoelectron detection. Horizontal errorbars indicate the XUV reflectors' 5 eV bandwidth and are only shown at 90 eV for clarity. The number of processed spectrograms for each molecule and energy is given in the figure.

5.5 Perspectives of molecular photoemission chronoscopy

The results presented in this chapter indicate that molecular photoemission chronoscopy experiments have the potential to become a quite valuable source of information and furthermore offers the possibility to thoroughtly test numerical methods for the assessment of the molecular photoionization process currently in developement. Some new questions the presented study spawned and how they are adressed from the experimental side are summarized below.

5.5.1 Photoemission time delays in iodobenzene and iodocyclohexane

The role of conformational isomerization in the formation of the observed absolute I4*d* photoemission time delay is studied in iodocyclohexane and iodobenzene in mixture with helium. The carbon 6-rings to which the iodine atom is attached are of roughly equal size as measured by their C – C bond lengths (cf. [135, 136]) with the cyclohexyl ring being prone to rapid conformational isomerization between multiple different configurations at room temperature (cf. [137, 103] and references therein). First photoemission timing experiments on these systems are at the time of writing being performed by Maximilian Forster in the course of his Master's thesis work, where at 90 eV a delay difference of about 15 as between the two species is observed (see fig. 5.22).

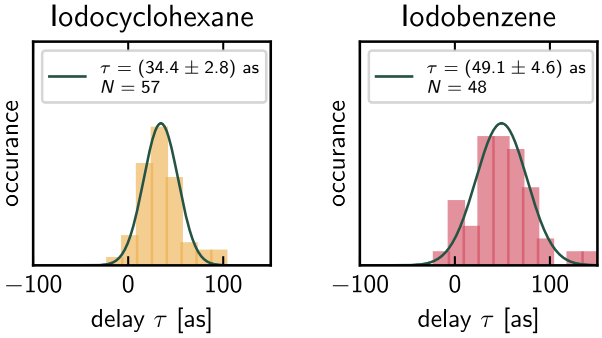

Figure 5.22: Photoemission time delays in iodobenzene and iodocyclohexane. A large difference in the relative I4*d*–He1*s* photoemission time delay at 90 eV between the molecules is measured.

5.5.2 Photoemission timing in the molecular frame

One weak point of the gas phase experiments presented in this chapter is the lack of molecular orientation and thereby angular resolution. One can however exploit the tendency of iodomethane and -ethane molecules to self-orient upon adsorption onto a metal surface as a function of the surface coverage [138, 139], lying down flat at low coverages and sticking up straight at higher coverages (see fig. 5.23).

The I4*d* photoemission is clocked against the substrates valence band emission in this experiment. By varying the coverage the dependence angle of the molecular axis w.r.t. the surface normal is varied and the dependency of the photoemission time delay on different parts of the molecular potential landscape can be probed as one can move the hydrocarbon chain into or out of the way of the leaving photoelectrons when they are detected parallel to the surface. Another possible approach is to rotate the substrate without changing the coverage. This experimental effort is led by Pascal Scigalla and Sven-Joachim Paul.

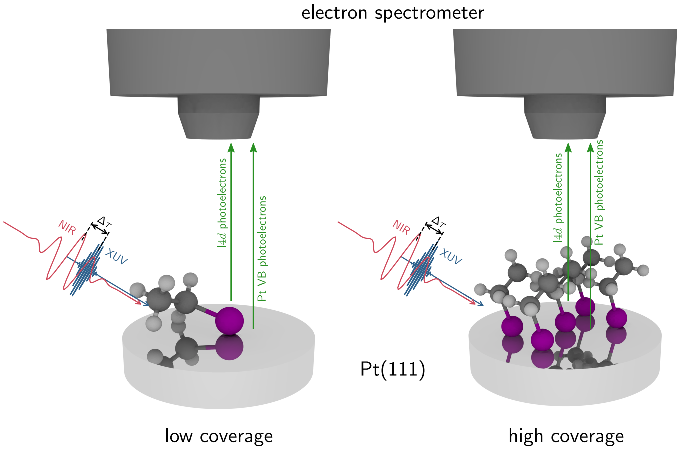

Figure 5.23: Photoemission timing via attosecond streaking on molecues aligned on a metal surface (in this case iodoehane on Pt(111)) via coverage control. In aligned molecules the photoemission can be accessed in the molecular frame of reference which enables vastly more detailed investigation of the I4*d* photoemission dynamics by assessing it in an angle-resolved manner (e.g. via variation of the coverage or rotation of the substrate).

5.5.3 Absolute photoemission timing of molecular valence states

With the absolute photoemission timing of the iodoalkanes known, they can be used as chronoscope species in further gas-phase measurements. By mixing iodomethane with small molecules (N_2, CO, N_2O, CO_2) in an attosecond streaking experiment the determination of the absolute photoemission times of their valence states comes into reach. Figure 5.24 shows an exemplary spectrogram recorded on a mixture of iodomethane ant CO_2.

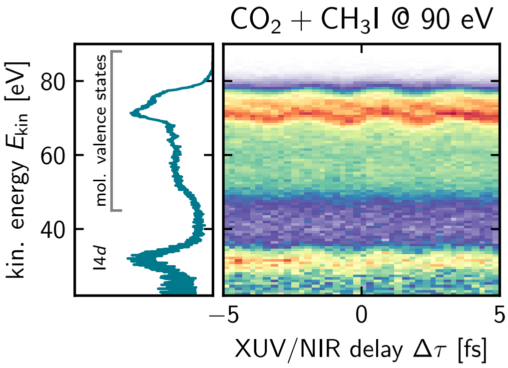

Figure 5.24: Attosecond streaking on a mixture of CO_2 and iodomethane at 90 eV photon energy. With iodomethane as a chronoscope species the absolute photoemission timing of the molecular valence state streaking features may become accessible. Courtesy of Maximilian Pollanka.

The major difficulty of such a study is to disentangle the contributions to the photoelectron signal from the many overlapping molecular valence states. The ptychographic wavepacket reconstruction may prove useful for this task. This experimental effort is led by Maximilian Pollanka.

5.6 Summary

Absolute photoemission times of the I4*d* photoemission in iodomethane, iodoethane, 1-iodopropane, 2-iodopropane 1-iodobutane and 2-iodobutane were measured across the giant resonance in the I4$d \rightarrow \varepsilon f$ photoemission channel at photon energies of 90 eV, 105 eV and 118 eV in un-oriented molecules in the gas-phase. The molecules are partitioned into a structurally rigid class (iodomethane, -ethane and 2-iodopropane) and a class of floppy molecules (1-iodopropane, 1-iodobutane, 2-iodobutane) which qualitatively and quantitatively show very different behaviour of the absolute I4*d* photoemission time delays. For iodoethane at 90 eV we find a different result from what has been published before [25]. By comparison of the experimental results with a recent atomic calculation [115] we find that core level photoemission time delays in a molecule can be altered significantly even by changes in the chemical structure of the molecule more remote to the atom the core level of which is studied, and that differences measured between molecules can be as large as (23 ± 4) as (iodomethane vs. 2-iodopropane at 105 eV). This implies that intra-molecular scattering strongly affects the observed core-level photoemission time delay even at high photon energies and when averaging over all molecular orientations. In the floppy iodoalkanes this effect seems to mostly wash out whereby the atomic calculation is reproduced very well by the experimentally determined absolute photoemission time delays. This enables the evaluation of the giant resonance purely in the time domain from the single-particle scattering model of Connerade [133] which yields a cross section of the resonance in qualitative accord with published experimental data. Overall we find no correlation of the photoemission time delay with the size of the molecule.

The delay differences observed between the different rigid molecules and furthermore the atomic prediction motivate revisiting the procedure of determining absolute photoemission times for the W(110) surface (cf. [18]) and re-estimating the uncertainties. This will be adressed in more detail in section 6.4.3. Overall we made the observation that in some iodoalkanes the I4*d* photoemission times almost exactly coincide across all studied photon energies (cf. the floppy molecules) while they differ between others (cf. 2-iodopropane and iodomethane/-ethane at 105 eV). In that sense not all iodine atoms in the iodoalkanes are equivalent, but some are more equivalent than others.

With the I4*d* photoemission time now known across three photon energies and multiple species each of these can be used as a chronoscope species in subsequent experiments. Due to its high vapor pressure iodomethane is probably the most convenient to use though, and it is already being applied in the study of absolute photoemission time delays on molecular valence states (cf. sec. 5.5.3).

We supplement the reported central photoemission delay times with a wavepacket reconstruction algorithm based on the extended ptychographic iterative engine which yields access to the energy dependence of the photoemission time delay around the central photon energy studied. Pronounced variations between the molecules are found, and even in the floppy iodoalkanes where the central time delays reproduce the atomic calculation some structure seems to survive. At the time of writing a detailed interpretation of these results cannot be given due to the lack of photoionization calculations at a sufficient level of theory, but our results may guide future developements of these methods.

Chapter 6

Attosecond dynamics of solid-state photoemission over a wide range of photon energies

The tungsten (110) surface is the first system on which a photoemission time delay has ever been measured directly [15]. In this groundbreaking experiment the relative time delay between photoelectrons emitted from the W4f states of tungsten and those emitted from the valence states was determined to be (110 ± 70) as. Inspired by this result and by the possibility to investigate solid state photoemission on the attosecond time scale a long-running experimental campaign to assess the energy dependence of the relative W4f-VB time delay was pursued, culminating in the determination of the absolute timing of the photoelectric effect at a photon energy of 105 eV in 2018 [18]. As such, many people have been involved in the experimental effort and the interpretation and their contributions shall be honored here. The project is supervised in its entirety by Reinhard Kienberger. The experiments have been performed by (in alphabetical order) Adrian Cavalieri, Andreas Kim, Ayman Akil, Dyonisios Potamianos, Elisabeth Bothschafter, Florian Blobner, Konrad Hütten, Marcus Ossiander, Martin Schäffer, Maximilian Schnitzenbaumer, Michael Gerl, Michal Jobst, Ralph Ernstorfer, Sebastian Jarosch, Stefan Neppl, and Wolfram Helml. The UHV surface-science beamline AS3 [140] which is the central experimental tool of the study was designed by Thomas Uphues, Ralph Ernstorfer, Elisabeth Magerl, Michael Stanislawski, Stefan Neppl and Peter Feulner. Numerical methods for the calculation of the escape time from the W(110) surface have been developed and applied by Eugene Krasovskii and Roman Kuzian. Jürgen Braun, Hubert Ebert and Jan Minar provided valuable insight in discussions on the topic. Silvano Lizzit, Daniel Lizzit and Luca Bignardi from the Elletra Sincrotrone Trieste supported the effort to obtain high-resolution photoelectron spectra of the W(110) valence band and the 4f states.

The project was advanced significantly with the dissertation of Johann Riemensberger [26] who carefully compiled, supplemented and analyzed the experimental data which also encompasses an experiment on the W(100) surface as well as the oxidized W(110) surface. The experimental apparatus and sample preparation are described in detail there. For the interpretation of the energy-dependence of the measured W4f-VB delay time semiclassical arguments based on the interplay of the localization of the photocurrent below the surface and the transport of the photoelectrons with a group velocity $v_g(\mathbf{k})$ determined from the materials band structure were made, but such models cannot explain the photoemission times observed on solid surfaces from first principles. A full *ab-initio* treatment of time delays in photoemission from surfaces based on the notion of the Eisenbud-Wigner-Smith delay was brought forward by Kuzian and Krasovskii [126] in 2020 and applied to the Mg(0001) photoemission. The realization that this formalism can be applied to solid surfaces, too closes the conceptual gap that has since existed between the understanding of photoemission times in atoms, in molecules and in solid-state systems. Its application to the W(110) surface and the subsequently arising new interpretation of the experimental results of [26] as well as an extension of the existing data analysis is reported upon in this chapter.

6.1 Photoemission timing on condensed matter

The heuristic *three-step picture* of photoemission from solid surfaces (cf. [141] and [8, chap. 1.6.3 and 6.1]) has enjoyed considerable success in the interpretation of static photoemission. It separates the photoemission process into optical excitation, propagation of the excited photoelectrons and finally their traversal of the surface. Due to the mechanistic and intuitive view it offers on the problem it has also become quite popular in the interpretation of photoemission time delays (cf. e.g. [142, 143, 144, 145, 146]). The fundamental flaw with the application of this approach to the interpretation of photoemission times though is that one implicitly assumes a time-ordering of the three steps within the photoemission process when there are no grounds to justify this assumption. A more accurate description that does not require this artificial dissection is one that treats the photoemission process in *one-step* as an optical transition between an initial Bloch state inside the solid and a damped wave exiting the crystal. It was pointed out by G. D. Mahan in a seminal 1970 paper [147] that the problem of determining the outgoing wave is essentially the same as it is encountered in the theory of low-energy electron diffraction (LEED) experiments thoroughly treated by J. B. Pendry [148, 149, 150], but in reverse direction. Consequently the LEED theory was adapted to the problem of photoemission and the final state of photoemission in the one-step picture is today still referred to as *time-reversed LEED state*. An exhaustive overview of the theory of photoemission based on this formalism is given in [151]. Three- and one-step picture are contrasted in figure 6.1.

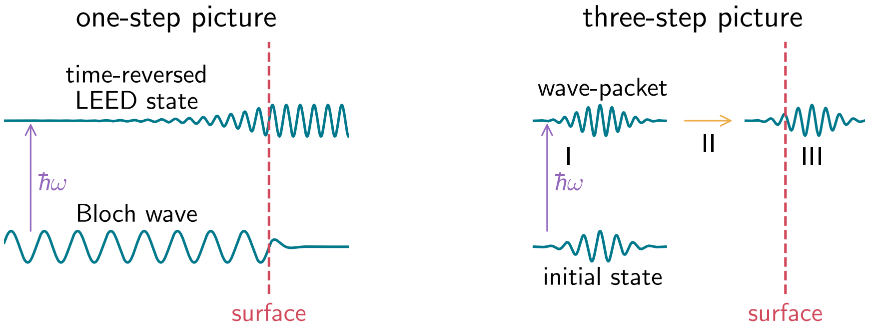

Figure 6.1: Illustration of the one-step picture (left) and three-step picture (right) of photoemission. In the one-step model the optically mediated transition occurs from an initial Bloch wave into a time-reversed LEED state which carries the photocurrent across the surface. Here only the part of the time-reversed LEED state travelling outwards is shown. It is damped inside the solid, the damping being determined by the optical potential $V_i(E_f)$. This damping corresponds to what is also referred to as inelastic mean free path. Within semiclassical considerations it determines the depth from which the photoelectron can be considered to originate. In the three-step model, the optical transition (first step) occurs between an initial effectively localized 'wave packet' inside the solid to a wave packet propagating towards the surface in the second step. The wave packet's traversal of the surface is the third step. Within this mechanistic view of the photoemission process it is of course tempting to apply semiclassical arguments especially to the second transport step.

The groundbreaking 2007 experiment on the W(110) surface [15] was interpreted within the framework of the three-step model in terms of a ballistic photoelectron with kinetic energy E_{kin} originating from about one inelastic mean free path $\lambda(E_{\text{kin}})$ under the surface and propagating outwards with a group velocity $v_\mathrm{g}(E_\mathrm{kin})$ determined by the materials band structure. Inelastic scattering of a photoelectron removes it energetically from the primary photoemission feature whereby it does not contribute to the photoemission timing signal. Early theoretical treatments of the problem within semiclassical transport theory [145] and a 1D quantum model [152] went along the same general line of arguments. Experimental support for the ballistic picture of photoemission time delays was provided in a key experiment [83] on adlayers of Mg(0001) epitactically grown on the W(110) surface.

That the idea of the photoelectrons being emitted from a depth of about $\lambda(E_\mathrm{kin})$ and travelling with a velocity $v_\mathrm{g}(E_\mathrm{kin})$, entering the streaking field which measures their timing at $\tau_\mathrm{esc.}(E_\mathrm{kin}) = \lambda(E_\mathrm{kin})/v_\mathrm{g}(E_\mathrm{kin})$ after their initial excitation is not necessarily incorrect was shown in [153]. However, this semiclassical picture only holds far away from strong variations in the optical transition probability with the final state energy (e.g. due to energy gaps) and when scattering of the electron off the lattice is weak. If that is the case the escape time reduces to

$$\tau_\mathrm{esc.}(E_\mathrm{kin}) = \frac{1}{2V_i(E_\mathrm{kin})}, \tag{6.1}$$

with $V_i(E)$ being the optical potential responsible for damping the outgoing photoelectron's wave function inside the crystal. More commonly referred to than the optical potential is the inelastic mean free path (IMFP)

$$\lambda(E_\mathrm{kin}) = \frac{1}{2}\frac{\sqrt{2E_\mathrm{kin}}}{V_i(E_\mathrm{kin})}. \tag{6.2}$$

Values for $\lambda(E_\mathrm{kin})$ determined with calculations based on a method developed by Penn which involve a model dielectric function ([154] and [155] for a more recent description) have been tabulated for many materials over a wide range of kinetic energies (cf. [156] and an extensive series of papers on the topic by the same authors referenced therein), but these results are prone to substantial uncertainties for slow electrons ($E_\mathrm{kin} < 50\,\mathrm{eV}$) and moderate uncertainties at higher energies. In the energy range of interest in attosecond streaking spectroscopy (electron kinetic energies between 20 eV and 150 eV) the inelastic mean free path (or $V_i(E)$, respectively) must be determined by different means.

The optical potential typically varies slowly with the final state energy E_f, vanishing at $E_\mathrm{f} = 0\,\mathrm{eV}$ and assuming typical values of some $2-4\,\mathrm{eV}$ at $E_\mathrm{f} = 100\,\mathrm{eV}$ [153]. An estimation for the variation of $V_i(E)$ with the final state energy is given in [150] as $V_i(E_\mathrm{f}) \propto E_\mathrm{f}^{3/4}$. With this dependency and published values for $V_i(E)$ for various materials [157, 158, 159, 160, 153] one can obtain an estimate of the inelastic mean free path (inset in fig. 6.2, top panel) and the semiclassical escape time eq. 6.1 (fig. 6.2, lower panel). It decreases slowly with increasing final state energy, and for valence band photoemission where the binding energy is small one finds escape times of about 50 as to 70 as in the photon energy range accessed by attosecond streaking (100 – 150 eV). The escape times in fig. 6.2 do not match absolute photoemission times for the W(110) valence states and $4f$ states determined in the experiment. The relative delay is also not reproduced well (inset in fig. 6.2). This indicates that the semiclassical approach cannot describe the photoemission dynamics of the W(110) surface, and a more sophisticated model is called for.

6.1.1 Eisenbud-Wigner-Smith delay times in condensed matter photoemission

That the concept of EWS time delays can be carried over to photoemission from surfaces is not straightforward. Firstly, inelastic scattering (implemented via the optical potential $V_i(E_\mathrm{f})$ in the time-reversed LEED formalism) absorbs electrons inside the crystal whereby the probability current is not conserved as it was the case in the derivation of eq. 4.6. Secondly, the asymptotics of the scattered wave (i.e. the photoemitted electron) is not the same as for the reference wave as free propagation only occurs above the surface, although a similar problem is encountered in atomic photoemission

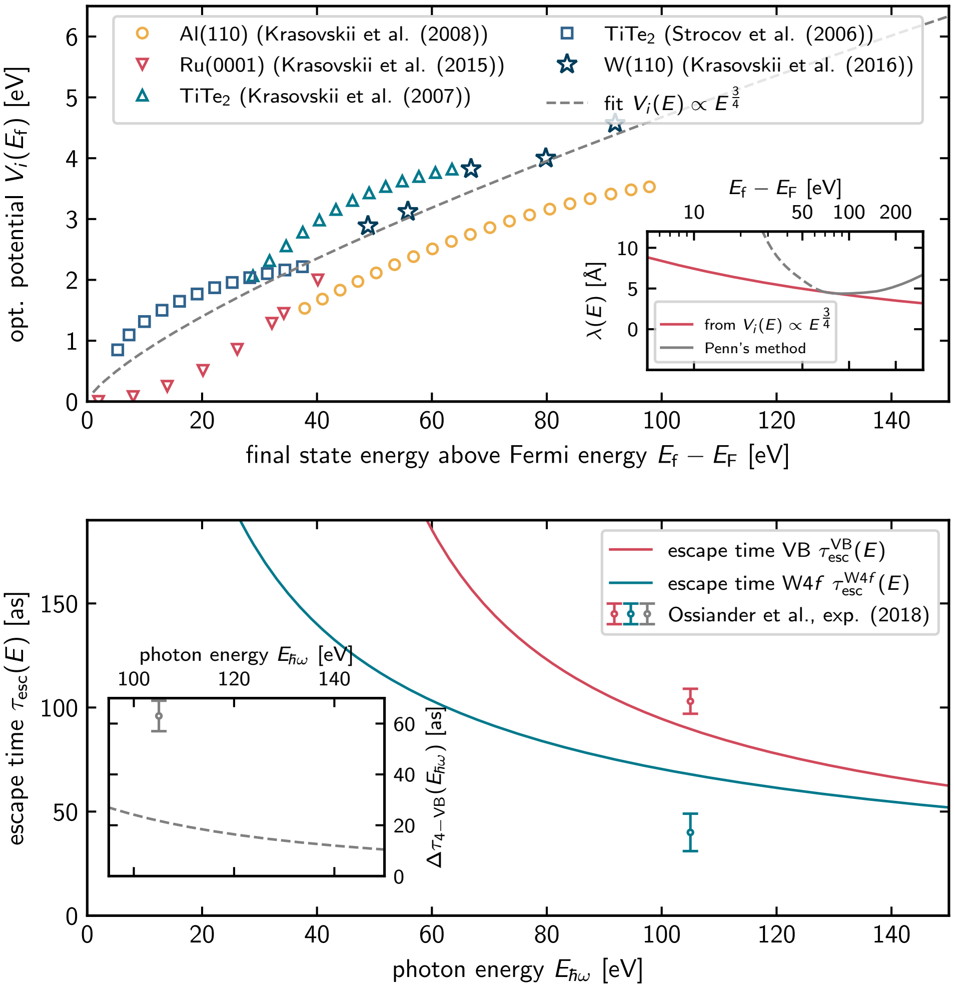

Figure 6.2: Following [150, p. 2285], the optical potential varies as $E_f^{3/4}$ with the final state energy. The top panel shows an analytical fit of this dependency to values for the optical potential determined for various materials, including W(110) [157, 158, 159, 160, 153]. The result for W(110) presented in [153] is reproduced well. The inset shows in red the IMFP calculated from the optical potential as well as a calculation with Penn's method from optical data [119, 161]. Penn's method is expected to be quite inaccurate for slow electrons ($< 50\,$eV) and the IMFP in this region is therefore shown as a dashed line. For electrons around $100 - 140\,$eV both IMFPs agree rather well with $\lambda(E) \sim 1 - 5\,$Å. With $V_i(E) \propto E^{3/4}$ equation 6.1 pedicts a monotonously decreasing semiclassical escape time (bottom panel). It is here plotted vor valence photoemission (negligible binding energy) and for the $4f$ states of the W(110) surface bound at $E_{\rm bin} = 32.5\,$eV. The stark disagreement with experimental results in the absolute delays as well as the relative delays (inset) by Ossiander et al. [18] is indicative of the inapplicability of the semiclassical model to the W(110) photoemission. As it will be seen later, the general trend of the relative photoemission time is predicted correctly by eq. 6.1, but strong lattice scattering and a gap-like feature in the final state band structure cause substantial deviations from the semiclassical result.

(recall figs. 4.2, 4.1 and 4.3 where the scattered and the reference wave share their asymptotics in the infinitely distant past and future, while the photoemitted wave only experiences 'half' the potential). Kuzian and Krasovskii showed [126] that the Wigner time delay formula

$$\tau_{i\to f}(E_\mathrm{f}) = \frac{\partial \eta_{i\to f}(E_\mathrm{f})}{\partial E_\mathrm{f}}, \tag{6.3}$$

with $\eta_{i\to f}(E_\mathrm{f})$ being the phase of the optical transition matrix element

$$\mathcal{M}_{i\to f}(E_\mathrm{f}) = \left\langle \Phi^*_{E_\mathrm{f}}(\mathbf{x}) \left| \mathbf{p}\cdot\mathbf{A}(\mathbf{x},t) + \mathbf{A}(\mathbf{x},t)\cdot\mathbf{p} \right| \Psi_i(\mathbf{x}) \right\rangle \tag{6.4}$$

associated with the transition from initial state Ψ_i to the time-reversed LEED state $\Phi^*_{E_\mathrm{f}}(\mathbf{x})$, holds for photoemission from the semi-infinite crystal. In eq. 6.4 $\mathbf{p}$ is the momentum operator and $\mathbf{A}(\mathbf{x},t)$ is the vector potential of the XUV light when the photoemitted wave packet (and therefore the XUV excitation) is very narrow in energy. Owing to the large bandwidth of the XUV pulse required to warrant its sub-femtosecond duration the photoexcited wavepackets will not be very narrow in energy, and equivalence of EWS time delays calculated via eq. 6.3 cannot be guaranteed, although in experience it holds.

6.1.2 Attosecond streaking on surfaces

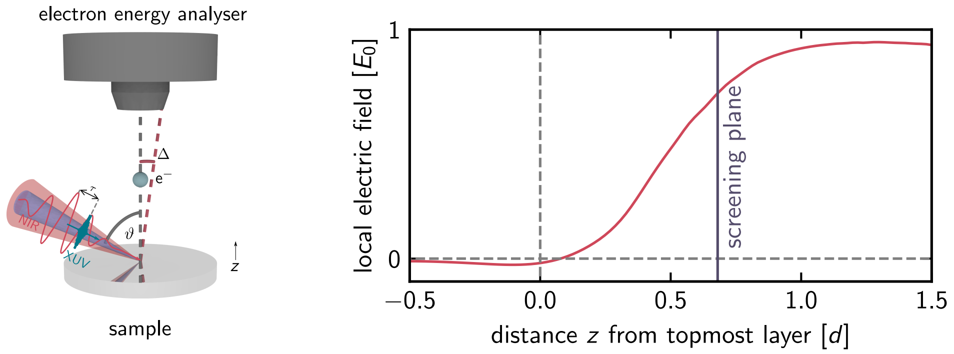

Figure 6.3: Attosecond streaking on a metal surface. Both XUV and NIR pulse are *p*-polarized, photoelectrons are collected from a cone with opening angle Δ oriented along the surface normal. The angle of incidence for XUV and NIR is 70°. The streaking field's normal component is screened strongly at the surface ([83] and its supplementary information). Here it is shown for W(110) in units of its maximal value E_0 versus the position z respective to the surface, measured in units of the interlayer spacing d. The plane of dynamical screening is located 67% of a layer spacing above the topmost atomic layer. It is this plane with respect to which attosecond streaking measures the escape time of the photoelectrons.

In the standard geometry for attosecond streaking spectroscopy on surfaces (fig. 6.3) the NIR and XUV are both *p*-polarized. The normal component of the streaking laser field is strongly suppressed below the metal surface [83], whereby the photoelectrons are only exposed to the streaking field once they have passed the screening plane (purple line in fig. 6.3). The position of this screening plane was determined in [83] to be roughly $0.7d$ (d is the interlayer spacing of the W(110) surface) above the topmost atomic layer from a 1D time-dependent density functional (TDDFT) calculation, mostly independent from the metal under study. It is important to note though that this finding does not generalize to attosecond streaking on non-metals where the penetration of the NIR field into the solid must be taken into account (cf. e.g. [162]).

Photoelectons are collected along the surface normal from a cone with opening angle Δ. An experimental difficulty encountered in attosecond streaking on surfaces is that due to the typically low repitition rate of the laser source (some 1–4 kHz) and the need to keep the XUV flux low enough as to minimize space-charge effects measurement times can be come unfeasibly low when choosing a small acceptance angle Δ. For this reason the TOF spectrometer in use at the AS3 beamline is equipped with an electrostatic lens system with which the acceptance cone can be increased from ±2° to ±22°. While the resulting increase of the photoelectron count rate is beneficial to the experiment, on single-crystal surfaces the resulting averaging over the complete angular distribution of the photoemitted electrons may be problematic. While an angular dependency of the photoemission time delay from metal surfaces has been observed at low photon energies (e.g. [142, 163]) and a variation of the EWS time delay has been predicted via calculation even at high photon energies [126], this effect seems to be not particularly relevant in attosecond streaking as it has been found in [81] and will later be seen in sec. 6.3.1 with regard to this study. In any case, whether or not the angular averaging due to the increased collection angle affects the observed photoemission time delays must be tested in each study anew.

Measuring photoemission time delays at metal surfaces

A connection between the time delay τ_{streak} measured by attosecond streaking and the EWS time delay (eq. 6.3) must be established. The Coulomb-laser-coupling delay (eq. 4.24) which is to be taken into account when interpreting photoemission times observed in molecules and atoms can be neglected in photoemission from metal surfaces as it amounts to low single-digit attoseconds at most for photoelectron kinetic energies above 50 eV (cf. sec. 4.2.3 and fig. 4.6). Absolute and total photoemission times determined at metal surfaces therefore coincide. The equivalence of streaking time delay and escape time (i.e. the time at which the photoelectron traverses the surface barrier) and later the equivalence of streaking time delay and EWS time has been shown by Krasovskii et al. and by Kuzian and Krasovskii in [153] and [126] to hold far from regions where the transition probability varies strongly with the final state energy. In the absense of such a modulation the photoexcited wave packet is spatially compressed and traverses the surface very quickly. In consequence it is exposed to the streaking field in its entirety (left panel in fig. 6.4) almost instantaneously when crossing the surface. In the vicinity of an intensity minimum or variation on the other hand the outgoing wave packet assumes a complex shape and larger spatial extent. Therefore, when traversing the surface a part of it is exposed to the streaking field before the entire packet has left the crystal (right panel of fig. 6.4). The timing information encoded in the spectrogram is then distorted and deviations of the streaking time from the EWS or escape time are to be expected. A more detailed depiction of this situation is given in fig. 3 of [153]. In summary though, we can expect the EWS time delay and the time delay determined via attosecond streaking to be in agreement, save for a situation where the final state is in a region of the conducting band structure where the transition probability varies substantially with energy.

6.2 The static W(110) photoemission

A brief summary of the photoemission features of the W(110) surface relevant to the timing experiment is given in this section. For a more detailed account the reader shall be referred to [26, chap. 4] and references therein. The $4f$ states of tungsten are spin-orbit split into a $4f_{\frac{5}{2}}$ and a $4f_{\frac{7}{2}}$ component bound at 33.6 eV and 31.4 eV respectively [164]. Each of these is accompanied by a surface-shifted replica at smaller binding energy (cf. [8, chap. 8.4]). The valence band photoemission can be partitioned into being due to emission from a band with sp-character at binding energies exceeding 5 eV, and a band due to the W5d electrons at binding energies between 3 eV and the Fermi energy. It is the latter that makes up the major contribution to the VB photoelectron signal in our energy range

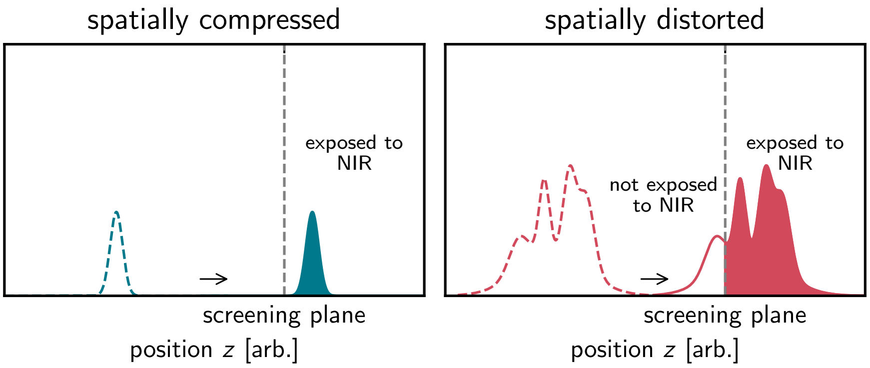

Figure 6.4: Illustration of a snapthot in time when a spatially compressed (left) and a distorted (right) wave packet traverse the screening plane. While the compressed wave packet essentially traverses the surface in one go and is quickly exposed to the NIR streaking field in its entirety this is not the case for a distorted wave packet. Due to its large spatial extent a significant portion of the wave packet is still below the surface and screened while the part that has traversed the surface is already exposed to the streaking field. A depiction based on a calculation for a 1D crystal is given in [153].

of interest. High resolution spectrograms of the W4f and VB region are shown in fig. 6.5 in the top panels, recorded at Elletra Sincrotrone Trieste by Johann Riemensberger and Peter Feulner. Especially notable is the *spoon-like* shape the 5d-band photoemission traces out as a function of photon energy.

The photoemission timing experiment was carried with attosecond pulses centered at photon energies of 103.1 eV, 110.1 eV, 117.1 eV, 124.4 eV, 133.7 eV and 145.0 eV. The XUV reflectors employed have FWHM bandwidths of 4.6 eV, 3.5 eV, 4.0 eV, 4.8 eV, 4.0 eV and 3.5 eV, respectively [26, chap. 4]. Additional measurements at 92.5 eV are also presented in [26], but a subsequent experimental characterizetion of the corresponding XUV multilayer reflector (see appendix E) revealed that it is prone to generating satellite XUV pulses which hamper the proper extraction of timing information and therefore call the results at 92.5 eV into question. The time delays measured at this energy are therefore excluded from the discussion. XUV-only spectra of the W(110) surface measured with isolated attosecond pulses are shown in the lower panels of fig. 6.5. Due to the large bandwidth of the XUV pulses the detailed structure of the W(110) photoemission (e.g. the splitting of the W4f states) is not resolved.

6.3 Measuring relative photoemission timing

The key observable in this experiment is the relative photoemission time $\tau_{\mathrm{W}4f-\mathrm{VB}}$ measured between the W4f states and the valence photoemission. First time delays at the energetic center of the respective wave packets are reported, then the analysis is extended towards a wave packet reconstruction with the extended ptychographic iterative engine. As the W5d states dominate the valence band photoelectron signal and the lower lying sp-band contributes negligibly all discussions pertaining the valence band refer to the 5d states unless noted otherwise. Exemplary streaking spectrograms are shown in fig. 6.6. Characteristic of the substantially higher atomic density of solid samples with respect to the gas phase is the larger photoelectron count rate. Therefore the streaking spectrograms shown here are substantially less noisy than spectrograms recorded in the gas phase (cf. fig. 5.11 and 5.4).

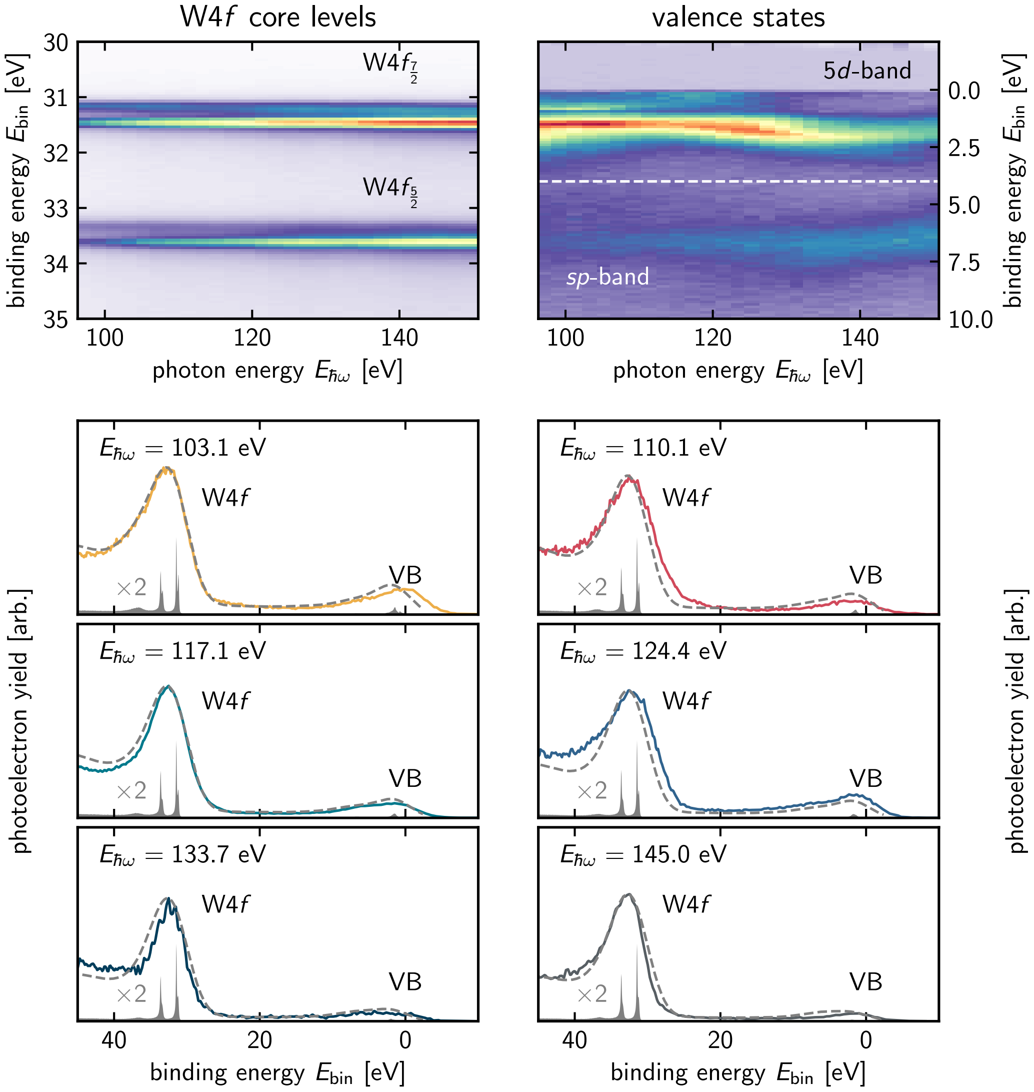

Figure 6.5: Static photoelectron spectra of the W(110) surface. The top panels show high resolution spectrograms of the W4f core-level photoemission (left) and the valence state photoemission (right) for photon energies between 96 eV and 150 eV. The 4f core-level photoemission is spin-orbit split into a $4f_{\frac{5}{2}}$ and a $4f_{\frac{7}{2}}$ component each of which is accompanied by a surface-shifted satellite at smaller binding energies. The valence band photoemission is dominated by the 5d band. A band with sp-character is found at larger binding energies, but it is quite weak an does not significantly contribute to the photoelectron signal in the attosecond experiment. The lower panels show lineouts of the high resolution spectrograms at the photon energies accesible to the attosecond experiment (colored lines). Due to the large bandwidth of the isolated attosecond pulses the fine structure of the spectra is not resolved. Good agreement with a convolution of the high resolution spectra with a 5 eV Gaussian is found, confirming that the spectra recorded with isolated attosecond pulses reflect the W(110) photoemission well.

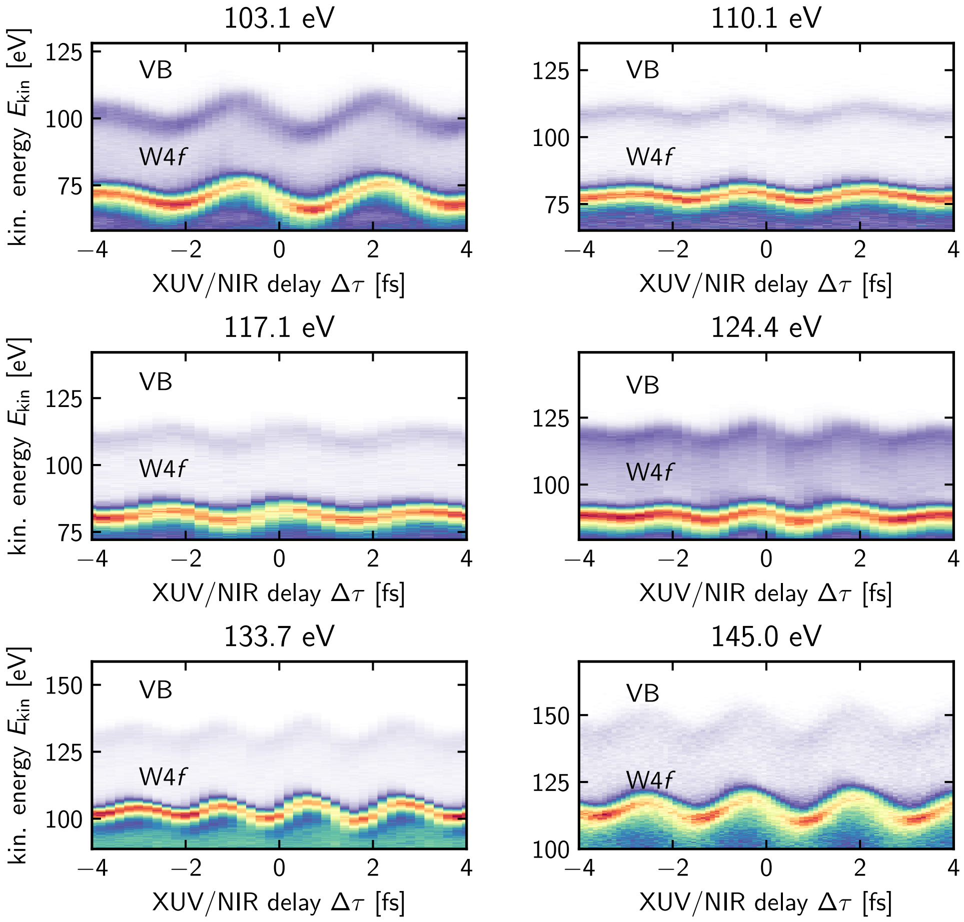

Figure 6.6: Exemplary streaking measurements on W(110).

6.3.1 Central time delays

Central photoemission times are reproduced from [26, chap. 4.3] and were determined with the diff. rTDSE method. In the delay extraction procedure the W4f photoemission feature is represented as being comprised of the two $4f_{\frac{5}{2}}$ and $4f_{\frac{7}{2}}$ components and a very small contribution (~ 10%) from the W5p photoemission. The valence band photoemission is modelled as comprised of ten individual contributions modelled to closely resemble the shape of the observed VB feature in the streaking experiment. Statistics are summarized in fig. 6.7, central delays are summarized in table 6.1 at the end of this section.

Effect of angular integration in the central delays

In order to gauge whether the the increase of the acceptance angle of the detector has an influence on the delay observed with attosecond streaking the central delays of a subset of spectrograms recorded with the detector's lens system switched off at photon energies of 110.1 eV, 124.4 eV and 133.7 eV is reevaluated with the diff. rTDSE method. Statistics are shown in fig. 6.8, a summary is given in table 6.1. The differences between the delay determined from the spectrograms recorded without lens and the whole ensemble of spectrograms are below the respective uncertainties except for 110.1 eV, where we find a difference of (14.1 ± 8.3) as to the result obtained for the entire set of spectrograms at this photon energy. Even though the diff. rTDSE results differ slightly at this photon energy, agreement with the value determined with the ptychographic spectrogram inversion algorithm (see sec. 6.3.2) is

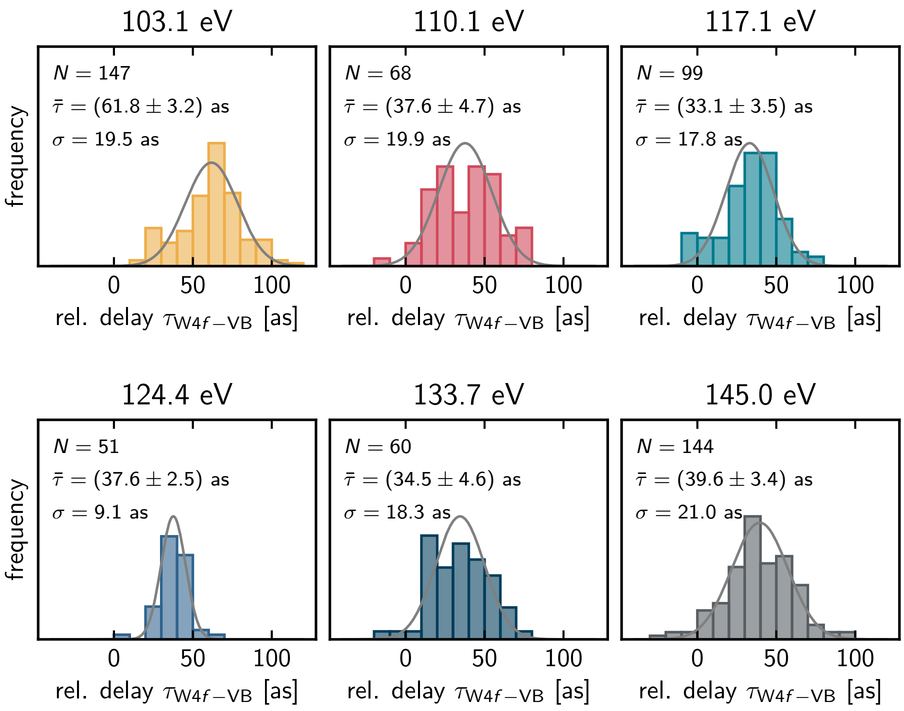

Figure 6.7: Statistics of the W(110) photoemission timing experiment. In excess of 50 scans were recorded at any photon energy.

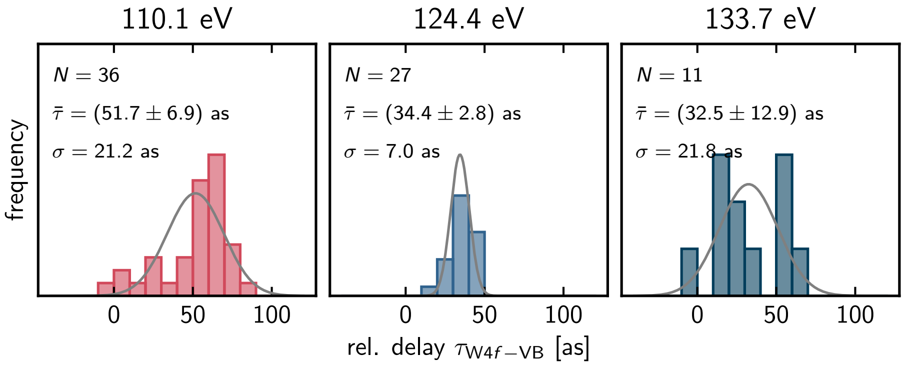

Figure 6.8: Statistics of the subset of measurements taken with a small acceptance cone of approx. ±2°.

found within its uncertainties. It can therefore be surmised that the effect of angular integration of the photoelectron yield in this experiment may be neglected.

6.3.2 Ptychographic delay extraction

The ptychographic spectrogram inversion algorithm is configured to retrieve one 'wave packet' for the valence band photoemission and one 'wave packet' for the W4f photoemission. Both of these photoemission features are incoherent averages of the split 4f states or the many states comprising the 5d band which contribute to the signal. Just as in chap. 5 the ptychographic method therefore reconstructs effective 'wave packets' from which time-energy information is inferred. Figure 6.9 summarizes the results.

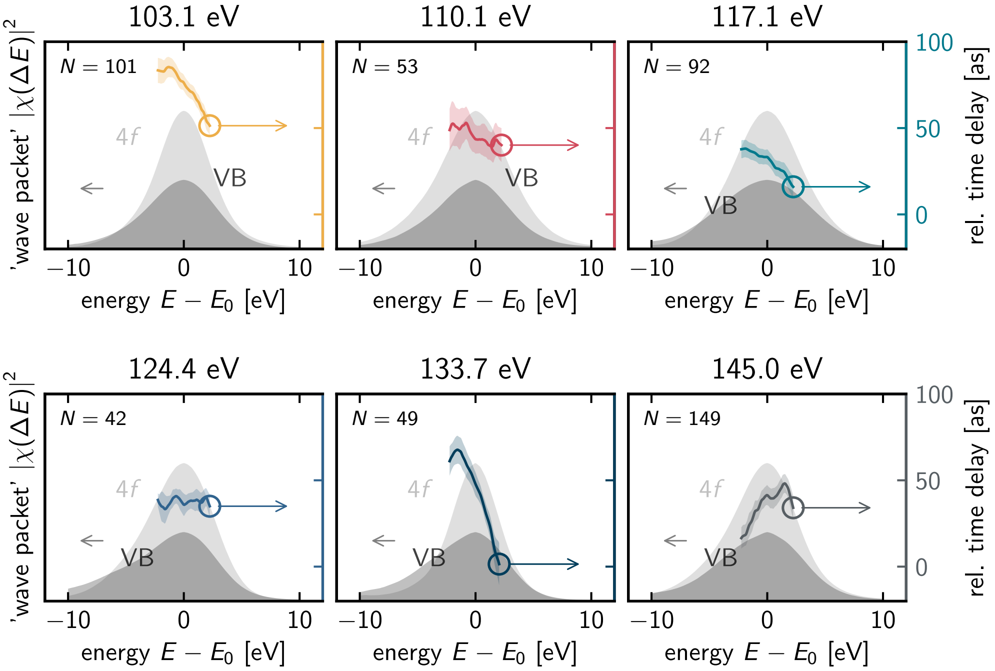

Figure 6.9: Application of the extended ptychographic iterative engine to the W(110) photoemission timing. Reconstructed 'wave packets' for W4f and VB photoemission are shown in light gray and gray respectively. The photoemission times are determined as the average of all processed scans at a particular energy and are shown as colored lines with shaded areas indicating uncertainties (95% confidence interval). As the ePIE does not converge for all scans to which it is applied the sample sizes N given in the top left corner of each plot differ from those in fig. 6.7.

Strikingly, a strong energy dependence of the relative photoemission time is revealed. The central delays obtained with the diff. rTDSE method and the relative delays at the energetic center of the VB and W4f 'wave packets' are in good agreement as seen from table 6.1.

Table 6.1: Relative central photoemission times $\Delta\tau_{\mathrm{W}4f-\mathrm{VB}}$.

photon energy	103.1 eV	110.1 eV	117.1 eV
diff. rTDSE $\Delta\tau_{\mathrm{W}4f-\mathrm{VB}}$	(61.8 ± 3.2) as	(37.6 ± 4.7) as	(33.1 ± 3.5) as
diff. rTDSE $\Delta\tau_{\mathrm{W}4f-\mathrm{VB}}$ (no lens)	–	(51.7 ± 6.9) as	–
ePIE $\Delta\tau^{\mathrm{c}}_{\mathrm{W}4f-\mathrm{VB}}$	(76.2 ± 4.6) as	(43.6 ± 8.4) as	(33.2 ± 4.4) as
one-step EWS $\Delta\tau^{\mathrm{calc}}_{\mathrm{W}4f-\mathrm{W}5d}$	65.0 as	51.1 as	19.8 as

photon energy	124.4 eV	133.7 eV	145.0 eV
diff. rTDSE $\Delta\tau_{\mathrm{W}4f-\mathrm{VB}}$	(37.6 ± 2.5) as	(34.5 ± 4.6) as	(39.6 ± 3.4) as,
diff. rTDSE $\Delta\tau_{\mathrm{W}4f-\mathrm{VB}}$ (no lens)	(34.4 ± 2.8) as	(32.5 ± 12.9) as	–
ePIE $\Delta\tau^{\mathrm{c}}_{\mathrm{W}4f-\mathrm{VB}}$	(35.9 ± 6.4) as	(47.8 ± 6.8) as	(41.4 ± 5.7) as
one-step EWS $\Delta\tau^{\mathrm{calc}}_{\mathrm{W}4f-\mathrm{W}5d}$	19.1 as	40.1 as	19.6 as

6.4 Discussion

The experimental results are contrasted with the one-step EWS calculation for photoemission along the surface normal by E. E. Krasovskii in fig. 6.10. The EWS time delays calculated for each individual transition $i \to f$ have been averaged, weighed by the photocurrent each respective transition carries. The calculation predicts a strong and irregular variation of the relative photoemission time with the excitation energy, generally in agreement with the diff. rTDSE result. The experimental ePIE result matches the slope of the calculation except for at 103.1 eV and 133.7 eV. A gray star in fig. 6.10 indicates the original result by Cavalieri et al. [15], but due to its large uncertainties no statement about whether it is in (qualitative) agreement with the calculation or not can be made. However, at the lower end of its error bar it is close to the calculated relative time delay. The semiclassical escape

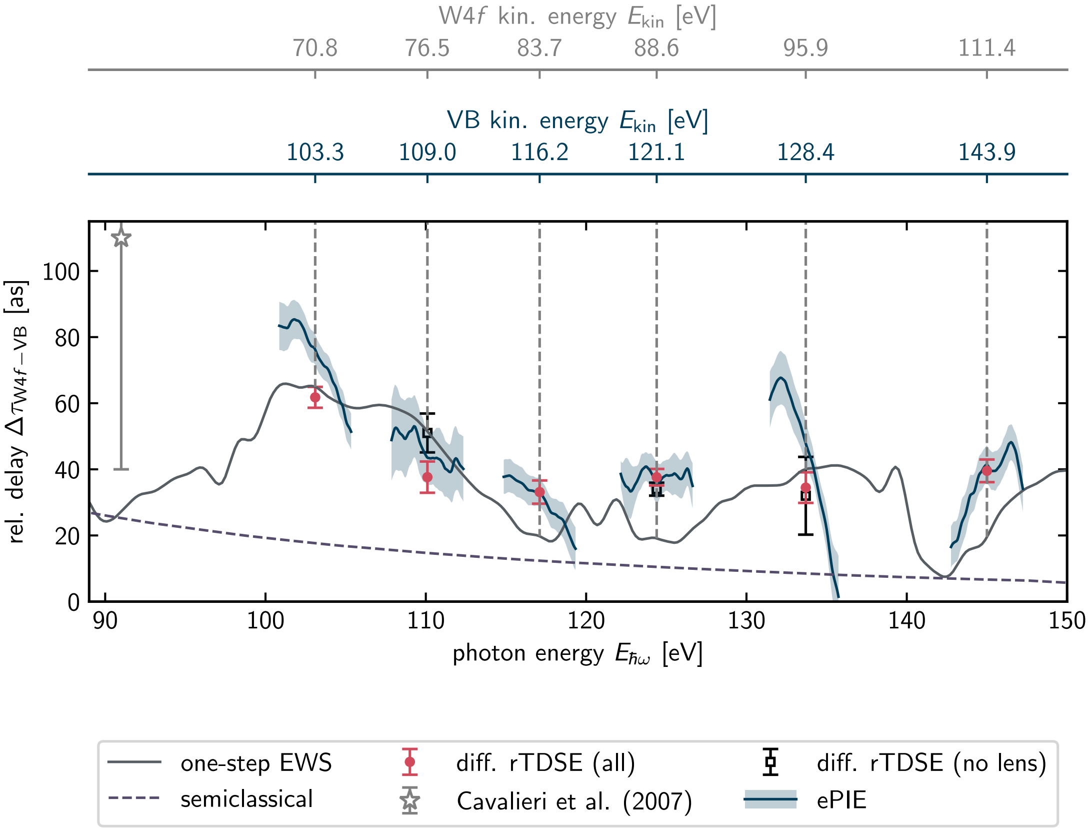

Figure 6.10: Relative W4f-VB photoemission time delays at the W(110) surface. The one-step EWS calculation by E. E. Krasovskii is shown as a gray line, the relative semiclassical esccape time (cf. eq. 6.1) is sown as a dashed line. A gray star indicates the measurement by Cavalieri et al. [15]. Red datapoints are the diff. rTDSE results, black datapoints are the diff. rTDSE results for the subset of the data recorded with a small acceptance angle. Blue lines show the ePIE results with shaded areas indicating the uncertainties. The 95% confidence interval is reported as the uncertainty. All experimental analysis methods are in agreement within their respective uncertainties. The calculation agrees with the experimental results well. Especially notable is that the ePIE result reproduces the slope of the calculated delay at all energies except for 103.1 eV and 133.7 eV. The kinetic energy of the 4f and VB photoelectrons at a given photon energy are indicated by the axes above the graph.

time difference (eq. 6.1, dashed line in fig. 6.10) cannot account for the complicated behaviour of the photoemission times which indicates that the assumptions under which it is expected to be a reasonable approximation – weak lattice scattering and no stark variation of the transition probability with the final state energy – are violated.

6.4.1 Photoemission time delays near strong variations of the transition probability

As pointed out in sec. 6.1.2 the EWS time delay and the time delay determined via attosecond streaking is expexted to *not* coincide in regions of the final state band structure where the transition probability varies strongly with the final state energy. Inspecting the conducting final state band structure of the W(110) surface (see fig. 6.11) one finds the main conducting branch of the band structure to split into two – an 'upper branch' and a 'lower branch' – around a final state energy of 100 eV. Photoelectrons emitted from the valence states coincide with this region of the final state band structure at an excitation energy of about 105 eV while for electrons emitted from the W4f states this is the case for excitation around 135 eV. It is exactly at these photon energies that one observes a

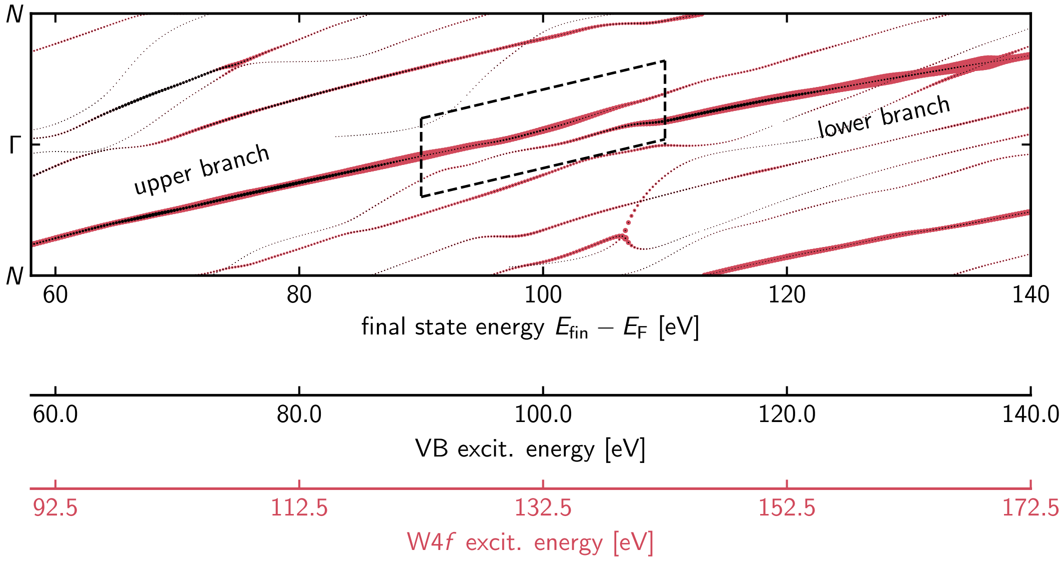

Figure 6.11: Final state band structure of the W(110) surface for normal emission ($\Gamma - N$), in black for the W4f and in red for the W5d states. The thickness of the curve indicates the contribution to the photocurrent. Around a final state energy of 100 eV (marked by dashed box) the main branch of the conducting band structure splits into an 'upper branch' and a 'lower branch'. While the portion of the photocurrent that the lower 'upper branch' carries decreases with increasing photon energy, that of the 'lower branch' increases such that no substantial variation of the static photoelectron signal (cf. fig. 6.5) can be observed. The accompanying variation of the transition probability with the final state energy, however constitutes a situation where the outgoing photoelectron wave packet may be strongly distorted and a deviation of the streaking time delay from the EWS time delay can be expected (cf. sec. 6.1.2). As indicated by the abscissae below the graph the photoelectrons photoemitted from the VB states coincide with this peculiar feature of the final state band structure at excitation energies arount 105 eV, while the W4f photoelectrons coincide with it when excited with photon around 135 eV – exactly the two photon energies for which the experimentally determined slope of the photoemission time delay strongly deviates from the EWS calculation. Furthermore, the large positive excursions of the EWS delay (and the experimental diff. rTDSE results) are indicative of the importance of strong coherent lattice scattering in this energy region. Data supplied by E. E. Krasovskii.

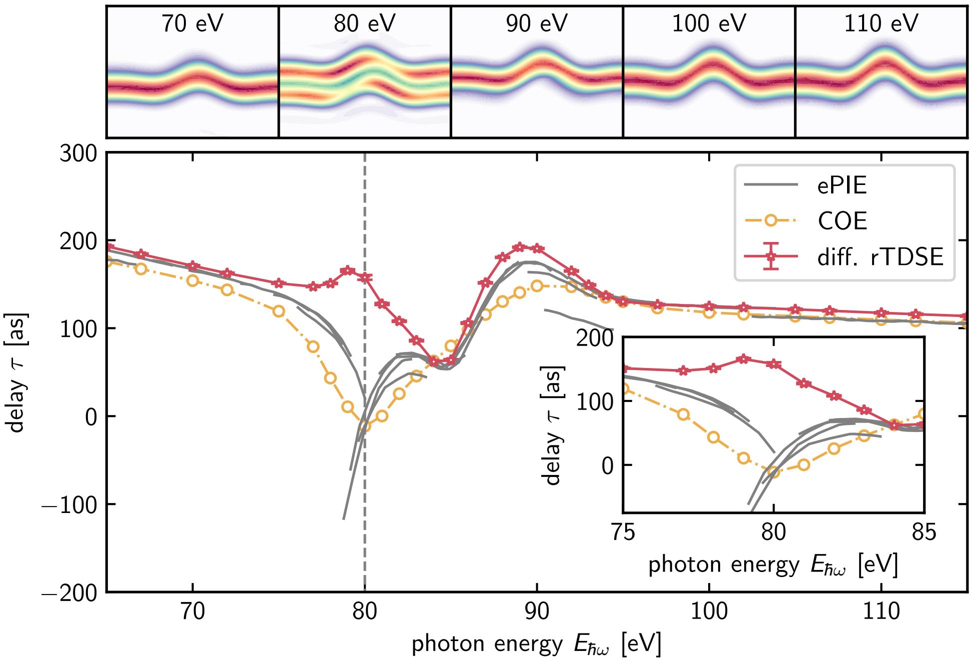

Figure 6.12: Re-evaluation of the numerical streaking experiment of ref. [153] via a center-of-energy (COE) fit, ePIE and the diff. rTDSE method. In the COE analysis a sinusoidal carrier with a gaussian envelope is fitted to the energetic first moment of the spectra comprising the calculated spectrogram. A striking difference between the results reported by the three methods around the gap energy at 80 eV is immediately apparent. For the diff. rTDSE method we attribute this to the spectrogram essentially decomposing into two traces on-gap (top panel). The ePIE result behaves similarly to the COE result, but the algorithm retrieves a strongly sloped energy dependence of the delay, reminiscent of the behaviour observed in experiment when the final state coincides with the 'branch splitting' around 100 eV above the Fermi energy (cf. figs. 6.10 and 6.11). Far from the modulation of the transition probability caused by the energy gap in the numerical experiment all three methods are in almost perfect accord. The inset shows a zoom-in on the region around the gap-energy. Calculated spectrograms have been supplied by E. E. Krasovskii and are shown in the top panel for selected energies.

distinct mismatch of the slope of the relative photoemission time predicted by the calculation and as determined via ePIE. Furthermore, large positive excursions from the semiclassical escape time are found in the relative photoemission times at these energies (fig. 6.10), highlighting the importance of coherent multiple scattering of the outgoing electron off the crystal lattice around these energies.

A more thorough investigation of the dynamics of the excited photoelectron wave packet in the streaking field as it traversed the surface is of course wished for, but not computationally feasible at the moment. In order to plausibilize that around a region of strong variation of the transition probability the delay determined via attosecond streaking spectroscopy shows a peculiar behaviour a numerical streaking experiment on a 1D-Kronig-Penney crystal originally reported in [153] is re-evaluated. A convenient feature of a numerical experiment is that the time-zero is accurately known whereby any reported delay can be seen as a total photoemission delay time. The 1D Kronig-Penney crystal exhibits an energy gap in its final state spectrum which is hit by the photoemission from a pseudo core-level bound at 41.2 eV at an excitation energy of ~ 80 eV. The photoemission dynamics of this pseudo core-level in the vicinity of the true energy gap of the Kronig-Penney crystal is now compared with the photoemission dynamics observed around the gap-like structure associated with the switching of the photocurrent from the 'upper branch' to the 'lower branch' encountered in the final state band structure of the W(110) surface.

In the original publication [153] the streaking delay is determined via a fit of a NIR waveform to the center-of-energy (COE) of the spectra comprising a spectrogram. The results of the COE analysis are shown in fig. 6.12 as yellow data points. We extend the analysis by furthermore applying the diff. rTDSE method and the ePIE to the calculated spectrograms which were supplied by E. E. Krasovskii. The results of the delay analysis are summarized in fig. 6.12 where the extracted delays are shown in the lower panel and calculated spectrograms at selected energies are shown in the upper panel. Characteristic of the strongly diminished photoelectron signal around a true energy gap is that the spectrogram calculated for $E_{\hbar\omega} = 80$ eV almost decomposes into two streaking traces. This poses a problem for the diff. rTDSE method which is not configured to handle such a situation. The ePIE and COE on the other hand are agnostic to the shape of the photoelectron spectrum and therefore do not have this problem. Their behaviour is also qualitatively similar in the vicinity of the gap. Notable is though that the ePIE reports an exaggerated slope on-gap which is qualitatively consistent with the experimental results when the photoemission of the VB or W4f hits the gap-like feature, i.e. around 103.1 eV and around 133.7 eV for the W4f states.

Noteworthy is that except for energies very close to the gap all ePIE results overlap. This demonstrates that the ePIE is in fact capable of resolving photoemission dynamics in a region around the central photon energy under study. An attosecond streaking measurement performed at a certain photon energy with broadband XUV optics can therefore substitute for measurements at photon energies within the XUV bandwidth. In order to generate most reliable results though one should choose central energies and bandwidths such that some energetic overlap between adjacent measurements is guaranteed as a 'sanity check' of the ePIE results.

Unfortunately, a calculation of the EWS escape time for the particular 1D Kronig-Penney crystal evaluated here is not available at the time of writing, so the deviations between the one-step EWS calculations and the COE streaking delay reported in [126] shall be taken as representative of the problem. However, the difficulties of relating the streaking delay extracted from a spectrogram to the EWS delay around a region of strongly varying transition probability (even though it may not influence the photoemission signal strength significantly as it is the case in the experiment) is illustrated well by the mismatch of the results reported by the three applied methods shown in fig. 6.12.

6.4.2 Position of the screening plane

In the one-step EWS calculation the photoemission time is defined with respect to a reference plane which can be positioned at an arbitrary positive distance from the topmost atomic layer. A shift of this reference plane will change the absolute escape times, but leave the relative escape times essentially unaffected. In the context of an attosecond streaking experiment the natural position of this reference plane is the position of the screening plane of the NIR field (cf. fig. 6.3) as this is the position where the streaking field measures the photoelectrons' timing.

We vary the position of the reference plane and compare the predicted escape times to the published absolute photoemission times determined by Ossiander et al. [18]. At 105 eV an absolute time delay of $\tau_{\mathrm{W}4f} = (103 \pm 6)$ as and $\tau_{\mathrm{VB}} = (40 \pm 9)$ as were found for the W4f emission and the VB emission respectively. Best simulaneous agreement for the calculated escape times with the experimentally determined absolute values is reached for a distance $z_{\mathrm{sc}} = 3\,\mathrm{a.u.} \approx 1.6\,\text{Å}$ of the reference plane above the topmost layer of tungsten atoms (see fig. 6.13), with a discrepancy of about ±0.5 Å between the values for the 4f and the VB. The reference plane displacement from the topmost layer of atoms amounts to about 70% of the interlayer spacing $d = 2.24\,\text{Å}$ of the W(110) crystal. This is in very close agreement with the screening plane position found in [83], where a value of $0.67d$ was determined. It should be noted though that the calculated relative delays agree with the experiment best when the reference plane is positioned 5.1 Å above the topmost layer, as it is in the calculation

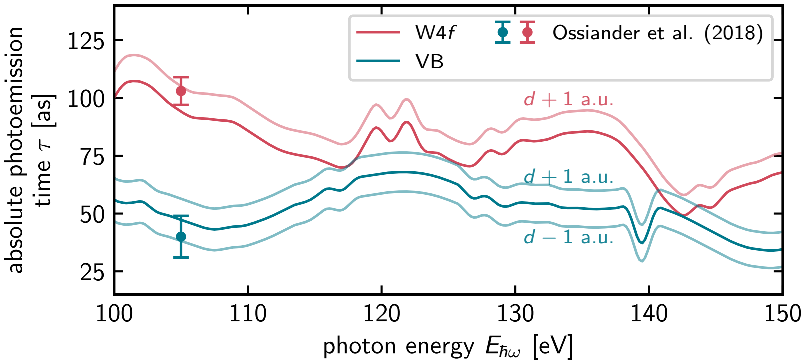

Figure 6.13: Determination of the reference plane position. When the reference plane is moved up or down the absolute photoemission time follows suit and also increases or decreases. By comparison with the absolute values determined by Ossiander et al. [18] we determine the best-fit position for the W4f and VB independently, finding simultaneous agreement for a distance $z_{\mathrm{sc}} = 3$ a.u. ≈ 1.6 Å above the topmost layer of tungsten atoms which corresponds to roughly 70% of the W(110) crystal's interlayer spacing $d = 2.24$ Å which agrees very well with the screening plane position determined in [83] at 67% of d.

shown in fig. 6.10.

6.4.3 Recalibration of the atomic chronoscope

The absolute results of Ossiander et al. [18] used to determine the reference plane position in the previous section were determined via the atomic chronoscope method: First, the I4d photoemission timing is assessed in the gas-phase in iodomethane and -ethane in mixture with helium as a reference (just as in chap. 5). The absolute W4f photoemission timing is then determined by referencing against iodine atoms adsorbed on the W(110) surface, extrapolating from measurements with varying coverage to the result for the pristine surface. The iodine atom serves as the atomic chronoscope. With the W4f photoemission time known, a relative measurement of $\tau_{\mathrm{W}4f-\mathrm{VB}}$ is then used to determine the absolute valence band timing. Figure 6.14 summmarizes the timing reference chain.

The weakest link of the reference chain in fig. 6.14 is the assumption that the I4d delay determined in the molecular gas-phase experiment coincides with that of adsorbate atom. Ossiander et al. [18] took great care to justify this assumption in the original publication, verifying numerically that the C-I bond in the molecule and the W-I bond on the surface impact the I4d orbital almost identically, as well as estimating the effect of intra-molecular scattering with a calculation using the `ePolyScat` software package. With the data available at the time their reasoning is absolutely sound. However, the new results presented in chapter 5 motivate revisiting the situation with closer scrutiny.

One of the key findings of chap. 5 is that overall the orientation-integrated molecular I4d photoemission times at any given photon energy (and especially at 105 eV) can show quite a large variation between molecules, likely due to intra-molecular scattering by which an iodine atom adsorbed on a surface should not be affected. The contrast between the rigid (iodomethane, -ethane and 2-iodopropane) and the floppy (1-iodopropane, 1- and 2-iodobutane) is especially remarkable as the I4d emission times measured in the latter are very close to the atomic calculation by Pi et al. [115] and can be used to evaluate an atomic model of the giant resonance in the I4d → εf channel. Table 6.2 summarizes the results of chap. 5 at 105 eV in terms of *total* photoemission times (i.e. with the Coulomb-laser-coupling delay included) and compares them to the result reported in [18] as well as a total photoemission time derived from the atomic calculation (see table 5.1 or 5.3).

Within this reasoning the total atomic I4d photoemission time delay is expected to be 17 as at

Table 6.2: Total I4*d* photoemission times at 105 eV across different experiments, molecular species (as investigated in this work) and from the atomic calculation of ref. [115]. The Result by Ossiander et al. [18] is the average of their measurements on iodomethane and -ethane.

	total I4*d* photoemission time delay $\tau_{\mathrm{I}4d}^{\mathrm{tot}}$
CH_3I/C_2H_5I (Ossiander et al. [18])	(26 ± 3) as
iodomethane	(28.7 ± 4.1) as
iodoethane	(27.3 ± 7.1) as
1-iodopropane	(10.9 ± 7.2) as
1-iodobutane	(19.5 ± 6.4) as
2-iodopropane	(51.7 ± 7.1) as
2-iodobutane	(23.1 ± 6.2) as
avg. floppy	(17.8 ± 11.46) as
at. calculation (ref. [115]) + τ_{clc}	17 as

105 eV which is again of course in very good agreement with the average of the floppy molecules for which one finds $\tau_{\mathrm{I}4d}^{\mathrm{tot}} = (17.8 \pm 11.46)$ as, but it is about 10 as lower than the value used in [18]. Assuming now that this difference is mostly due to intra-molecular scattering of the outgoing photoelectron in iodomethane and -ethane it follows that the photoemission time of adsorbed iodine atoms should be closer to the atomic value. Substituting now the average total I4*d* emission delay of the floppy molecules determined here for the result Ossiander et al. determined on iodomethane and -ethane in [18] (it should be noted that both results agree within their respective uncertainties) we can re-evaluate the reference chain of the absolute W(110) photoemission and thereby re-calibrate the atomic chronoscope method.

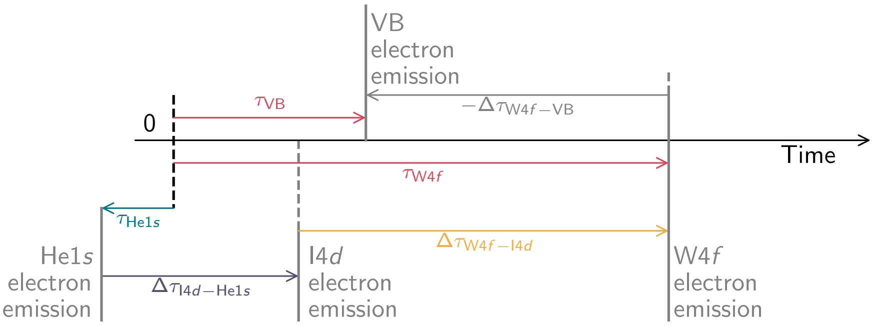

Figure 6.14: Determination of absolute photoemission times at the W(110) surface according to Ossiander et al. [18] at a photon energy of 105 eV. The emission time of the W4*f* is referenced against that of the I4*d* of iodine atoms adsorbed on the surface. Via extrapolation towards zero coverage a value of $\tau_{\mathrm{W}4f} = (103 \pm 6)$ as is determined. Relative measurements on the clean W(110) surface between the W4*f* and VB are then used to determine a VB emission time delay of $\tau_{\mathrm{VB}} = (40 \pm 9)$ as. The relative I4*d*-He1*s* delay determined in the gas phase against helium provides the total photoemission time of the I4*d* emission. The assumption of its equivalence in the molecule and as an adsorbate which cannot readily be determined experimentally is the weakest link of the referencing chain.

In [18] the W4f photoemission time is determined as

$$\tau_{\mathrm{W}4f}(\theta) = (77 \pm 5)\,\mathrm{as} + \theta \cdot (8 \pm 7)\,\mathrm{as} + \tau_{I4\mathrm{d}}^{\mathrm{tot}}, \tag{6.5}$$

as a function of the fractional iodine coverage θ in units of saturated monolayers, which following the above reasoning yields a delay of $\tau_{\mathrm{W}4f} = (94.8 \pm 12.5)$ as. With the relative W4f-VB delay of $\tau_{\mathrm{W}4f-\mathrm{VB}} = (63 \pm 6)$ as given in [18] one furthermore finds $\tau_{\mathrm{VB}} = (31.8 \pm 13.9)$ as.

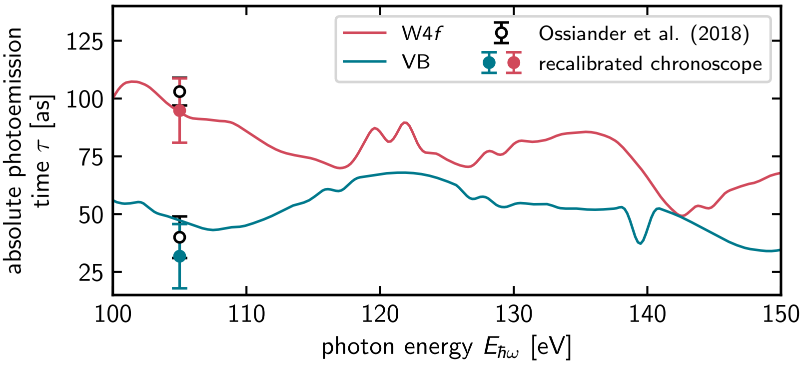

Figure 6.15: Results of the recalibration of the atomic chronoscope in comparison to the EWS escape time calculation. The excellent agreement of the W4f result is notable. The calculation for the VB no longer falls into the uncertainties of the recalibrated experimental value, but this may be due to the final states for the VB emission coinciding with the gap-like structure in discussed in 6.11 at this energy, where according to sections 6.1.2 and 6.4.1 agreement between the streaking delay and the EWS delay is not guaranteed. The results of Ossiander et al. [18] are now shown in a single color for clarity.

This can now be compared to the EWS calculation again, as it is shown in fig. 6.15. This figure is very similar to what is shown in fig. 6.13, but in order to visualize these new results some repetition seems permissible. Especially notable is the excellent agreement of the W4f delay with the calculation. The calculated VB delay now lies outside of the uncertainty of the recalibrated experimental value, but this is not necessarily unexpected as the final states for VB photoemission coincide with the gap-like structure seen in fig. 6.11 at this photon energy around which according to the discussion in sec. 6.1.2 and 6.4.1 agreement between the EWS delay time and the delay determined via attosecond streaking cannot be guaranteed.

6.5 Summary

The results of the long-running experimental campaing in which the photoemission times observed at the W(110) surface were measured are interpreted within a fully quantum mechanical calculation of the Eisenbud-Wigner-Smith (EWS) delay from first principles. We find good agreement between the results of the calculation and the relative central emission time delays between the W4f and valence states determined in [26]. The central time delay results are supplemented with a 'wave packet' reconstruction based on the extended ptychographic iterative engine (ePIE). As a result we are able to infer upon the slope of the relative W4f-VB photoemission time delay in a small region around the central photon energy under study. We find these slopes to be in good accord with the *ab-initio* calculation, save for cases where the final states of the VB or W4f electrons coincide with a 'splitting' of the main conducting branch of the final state band stucture. The inequivalence of the photoemission times determined via attosecond streaking and the EWS time delay in the vicinity of regions where the transition probability varies strongly with the final state energy has previously been observed by

Kuzian and Krasovskii [126] in a numerical streaking experiment. It is due to the photoelectron wave packet taking a complicated spatial shape around such a feature [153] whereby complex dynamics not included within the EWS theory ensue upon its traversal of the surface and partial exposure to the streaking field which measures its timing.

Using the absolute photoemission times for the W4*f* and the VB emission determined by Ossiander et al. [18] at a photon energy of 105 eV at the W(110) surface we determine the position of the NIR screening plane. This is possible as the calculation yields absolute photoemission times which are defined with respect to a reference plane the position of which can be shifted, whereby also the absolute photoemission times shift but the relative W4*f*-VB time delay remains mostly unaffected. We find best agreement with the experimental results for the screening plane being positioned $z_{sc} = 3$ a.u. ≈ 1.6 Å above the topmost layer of tungsten atoms which amounts to ~ 70% of the inlerlayer spacing of the W(110) surface and is in excellent agreement with the value determined in [83].

By revisiting the results of chapter 5 and recalling the close coincidence of the photoemission time delays determined on the floppy iodoalkanes with the atomic calculation by Pi and Landsman [115] we propose a re-calibration of the atomic chronoscope method employed in the determination of the absolute emission times of the W(110) surface in [18] by ~ −10 as. With the re-calibration in place we find now almost perfect agreement of the absolute W4*f* time and the EWS calculation. The calculated VB emission time now falls outside of the uncertainties of the re-calibrated experimental value, but this is not necessarily unexpected as per above discussion the final states for the VB now coincide with the 'splitting' of the main conducting branch of the final state band structure whereby the equivalence of streaking time delays and EWS time delays is not guaranteed.

Overall, the results presented in this chapter and their new interpretation together with the re-calibration of the atomic chronoscope are consistent with previous key experiments assessing photoemission timing from surfaces [18, 83] and close the conceptual gap between the interpretation of photoemission times measured in atoms and molecules and those measured at solid surfaces by demonstrating good agreement of experimental results with the one-step EWS theory of Kuzian and Krasovskii [126].

Chapter 7

Conclusion

This work presents two advances to the field of photoemission chronoscopy. The first advance is the systematic determination of absolute photoemission times in a group of molecules, the iodoalkanes from iodomethane upt to 2-iodobutane. The study reveals substantial differences in the behavior of the absolute photoemission time of the I4*d* core-level between molecular molecular species for photon energies between 90 eV and 118 eV, across the giant resonance present in the I4$d \rightarrow \varepsilon f$ photoemission channel. This finding is relevant for two reasons:

- The giant resonance itself is expected to be largely independent in its emission characteristics from its chemical environment. As in the experiment the immediate chemical environment of the Iodine atom (the I–C bond) is preserved, but the more remote parts of the molecule is altered when switching between the studied species, this implies that intra-molecular scattering of the outgoing photoelectron is responsible for the significant differences of the observed photoemission time delays, even at high photon energies and in small molecules. This can be related to a previous observation of strong intra-molecular scattering in photoemission from some organic molecules solely in the spectral domain [102] at high energies and indicates that a close symbiosis between measurement of the photoelectron asymmety parameter β and the spectrum with high energy resolution as well as the assessment of photoemission time delays with good temporal resolution should be strived for. Ultimately, photoelectron spectroscopy on molecules in the time domain with attosecond resolution is experimental reality today, with the continuing developement of theoretical methods to predict the observed photoemission times it will be exciting to see what the future of this field holds.
- Surprisingly, the I4*d* photoemission time delay in the large and floppy 1-iodopropane and 1- and 2-iodobutane hardly differ, and across the investigated photon energies closely replicate an accurate atomic calculation [115] of the I4*d* photoemission time. It is shown that the absolute photoemission times can be used to evaluate a single-particle model of the giant resonance (cf. [133, 111] and references therein) where qualitative agreement with spectroscopic data is found in the predicted cross-section. This may be seen as supporting the hypothesis that the the absolute photoemission time delay of the I4*d* in the floppy iodoalkanes is essentially that of an isolated iodine atom, as intra-molecular scattering seems to be strongly suppressed. If so, this motivates revisiting the I4*d* photoemission as a chronoscopy reference used for the determination of absolute photoemission times from solid surfaces [18], as it is done at the end of chapter 6.

The second advance presented here is the application of a recently developed theory of photoemission delays at solid surfaces [126] to the results of a long-running campaign on the energy dependence of the photoemission dynamics of the W(110) surface. This theory closes the conceptual gap between photoemission times observed in atoms and molecules and those observed in solids and renders the time delay difference between emission from the $4f$ states of tungsten and the W(110) valence band well. It is – contrary to previous models – completely *ab-initio* and describes the photoemission process in a single step, in full consistence with the established theory of stationary photoemission.

Within this one-step approach the photoelectron escape time is derived as the Eisenbud-Wigner-Smith time delay associated with the phase of the final state of the photoemission process. A mismatch of the EWS time delay and the photoemission time delay determined via attosecond streaking is expected whenever the final state of the photoemission process falls into a region of the conducting high energy band structure of the crystal where the transition probability varies significantly with energy. Such a variation is found at the W(110) surface at an energy of ~ 105 eV above the Fermi level, and in fact, when the final states for valence band photoemission or those for emission from the $4f$ levels land in this region a strong deviation of the slope of the energy dependent the photoemission time in determined from the streaking measurement via a wave packet reconstruction algorithm from the calculation is observed.

Chapter 8

Outlook

With the I4*d* photoemission timing in the iodoalkanes up to 2-iodobutane now known across a larger energy range one can use any of these molecules as a chronoscopy reference in the gas phase. This will enable the measurement of the photoemission dynamics in other molecules. The determination of absolute photoemission times via iodoalkane-mediated photoemission chronoscopy is therefore instrumental to the testing and further developement of the theory of molecular photoionization. For example, small molecules like CO_2 exhibit complex ionization dynamics on the attosecond time scale driven by the streaking laser field [127]. Temporally resolving these dynamics via absolute photoemission times opens the door to studying electronic correlations in molecular systems with attosecond precision.

Another thrilling aspect of molecular photoemission chronoscopy is the possibility to access the molecular frame. This is facilitated by the surface science experiment briefly outlined in sec. 5.5. The gas-phase study presented in this work lays the necessary groundwork for the interpretation of this experiment as it assesses the photoemission time of the isolated molecule. Next to studying photoemission times in an orientationally resolved manner, the application of attosecond streaking spectroscopy to molecular adsorbates will offer a novel view onto the interaction of light with molecules in the vicinity of a surface. Such future studies will benefit from the now known origin of the energy-dependence of photoemission times observed at metal surfaces (chap. 6).

With the one-step theory of solid-state photoemission now established as the gold-standard for the interpretaion of photoemission times measured in attosecond streaking experiments at surfaces, the next step is to introduce controlled changes to the screening scenario near the surface in order to probe the interaction of the leaving photoelectron wave packet with the light field. A general and systematic survey comparing different surface adsorbates would be the most thorough and exhaustive way of doing so. Iodomethane and -ethane as well as atomic iodine are especially suited as first candidates for adsorbates. By varying not only the excitation energy but also the atomic/molecular surface coverage *and* the adsorbed species photoemission chronoscopy becomes multi-dimensional in the information it assesses.

The work presented here illustrates that the application of photoemission chronoscopy has the potential to resolve directly in the time-domain what is otherwise only accessible quite indirectly with other spectroscopy techniques (cf. intra-molecular scattering and lattice scattering of the outgoing photoelectron wave packet). With the ongoing refinement of the theoretical assessment of photoemission from atomic, molecular and solid-state systems experimentally determined photoemission time delays remain an important benchmark for this theory. Therefore, upcoming studies pertaining absolute photoemission chronoscopy of small molecules and at surfaces are to be anticipated with great excitement.

Appendix A

The Haus Master Equation

Inserting the ansatz 2.19 into the Haus master equation 2.18, one can split the resulting equation into a real- and an imaginary part. The real part is

$$|A_0|^2 \Omega_f^2 \left(\mathcal{T}_e^4 - \mu t^2 \mathcal{T}_e^2\right) \gamma + G \Omega_f^2 \mathcal{T}_e^4 + (2D\beta\Omega_f^2 - 2)\mathcal{T}_e^2 - (8D\beta\Omega_f^2 + 4\beta^2 - 4)t^2 = 0, \tag{A.1}$$

and the imaginary part is

$$\Omega_f^2 \mathcal{T}_e^4 \left(\Phi_{\text{ce}} - |A_0|^2 \delta\right) + (|A_0|^2 \delta\mu\Omega_f^2 t^2 - dD\Omega_f^2 - 2\beta)\mathcal{T}_e^2 + \left(4D\left(1 - \beta^2\right)\Omega_f^2 + 8\beta\right) t^2 = 0. \tag{A.2}$$

As eq. 2.19 is to solve eq. 2.18 for all times t, one can further separate these equations into time-dependent and time-independent parts, all of which have to vanish individually. This yields the following system of equations:

$$- |A_0|^2 \mu \mathcal{T}_e^2 \gamma - \frac{4\beta^2}{\Omega_f^2} + \frac{4}{\Omega_f^2} - 8D\beta = 0 \tag{A.3}$$

$$|A_0|^2 \mathcal{T}_e^2 \gamma + G\mathcal{T}_e^2 - \frac{2}{\Omega_f^2} + 2D\beta = 0 \tag{A.4}$$

$$|A_0|^2 \delta\mu\mathcal{T}_e^2 + \frac{8\beta}{\Omega_f^2} - 4D\beta^2 + 4D = 0 \tag{A.5}$$

$$\Phi_{\text{ce}}\mathcal{T}_e^2 - |A_0|^2 \delta\mathcal{T}_e^2 - \frac{2\beta}{\Omega_f^2} - 2D = 0 \tag{A.6}$$

Solving eqns. A.3 and A.5 for β and $\mathcal{T}_e$ yields

$$\beta = -\frac{\sqrt{D^2\Omega_f^4 + 1}\sqrt{\gamma^2 + \delta^2} - \gamma + D\delta\Omega_f^2}{D\Omega_f^2\gamma + \delta} \tag{A.7}$$

$$\mathcal{T}_e = \frac{2^{\frac{2}{3}}\sqrt{D^2\Omega_f^4 + 1}\sqrt{\frac{\sqrt{D^2\Omega_f^4+1}\sqrt{\gamma^2+\delta^2}-\gamma+D\delta\Omega_f^2}{\mu}}}{|A_0|\, D\Omega_f^3\gamma + |A_0|\,\delta\Omega_f} \tag{A.8}$$

Equations A.4 and A.6 can then be solved for G and Φ_{ce}, yielding

$$G = -\frac{|A_0|^2 \Omega_f^2\mathcal{T}_e^2\gamma + 2D\beta\Omega_f^2 - 2}{\Omega_f^2\mathcal{T}_e^2} \tag{A.9}$$

$$\Phi_{\text{ce}} = \frac{|A_0|^2 \delta\Omega_f^2\mathcal{T}_e^2 + 2D\Omega_f^2 + 2\beta}{\Omega_f^2\mathcal{T}_e^2} \tag{A.10}$$

Table A.1: Parameters used in fig. 2.5 which are not given in the main text.

parameter	value
Ω_f	110 THz
A_0	500 kW
μ	$15 \cdot 10^{-7}$ radW^{-1}
γ	$50 \cdot 10^{-7}$ radW^{-1}

in terms of β and $\mathcal{T}_e$. The equations have been solved with the aid of the Maxima computer algebra system, version 5.42.1.

The parameters of the visualization in fig. 2.5 are given in table A.1.

Appendix B

Molecular geometry and visualizations

The molecular geometries presented in chap. 5 were fetched with `Avogadro` [165] and exported from there to render in `PovRay` [166]. Internally, `Avogadro` uses the *Chemical Identifier Resolver*[1] of the CADD Group Chemoinformatics Tools and User Services of the US National Cancer Institute. Alternatively, 3D structures are available from the PubChem database [167].

The `GAMESS` input files for the Hartree-Fock calculations were created with `Avogadro`'s input generator and modified by hand to e.g. enable exploiting of symmetries in the HF calculations (translations/rotations and removal of atoms which are symmetry-equivalent within the molecular point group). They are listed below. The molecular geometries can be extracted from them.

B.1 Hydrogen Iodide

```
!   File created by the GAMESS Input Deck Generator Plugin for Avogadro
 $BASIS GBASIS=SPK-TZP $END
 $CONTRL SCFTYP=RHF RUNTYP=ENERGY ISPHER=1 PLTORB=.TRUE. $END
 $SCF NPUNCH=1 $END

 $DATA
Hydrogen Iodide
CNV 4

I    53.0     0.00000     0.00000     0.00000
H     1.0     0.00000     0.00000     1.60900
 $END
```

B.2 Iodomethane

Symmetry-equivalent atoms (C_{3V}) have been removed.

```
!   File created by the GAMESS Input Deck Generator Plugin for Avogadro
 $BASIS GBASIS=SPK-TZP $END
 $CONTRL SCFTYP=RHF RUNTYP=ENERGY ISPHER=1 PLTORB=.TRUE. $END
 $SCF NPUNCH=1 $END

 $DATA
Iodomethane
Cnv 3

```

---

[1] `https://cactus.nci.nih.gov/chemical/structure`, visited May 23, 2023

```
I     53.0     -0.00000      0.00000      0.23670
C      6.0      0.00000      0.00000     -1.92530
H      1.0      1.02770      0.00000     -2.28860
 $END
```

B.3 Iodoethane

Symmetry-equivalent atoms (C_S) have been removed.

```
!   File created by the GAMESS Input Deck Generator Plugin for Avogadro
 $BASIS GBASIS=SPK-TZP $END
 $CONTRL SCFTYP=RHF RUNTYP=ENERGY ISPHER=1 PLTORB=.TRUE. $END
 $SCF NPUNCH=1 $END


 $DATA
Iodoethane
CS

C      6.0     -2.03080      0.74180      0.00000
C      6.0     -3.00470     -0.43810      0.00000
I     53.0      0.00000      0.00000      0.00000
H      1.0     -2.19570      1.34910     -0.89000
H      1.0     -4.02860     -0.06410      0.00000
H      1.0     -2.83980     -1.04540     -0.89000
 $END
```

B.4 1-Iodopropane

```
!   File created by the GAMESS Input Deck Generator Plugin for Avogadro
 $BASIS GBASIS=SPK-TZP $END
 $CONTRL SCFTYP=RHF RUNTYP=ENERGY ISPHER=1 $END

 $DATA
1-Iodopropane
C1
I     53.0     -0.81500      0.02500     -0.00000
C      6.0      1.22500     -0.69100      0.00000
C      6.0      2.18400      0.50100      0.00000
C      6.0      3.62800     -0.00600     -0.00000
H      1.0      3.80100     -0.61100      0.89000
H      1.0      1.39800     -1.29600      0.89000
H      1.0      1.39800     -1.29600     -0.89000
H      1.0      2.01100      1.10600     -0.89000
H      1.0      2.01100      1.10600      0.89000
H      1.0      3.80100     -0.61100     -0.89000
H      1.0      4.31100      0.84400     -0.00000
 $END
```

B.5 2-Iodopropane

Symmetry-equivalent atoms (C_S) have been removed.

```
 $BASIS GBASIS=SPK-TZP $END
 $CONTRL SCFTYP=RHF RUNTYP=ENERGY ISPHER=1 PLTORB=.TRUE. $END
 $SCF NPUNCH=1 $END

 $DATA
2-Iodopropane
CS

I     53.0     -0.65710     -0.01140      0.00000
C      6.0      1.45620      0.44510     -0.00000
C      6.0      2.10700     -0.15220      1.24920
H      1.0      1.59430      1.52630     -0.00000
H      1.0      1.96890     -1.23340      1.24920
H      1.0      3.17240      0.07800      1.24920
H      1.0      1.64330      0.27340      2.13920
 $END
```

B.6 1-Iodobutane

Symmetry-equivalent atoms (C_S) have been removed.

```
!   File created by the GAMESS Input Deck Generator Plugin for Avogadro
 $BASIS GBASIS=SPK-TZP $END
 $CONTRL SCFTYP=RHF RUNTYP=ENERGY ISPHER=1 PLTORB=.TRUE. $END
 $SCF NPUNCH=1 $END


 $DATA
1-Iodobutane
CS

I     53.0     -1.17000      0.06800     -0.00000
C      6.0      0.77000     -0.88700      0.00000
C      6.0      1.86400      0.18200      0.00000
C      6.0      3.23700     -0.49300     -0.00000
C      6.0      4.33200      0.57600      0.00000
H      1.0      4.23300      1.19700     -0.89000
H      1.0      0.87000     -1.50800     -0.89000
H      1.0      1.76500      0.80400     -0.89000
H      1.0      3.33600     -1.11500     -0.89000
H      1.0      5.31000      0.09400     -0.00000
 $END
```

B.7 2-Iodobutane

```
!   File created by the GAMESS Input Deck Generator Plugin for Avogadro
 $BASIS GBASIS=SPK-TZP $END
 $CONTRL SCFTYP=RHF RUNTYP=ENERGY ISPHER=1 PLTORB=.TRUE. $END
 $SCF NPUNCH=1 $END

 $DATA
2-Iodobutane
C1
I     53.0     -0.79260     -0.09530      0.01380
```

```
C      6.0      1.20320     0.62600     -0.39920
C      6.0      1.31560     2.09000      0.03090
C      6.0      2.21970    -0.21330      0.37750
C      6.0      2.19440    -1.65280     -0.14010
H      1.0      1.40520     0.54450     -1.46730
H      1.0      1.11370     2.17140      1.09890
H      1.0      2.32190     2.45360     -0.17740
H      1.0      0.59150     2.68780     -0.52250
H      1.0      3.21690     0.20480      0.23990
H      1.0      1.96480    -0.20370      1.43720
H      1.0      2.91860    -2.25070      0.41320
H      1.0      1.19720    -2.07090     -0.00260
H      1.0      2.44930    -1.66240     -1.19990
 $END
```

Appendix C

Photoemission delay retrieval

C.1 The diff. rTDSE method

In the rTDSE class of delay extraction methods a spectrogram recorded in the experiment is modeled as an incoherent sum of spectrograms, one for each photoemission feature. The individual spectrograms are parametrized in terms of their corresponding photoelectron wave packets and one NIR vector potential $A(t)$ common for all. The relative time delays between photoemission features in a spectrogram are then simply parameters of the model and can be detemined via a least-squares fit to the experimental data. Photoemission features comprised of multiple photolines which overlap due to the large XUV bandwidth (cf. the I$4d$ spin-orbit doublet encountered in chap. 5 or the W$4f$ doublet in chap. 6) are conflated and share the same delay parameter. We exploit that due to the application of the central momentum approximation a spectrogram can be calculated very efficiently via the `fft` algorithm. Defining

$$G(E_0, t) = \exp\left(-i\Phi_V\left(\sqrt{2E_0}, t\right)\right), \tag{C.1}$$

the model spectrogram can be written as

$$\begin{aligned} S_{\mathrm{rTDSE}}(E, \Delta\tau) = \sum_i^{N_i} \sum_j^{N_j^{(i)}} a_{i,j} \Big| \mathscr{F}^{-1} \Big\{ & \chi(t + \Delta\tau; \omega_{\mathrm{XUV}} - I_p^{i,j}, \delta_i, \beta_i, \Delta\omega) \\ & \times G(t; \omega_{\mathrm{XUV}} - I_p^{i,j}; A_0, \mathscr{T}, \omega_L, \beta_L, \varphi) \Big\} \Big|^2, \end{aligned} \tag{C.2}$$

with $I_p^{i,j}$ being the ionization potential of the j-th component of the i-th photoemission feature and $a_{i,j}$ its respective amplitude with which it contributes to the spectrogram. The inner sum runs over the j components of a photoemission feature (e.g. the W$4f_{5/2}$ and W$4f_{7/2}$), the outer sum runs over the photoemission features (e.g. the entirety of the tungsten VB and the W$4f$ emission). The ansatz for the wave packet

$$\chi(t; \omega_0, \delta, \beta, \Delta\omega) = \mathscr{F}^{-1}\left\{ \mathrm{e}^{-4\log 2\left(\frac{\omega-\omega_0}{\Delta\omega}\right)^2} \mathrm{e}^{\mathrm{i}\delta(\omega-\omega_0) + \frac{1}{2}\mathrm{i}\beta(\omega-\omega_0)^2} \right\} \tag{C.3}$$

is made in the spectral domain (and brought to the time domain numerically) as a gaussian of width $\Delta\Omega$ centered around ω_0. Its chirp parameter is β, and δ is its temporal offset from the center of the NIR pulse. The relative photoemission times are the differences between the δ_i determined in the fit. The NIR vector potential

$$A_{\mathrm{NIR}}(t; A_0, \mathscr{T}, \omega_L, \beta_L, \varphi) = A_0 \exp\left(-4\log 2\left(\frac{t}{\mathscr{T}}\right)^2\right) \sin\left(\omega_L t + \frac{1}{2}\beta_L t^2 + \varphi\right) \tag{C.4}$$

is parametrized in the time domain as a sinusoidal carrier with frequency ω_L, ce-phase φ, chirp parameter β_L, and an envelope with temporal width $\mathcal{T}$ and maximal value A_0.

In order to make the fit insensitive to static background in the spectrogram both the data and the model spectrogram are differentiated numerically along the XUV/NIR delay dimension before calculating the error function. Figure C.1 illustrates the fitting principle.

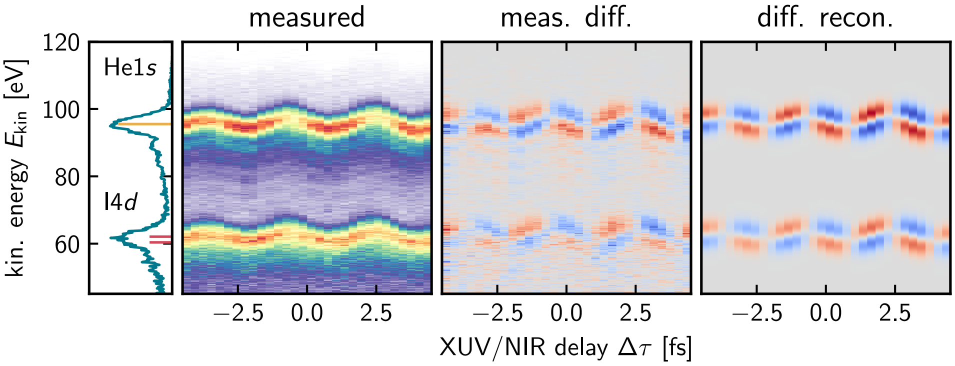

Figure C.1: Example of the diff. rTDSE fitting method, here applied to a spectrogram recorded on a mixture of iodoethane and Helium at 118 eV. The leftmost spectrum of the experimental spectrogram is shown in the leftmost panel. The energetic position and amplitude of the wave packet modelling the He1*s* photoemission is shown as a yellow stick, for the I4*d* the same is shown in red. The relative delay is determined between these two photoemission features. This means that in order to model this spectrogram the inner sum in eq. C.3 has two terms for the I4*f*, and one term for the He1*s*. The total model spectrogram is then the sum of these. The delay-derivative of the experimental spectrogram is shown in the third panel, and the last panel shows the result of the fit.

While it is possible to use eq. C.3 to fit experimental data after background subtraction and without differentiation along the delay dimension this approach is not used within this work.

C.2 The extended ptychographic iterative engine

The implementation of the extended ptychographic iterative engine (ePIE) used in this work is based on the algorithm described in [69]. As the purpose of the algorithm in the original publication is pulse characterization and therefore the application to a single streaking trace and not the extraction of time delays between two streaking traces it needed to be modified. First, the algorithm in its single-trace formulation is presented, then its extension towards photoemission delay extraction.

C.2.1 Reconstructing a single wave packet

Starting point for the ePIE is eq. 4.15. Defining the gate function

$$G(E_0, t) = \exp\left(-i\Phi_V\left(\sqrt{2E_0}, t\right)\right), \tag{C.5}$$

4.15 takes the form

$$S(E, \Delta\tau) \propto \left| \int_{-\infty}^{\infty} dt \chi(t + \Delta\tau) G(t) \mathrm{e}^{-iEt} \right|^2, \tag{C.6}$$

where the dependency of the Gate function on the energy is dropped for notational clarity in the following. The NIR vector potential can be extracted from $G(E_0, t)$ using equation 4.10. Starting out from an initial guess for $\chi(t)$ and $G(t)$ generated from an unstreaked photoelectron spectrum and a center-of-energy analysis of the streaking trace, the algorithm walks through all spectra in a spectrogram in every iteration and alternatively applies an error-minimization to the time-domain wave packet $\chi(t)$ and the gate function $G(t)$. Exploiting that $|G(t)| = 1$ must be fulfilled at all times one can implement the enforcement of a constraint (normalizing the gate function in each iteration) in the reconstruction which significantly aids convergence. Figure C.2 shows an overview of the workings of the ePIE when applied to a single streaking trace. The error correction strength parameters are set to $\beta_\chi = 0.05$ and $\beta_P = 0.1$ for the wave packet $\chi(t)$ and the gate function $G(t)$ respectively.

Generally, before the ePIE can be applied to a spectrogram any static background must be removed. A piecewise implementation of the Shirley-Proctor-Sherwood [168] method in the passive approach is used for background subtraction.

C.2.2 Simultaneous reconstruction of two wave packets

In order to extract the group delay between two streaking traces in one spectrogram they need to be reconstructed simultaneously under the constraint of being streaked by the same NIR pulse. The spectrogram is separated into two smaller spectograms containing only one streaking trace each, then ePIE is appplied where after each iteration the vector potentials $A(t)$ are extracted from the corresponding gate functions and averaged, before being fed into the next iteration in the calculation of the gate functions. After some hundred iterations the NIR fields/gate functions are no longer updated, all corrections are applied to the wave packets to ensure that their respective phases converge to the proper relative photoemission time delay. Figure C.3 illustrates the procedure. Typically 1000 iterations are sufficient, where the gate functions are frozen after 600 iterations.

C.2.3 Numerical differentiation of a phase

The spectral phases retrieved by the ePIE may suffer from phase jumps due to the equivalence of a phase φ and $\varphi+2\pi$ in this numerical problem (cf. also [29, p. 17ff]), but these jumps hinder the direct determination of the wave packet group delay by differentiation. We found that the available phase-unwrapping routines in `numpy` also don't always perform satisfactorily so that for the evaluation of large datasets of ePIE retrievals another method must be sought.

A combined numerical finite-differences derivative and unwrapping algorithm in implemented in `python` (using the `numpy` library) is listed below.

```python
import numpy as np

def phase_derivative(p, E, discont = np.pi * .75):
    out = np.zeros_like(p)
    for i, p_i in enumerate(p[:-1]):
        dp = p[i + 1] - p[i]
        dE = E[i + 1] - E[i]
        if(np.abs(dp) > discont):
            dp -= np.sign(dp) * 2. * np.pi
        if(np.abs(dp) > discont):
            out[i] = np.nan
        else:
            out[i] = dp / dE
    out[-1] = out[-2]
    return out
```

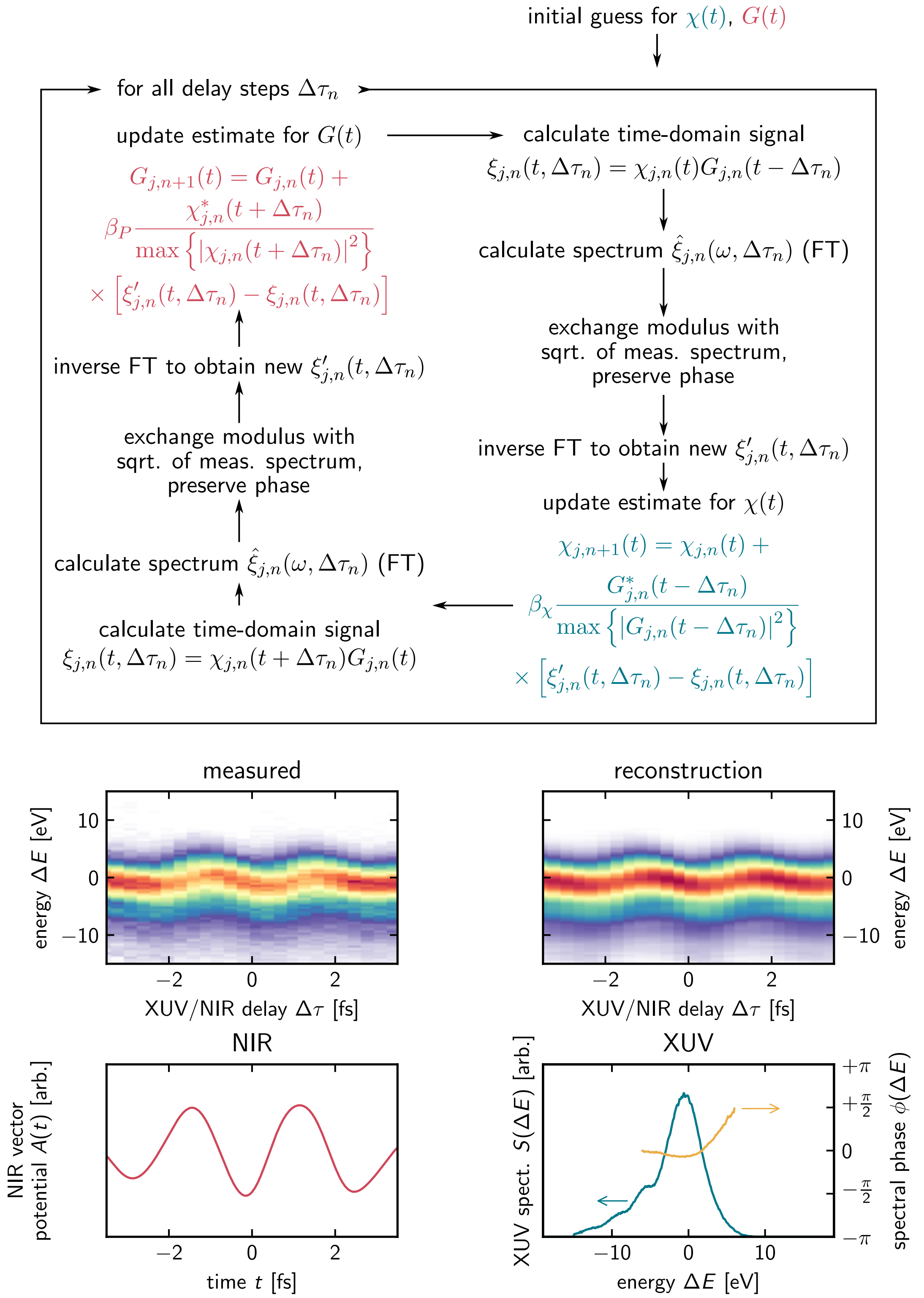

Figure C.2: . The flow-chart illustrates what happens in a single iteration of the ePIE (the *ePIE loop*). This procedure is applied many times to a spectrogram until satisfactory convergence is reached. As it is seen from the lower panels the retrieval quality attainable with ePIE is excellent. The NIR vector potential $A(t)$ can be extracted from $G(p_0, t)$. It is beneficial to walk through the spectra in a spectrogram in random order to prevent walk-off of the NIR pulse from the wave packet. The index n denotes the individual spectra comprising a spectrogram, j denotes iterations.

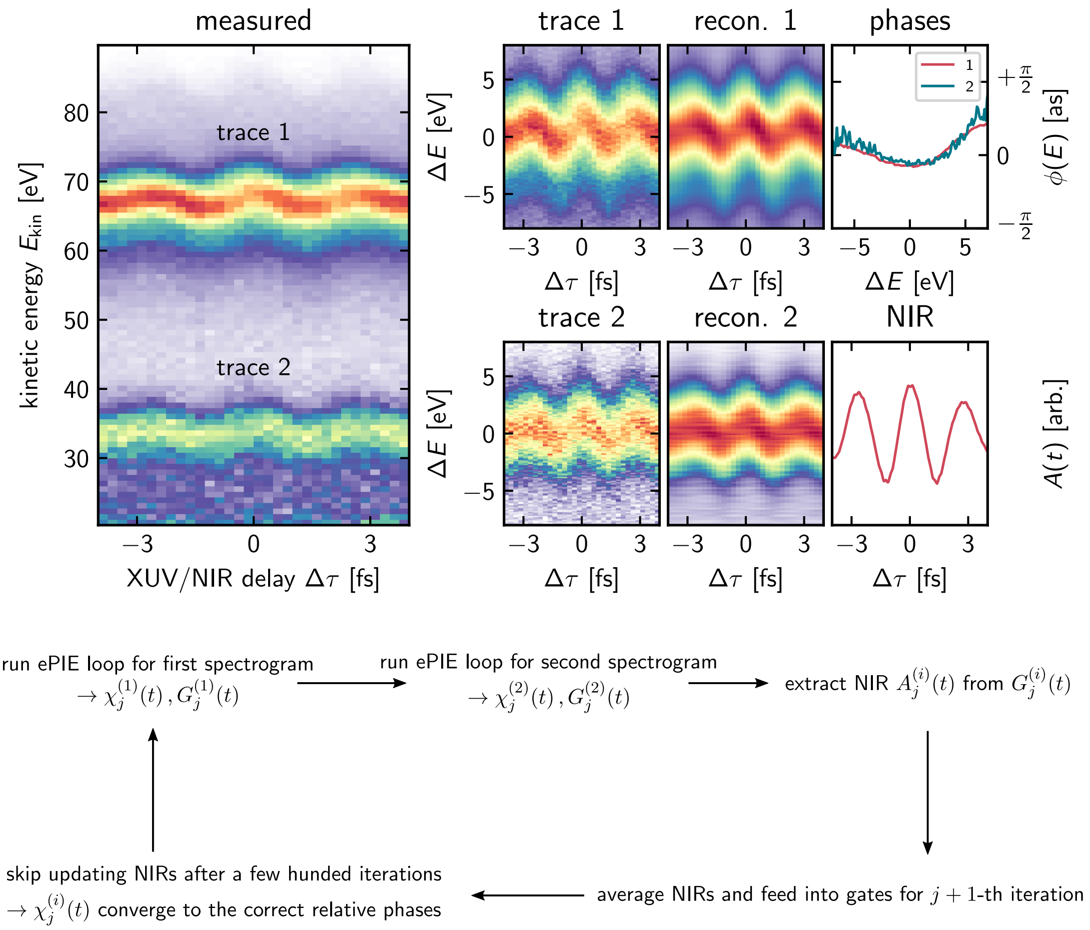

Figure C.3: In order to determine the delay between trace 1 and trace 2 the spectrogram is split, and ePIE is applied to both traces, under the constraint that they both share she same vector potential $A(t)$. After a few hundred iterations the gate functions are frozen and no longer updated to ensure convergence of the wave packets.

Appendix D

Back-end of the experimental setup

The AS101 setup has been described in thorough detail in [117], an in-depth review of the AS3 beamline has been published in [140]. For the sake of completeness the AS101 beamline's backend is described here. At its heart is a commercial Femtopower HE/HR CEP4 laser system which nominally delivers ce-phase stabilized pulses of ~ 20 fs duration and ~ 3 mJ pulse energy at a repetition rate of 4 kHz at its output. Internal to it, a mode-locked Ti:Sa oscillator delivers ce-phase stabilized pulses of ~ 6 fs duration at a repetition rate of ~ 80 MHz and a pulse energy of ~ 4 nJ. The ce-phase stabilization works in a simultaneous feed-forward and feed-back scheme with the f_{ce} detection being done in-line via $f - 0$ interferometry (cf. sec. 3.1.1). The slow feedback line regulates f_{ce} via the intracavity dispersion to a fixed value, while a frequency shifting unit following the oscillator pulls the f_{ce} offset to zero. In a subsequent two-stage chirped-pulse multipass amplifier the repetition rate is reduced to 4 kHz. After re-compression with a grating compressor one reaches the nominal specifications of the apparatus.

These pulses are spectrally broadened in a differentially pumped hollow core fiber wave guide filled with He gas (cf. sec. 3.1.2). After subsequent compression with dispersive (chirped) mirrors the pulse duration is about ~ 5 fs and the pulse energy some 1.5 mJ with which the attosecond beamline (high harmonic generation and the experiment) is driven. CE-phase drifts in the amplification and broadening stage are measured via $f - 2f$ interferometry (cf. sec. 3.1.1) directly before the high harmonic generation and corrected via feed back to the controllable stretcher before the amplifier. Figure D.1 shows a coarse sketch of the system.

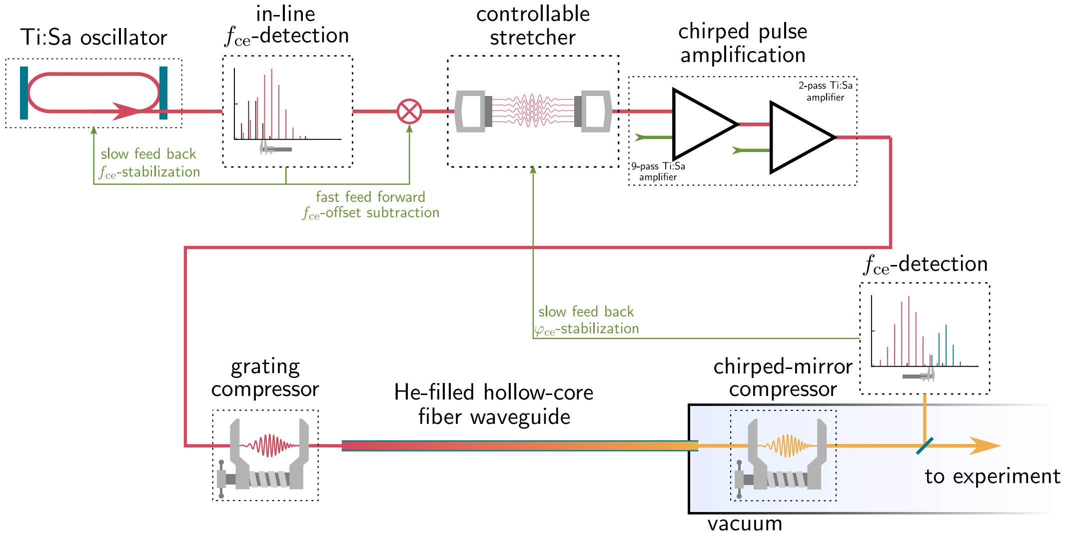

Figure D.1: Overview of the backend of the AS101 beamline.

Appendix E

Characterization of two multilayer XUV mirrors for attosecond streaking experiments at 90 eV and 92.5 eV

The pool of XUV reflectors available at the attosecond beamlines of the Technische Universität München contains a quite peculiar mirror centered at 92.5 eV with a band-width of 3.5 eV as characterized by a reflectometry measurement [169, p. 72f]. While the the static reflectivity of this mirror is known accurately, its temporal properties are unknown as its reflection phase, which is a crucial parameter for the characterization of XUV reflectors to be used in attosecon chronoscopy (cf. [170]) is not known. Furthermore, it has been remarked in [169, p. 72f] that the shape of the mirror's reflectivity curve might make it unsuitable for the generation of isolated attosecond pulses, and thereby in extension unsuitable for attosecond streaking experiments. While an awkward reflection profile alone is not enough to disqualify a reflector from use in attosecond experiments, it is shown here that the respective mirror introduces a spectral phase of third order to the XUV pulse, which as described in sec. 2.2 lead to the pulse exibiting satellites in the time domain.

We use the 92.5 eV reflector in an attosecond streaking experiment on the Ne2p level which does not exhibit significant photoemission dynamics around this energy [125] whereby we can expect the streaking measurement to faithfully characterize the syntehsized XUV pulse. After reconstruction via ePIE, the group delay, chirp and second order chirp (third order spectral phase) of the XUV pulses are determined via a polynomial fit to the retrieved spectral phases. In total 57 scans are evaulated, which were recorded over the course of multiple days and therefore different alignments of laser and beamline. We find that the third-order term of the spectral phase of the pulses synthesized with the 92.5 eV mirror is on average drastically different from zero (cf. fig. E.1), especially in comparison with pulses retrieved from measurements with an XUV mirror centered at 90 eV (the one used in the experiments in chap. 5) recorded on the He1s photoemission (here, 67 scans were evaluated).

The signature of the third-order term in the attosecond streaking measurement is the 'fin-like' pattern seen in the 92.5 eV around $\Delta E \approx -2$ eV, tilting towards lower XUV/NIR time delays.

While mostly qualitatively these results should demonstrate sufficiently that the 92.5 eV mirror is unfit for use in attosecond streaking experiments and should best be discarded.

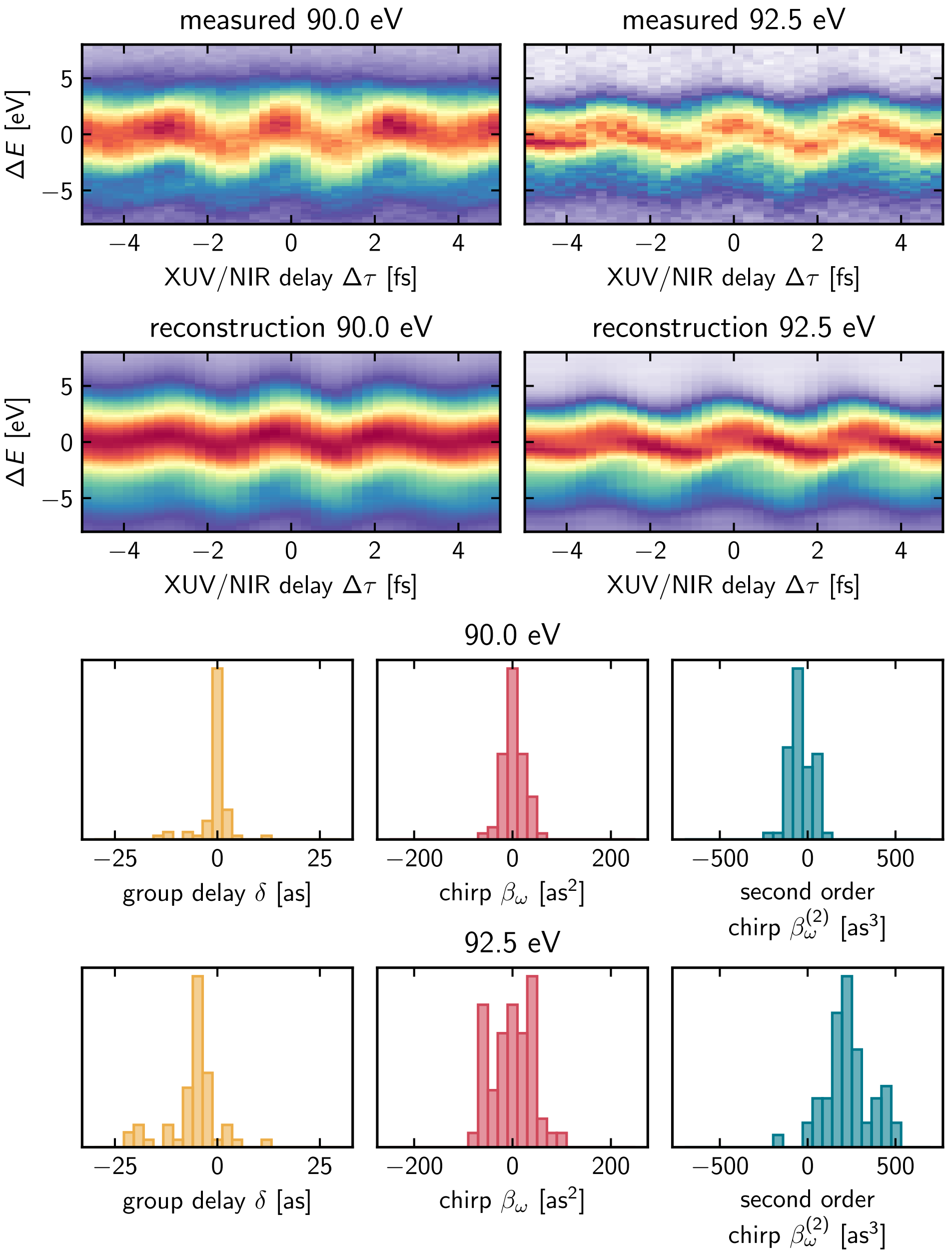

Figure E.1: Comparison of the spectral phase components of XUV pulses synthesized with a 'good' 90 eV mirror and the 92.5 eV mirror of unknown design. The measurements with the former reflector were done using the He1*s* photoemission, the latter are done on the Ne2*p*, but as neither of these exhibit strong variations in their photoemission dynamics both measurements can be seen as sufficiently representative of a characterization of the synthesized XUV pulse. The top panels show measured and reconstructed streaking traces, the bottom panels show the statistics of the first-, second- and third-order phase term of the XUV pulse as retrieved via ePIE. The immensely large third-order term observed for the 92.5 eV mirror disqualifies it from use in attosecond streaking experiments. The third-order phase distortion is also seen in the measured and retrieved streaking spectrograms as a 'fin-like' pattern around $\Delta E \approx -2$ eV tilting towards lower XUV/NIR delay times $\Delta\tau$ which is completely absent for the 90 eV mirror.

Appendix F

Open source software used in this work

This thesis was typeset using LuaTEX[1]. Graphs, figures and visualizations were created with

- `PovRay` [166]
- `Inkscape`[2]
- `matplotlib` [171]
- `imagemagick` [172]

Data analysis made heavy use of the `python` programming language and its standard library as well as the `numpy` [173] and `scipy` [174] packages. The Debian GNU+Linux operating system[3] provided the computing environment.

---

[1] `https://www.luatex.org/`, retrieved May 15, 2023

[2] `https://inkscape.org/credits/`, retrieved May 15, 2023

[3] `https://www.debian.org/`, retrieved May 15, 2023

List of Figures

Bibliography

[1] E. Arnold. *Bhagavadgita*. Dover thrift editions. Dover Publications, 1993. ISBN: 9780486277820. URL: https://books.google.de/books?id=KOd6N2%5C_t6XoC.

[2] D. R. Hartree. "The Wave Mechanics of an Atom with a Non-Coulomb Central Field. Part I. Theory and Methods". In: *Mathematical Proceedings of the Cambridge Philosophical Society* 24.1 (1928), pp. 89–110. DOI: 10.1017/S0305004100011919.

[3] E. Tiesinga et al. "CODATA Recommended Values of the Fundamental Physical Constants: 2018*". In: *Journal of Physical and Chemical Reference Data* 50.3 (Sept. 2021). 033105. ISSN: 0047-2689. DOI: 10.1063/5.0064853. eprint: https://pubs.aip.org/aip/jpr/article-pdf/doi/10.1063/5.0064853/16697641/033105_1_online.pdf. URL: https://doi.org/10.1063/5.0064853.

[4] H. Hertz. "Ueber einen Einfluss des ultravioletten Lichtes auf die electrische Entladung". In: *Annalen der Physik* 267.8 (1887), pp. 983–1000.

[5] W. Hallwachs. "Ueber die Elektrisierung von Metallplatten durch Bestrahlung mit elektrischem Licht". In: *Nachrichten von der Königl. Gesellschaft der Wissenschaften und der Georg-Augusts-Universität zu Göttingen* 1888 (1888), pp. 174–176.

[6] A. Einstein. "Über einen die Erzeugung und Verwandlung des Lichtes betreffenden heuristischen Gesichtspunkt". In: *Annalen der Physik* 17 (1905), p. 132.

[7] R. A. Millikan. "A Direct Photoelectric Determination of Planck's ”*h*””. In: *Phys. Rev.* 7 (3 Mar. 1916), pp. 355–388. DOI: 10.1103/PhysRev.7.355. URL: https://link.aps.org/doi/10.1103/PhysRev.7.355.

[8] S. Hüfner. *Photoelectron Spectroscopy : Principles and Applications*. Springer Series in Solid-State Sciences ; 82. Berlin, Heidelberg: Springer Berlin Heidelberg, 1995, 1 Online–Ressource (XII, 515 p). ISBN: 978-3-662-03150-6 - 978-3-662-03152-0. URL: https://doi.org/10.1007/978-3-662-03150-6.

[9] K. M. G. Siegbahn, W. C. Price, and D. W. Turner. "A Discussion on photoelectron spectroscopy - Electron spectroscopy for chemical analysis (e.s.c.a.)" In: *Philosophical Transactions of the Royal Society of London. Series A, Mathematical and Physical Sciences* 268.1184 (1970), pp. 33–57. DOI: 10.1098/rsta.1970.0060. eprint: https://royalsocietypublishing.org/doi/pdf/10.1098/rsta.1970.0060. URL: https://royalsocietypublishing.org/doi/abs/10.1098/rsta.1970.0060.

[10] A. Damascelli. "Probing the electronic structure of complex systems by ARPES". In: *Physica Scripta* 2004.T109 (2004), p. 61.

[11] A. H. Zewail. "Femtochemistry: Atomic-Scale Dynamics of the Chemical Bond". In: *The Journal of Physical Chemistry A* 104.24 (2000), pp. 5660–5694. DOI: 10.1021/jp001460h. eprint: https://doi.org/10.1021/jp001460h. URL: https://doi.org/10.1021/jp001460h.

[12] F. Krausz and M. Ivanov. "Attosecond physics". In: *Rev. Mod. Phys.* 81 (1 Feb. 2009), pp. 163–234. DOI: `10.1103/RevModPhys.81.163`. URL: `https://link.aps.org/doi/10.1103/RevModPhys.81.163`.

[13] R. Haight et al. "Picosecond Time-Resolved Photoemission Study of the InP(110) Surface". In: *Phys. Rev. Lett.* 54 (12 Mar. 1985), pp. 1302–1305. DOI: `10.1103/PhysRevLett.54.1302`. URL: `https://link.aps.org/doi/10.1103/PhysRevLett.54.1302`.

[14] M. Puppin et al. "500 kHz OPCPA delivering tunable sub-20 fs pulses with 15 W average power based on an all-ytterbium laser". In: *Opt. Express* 23.2 (Jan. 2015), pp. 1491–1497. DOI: `10.1364/OE.23.001491`. URL: `https://opg.optica.org/oe/abstract.cfm?URI=oe-23-2-1491`.

[15] A. L. Cavalieri et al. "Attosecond spectroscopy in condensed matter". In: *Nature* 449.7165 (2007), p. 1029.

[16] M. Schultze et al. "Delay in Photoemission". In: *Science* 328.5986 (2010), pp. 1658–1662. ISSN: 0036-8075. DOI: `10.1126/science.1189401`. eprint: `http://science.sciencemag.org/content/328/5986/1658.full.pdf`. URL: `http://science.sciencemag.org/content/328/5986/1658`.

[17] S. Grundmann et al. "Zeptosecond birth time delay in molecular photoionization". In: *Science* 370.6514 (2020), pp. 339–341. DOI: `10.1126/science.abb9318`. eprint: `https://www.science.org/doi/pdf/10.1126/science.abb9318`. URL: `https://www.science.org/doi/abs/10.1126/science.abb9318`.

[18] M. Ossiander et al. "Absolute timing of the photoelectric effect". In: *Nature* 561.7723 (Sept. 2018), pp. 374–377. ISSN: 1476-4687. URL: `https://doi.org/10.1038/s41586-018-0503-6`.

[19] H. G. Muller. "Reconstruction of attosecond harmonic beating by interference of two-photon transitions". In: *Applied Physics B* 74.1 (June 2002), s17–s21. ISSN: 1432-0649. URL: `https://doi.org/10.1007/s00340-002-0894-8`.

[20] R. Kienberger et al. "Atomic transient recorder". In: *Nature* 427.6977 (Feb. 2004), pp. 817–821. ISSN: 1476-4687. URL: `https://doi.org/10.1038/nature02277`.

[21] E. Goulielmakis et al. "Direct Measurement of Light Waves". In: *Science* 305.5688 (2004), pp. 1267–1269. DOI: `10.1126/science.1100866`. eprint: `https://www.science.org/doi/pdf/10.1126/science.1100866`. URL: `https://www.science.org/doi/abs/10.1126/science.1100866`.

[22] L. Cattaneo et al. "Comparison of attosecond streaking and RABBITT". In: *Opt. Express* 24.25 (Dec. 2016), pp. 29060–29076. DOI: `10.1364/OE.24.029060`. URL: `https://opg.optica.org/oe/abstract.cfm?URI=oe-24-25-29060`.

[23] M. Ossiander et al. "Attosecond correlation dynamics". In: *Nature Physics* 13.3 (Mar. 2017), pp. 280–285. ISSN: 1745-2481. URL: `https://doi.org/10.1038/nphys3941`.

[24] M. Ossiander. *Absolute Photoemission Timing*. en. 2018.

[25] S. Biswas et al. "Probing molecular environment through photoemission delays". In: *Nature Physics* 16.7 (July 2020), pp. 778–783. ISSN: 1745-2481. URL: `https://doi.org/10.1038/s41567-020-0887-8`.

[26] J. E. Riemensberger. "Time-Frequency-Resolved Absolute Time Delay of the Photoelectric Effect". PhD thesis. Technische Universität München, 2018.

[27] T. Boyle. *Outside Looking In*. Bloomsbury Publishing, 2019. ISBN: 9781526604668. URL: `https://books.google.de/books?id=IOONDwAAQBAJ`.

[28] J.-C. Diels. *Ultrashort laser pulse phenomena*. Ed. by W. Rudolph. 2nd ed. Optics and photonics. Amsterdam ; ; London: Elsevier/Academic Press, 2006, : illustrations. ISBN: 0080466400 - 9780080466408 - 1280728892.

[29] R. Trebino. *Frequency-Resolved Optical Gating: The Measurement of Ultrashort Laser Pulses*. Boston, MA: Springer US, 2000. ISBN: 9781461511816 - 9781461354321.

[30] S. B. Park et al. "Direct sampling of a light wave in air". In: *Optica* 5.4 (Apr. 2018), pp. 402–408. DOI: `10.1364/OPTICA.5.000402`. URL: `https://opg.optica.org/optica/abstract.cfm?URI=optica-5-4-402`.

[31] H. Haus. "Mode-locking of lasers". In: *IEEE Journal of Selected Topics in Quantum Electronics* 6.6 (2000), pp. 1173–1185. DOI: `10.1109/2944.902165`.

[32] C. Spielmann et al. "Ultrabroadband femtosecond lasers". In: *IEEE Journal of Quantum Electronics* 30.4 (1994), pp. 1100–1114. DOI: `10.1109/3.291379`.

[33] T. W. Hänsch. "Nobel Lecture: Passion for precision". In: *Rev. Mod. Phys.* 78 (4 Nov. 2006), pp. 1297–1309. DOI: `10.1103/RevModPhys.78.1297`. URL: `https://link.aps.org/doi/10.1103/RevModPhys.78.1297`.

[34] A. Baltuška et al. "Attosecond control of electronic processes by intense light fields". In: *Nature* 421.6923 (Feb. 2003), pp. 611–615. ISSN: 1476-4687. URL: `https://doi.org/10.1038/nature01414`.

[35] H. Haus. "The master equations of mode-locking". In: *Technical Digest. Summaries of papers presented at the Conference on Lasers and Electro-Optics. Postconference Edition. CLEO '99. Conference on Lasers and Electro-Optics (IEEE Cat. No.99CH37013).* 1999, pp. 57–. DOI: `10.1109/CLEO.1999.833873`.

[36] G. A. Reider. *Photonik*. 3. Aufl. Wien [u.a.]: Springer, 2012. ISBN: 9783709115206 - 9783709115213.

[37] H. R. Telle et al. "Carrier-envelope offset phase control: A novel concept for absolute optical frequency measurement and ultrashort pulse generation". In: *Applied Physics B* 69.4 (Oct. 1999), pp. 327–332. ISSN: 1432-0649. URL: `https://doi.org/10.1007/s003400050813`.

[38] T. Fuji et al. "Monolithic carrier-envelope phase-stabilization scheme". In: *Opt. Lett.* 30.3 (Feb. 2005), pp. 332–334. DOI: `10.1364/OL.30.000332`. URL: `https://opg.optica.org/ol/abstract.cfm?URI=ol-30-3-332`.

[39] T. Brabec et al. "Kerr lens mode locking". In: *Opt. Lett.* 17.18 (Sept. 1992), pp. 1292–1294. DOI: `10.1364/OL.17.001292`. URL: `https://opg.optica.org/ol/abstract.cfm?URI=ol-17-18-1292`.

[40] G. P. Agrawal. *Nonlinear fiber optics*. Fifth edition. Amsterdam: Academic Press, 2013, xx, 629 SeitenIllustrationen, Diagramme.

[41] M. Nisoli, S. De Silvestri, and O. Svelto. "Generation of high energy 10 fs pulses by a new pulse compression technique". In: *Applied Physics Letters* 68.20 (1996), pp. 2793–2795. DOI: `10.1063/1.116609`. eprint: `https://doi.org/10.1063/1.116609`. URL: `https://doi.org/10.1063/1.116609`.

[42] M. Nisoli et al. "Toward a terawatt-scale sub-10-fs laser technology". In: *IEEE Journal of Selected Topics in Quantum Electronics* 4.2 (1998), pp. 414–420. DOI: `10.1109/2944.686749`.

[43] J. C. Travers et al. "High-energy pulse self-compression and ultraviolet generation through soliton dynamics in hollow capillary fibres". In: *Nature Photonics* 13.8 (Aug. 2019), pp. 547–554. ISSN: 1749-4893. URL: `https://doi.org/10.1038/s41566-019-0416-4`.

[44] N. H. Burnett et al. "Harmonic generation in CO2 laser target interaction". In: *Applied Physics Letters* 31.3 (1977), pp. 172–174. DOI: `10.1063/1.89628`. eprint: `https://doi.org/10.1063/1.89628`. URL: `https://doi.org/10.1063/1.89628`.

[45] A. McPherson et al. "Studies of multiphoton production of vacuum-ultraviolet radiation in the rare gases". In: *J. Opt. Soc. Am. B* 4.4 (Apr. 1987), pp. 595–601. DOI: `10.1364/JOSAB.4.000595`. URL: `https://opg.optica.org/josab/abstract.cfm?URI=josab-4-4-595`.

[46] M. Ferray et al. "Multiple-harmonic conversion of 1064 nm radiation in rare gases". In: *Journal of Physics B: Atomic, Molecular and Optical Physics* 21.3 (Feb. 1988), p. L31. DOI: `10.1088/0953-4075/21/3/001`. URL: `https://dx.doi.org/10.1088/0953-4075/21/3/001`.

[47] X. F. Li et al. "Multiple-harmonic generation in rare gases at high laser intensity". In: *Phys. Rev. A* 39 (11 June 1989), pp. 5751–5761. DOI: `10.1103/PhysRevA.39.5751`. URL: `https://link.aps.org/doi/10.1103/PhysRevA.39.5751`.

[48] A. L'Huillier, K. J. Schafer, and K. C. Kulander. "Theoretical aspects of intense field harmonic generation". In: *Journal of Physics B: Atomic, Molecular and Optical Physics* 24.15 (Aug. 1991), p. 3315. DOI: `10.1088/0953-4075/24/15/004`. URL: `https://dx.doi.org/10.1088/0953-4075/24/15/004`.

[49] P. B. Corkum. "Plasma perspective on strong field multiphoton ionization". In: *Phys. Rev. Lett.* 71 (13 Sept. 1993), pp. 1994–1997. DOI: `10.1103/PhysRevLett.71.1994`. URL: `https://link.aps.org/doi/10.1103/PhysRevLett.71.1994`.

[50] J. L. Krause, K. J. Schafer, and K. C. Kulander. "High-order harmonic generation from atoms and ions in the high intensity regime". In: *Phys. Rev. Lett.* 68 (24 June 1992), pp. 3535–3538. DOI: `10.1103/PhysRevLett.68.3535`. URL: `https://link.aps.org/doi/10.1103/PhysRevLett.68.3535`.

[51] M. Lewenstein et al. "Theory of high-harmonic generation by low-frequency laser fields". In: *Phys. Rev. A* 49 (3 Mar. 1994), pp. 2117–2132. DOI: `10.1103/PhysRevA.49.2117`. URL: `https://link.aps.org/doi/10.1103/PhysRevA.49.2117`.

[52] A. L'Huillier et al. "High-order Harmonic-generation cutoff". In: *Phys. Rev. A* 48 (5 Nov. 1993), R3433–R3436. DOI: `10.1103/PhysRevA.48.R3433`. URL: `https://link.aps.org/doi/10.1103/PhysRevA.48.R3433`.

[53] P. Antoine et al. "Theory of high-order harmonic generation by an elliptically polarized laser field". In: *Phys. Rev. A* 53 (3 Mar. 1996), pp. 1725–1745. DOI: `10.1103/PhysRevA.53.1725`. URL: `https://link.aps.org/doi/10.1103/PhysRevA.53.1725`.

[54] M. Högner. "Optical High-Order Harmonic Generation in Gas Targets with Spatially Tailored Driving Fields". MA thesis. Ludwig-Maximilians-Universität München, Fakultät für Physik, 2013.

[55] C. Kan et al. "Coherent XUV Generation from Gases Ionized by Several Cycle Optical Pulses". In: *Phys. Rev. Lett.* 79 (16 Oct. 1997), pp. 2971–2974. DOI: `10.1103/PhysRevLett.79.2971`. URL: `https://link.aps.org/doi/10.1103/PhysRevLett.79.2971`.

[56] I. P. Christov, M. M. Murnane, and H. C. Kapteyn. "High-Harmonic Generation of Attosecond Pulses in the "Single-Cycle" Regime". In: *Phys. Rev. Lett.* 78 (7 Feb. 1997), pp. 1251–1254. DOI: `10.1103/PhysRevLett.78.1251`. URL: `https://link.aps.org/doi/10.1103/PhysRevLett.78.1251`.

[57] A. de Bohan et al. "Phase-Dependent Harmonic Emission with Ultrashort Laser Pulses". In: *Phys. Rev. Lett.* 81 (9 Aug. 1998), pp. 1837–1840. DOI: `10.1103/PhysRevLett.81.1837`. URL: `https://link.aps.org/doi/10.1103/PhysRevLett.81.1837`.

[58] M. Högner, V. Yakovlev, and I. Pupeza. *HHGmax*. 2015. URL: `https://mhoegner.gitlab.io/hhgmax-homepage/`.

[59] P. Balcou and A. L'Huillier. "Phase-matching effects in strong-field harmonic generation". In: *Phys. Rev. A* 47 (2 Feb. 1993), pp. 1447–1459. DOI: `10.1103/PhysRevA.47.1447`. URL: `https://link.aps.org/doi/10.1103/PhysRevA.47.1447`.

[60] P. Salières, A. L'Huillier, and M. Lewenstein. "Coherence Control of High-Order Harmonics". In: *Phys. Rev. Lett.* 74 (19 May 1995), pp. 3776–3779. DOI: `10.1103/PhysRevLett.74.3776`. URL: `https://link.aps.org/doi/10.1103/PhysRevLett.74.3776`.

[61] P. Balcou et al. "Generalized phase-matching conditions for high harmonics: The role of field-gradient forces". In: *Phys. Rev. A* 55 (4 Apr. 1997), pp. 3204–3210. DOI: `10.1103/PhysRevA.55.3204`. URL: `https://link.aps.org/doi/10.1103/PhysRevA.55.3204`.

[62] T. Popmintchev et al. "Phase matching of high harmonic generation in the soft and hard X-ray regions of the spectrum". In: *Proceedings of the National Academy of Sciences* 106.26 (2009), pp. 10516–10521. DOI: `10.1073/pnas.0903748106`. eprint: `https://www.pnas.org/doi/pdf/10.1073/pnas.0903748106`. URL: `https://www.pnas.org/doi/abs/10.1073/pnas.0903748106`.

[63] C. M. Heyl et al. "High-order harmonic generation with μJ laser pulses at high repetition rates". In: *Journal of Physics B: Atomic, Molecular and Optical Physics* 45.7 (Mar. 2012), p. 074020. DOI: `10.1088/0953-4075/45/7/074020`. URL: `https://dx.doi.org/10.1088/0953-4075/45/7/074020`.

[64] M. Lewenstein, P. Salières, and A. L'Huillier. "Phase of the atomic polarization in high-order harmonic generation". In: *Phys. Rev. A* 52 (6 Dec. 1995), pp. 4747–4754. DOI: `10.1103/PhysRevA.52.4747`. URL: `https://link.aps.org/doi/10.1103/PhysRevA.52.4747`.

[65] A. Paul et al. "Phase-matching techniques for coherent soft X-ray generation". In: *IEEE Journal of Quantum Electronics* 42.1 (2006), pp. 14–26. DOI: `10.1109/JQE.2005.859914`.

[66] G. Farkas and C. Tóth. "Proposal for attosecond light pulse generation using laser induced multiple-harmonic conversion processes in rare gases". In: *Physics Letters A* 168.5 (1992), pp. 447–450. ISSN: 0375-9601. DOI: `https://doi.org/10.1016/0375-9601(92)90534-S`. URL: `https://www.sciencedirect.com/science/article/pii/037596019290534S`.

[67] P. M. Paul et al. "Observation of a Train of Attosecond Pulses from High Harmonic Generation". In: *Science* 292.5522 (2001), pp. 1689–1692. DOI: `10.1126/science.1059413`. eprint: `https://www.science.org/doi/pdf/10.1126/science.1059413`. URL: `https://www.science.org/doi/abs/10.1126/science.1059413`.

[68] M. Hentschel et al. "Attosecond metrology". In: *Nature* 414.6863 (Nov. 2001), pp. 509–513. ISSN: 1476-4687. URL: `https://doi.org/10.1038/35107000`.

[69] M. Lucchini et al. "Ptychographic reconstruction of attosecond pulses". In: *Opt. Express* 23.23 (Nov. 2015), pp. 29502–29513. DOI: `10.1364/OE.23.029502`. URL: `https://opg.optica.org/oe/abstract.cfm?URI=oe-23-23-29502`.

[70] V. S. Yakovlev et al. "Attosecond Streaking Enables the Measurement of Quantum Phase". In: *Phys. Rev. Lett.* 105 (7 Aug. 2010), p. 073001. DOI: 10.1103/PhysRevLett.105.073001. URL: https://link.aps.org/doi/10.1103/PhysRevLett.105.073001.

[71] Y. Mairesse and F. Quéré. "Frequency-resolved optical gating for complete reconstruction of attosecond bursts". In: *Phys. Rev. A* 71 (1 Jan. 2005), p. 011401. DOI: 10.1103/PhysRevA.71.011401. URL: https://link.aps.org/doi/10.1103/PhysRevA.71.011401.

[72] J. Gagnon, E. Goulielmakis, and V. S. Yakovlev. "The accurate FROG characterization of attosecond pulses from streaking measurements". In: *Applied Physics B* 92.1 (July 2008), pp. 25–32. ISSN: 1432-0649. URL: https://doi.org/10.1007/s00340-008-3063-x.

[73] E. P. Wigner. "Lower Limit for the Energy Derivative of the Scattering Phase Shift". In: *Phys. Rev.* 98 (1 Apr. 1955), pp. 145–147. DOI: 10.1103/PhysRev.98.145. URL: https://link.aps.org/doi/10.1103/PhysRev.98.145.

[74] L. Eisenbud. "The formal properties of nuclear collisions". PhD thesis. 1948, : Illustrationen, Diagramme.

[75] F. T. Smith. "Lifetime Matrix in Collision Theory". In: *Phys. Rev.* 118 (1 Apr. 1960), pp. 349–356. DOI: 10.1103/PhysRev.118.349. URL: https://link.aps.org/doi/10.1103/PhysRev.118.349.

[76] C. W. Clark. "Coulomb phase shift". In: *American Journal of Physics* 47.8 (1979), pp. 683–684. DOI: 10.1119/1.11721. eprint: https://doi.org/10.1119/1.11721. URL: https://doi.org/10.1119/1.11721.

[77] R. Pazourek, S. Nagele, and J. Burgdörfer. "Attosecond chronoscopy of photoemission". In: *Rev. Mod. Phys.* 87 (3 Aug. 2015), pp. 765–802. DOI: 10.1103/RevModPhys.87.765. URL: https://link.aps.org/doi/10.1103/RevModPhys.87.765.

[78] J. Itatani et al. "Attosecond Streak Camera". In: *Phys. Rev. Lett.* 88 (17 Apr. 2002), p. 173903. DOI: 10.1103/PhysRevLett.88.173903. URL: https://link.aps.org/doi/10.1103/PhysRevLett.88.173903.

[79] M. Kitzler et al. "Quantum Theory of Attosecond XUV Pulse Measurement by Laser Dressed Photoionization". In: *Phys. Rev. Lett.* 88 (17 Apr. 2002), p. 173904. DOI: 10.1103/PhysRevLett.88.173904. URL: https://link.aps.org/doi/10.1103/PhysRevLett.88.173904.

[80] J. Gagnon. "Attosecond Electron Spectroscopy". Jan. 2011. URL: http://nbn-resolving.de/urn:nbn:de:bvb:19-125375.

[81] J. Riemensberger et al. "Attosecond Dynamics of *sp*-Band Photoexcitation". In: *Phys. Rev. Lett.* 123 (17 Oct. 2019), p. 176801. DOI: 10.1103/PhysRevLett.123.176801. URL: https://link.aps.org/doi/10.1103/PhysRevLett.123.176801.

[82] S. Neppl et al. "Attosecond Time-Resolved Photoemission from Core and Valence States of Magnesium". In: *Phys. Rev. Lett.* 109 (8 Aug. 2012), p. 087401. DOI: 10.1103/PhysRevLett.109.087401. URL: https://link.aps.org/doi/10.1103/PhysRevLett.109.087401.

[83] S. Neppl et al. "Direct observation of electron propagation and dielectric screening on the atomic length scale". In: *Nature* 517.7534 (Jan. 2015), pp. 342–346. ISSN: 1476-4687. URL: https://doi.org/10.1038/nature14094.

[84] J. M. Rodenburg and H. M. L. Faulkner. "A phase retrieval algorithm for shifting illumination". In: *Applied Physics Letters* 85.20 (2004), pp. 4795–4797. DOI: 10.1063/1.1823034. eprint: https://doi.org/10.1063/1.1823034. URL: https://doi.org/10.1063/1.1823034.

[85] A. M. Maiden and J. M. Rodenburg. "An improved ptychographical phase retrieval algorithm for diffractive imaging". In: *Ultramicroscopy* 109.10 (2009), pp. 1256–1262. ISSN: 0304-3991. DOI: `https://doi.org/10.1016/j.ultramic.2009.05.012`. URL: `https://www.sciencedirect.com/science/article/pii/S0304399109001284`.

[86] C. Brunner et al. "Deep learning in attosecond metrology". In: *Opt. Express* 30.9 (Apr. 2022), pp. 15669–15684. DOI: `10.1364/OE.452108`. URL: `https://opg.optica.org/oe/abstract.cfm?URI=oe-30-9-15669`.

[87] P. D. Keathley et al. "Volkov transform generalized projection algorithm for attosecond pulse characterization". In: *New Journal of Physics* 18.7 (July 2016), p. 073009. DOI: `10.1088/1367-2630/18/7/073009`. URL: `https://dx.doi.org/10.1088/1367-2630/18/7/073009`.

[88] M. Lucchini and M. Nisoli. "Refined Ptychographic Reconstruction of Attosecond Pulses". In: *Applied Sciences* 8.12 (2018). ISSN: 2076-3417. DOI: `10.3390/app8122563`. URL: `https://www.mdpi.com/2076-3417/8/12/2563`.

[89] L. Pedrelli et al. "Complete phase retrieval of photoelectron wavepackets". In: *New Journal of Physics* 22.5 (May 2020), p. 053028. DOI: `10.1088/1367-2630/ab83d7`. URL: `https://dx.doi.org/10.1088/1367-2630/ab83d7`.

[90] J. White and Z. Chang. "Attosecond streaking phase retrieval with neural network". In: *Opt. Express* 27.4 (Feb. 2019), pp. 4799–4807. DOI: `10.1364/OE.27.004799`. URL: `https://opg.optica.org/oe/abstract.cfm?URI=oe-27-4-4799`.

[91] S. Nagele et al. "Time-resolved photoemission by attosecond streaking: extraction of time information". In: *Journal of Physics B: Atomic, Molecular and Optical Physics* 44.8 (Apr. 2011), p. 081001. DOI: `10.1088/0953-4075/44/8/081001`. URL: `https://dx.doi.org/10.1088/0953-4075/44/8/081001`.

[92] J. Rundgren and G. Malmstrom. "Transmission and reflection of low-energy electrons at the surface barrier of a metal". In: *Journal of Physics C: Solid State Physics* 10.23 (Dec. 1977), p. 4671. DOI: `10.1088/0022-3719/10/23/004`. URL: `https://dx.doi.org/10.1088/0022-3719/10/23/004`.

[93] E. Chulkov, V. Silkin, and P. Echenique. "Image potential states on metal surfaces: binding energies and wave functions". In: *Surface Science* 437.3 (1999), pp. 330–352. ISSN: 0039-6028. DOI: `https://doi.org/10.1016/S0039-6028(99)00668-8`. URL: `https://www.sciencedirect.com/science/article/pii/S0039602899006688`.

[94] R. Pazourek et al. "Attosecond Streaking of Correlated Two-Electron Transitions in Helium". In: *Phys. Rev. Lett.* 108 (16 Apr. 2012), p. 163001. DOI: `10.1103/PhysRevLett.108.163001`. URL: `https://link.aps.org/doi/10.1103/PhysRevLett.108.163001`.

[95] F. A. Gianturco, R. R. Lucchese, and N. Sanna. "Calculation of low-energy elastic cross sections for electron-CF4 scattering". In: *The Journal of Chemical Physics* 100.9 (1994), pp. 6464–6471. DOI: `10.1063/1.467237`. eprint: `https://doi.org/10.1063/1.467237`. URL: `https://doi.org/10.1063/1.467237`.

[96] A. P. P. Natalense and R. R. Lucchese. "Cross section and asymmetry parameter calculation for sulfur 1s photoionization of SF6". In: *The Journal of Chemical Physics* 111.12 (1999), pp. 5344–5348. DOI: `10.1063/1.479794`. eprint: `https://doi.org/10.1063/1.479794`. URL: `https://doi.org/10.1063/1.479794`.

[97] D. W. Lindle et al. "Inner-shell photoemission from the iodine atom in CH_3I". In: *Phys. Rev. A* 30 (1 July 1984), pp. 239–244. DOI: `10.1103/PhysRevA.30.239`. URL: `https://link.aps.org/doi/10.1103/PhysRevA.30.239`.

[98] T. N. Olney, G. Cooper, and C. Brion. “Quantitative studies of the photoabsorption (4.5–488 eV) and photoionization (9–59.5 eV) of methyl iodide using dipole electron impact techniques”. In: *Chemical Physics* 232.1 (1998), pp. 211–237. ISSN: 0301-0104. DOI: `https://doi.org/10.1016/S0301-0104(97)00368-6`. URL: `https://www.sciencedirect.com/science/article/pii/S0301010497003686`.

[99] F. Forstmann, W. Berndt, and P. Büttner. “Determination of the Adsorption Site by Low-Energy Electron Diffraction for Iodine on Silver (111)”. In: *Phys. Rev. Lett.* 30 (1 Jan. 1973), pp. 17–19. DOI: `10.1103/PhysRevLett.30.17`. URL: `https://link.aps.org/doi/10.1103/PhysRevLett.30.17`.

[100] B. C. Schardt, S.-L. Yau, and F. Rinaldi. “Atomic Resolution Imaging of Adsorbates on Metal Surfaces in Air: Iodine Adsorption on Pt(111)”. In: *Science* 243.4894 (1989), pp. 1050–1053. DOI: `10.1126/science.243.4894.1050`. eprint: `https://www.science.org/doi/pdf/10.1126/science.243.4894.1050`. URL: `https://www.science.org/doi/abs/10.1126/science.243.4894.1050`.

[101] S. K. Jo and J. White. “Characterization of adsorption states of atomic iodine on Pt(111)”. In: *Surface Science* 261.1 (1992), pp. 111–117. ISSN: 0039-6028. DOI: `https://doi.org/10.1016/0039-6028(92)90222-R`. URL: `https://www.sciencedirect.com/science/article/pii/003960289290222R`.

[102] M. Patanen et al. “Laboratory-frame electron angular distributions: Probing the chemical environment through intramolecular electron scattering”. In: *Phys. Rev. A* 87 (6 June 2013), p. 063420. DOI: `10.1103/PhysRevA.87.063420`. URL: `https://link.aps.org/doi/10.1103/PhysRevA.87.063420`.

[103] V. Dragojlovic. “Conformational analysis of cycloalkanes”. In: *ChemTexts* 1.3 (Aug. 2015), p. 14. ISSN: 2199-3793. URL: `https://doi.org/10.1007/s40828-015-0014-0`.

[104] Y. Mo. “Rotational barriers in alkanes”. In: *WIREs Computational Molecular Science* 1.2 (2011), pp. 164–171. DOI: `https://doi.org/10.1002/wcms.22`. eprint: `https://wires.onlinelibrary.wiley.com/doi/pdf/10.1002/wcms.22`. URL: `https://wires.onlinelibrary.wiley.com/doi/abs/10.1002/wcms.22`.

[105] W. A. Herrebout et al. “Enthalpy Difference between Conformers of n-Butane and the Potential Function Governing Conformational Interchange”. In: *The Journal of Physical Chemistry* 99.2 (1995), pp. 578–585. DOI: `10.1021/j100002a020`. eprint: `https://doi.org/10.1021/j100002a020`. URL: `https://doi.org/10.1021/j100002a020`.

[106] G. M. J. Barca et al. “Recent developments in the general atomic and molecular electronic structure system”. en. In: *The Journal of Chemical Physics* 152.15 (Apr. 2020), p. 154102. ISSN: 0021-9606, 1089-7690. DOI: `10.1063/5.0005188`. URL: `http://aip.scitation.org/doi/10.1063/5.0005188` (visited on 06/18/2020).

[107] J. Dykyj et al. *4 Halogen Containing Organic Compounds, C1: Datasheet from Landolt-Börnstein - Group IV Physical Chemistry · Volume 20A: “Vapor Pressure and Antoine Constants for Hydrocarbons, and S, Se, Te, and Halogen Containing Organic Compounds” in SpringerMaterials (https://doi.org/10.1007/10680373_12).* Ed. by K. R. Hall. Copyright 1999 Springer-Verlag Berlin Heidelberg. DOI: `10.1007/10680373_12`. URL: `https://materials.springer.com/lb/docs/sm_lbs_978-3-540-69071-9_12`.

[108] J. Dykyj et al. *4 Halogen Containing Organic Compounds, C2: Datasheet from Landolt-Börnstein - Group IV Physical Chemistry · Volume 20A: "Vapor Pressure and Antoine Constants for Hydrocarbons, and S, Se, Te, and Halogen Containing Organic Compounds" in SpringerMaterials (https://doi.org/10.1007/10680373_13).* Ed. by K. R. Hall. Copyright 1999 Springer-Verlag Berlin Heidelberg. DOI: `10.1007/10680373_13`. URL: `https://materials.springer.com/lb/docs/sm_lbs_978-3-540-69071-9_13`.

[109] J. Dykyj et al. *4 Halogen Containing Organic Compounds, C3 to C4: Datasheet from Landolt-Börnstein - Group IV Physical Chemistry · Volume 20A: "Vapor Pressure and Antoine Constants for Hydrocarbons, and S, Se, Te, and Halogen Containing Organic Compounds" in SpringerMaterials (https://doi.org/10.1007/10680373_14).* Ed. by K. R. Hall. Copyright 1999 Springer-Verlag Berlin Heidelberg. DOI: `10.1007/10680373_14`. URL: `https://materials.springer.com/lb/docs/sm_lbs_978-3-540-69071-9_14`.

[110] M. Y. Amusia and J.-P. Connerade. "The theory of collective motion probed by light". In: *Reports on Progress in Physics* 63.1 (Jan. 2000), p. 41. DOI: `10.1088/0034-4885/63/1/202`. URL: `https://dx.doi.org/10.1088/0034-4885/63/1/202`.

[111] J. P. Connerade. "Controlled Collapse and the Profiles of 'Giant Resonances'". In: *Giant Resonances in Atoms, Molecules, and Solids*. Ed. by J. P. Connerade, J. M. Esteva, and R. C. Karnatak. Boston, MA: Springer US, 1987, pp. 3–23. ISBN: 978-1-4899-2004-1. DOI: `10.1007/978-1-4899-2004-1_1`. URL: `https://doi.org/10.1007/978-1-4899-2004-1_1`.

[112] Y.-J. Chen et al. "Theoretical characterization of the collective resonance states underlying the xenon giant dipole resonance". In: *Phys. Rev. A* 91 (3 Mar. 2015), p. 032503. DOI: `10.1103/PhysRevA.91.032503`. URL: `https://link.aps.org/doi/10.1103/PhysRevA.91.032503`.

[113] F. J. Comes, U. Nielsen, and W. H. E. Schwarz. "Inner electron excitation of iodine in the gaseous and solid phase". In: *The Journal of Chemical Physics* 58.6 (1973), pp. 2230–2237. DOI: `10.1063/1.1679497`. eprint: `https://doi.org/10.1063/1.1679497`. URL: `https://doi.org/10.1063/1.1679497`.

[114] L. Nahon, A. Svensson, and P. Morin. "Experimental study of the 4d ionization continuum in atomic iodine by photoelectron and photoion spectroscopy". In: *Phys. Rev. A* 43 (5 Mar. 1991), pp. 2328–2337. DOI: `10.1103/PhysRevA.43.2328`. URL: `https://link.aps.org/doi/10.1103/PhysRevA.43.2328`.

[115] L.-W. Pi and A. S. Landsman. "Attosecond Time Delay in Photoionization of Noble-Gas and Halogen Atoms". In: *Applied Sciences* 8.3 (2018). ISSN: 2076-3417. DOI: `10.3390/app8030322`. URL: `https://www.mdpi.com/2076-3417/8/3/322`.

[116] J. N. Cutler, G. M. Bancroft, and K. H. Tan. "Ligand-field splittings and core-level linewidths in I 4d photoelectron spectra of iodine molecules". In: *The Journal of Chemical Physics* 97.11 (1992), pp. 7932–7943. DOI: `10.1063/1.463468`. eprint: `https://doi.org/10.1063/1.463468`. URL: `https://doi.org/10.1063/1.463468`.

[117] A. M. Duensing. *Absolute Timing of Photoionization in H2O*. en. 2023.

[118] J. A. Bearden and A. F. Burr. "Reevaluation of X-Ray Atomic Energy Levels". In: *Rev. Mod. Phys.* 39 (1 Jan. 1967), pp. 125–142. DOI: `10.1103/RevModPhys.39.125`. URL: `https://link.aps.org/doi/10.1103/RevModPhys.39.125`.

[119] B. Henke, E. Gullikson, and J. Davis. "X-Ray Interactions: Photoabsorption, Scattering, Transmission, and Reflection at E = 50-30,000 eV, Z = 1-92". In: *Atomic Data and Nuclear Data Tables* 54.2 (1993), pp. 181–342. ISSN: 0092-640X. DOI: `https://doi.org/10.1006/adnd.1993.1013`. URL: `https://www.sciencedirect.com/science/article/pii/S0092640X83710132`.

[120] R. Forbes et al. "Photoionization of the I 4d and valence orbitals of methyl iodide". In: *Journal of Physics B: Atomic, Molecular and Optical Physics* 53.15 (June 2020), p. 155101. DOI: `10.1088/1361-6455/ab8c5a`. URL: `https://dx.doi.org/10.1088/1361-6455/ab8c5a`.

[121] L. Karlsson et al. "The NVV Auger electron spectrum of the HI molecule". In: *Journal of Physics B: Atomic, Molecular and Optical Physics* 22.19 (Oct. 1989), p. 3001. DOI: `10.1088/0953-4075/22/19/014`. URL: `https://dx.doi.org/10.1088/0953-4075/22/19/014`.

[122] M. Drescher et al. "Time-resolved atomic inner-shell spectroscopy". In: *Nature* 419.6909 (Oct. 2002), pp. 803–807. ISSN: 1476-4687. URL: `https://doi.org/10.1038/nature01143`.

[123] M. Ostner. *Estimation of the Influence of Auger Electrons on Photoemission Timing via Attosecond Streaking*.

[124] U. Saalmann and J. M. Rost. "Proper Time Delays Measured by Optical Streaking". In: *Phys. Rev. Lett.* 125 (11 Sept. 2020), p. 113202. DOI: `10.1103/PhysRevLett.125.113202`. URL: `https://link.aps.org/doi/10.1103/PhysRevLett.125.113202`.

[125] M. Isinger et al. "Photoionization in the time and frequency domain". In: *Science* 358.6365 (2017), pp. 893–896. DOI: `10.1126/science.aao7043`. eprint: `https://www.science.org/doi/pdf/10.1126/science.aao7043`. URL: `https://www.science.org/doi/abs/10.1126/science.aao7043`.

[126] R. O. Kuzian and E. E. Krasovskii. "One-step theory of photoelectron escape time: Attosecond spectroscopy of Mg(0001)". In: *Phys. Rev. B* 102 (11 Sept. 2020), p. 115116. DOI: `10.1103/PhysRevB.102.115116`. URL: `https://link.aps.org/doi/10.1103/PhysRevB.102.115116`.

[127] J. Benda, Z. Ma šín, and J. D. Gorfinkiel. "Analysis of RABITT time delays using the stationary multiphoton molecular *R*-matrix approach". In: *Phys. Rev. A* 105 (5 May 2022), p. 053101. DOI: `10.1103/PhysRevA.105.053101`. URL: `https://link.aps.org/doi/10.1103/PhysRevA.105.053101`.

[128] P. Hockett et al. "Time delay in molecular photoionization". In: *Journal of Physics B: Atomic, Molecular and Optical Physics* 49.9 (Apr. 2016), p. 095602. DOI: `10.1088/0953-4075/49/9/095602`. URL: `https://dx.doi.org/10.1088/0953-4075/49/9/095602`.

[129] D. Baykusheva and H. J. Wörner. "Theory of attosecond delays in molecular photoionization". In: *The Journal of Chemical Physics* 146.12 (2017), p. 124306. DOI: `10.1063/1.4977933`. eprint: `https://doi.org/10.1063/1.4977933`. URL: `https://doi.org/10.1063/1.4977933`.

[130] M. Magrakvelidze, M. E.-A. Madjet, and H. S. Chakraborty. "Attosecond delay of xenon 4*d* photoionization at the giant resonance and Cooper minimum". In: *Phys. Rev. A* 94 (1 July 2016), p. 013429. DOI: `10.1103/PhysRevA.94.013429`. URL: `https://link.aps.org/doi/10.1103/PhysRevA.94.013429`.

[131] A. C. Brown et al. "RMT: R-matrix with time-dependence. Solving the semi-relativistic, time-dependent Schrödinger equation for general, multielectron atoms and molecules in intense, ultrashort, arbitrarily polarized laser pulses". In: *Computer Physics Communications* 250 (2020), p. 107062. ISSN: 0010-4655. DOI: `https://doi.org/10.1016/j.cpc.2019.107062`. URL: `https://www.sciencedirect.com/science/article/pii/S0010465519303856`.

[132] Z. Mašín et al. "UKRmol+: A suite for modelling electronic processes in molecules interacting with electrons, positrons and photons using the R-matrix method". In: *Computer Physics Communications* 249 (2020), p. 107092. ISSN: 0010-4655. DOI: `https://doi.org/10.1016/j.cpc.2019.107092`. URL: `https://www.sciencedirect.com/science/article/pii/S0010465519303972`.

[133] J. P. Connerade. "A general formula for the profiles of 'giant resonances"'. In: *Journal of Physics B: Atomic and Molecular Physics* 17.6 (Mar. 1984), p. L165. DOI: `10.1088/0022-3700/17/6/003`. URL: `https://dx.doi.org/10.1088/0022-3700/17/6/003`.

[134] J. .-. Connerade and A. M. Lane. "Interacting resonances in atomic spectroscopy". In: *Reports on Progress in Physics* 51.11 (Nov. 1988), p. 1439. DOI: `10.1088/0034-4885/51/11/002`. URL: `https://dx.doi.org/10.1088/0034-4885/51/11/002`.

[135] G. E. Bacon et al. "A crystallographic study of solid benzene by neutron diffraction". In: *Proceedings of the Royal Society of London. Series A. Mathematical and Physical Sciences* 279.1376 (1964), pp. 98–110. DOI: `10.1098/rspa.1964.0092`. eprint: `https://royalsocietypublishing.org/doi/pdf/10.1098/rspa.1964.0092`. URL: `https://royalsocietypublishing.org/doi/abs/10.1098/rspa.1964.0092`.

[136] E. Białkowska-Jaworska, M. Jaworski, and Z. Kisiel. "The structure of cyclohexane, F-, Cl-, Br- and I-cyclohexane". In: *Journal of Molecular Structure* 350.3 (1995), pp. 247–254. ISSN: 0022-2860. DOI: `https://doi.org/10.1016/0022-2860(94)08481-V`. URL: `https://www.sciencedirect.com/science/article/pii/002228609408481V`.

[137] F. R. Jensen and C. H. Bushweller. "Separation of conformers. II. Axial and equatorial isomers of chlorocyclohexane and trideuteriomethoxycyclohexane". In: *Journal of the American Chemical Society* 91.12 (1969), pp. 3223–3225. DOI: `10.1021/ja01040a022`. eprint: `https://doi.org/10.1021/ja01040a022`. URL: `https://doi.org/10.1021/ja01040a022`.

[138] H. Hoffmann, P. Griffiths, and F. Zaera. "A RAIRS study on the surface chemistry of ethyl iodide on Pt(111)". In: *Surface Science* 262.1 (1992), pp. 141–150. ISSN: 0039-6028. DOI: `https://doi.org/10.1016/0039-6028(92)90466-J`. URL: `https://www.sciencedirect.com/science/article/pii/003960289290466J`.

[139] F. Zaera. "Preparation and reactivity of alkyl groups adsorbed on metal surfaces". In: *Accounts of chemical research* 25.6 (1992), pp. 260–265.

[140] E. Magerl et al. "A flexible apparatus for attosecond photoelectron spectroscopy of solids and surfaces". In: *Review of Scientific Instruments* 82.6 (2011), p. 063104. DOI: `10.1063/1.3596564`. eprint: `https://doi.org/10.1063/1.3596564`. URL: `https://doi.org/10.1063/1.3596564`.

[141] C. N. Berglund and W. E. Spicer. "Photoemission Studies of Copper and Silver: Theory". In: *Phys. Rev.* 136 (4A Nov. 1964), A1030–A1044. DOI: `10.1103/PhysRev.136.A1030`. URL: `https://link.aps.org/doi/10.1103/PhysRev.136.A1030`.

[142] Z. Tao et al. “Direct time-domain observation of attosecond final-state lifetimes in photoemission from solids”. In: *Science* 353.6294 (2016), pp. 62–67. DOI: `10.1126/science.aaf6793`. eprint: `https://www.science.org/doi/pdf/10.1126/science.aaf6793`. URL: `https://www.science.org/doi/abs/10.1126/science.aaf6793`.

[143] L. Kasmi et al. “Effective mass effect in attosecond electron transport”. In: *Optica* 4.12 (Dec. 2017), pp. 1492–1497. DOI: `10.1364/OPTICA.4.001492`. URL: `https://opg.optica.org/optica/abstract.cfm?URI=optica-4-12-1492`.

[144] S. Heinrich et al. “Attosecond intra-valence band dynamics and resonant-photoemission delays in W(110)”. In: *Nature Communications* 12.1 (June 2021), p. 3404. ISSN: 2041-1723. URL: `https://doi.org/10.1038/s41467-021-23650-7`.

[145] C. Lemell et al. “Simulation of attosecond streaking of electrons emitted from a tungsten surface”. In: *Phys. Rev. A* 79 (6 June 2009), p. 062901. DOI: `10.1103/PhysRevA.79.062901`. URL: `https://link.aps.org/doi/10.1103/PhysRevA.79.062901`.

[146] C. Lemell et al. “Real-time observation of collective excitations in photoemission”. In: *Phys. Rev. B* 91 (24 June 2015), p. 241101. DOI: `10.1103/PhysRevB.91.241101`. URL: `https://link.aps.org/doi/10.1103/PhysRevB.91.241101`.

[147] G. D. Mahan. “Theory of Photoemission in Simple Metals”. In: *Phys. Rev. B* 2 (11 Dec. 1970), pp. 4334–4350. DOI: `10.1103/PhysRevB.2.4334`. URL: `https://link.aps.org/doi/10.1103/PhysRevB.2.4334`.

[148] J. B. Pendry. “The application of pseudopotentials to low-energy electron diffraction I. Calculation of the potential and ‘inner potential’”. In: *Journal of Physics C: Solid State Physics* 2.7 (July 1969), p. 1215. DOI: `10.1088/0022-3719/2/7/314`. URL: `https://dx.doi.org/10.1088/0022-3719/2/7/314`.

[149] J. B. Pendry. “The application of pseudopotentials to low-energy electron diffraction II: Calculation of the reflected intensities”. In: *Journal of Physics C: Solid State Physics* 2.12 (Dec. 1969), p. 2273. DOI: `10.1088/0022-3719/2/12/310`. URL: `https://dx.doi.org/10.1088/0022-3719/2/12/310`.

[150] J. B. Pendry. “The application of pseudopotentials to low-energy electron diffraction III: The simplifying effect of inelastic scattering”. In: *Journal of Physics C: Solid State Physics* 2.12 (Dec. 1969), p. 2283. DOI: `10.1088/0022-3719/2/12/311`. URL: `https://dx.doi.org/10.1088/0022-3719/2/12/311`.

[151] J. Pendry. “Theory of photoemission”. In: *Surface Science* 57.2 (1976), pp. 679–705. ISSN: 0039-6028. DOI: `https://doi.org/10.1016/0039-6028(76)90355-1`. URL: `https://www.sciencedirect.com/science/article/pii/0039602876903551`.

[152] C.-H. Zhang and U. Thumm. “Attosecond Photoelectron Spectroscopy of Metal Surfaces”. In: *Phys. Rev. Lett.* 102 (12 Mar. 2009), p. 123601. DOI: `10.1103/PhysRevLett.102.123601`. URL: `https://link.aps.org/doi/10.1103/PhysRevLett.102.123601`.

[153] E. E. Krasovskii et al. “Rapid propagation of a Bloch wave packet excited by a femtosecond ultraviolet pulse”. In: *Phys. Rev. B* 94 (19 Nov. 2016), p. 195434. DOI: `10.1103/PhysRevB.94.195434`. URL: `https://link.aps.org/doi/10.1103/PhysRevB.94.195434`.

[154] D. R. Penn. “Electron mean-free-path calculations using a model dielectric function”. In: *Phys. Rev. B* 35 (2 Jan. 1987), pp. 482–486. DOI: `10.1103/PhysRevB.35.482`. URL: `https://link.aps.org/doi/10.1103/PhysRevB.35.482`.

[155] S. Mao et al. “Electron inelastic scattering and secondary electron emission calculated without the single pole approximation”. In: *Journal of Applied Physics* 104.11 (2008), p. 114907.

[156] S. Tanuma, C. J. Powell, and D. R. Penn. "Calculations of electron inelastic mean free paths. IX. Data for 41 elemental solids over the 50 eV to 30 keV range". In: *Surface and Interface Analysis* 43.3 (2011), pp. 689–713. DOI: `https://doi.org/10.1002/sia.3522`. eprint: `https://analyticalsciencejournals.onlinelibrary.wiley.com/doi/pdf/10.1002/sia.3522`. URL: `https://analyticalsciencejournals.onlinelibrary.wiley.com/doi/abs/10.1002/sia.3522`.

[157] E. E. Krasovskii et al. "Determination of the Hole Lifetime from Photoemission: Ti 3*d* States in $TiTe_2$". In: *Phys. Rev. Lett.* 98 (21 May 2007), p. 217604. DOI: `10.1103/PhysRevLett.98.217604`. URL: `https://link.aps.org/doi/10.1103/PhysRevLett.98.217604`.

[158] E. E. Krasovskii et al. "Photoemission from Al(100) and (111): Experiment and ab initio theory". In: *Phys. Rev. B* 78 (16 Oct. 2008), p. 165406. DOI: `10.1103/PhysRevB.78.165406`. URL: `https://link.aps.org/doi/10.1103/PhysRevB.78.165406`.

[159] V. N. Strocov et al. "Three-dimensional band structure of layered $TiTe_2$: Photoemission final-state effects". In: *Phys. Rev. B* 74 (19 Nov. 2006), p. 195125. DOI: `10.1103/PhysRevB.74.195125`. URL: `https://link.aps.org/doi/10.1103/PhysRevB.74.195125`.

[160] E. E. Krasovskii et al. "Surface resonances in electron reflection from overlayers". In: *Journal of Physics: Condensed Matter* 27.3 (Dec. 2014), p. 035501. DOI: `10.1088/0953-8984/27/3/035501`. URL: `https://dx.doi.org/10.1088/0953-8984/27/3/035501`.

[161] W. S. M. Werner, K. Glantschnig, and C. Ambrosch-Draxl. "Optical Constants and Inelastic Electron-Scattering Data for 17 Elemental Metals". In: *Journal of Physical and Chemical Reference Data* 38.4 (2009), pp. 1013–1092. DOI: `10.1063/1.3243762`. eprint: `https://doi.org/10.1063/1.3243762`. URL: `https://doi.org/10.1063/1.3243762`.

[162] F. Siek et al. "Angular momentum–induced delays in solid-state photoemission enhanced by intra-atomic interactions". In: *Science* 357.6357 (2017), pp. 1274–1277. DOI: `10.1126/science.aam9598`. eprint: `https://www.science.org/doi/pdf/10.1126/science.aam9598`. URL: `https://www.science.org/doi/abs/10.1126/science.aam9598`.

[163] C. Chen et al. "Distinguishing attosecond electron–electron scattering and screening in transition metals". In: *Proceedings of the National Academy of Sciences* 114.27 (2017), E5300–E5307. DOI: `10.1073/pnas.1706466114`. eprint: `https://www.pnas.org/doi/pdf/10.1073/pnas.1706466114`. URL: `https://www.pnas.org/doi/abs/10.1073/pnas.1706466114`.

[164] J. C. Fuggle and N. Mårtensson. "Core-level binding energies in metals". In: *Journal of Electron Spectroscopy and Related Phenomena* 21.3 (1980), pp. 275–281. ISSN: 0368-2048. DOI: `https://doi.org/10.1016/0368-2048(80)85056-0`. URL: `https://www.sciencedirect.com/science/article/pii/0368204880850560`.

[165] M. D. Hanwell et al. "Avogadro: an advanced semantic chemical editor, visualization, and analysis platform". In: *Journal of Cheminformatics* 4.1 (Aug. 2012), p. 17. ISSN: 1758-2946. URL: `https://doi.org/10.1186/1758-2946-4-17`.

[166] Persistence of Vision Pty. Ltd. *Persistence of Vision Raytracer (Version 3.7) [Computer Software]*. Retrieved from http://www.povray.org/download/. 2023.

[167] S. Kim et al. "PubChem 2023 update". In: *Nucleic Acids Research* 51.D1 (Oct. 2022), pp. D1373–D1380. ISSN: 0305-1048. DOI: `10.1093/nar/gkac956`. eprint: `https://academic.oup.com/nar/article-pdf/51/D1/D1373/48441598/gkac956.pdf`. URL: `https://doi.org/10.1093/nar/gkac956`.

[168] A. Herrera-Gomez et al. "Practical methods for background subtraction in photoemission spectra". In: *Surface and Interface Analysis* 46.10-11 (2014), pp. 897–905. DOI: `10.1002/sia.5453`. eprint: `https://onlinelibrary.wiley.com/doi/pdf/10.1002/sia.5453`. URL: `https://onlinelibrary.wiley.com/doi/abs/10.1002/sia.5453`.

[169] A. Kim. *Attosecond time-resolved photoemission from solid samples*. en. 2015.

[170] A. Guggenmos et al. "Chromium/scandium multilayer mirrors for isolated attosecond pulses at 145 eV". In: *Opt. Lett.* 40.12 (June 2015), pp. 2846–2849. DOI: `10.1364/OL.40.002846`. URL: `https://opg.optica.org/ol/abstract.cfm?URI=ol-40-12-2846`.

[171] J. D. Hunter. "Matplotlib: A 2D graphics environment". In: *Computing In Science & Engineering* 9.3 (2007), pp. 90–95. DOI: `10.1109/MCSE.2007.55`.

[172] ImageMagick Studio LLC. *ImageMagick*. Version 7.0.10. Jan. 4, 2023. URL: `https://imagemagick.org`.

[173] C. R. Harris et al. "Array programming with NumPy". In: *Nature* 585.7825 (Sept. 2020), pp. 357–362. DOI: `10.1038/s41586-020-2649-2`. URL: `https://doi.org/10.1038/s41586-020-2649-2`.

[174] P. Virtanen et al. "SciPy 1.0: Fundamental Algorithms for Scientific Computing in Python". In: *Nature Methods* 17 (2020), pp. 261–272. DOI: `10.1038/s41592-019-0686-2`.

Acknowledgements

In the roughly 4.5 years I spent working on the results presented here (and also in the 28 years leading up to now) I was accompanied by wonderful people to whom I am indebted to sincere gratitude. They have not only greatly contributed to the professional aspect of my life in that time, but also on a personal level.

First and foremost, I want to thank **Prof. Reinhard Kienberger** for the opportunity to do exciting research at the forefront of attosecond science. The freedom and encouragement to pursue one's own ideas you propagate has led to the inception of the project on the Iodoalkanes, and in extension ultimately to more experimental studies, which will continue to yield interesting results of great relevance to our field. I am grateful for having been able to study and work under your supervision since my Bachelor's. It has been a wonderful time.

My mentor **Dr. Johann Riemensberger** has been a major formative influence on my developement as a researcher. Thank you for your eagerness to share your immense knowledge, and thank you for your encouragement and for offering experienced judgement. You are a role-model to me.

Spending long days and nights in the lab, struggling with an exceptionally skittish and moody laser and wrestling with the quirks of an attosecond beamline can be daunting, but it is less so with **Maximilian Pollanka** by your side. Thank you for being there and actively supporting my experiments. I believe that we have used the AS101 beamline to what is currently its full potential and at **max**imum efficiency. Travelling to Vilnius, Orlando, New York City and Hannover with you was an incredible experience.

Pascal Scigalla and I have been colleagues since our Bachelor's. Your outstanding technical skills and your ability to procure laughter and thereby foster the utter resilience necessary to persist in the face of even the most forlorn situations one may encounter in the lab have been nothing but a blessing. Thank you!

Dr. Andreas Duensing and **Michael Mittermair** taught me the art of attosecond streaking, how to work with vacuum appliances, how to handle a laser beam and countless other things. You have been with me since my first day at E11, and I am eternally grateful for having been able to learn from your immense experience and knowledge.

The supervision of the Bachelor's theses of **Martin Wanckel** and **Matthias Ostner** was an enjoyable experience. Students like you are responsible for the most wonderful moments one can have in teaching. I wish the two of you all the best for your future endeavors, and I hope that you remember your time at E11 with as much fondness as I remember yours.

Maximilian Forster, **Sven Paul** and **Konstantin Seidenfus** are not only amazing Master's students but also great lab companions. Engaging with you in the process of planning and performing experiments as well as discussing their evaluations and the results' implications is so much fun! So is playing

Quake and *SuperTux Kart* with you guys, even though all three of you make sure to regularly put me in my place there.

Peter Müller and **Rafael Jahrsdorfer** have supported our experiments with their invaluable machining and mechanical contrsuction skills. Thank you for delivering urgently needed parts in record time and offering valuable insights and improvements. I also want to thank **Stefanie Völkl** and **Susanne Würzinger** for helping me navigate the the thicket of administrative tasks. A **big** "Thank you!" goes out to everyone else at E11 for making it the wonderful place to work at that it is.

In the last 1.5 years we have been able to foster a wonderful cooperation with **Dr. Zdeněk Mašín** and **Dr. Jakub Benda**. Thank you for many enlightening discussions on the topic of molecular photoemission. I have learned a lot and I am confident that in the course of our ongoing pursuit to unravel the secrets of molecular photoionization I will learn a lot more. One of my favorite trips I was able to take during my time as a PhD student was to visit you in Prague.

One should never pass up an opportunity to learn new things, and in intense discussions with **Eugene Krasovskii** I learned plenty. Thank you for patiently explaining the intricacies of solid-state photoemission and the pitfalls of the measurement of photoemission timing at surfaces to me, and thank you for your efforts in the conquest to unravel the mysteries of the W(110) surface.

My therapist **Jennifer Pöhl** has made major positive contributions to my life. Thank you for your counsel and guidance, and thank you for teaching me how to cope with my obsessive-compulsive disorder. Mental illness is a harsh and cruel master. The pain and damage it inflicts upon a person is very real, but one must not forget that so is hope. *Reach out for help if you feel like you cannot continue on your own.* ***You are not alone!***

My partner **Purva Choudhary** has stood by my side through some of the most stressful times of my PhD. Thank you for bringing balance into my life, thank you for being so supportive of me and my plans, and thank you for lifting me up whenever things seem to go sideways. You are the light of my life. You are happiness.

I am grateful for the strong and friendly bond my brothers **Peter** and **Lukas** and I have, and I am grateful for the environment my parents **Peter** and **Andrea** created, which enabled us to grow and find our own ways in life. Your encouragement, as well as your unconditional love and support is invaluable.